# Rotational Spectroscopic and Computational Studies on Inter/Intramolecular Bonding

A Thesis
Submitted for the Degree of
*Doctor of Philosophy*
in the Faculty of Science

by

**Sharon Priya Gnanasekar**


**Department of Inorganic and Physical Chemistry**
**INDIAN INSTITUTE OF SCIENCE**
Bangalore-560012, India
September, 2020

# DECLARATION

I hereby declare that the work presented in this thesis titled **Rotational Spectroscopic and Computational Studies on Inter/Intramolecular Bonding** has been carried out by me at the Department of Inorganic and Physical Chemistry, Indian Institute of Science, Bangalore, India, under the supervision of Prof. E. Arunan.

Sharon Priya Gnanasekar

September, 2020. Sharon Priya Gnanasekar

# CERTIFICATE

I hereby certify that the work presented in this thesis titled **Rotational Spectroscopic and Computational Studies on Inter/Intramolecular Bonding** has been carried out by Sharon Priya Gnanasekar at the Department of Inorganic and Physical Chemistry, Indian Institute of Science, Bangalore, India, under my supervision.

September, 2020. Prof. E. Arunan

Soli Deo gloria

# ACKNOWLEDGEMENTS

This Thesis would not have been possible without the help of many people and I am extremely obliged for all their assistance. I apologize if I have missed any names.

I take this opportunity to express my heartfelt gratitude to Prof. Arunan. I am thankful to him for allowing me to work in his lab. I am extremely fortunate to have been allowed to do whatever I wanted. Sir has always encouraged me to pursue whatever I wanted to do. He has been extremely supportive and especially when the spectrometer had stopped working for nearly a year, he was always there in the lab with us trying to make things work. He has always been available, even at odd hours to answer my doubts. He has patiently answered the same questions over and over again till I have understood them. I am grateful to him for teaching me, for being there for me, and for his constant guidance, support and encouragement.

As an Int. PhD student I was required to take many courses and I express my gratitude to all my course instructors for teaching with such sincerity and helping me understand the difficult parts of a subject. I would like to specially thank Prof. Vempati and Prof. Vasu for having to teach someone who was unfamiliar with the field.

I thank Prof. Sebastian for the opportunity to be a TA for his course. I learnt a lot from him.

I appreciate the assistance provided by Prof. Sai Ramesh regarding all things computational. He was always available to help, even with the smallest of problems, for which I am grateful. I would also like to thank Dr. Jayashree Nagesh for her help with understanding the NBO calculations.

I am thankful to Prof. Mathias for his help fixing and repairing the various components of the spectrometer. I would also like to thank Dr. Mausumi Goswami for her help with understanding the programs that control the spectrometer.

The assistance of Prof. Robert Georges and Prof. Therese Huet in making the visit to Lille possible is acknowledged. I am extremely grateful to Dr. Manuel Goubet for making the experiments with $CH_3F$ possible, for his guidance with the experiments and his generous hospitality during my stay in Lille. I am thankful to Dr. Sabath Bteich for her assistance and friendship during my visit to Lille.

I would like to acknowledge the fruitful discussions with Dr. Jon Hougen regarding the $CH_3CN$-$CO_2$ spectra. The internal rotor program given to us by Prof. Vadim Ilyushin is deeply appreciated. I would also like to thank Prof. Balaram for giving us a large bottle of acetonitrile.

I am grateful to Lakshay Kathuria and Nidhi Sharma for distilling the propargyl alcohol. I acknowledge the help provided by Mr. Lokenathan and Mr. Arul Nambi regarding all electrical and plumbing requirements. The help provided by the cleaning staff in maintaining our lab is deeply appreciated.

I would like to thank the past and present Chairmen of IPC and the office staff for all their help with the administrative and official matters. I acknowledge IISc and CSIR for the scholarship. I am thankful to CEFIPRA for the funding to carry out experiments in Lille. I am also thankful to ODAA for the funding to present my work at ISMS-Illinois.

I would like to thank Mrs. Arunan for her kindness and generosity. She has always welcomed us to her home for dinners during festivals. She has always extended her assistance whenever I have required it, and I am extremely grateful for the same.

I acknowledge my lab mates Dr. Devendra Mani, Dr. Abhishek Shahi, Dr. Sharath, Dr. Emmanuel Etim, Kunal, Kiran, Kabir, Govinda, Arijit, Subharaj, Surabhi, Dipak, Sumaiya, Dr. Sarvesh Pandey for all their help and support. I am also thankful to all the project and UG students who visited our lab. I would like to specially thank Devendra bhaiya and Abhishek bhaiya for patiently answering all my questions, and for teaching me about the spectrometer and the experiment. I am grateful for their constant help and guidance.

I would like to thank all the members of the Chemical Dynamics Group meeting. I have learnt a lot from them. I would like to thank Prof. Sebastian, Prof. P. K. Das, Prof. Arunan, Prof. Harbola, Prof. Sai Ramesh and Prof. Bhattacharya for enthusiastically asking questions and explaining concepts. I would like to specially thank Dr. Deepika Janakiraman and Dr. Pallavi Bhattacharya for helping me understand the difficult topics being discussed so that I would be able to follow the presentations.

I would like to acknowledge the friendship, encouragement and help extended towards me by my Int. Phd. Batchmates, Aishani, Balaka, Kritika, Nidhi, Veena, Debanjan, Jyotirmoy, Rajesh, Ramkrishna, Rudra, Rupak, Sabyasachi, and Sourav. I would like to thank Sourav for teaching us how to program in LabView. I am especially thankful for the friendship and company of Rudra, Rupak, Balaka, Nidhi and Jyotirmoy. I would also like to thank Kamini di for her friendship. I am thankful to everyone who adopted me to eat with them, so that I never had to eat alone. I am especially thankful to Deep and Arijit for their friendship and all the funny stories.

I am grateful to the IISc Basketball Team, for being a place where I could unwind and relax. I am especially thankful to our coach, Digvijay Sir, for taking so much trouble to make sure we were ready for the tournaments. I am thankful to Jaya and Warsha for their friendship.

I am extremely grateful to Chirasmita for her love and friendship and for all her help. For being available at odd hours to help me, for encouraging me and supporting me, for their love and friendship, I am forever grateful to my friends Srija and Subhasish, though we are miles apart.

For teaching me with enthusiasm and for encouraging my interest in science and maths and for being there for me, I thank my school teachers, Mrs. S. Das, Mrs. B. Elias and Mrs. M. Subramaniam. I express my sincere gratitude to Dr. I Chakraborty and Dr. R.

Sharma for making me fall in love with physical chemistry and for their advice, support and constant encouragement.

For being my home away from home, I am extremely thankful for Debarati di and Dev bhaiya. I thank them for their advice and encouragement throughout my PhD and am indebted for their help with all my presentations and writing and for proofreading this Thesis. I am deeply grateful to Debarati di for her kindness and affection. I acknowledge her help, support and friendship. I am extremely grateful to Dev bhaiya for his patience and friendship.

For being my pillars of support and for their constant prayers and encouragement, I thank my grandparents and parents. I am thankful to them for letting me do whatever I wanted to do and for tolerating the tantrums. I am especially thankful to my mother for proofreading this Thesis despite having no knowledge of Chemistry and for remembering all the molecules I worked with and listening to all the problems with the spectra. I am forever thankful to my sister, for her love and friendship, and for being the cheerleader and critic for everything I do.

Lastly, whatever I am able to do, would not be possible without the Almighty. I acknowledge his guiding presence in my life.

# SYNOPSIS

The importance of non-covalent interactions cannot be undermined, as it permeates nearly every sphere of chemistry. The hydrogen bond is the most well-known and ubiquitous non-covalent interaction. In recent times similar interactions involving other elements, that include nearly half the periodic table, have been proposed and studied. The tetrel bond (Group 14 elements) is one such interaction which is analogous to the hydrogen bond[1,2]. The 'carbon bond' is an important subset of these interactions[1]. Our objective is to understand these non-covalent interactions by studying the structures of weakly bound complexes.

Rotational spectroscopy is an extremely accurate technique to obtain the geometrical parameters of molecules in the gas phase. We have used a home-built pulsed nozzle Fourier transform microwave (PNFTMW) spectrometer to record the spectra[3]. Weakly bound complexes are formed via a supersonic expansion of the gases into a vacuum chamber. These complexes interact with the microwave radiation to give a rotational spectrum. Structural information is then extracted from the rotational spectrum. The rotational spectroscopic studies are supplemented by computational studies such as the Atoms in Molecules theory. There is a paucity of experimental data involving tetrel bonded interactions. This *Thesis* focusses on hydrogen and tetrel bonded complexes.

*Chapter 1* of this thesis gives a brief introduction to non-covalent interactions and expounds on the hydrogen and tetrel bonding interactions. This chapter also provides pertinent details about rotational spectroscopy. *Chapter 2* details the functioning of the microwave spectrometer and other computational methods used in the *Thesis*.

*Chapter 3* discusses the rotational spectra of the propargyl alcohol (PA)···water complex. PA is multifunctional molecule having a hydroxyl group and an acetylenic moiety. The hydroxyl group present in both alcohol and water can act as either an H-bond donor or as an H-bond acceptor. This offers different binding options leading to a number of different possible hydrogen bonded structures for the PA···$H_2O$ complex. The two lowest energy structures calculated for the complex differ only in the position of the non-bonded hydrogen atom. The spectrum obtained indicates the presence of the global minimum structure, G-PW-1a. In this structure, PA donates an

O-H···O H-bond to $H_2O$ and accepts an O-H···π H-bond from $H_2O$. The spectra for the isotopologues help to determine the position of the non-bonded hydrogen atom of water. This helps to differentiate between the two lowest energy structures. The matrix isolation IR spectroscopic study on the PA···$H_2O$ complex fails to differentiate between these two structures. The rotational spectrum shows a doubling of the lines caused by the internal rotation of the $H_2O$ moiety about its $C_2$ axis. We were also able to generalize the H-bond donor/acceptor capabilities of the hydroxyl groups in an alcohol···water complex based on the electron donating/withdrawing abilities of the groups present in the alcohol.

The rotational spectra for the acetonitrile···carbon dioxide are discussed in *Chapter 4*. The *ab initio* calculations for the $CH_3CN$···$CO_2$ complex optimized four tetrel bonded structures. Therefore, investigating this complex provides an opportunity to study tetrel bonded structures in the gas phase. We have observed the rotational spectra corresponding to the two lowest energy structures, the π-stacked and the T-shaped. The spectra for the isotopologues were also recorded. The spectra show hyperfine splitting due to the nuclear quadrupole coupling of the N-14 nucleus. The π-stacked structure has $CO_2$ and $CH_3CN$ stacked in a parallel manner with the oxygen end of $CO_2$ interacting with the positively charged C atom of the cyano group in $CH_3CN$. The Atoms in Molecules analysis finds that the methyl C-H forms a hydrogen bond with the same oxygen atom leading to a closed network of non-covalent interactions. In the T-shaped structure the nitrogen end of $CH_3CN$ donates electron density to the central positively charged C atom of $CO_2$. The spin-less indistinguishable oxygen nuclei in the $C_{2v}$ symmetry of the T-shaped structure dictates that odd |K-m| levels will be missing. We find no K=1 lines for the m=0 state confirming that T-shaped structure has been observed.

The structure of $CH_5^+$ has been highly debated upon. *Chapter 5* studies the structure of $CH_5^+$ using Atom in Molecules (AIM), natural bond orbital (NBO), and normal coordinate analyses. We find that the structure of $CH_5^+$ cannot be considered as the complex between $CH_3^+$ and $H_2$. It has a pentacoordinate carbon center having five C-H bonds[4]. The congeners of $CH_5^+$, $SiH_5^+$ and $GeH_5^+$ were also explored to see if they form similar structures as $CH_5^+$ or not. We find that the structures are different from $CH_5^+$. The structures of $SiH_5^+$ and $GeH_5^+$ form a complex between the $TH_3^+$ and $H_2$. The identity of the $H_2$ moiety is retained in these complexes. The $H_2$ moiety donates

electron density to the positively charged T atom forming a tetrel bonded complex. This work led us to classify the 3c-2e bonds based on the connectivity patterns of the three nuclei involved in the 3c-2e. We were able to classify them into V, L, Δ, T, and I (linear) types[5].

*Chapter 6* explores the structures and rotational spectra of the weakly bound complexes of methyl fluoride with water, argon, and itself. We intended to observe a tetrel bonded structure for the $CH_3F\cdots H_2O$ complex. However only the global minimum hydrogen bonded structure having a bent O-H···F bond was observed. Three structures are possible for the $CH_3F\cdots Ar$ complex, the T-shaped, tetrel bonded, and linear structures. These three structures are very close in energy. We have evidence for the formation of the T-shaped structure, where the Ar atom is positioned perpendicular to the C-F bond. The large number of unassigned lines could belong to the other two structures. The global minimum structure for the $CH_3F\cdots CH_3F$ dimer is an antiparallel structure where the two $CH_3F$ units are bound by two symmetrical C-H···F hydrogen bonds. However, it is not possible to observe this structure because it has a net zero electric dipole moment. So, the lines observed could possibly belong to the tetrel bonded structures, linear or skewed linear. In both these structures the electron rich F atom donates electron density to the σ-hole formed over the methyl face of $CH_3F$.

*Chapter 7* summarizes the results and conclusions for the molecular structures investigated in this *Thesis*.

References


(1) Mani, D.; Arunan, E. The X–C⋯ Y (X= O/F, Y= O/S/F/Cl/Br/N/P) 'Carbon Bond' and Hydrophobic Interactions. *Physical Chemistry Chemical Physics* **2013**, *15*, 14377–14383.

(2) Bauzá, A.; Mooibroek, T. J.; Frontera, A. Tetrel-Bonding Interaction: Rediscovered Supramolecular Force? *Angew. Chem. Int. Ed.* **2013**, *52*, 12317–12321.

(3) Arunan, E.; Tiwari, A.P.; Mandal, P.K.; Mathias, P.C. Pulsed nozzle Fourier transform microwave spectrometer: Ideal to define hydrogen bond radius. *Curr. Sci.* **2002**, *82*, 533-540

(4) Gnanasekar, S. P.; Arunan, E. Inter/Intramolecular Bonds in $TH_5^+$ (T= C/Si/Ge): $H_2$ as Tetrel Bond Acceptor and the Uniqueness of Carbon Bonds. *The Journal of Physical Chemistry A* **2019**, *123*, 1168–1176.

(5) Gnanasekar, S. P.; Arunan, E. A Detailed Classification of Three-Centre Two-Electron Bonds. *Australian Journal of Chemistry* **2020**, *73*, 767–774.

# Table of Contents

# LIST OF TABLES

# LIST OF FIGURES

# CHAPTER 1
# Introduction

CHAPTER 1

# INTRODUCTION

*"No one really understands the behavior of a molecule until he knows its structure that is to say: its size, and shape, and the nature of its bonds"* – C. A. Coulson[1] (1973)

Microwave spectroscopy allows for the accurate determination of geometrical parameters such as bond lengths and bond angles. These parameters are used to characterize the equilibrium structure of a molecule. Molecular structure refers to the framework of the bonds that connect the nuclei in a specific manner to form a molecule. Structural information concerning a molecule often emphasizes only on the geometry.

The following remark appears in a chapter of *Advances in Molecular Structure Research* and encapsulates the notion of molecular structure perfectly[2]. "It is to be stressed, of course, that the geometry of the molecule is only one of the three major aspects of molecular structure. The other two are the *intramolecular motion*, which comprises the relative displacements of the atomic nuclei with respect to their equilibrium positions, and the *electron density distribution*."

It is unmistakable that the properties and functions of a molecule are highly dependent on its structure. This Thesis explores the structures of weakly bound complexes to understand non-covalent interactions. Rotational spectroscopy is used to derive the shape of the molecule (rotational constants) and more precisely the bond angles and bond lengths (via isotopic substitution). Bader's Atoms in Molecules theory[3] is used in conjunction with the rotational spectroscopic results. This examines the

electron density topology of the complexes in order to understand the molecular structure and the nature of the intermolecular interactions.

## 1.1. Non-covalent interactions

It would not be an exaggeration to claim that life on earth exists because of non-covalent interactions. The liquid state of water is possible because of hydrogen bonding. The functioning of important biological molecules (such as enzymes, proteins, RNA, DNA, etc.) are possible because of the weak interactions that order these molecules in the required configuration. It is a key idea in biology that the function of a biomolecule is highly dependent on its structure. The extremely complex tertiary and quaternary structures of proteins and the higher order structural motifs of nucleic acids are all formed and maintained by the weak non-covalent interactions, thereby preventing their malfunction. Chemists borrow this use of non-covalent interactions from nature to manipulate the synthesis of supramolecular assemblies with the intention of having a particular property or exhibiting a specific function. The fields of supramolecular chemistry and crystal engineering coax non-covalent interactions to form structures that are designed for specific purposes with tunable properties.

Intermolecular interactions had to be invoked by van der Waals to explain the non-ideal behavior of gases[4]. This led to the rectification of the gas law which had thus far assumed that the atoms and molecules which make up the gas were point masses that do not interact with each other. It was later understood that the van der Waals forces responsible for the intermolecular interactions included dipole-dipole interactions (Keesom force), dipole-induced dipole interactions (Debye force), and the instantaneous dipole-induced dipole interactions (London dispersion forces)[5]. Non-covalent interactions are long-range interactions. The sources responsible for the attractive interaction over large distances are electrostatic, induction, and dispersion[6]. Electrostatic interaction is the interaction between charges, dipoles, and higher multipoles. The electrostatic interaction energy is inversely proportional to the distance. Induction refers to the interaction between the permanent and induced multipoles. Dispersion arises due to the fluctuations of the electron cloud which causes instantaneous multipole-induced multipole moment interactions. The dispersion interaction is of quantum mechanical origin and the interaction energy is proportional to the polarizabilities of the interacting species and inversely proportional to the sixth

power of the distance between the species. The exchange-repulsion term is also of quantum origin and is of repulsive nature, arising as a consequence of Pauli's exclusion principle[6]. Therefore, non-covalent interactions are a manifestation of various intermolecular forces such as electrostatics, induction, exchange repulsion, dispersion, and also some charge transfer/covalency.

A number of weak interactions have been defined in recent times going beyond the hydrogen bond and van der Waals interaction classification of the previous century. Interactions for each group are given names such as triel (13)[7], tetrel (14)[8,9], pnictogen/pnicogen(15)[10,11], chalcogen (16)[12,13], halogen(17)[14–16], and aerogen(18)[17] bonds. However, are any of the elements in the group unique like the hydrogen bond or do all group members shows similar interactions? Is the term carbon bond necessary or does tetrel bond suffice? In this Thesis we focus on the hydrogen bonded and tetrel bonded complexes with an aim to understand these two interactions. Both these interactions seem to be important in biologically active molecules. From a chemist's point of view these interactions are responsible for two important reactions. The first one is the proton transfer reaction where a hydrogen bonded structure is an intermediate. The second one is the $S_N2$ reaction where a carbon bonded structure is reminiscent of the pre-transition state.

### 1.1.1 Hydrogen bond

The hydrogen bond is the most ubiquitous and widely studied non-covalent interaction. Latimer and Rodebush were the first to mention the hydrogen bond[18]. This year (2020) marks the centenary of their work[19,20]. For over a century this interaction has fascinated researchers and there are facets of the H-bond yet to be learnt. The IUPAC recommendation[21] for a new definition of the hydrogen bond reads "the hydrogen bond is an attractive interaction between a hydrogen atom from a molecule or a molecular fragment X-H in which X is more electronegative than H, and an atom or a group of atoms in the same or a different molecule, in which there is evidence of bond formation."

The structure of solid $H_2S$ and ice are very different[5]. Each water molecule in ice is surrounded by four other water molecules in a tetrahedral arrangement. The central water molecule of the repeating unit donates two O-H···O hydrogen bonds and accepts two O-H···O hydrogen bonds. Solid $H_2S$ on the other hand has a $H_2S$ molecule

surrounded by twelve other molecules of $H_2S$. This difference in the structures of $H_2O$ and $H_2S$ in the solid-state lead to them being differentiated as hydrogen bonded and van der Waals interaction in the past century. However, recent microwave spectroscopic investigations reveal that the $H_2S$ dimer is hydrogen bonded[22], justifying the recent IUPAC definition of the hydrogen bond which is more inclusive.

Multiple hydrogen binding sites on a molecule lead to a variety of interesting structures when forming a hydrogen bonded complex. The hydroxyl group can donate or accept an H-bond. Both alcohols and water contain hydroxyl groups. It is of interest to study the donor/acceptor role of each moiety in an alcohol-water complex. *Chapter 3* of this Thesis studies the rotational spectra of a multifunctional alcohol (propargyl alcohol)-water complex. Hydrogen bonds involving fluorine are not so common. *Chapter 6* of this Thesis explores the structures and rotational spectra of the hydrogen bonded $CH_3F\cdots H_2O$ and $CH_3F\cdots CH_3F$ complexes.

### 1.1.2 Tetrel bond/Carbon bond

Investigations on $CH_3X$ molecules (X more electronegative than carbon) with various electron rich donors (such as $NH_3$ and $H_2O$) led Mani and Arunan to propose a weak interaction, X-C···Y termed as the 'carbon bond'[8]. The X-C···Y carbon bond is defined analogous to the hydrogen bond. The electron withdrawing capabilities of the X group makes the central carbon atom positively charged which can then easily accept electron density from electron rich donor moieties (Y) forming an X-C···Y bond. Subsequently it was realized that these interactions were similar to other σ-hole interactions leading Frontera and coworkers to generalize this interaction for the other elements of group 14 and coin the term tetrel bond[9].

The tetrel bond led to the understanding of interactions in several supramolecular structures. It was proposed that these newly found interactions would play an important role in supramolecular chemistry and crystal engineering[9]. Life on earth is carbon based and thus one can expect that these interactions might play an important role in biological molecules such as proteins[23]. They also have relevance in $S_N2$ reactions[24].

Experimental evidence for the 'carbon bond' was first reported in the X-ray charge density analysis of fenobam and dimethylammonium-4-hydroxybenzoate[25]. Later tetrel

bonds were observed in NMR[26] and microwave spectroscopic studies as well. Legon observed that the tetrel bond and other newly named non-covalent interactions had been observed in various complexes studied using microwave spectroscopy but were never labelled as such[27]. Tetrel bonds could involve both π-hole as well as σ-hole interactions. Which begs the question are n-π* interactions especially those involving the carbonyl group then a carbon bond? Recent data shows that for the tetrel bond the π-hole interactions are generally stronger than the σ-hole interactions[28].

Since the proposal of this new interaction, a large number of reports have focussed on computational studies involving a variety of molecules while there has been a paucity of experimental investigations concerning the tetrel bond. A recent review on rotational spectroscopic investigations of non-covalent interactions comments that "specific searches for tetrel bond are now appearing at a slow pace"[29]. Experimental studies on the tetrel bond will help improve our understanding of this interaction. In this Thesis, we report the rotational spectra of several tetrel bonded complexes such as the acetonitrile···carbon dioxide complex (*Chapter 4*) and the complexes of methyl fluoride: $CH_3F\cdots H_2O$, $CH_3F\cdots Ar$, and $CH_3F\cdots CH_3F$ (*Chapter 6*). The tetrel bonded interactions in $TH_5^+$ (T=C, Si, and Ge) are also studied using AIM, NBO and normal coordinate analyses (*Chapter 5*).

## 1.2. Rotational spectroscopy

Rotational spectroscopy is the most accurate technique available for structure determination in the gas phase. The rotational levels of the molecule being investigated are excited by interaction with radiation from the microwave and millimeter wave regions. These rotational levels depend on the shape of the molecule that is, its moments of inertia. Rotational constants obtained from the observed rotational spectra are inversely proportional to the moments of inertia. The moments of inertia are related to the bond lengths and from this a detailed experimental structure can be obtained. Changes in the moments of inertia caused by isotopic substitutions can be easily identified. Therefore, rotational spectroscopy is an extremely accurate and sensitive method for structure determination. However, the molecules to be investigated must be brought into gas phase and must possess a permanent electric dipole moment.

# INTRODUCTION

Rotational motion can be resolved along three mutually perpendicular body fixed axes, known as the principal axis system. Direction of the principal axes and the moment of inertia (I) along each of them can be obtained by diagonalization of the moments of inertia tensor. The principal axes are denoted as *a, b,* and *c* axis such that $I_a \leq I_b \leq I_c$ i.e. the *a* axis is the axis with the least moment of inertia and the *c* axis is the one with the maximum moment of inertia. On the basis of the moments of inertia along the three principal axes, molecules can be classified into the following categories:

- Linear top ($I_a$=0, $I_b = I_c$)
- Symmetric top ($I_a$=$I_b$< $I_c$ or $I_a$< $I_b$= $I_c$)
- Asymmetric top ($I_a$< $I_b$ < $I_c$)
- Spherical top ($I_a$= $I_b$ = $I_c$)

Rotational spectra are obtained as the transitions between rotational levels. The energy levels are obtained by solving for a semi-rigid rotor Hamiltonian. To predict the rotational spectrum and assign the transitions, one must have an idea about the rotational energy levels; this can be found by solving the Schrödinger equation. The Hamiltonian for the rotational motion can be constructed from the classical rotational energies.

The Hamiltonian ($H_r$) for a rigid rotor contains only the kinetic energy term and is given below[30].

$$H_r = \frac{1}{2}\left(\frac{P_a^2}{I_a} + \frac{P_b^2}{I_b} + \frac{P_c^2}{I_c}\right)$$

Where $P_x$ is the angular momentum along *x*-axis.

The wavefunction describing the molecular system is Ψ. The solution of the Schrödinger equation gives us the energy of the system. The molecule can be considered to be a rigid rotor and the rigid rotor Hamiltonian can be used to solve for the rotational energies of the molecule. It is known that the square of the total angular momentum operator ($P^2$) commutes with the rigid rotor Hamiltonian and the following eigenvalue equation is satisfied.

$$P^2\Psi = \hbar^2 J(J+1)\Psi$$

Where J can have values 0, 1, 2, 3…

The operator for the projection of the total angular momentum on the space fixed axis ($P_Z$) commutes with the rigid rotor Hamiltonian and the following eigenvalue equation is satisfied.

$$P_Z\Psi = \hbar M\Psi$$

M takes values from –J to +J.

The operator for the projection of the total angular momentum on the body fixed axis ($P_z$) commutes with the rigid rotor Hamiltonian and the following eigenvalue equation is satisfied.

$$P_z\Psi = \hbar K\Psi$$

K can take values from –J to +J. The $P_z$ operator commutes with the rigid rotor Hamiltonian only for the symmetric and spherical tops.

Substituting the quantum mechanical operators for the angular momentum, the Hamiltonian for the rotating molecule is obtained.

### 1.2.1 Symmetric top molecules

A symmetric top rotor is one where two of the principal moments of inertia are equal and this condition is generally met when the molecule has an axis of symmetry $C_n$ where $n \geq 3$. A linear molecule is a special case of the symmetric top where the angular momentum about the symmetry axis is zero. For a symmetric top, one of the principal axes of inertia is along the molecular axis of symmetry while the other two are mutually perpendicular to it. Symmetric top molecules are further categorized as:

1. **Prolate symmetric top**, ($I_a < I_b = I_c$ ; e.g. $CH_3F$).
2. **Oblate symmetric top**, ($I_a = I_b < I_c$ ; e.g. $BCl_3$).

The Hamiltonian for a rigid prolate symmetric top is given below[30]

$$H_{prolate} = \frac{P^2}{2I_b} + \frac{P_a^2}{2}\left(\frac{1}{I_a} - \frac{1}{I_b}\right)$$

The energy obtained is,

$$E_{J,K} = h [ B J(J+1) + (A-B) K^2]$$

For an oblate top the second term in brackets (A-B) is replaced by (C-B), where,

$A=\frac{h}{8\pi^2 I_a}$, $B=\frac{h}{8\pi^2 I_b}$, and $C=\frac{h}{8\pi^2 I_c}$ are the rotational constants.

### 1.2.2 Asymmetric top molecules

When the three principal moments of inertia of a molecule are non-zero and no two of them are equal, they are categorized as asymmetric tops. The rotational spectra for such molecules are complex. There are no closed form expressions for the energy levels for such molecules, and even when the effects of the centrifugal distortion are neglected, closed form expressions are obtained only for the low J values[30]. In general, the procedure is to expand the wavefunctions in terms of an orthogonal set of functions such as the symmetric top wavefunctions and solve the secular equations for the unknown coefficients and energies. Though the spectrum is complex, a lot of information about the molecule can be easily obtained.

For an asymmetric rotor, $P_z$, no longer commutes with the Hamiltonian and only J and M are "good" quantum numbers. The asymmetric rotor can be described in terms of Ray's asymmetry parameter ($\kappa$)[30],

$$\kappa = (2B-A-C)/ (A-C)$$

where A, B, and C are the rotational constants. The limiting values for $\kappa$ are, -1 (prolate symmetric top) and +1 (oblate symmetric top). The energy levels for an asymmetric top are labelled using the King-Hainer-Cross notation ($J_{K_{-1}\,K_{+1}}$), where $K_{-1}$ is for the limiting prolate symmetric top and $K_{+1}$ for the oblate symmetric top[30]. The essential difference between the energy levels of asymmetric rotors and the limiting symmetric tops is that the K levels that are always degenerate in the symmetric rotor are separated in the asymmetric rotor. Therefore, for each value of J, an asymmetric rotor has (2J+1) distinct rotational sublevels whereas the symmetric rotor has only (J+1) distinct sublevels.

### 1.2.3 Centrifugal distortion

Considering the molecule to be a rigid rotor is a useful approximation, however, in a real situation the nuclei in the molecule are held together by finite restoring forces. The bond distances and angles will change because of the centrifugal force produced by the rotation, distorting the shape of the molecule. The rotational spectrum cannot be considered to be a simple rigid rotor spectrum for a set of equilibrium moments of inertia. Microwave measurements are precise enough to observe the effects of centrifugal distortion. Though the effects of centrifugal distortion are large enough to be observed they are small compared to the rotational energy and can therefore be treated as a perturbation to the rigid rotor Hamiltonian. The theory of centrifugal distortion is quite complex for asymmetric rotors and its effects are also larger compared to linear or symmetric tops. Watson's reduced Hamiltonian is used to fit the experimental data for asymmetric tops[30]. The stretching force constant ($k_s$) for a weakly bound dimer can be determined from the centrifugal distortion constant ($D_J$ or $\Delta_J$) assuming a pseudo-diatomic model. Various expressions that relate $k_s$ with $D_J$ / $\Delta_J$ have been derived by Millen for different semi-rigid rotors[31].

### 1.2.4 Internal rotation

Internal motions such as the hindered internal rotation of the methyl group are considered as large amplitude motions and can be easily separated from other vibrational motions. These internal motions however interact with the overall rotation leading to the splitting of the observed transitions. The fine structure of the observed spectra depends on the height of the potential barrier hindering the motion[30]. The rotational spectra can give valuable information of the barrier height for such internal motions. In *Chapter 3* we observe the splitting of the rotational spectra due to the internal rotation of the $H_2O$ moiety in the propargyl alcohol···water complex. The free rotation of the methyl group in the acetonitrile···carbon dioxide complex leads to a complicated spectrum which is discussed in *Chapter 4*. The methyl fluoride···water complex discussed in *Chapter 6* shows a doubling of the observed rotational transitions, which could either be due to the internal rotations of water about its $C_2$ axis or the rotation of the methyl group about its $C_3$ axis.

### 1.2.5 Nuclear quadrupole coupling

A non-spherical nuclear charge results in a nuclear quadrupole moment. This is typical for nuclei having nuclear spin (I) greater than ½. Nuclei having, I = 0 or ½ are spherically symmetric and therefore have no quadrupole moments. The nuclear quadrupole moment interacts with the electric field gradient at the nucleus, putting a twisting torque on the nucleus, which tends to align its spin moment in the direction of the electric field gradient. The precession of the spin axis about the direction of the resultant field gradient leads to the nuclear quadrupole hyperfine structure in the rotational spectrum. The hyperfine structure provides a measure of the molecular field gradients. Information about the electronic structure and the nature of the bonds can be obtained from the field gradient. In *Chapter 4* we observe the hyperfine splitting of the rotational transitions due to the nuclear quadrupole coupling of the N-14 nucleus in the acetonitrile···carbon dioxide complex.

## 1.3. Present investigations

This Thesis explores the structure and dynamics of weakly bonded complexes using rotational spectroscopy and computational methods. The Thesis aims to understand non-covalent interactions, focussing on the hydrogen and tetrel bonds. The experimental and computational methods employed are elaborated in *Chapter 2*. The rotational spectrum of the propargyl alcohol···water complex has been discussed in *Chapter 3*. The spectrum for this complex provides an understanding of hydrogen bonds when multiple donor/acceptor sites are available for H-bonding and also sheds light on alcohol-water interactions. *Chapter 4* reports the rotational spectra of the acetonitrile···carbon dioxide complex. All the three carbon atoms for this system can potentially form tetrel bonds and provide an opportunity to study the tetrel bond in gas phase. In *Chapter 5* the electron density topology (Atoms in Molecules analysis) and other computational studies help to identify the bonding pattern in the $TH_5^+$ systems. The objective of this work is to determine if $CH_5^+$ is a complex between $CH_3^+$ and $H_2$ or a covalent molecule having a pentacoordinated carbon center, and also if the structures of $SiH_5^+$ and $GeH_5^+$ are similar to $CH_5^+$ or not. *Chapter 5* also discusses the classification of 3c-2e bonds based on the connectivity patterns of the nuclei involved in the 3c-2e bonds. Preliminary rotational spectroscopic results for the $CH_3F···H_2O$, $CH_3F···Ar$, and $CH_3F···CH_3F$ dimers are reported in *Chapter 6* of this Thesis.

## 1.4. References


(1) Coulson, C. A. *The Shape and Structure of Molecules*; Oxford Chemistry Series; Clarendon Press: Oxford, England, **1973**.

(2) Hargittai, I.; Hargittai, M. Some Perspectives in Molecular Structure Research: An Introduction. In *Advances in Molecular Structure Research*; Hargittai, M.; Hargittai, I., Eds.; Elsevier, **1995**; Vol. 1, pp 33–62.

(3) Bader, R. F. W. *Atoms in Molecules: A Quantum Theory*; International Series of Monographs on Chemistry; Oxford University Press: Oxford, New York, **1994**.

(4) van der Waals, J. D. Over de Continuiteit van Den Gas- En Vloeistoftoestand. PhD Thesis, Leiden, **1873**.

(5) Gnanasekar, S. P.; Arunan, E. Molecular Beam and Spectroscopic Techniques: Towards Fundamental Understanding of Intermolecular Interactions/Bonds. In *Intermolecular Interactions in Crystals: Fundamentals of Crystal Engineering*; Novoa, J. J., Eds.; Royal Society of Chemistry, **2017**.

(6) Hobza, P.; Muller-Dethlefs, K. *Non-Covalent Interactions: Theory and Experiment*; Theoretical and Computational Chemistry Series; Royal Society of Chemistry, **2009**.

(7) Grabowski, S. J. π-Hole Bonds: Boron and Aluminum Lewis Acid Centers. *ChemPhysChem* **2015**, *16*, 1470–1479.

(8) Mani, D.; Arunan, E. The X–C···Y (X= O/F, Y= O/S/F/Cl/Br/N/P) 'Carbon Bond' and Hydrophobic Interactions. *Phys. Chem. Chem. Phys.* **2013**, *15*, 14377–14383.

(9) Bauzá, A.; Mooibroek, T. J.; Frontera, A. Tetrel-Bonding Interaction: Rediscovered Supramolecular Force? *Angew. Chem. Int. Ed.* **2013**, *52*, 12317–12321.

(10) Grabowski, S. J.; Alkorta, I.; Elguero, J. Complexes between Dihydrogen and Amine, Phosphine, and Arsine Derivatives. Hydrogen Bond versus Pnictogen Interaction. *J. Phys. Chem. A* **2013**, *117*, 3243–3251.

(11) Scheiner, S. A New Noncovalent Force: Comparison of P···N Interaction with Hydrogen and Halogen Bonds. *J. Chem. Phys.* **2011**, *134*, 094315-1-094315-9.

(12) Wang, W.; Ji, B.; Zhang, Y. Chalcogen Bond: A Sister Noncovalent Bond to Halogen Bond. *J. Phys. Chem. A* **2009**, *113*, 8132–8135.

(13) Manna, D.; Mugesh, G. Regioselective Deiodination of Thyroxine by Iodothyronine Deiodinase Mimics: An Unusual Mechanistic Pathway Involving Cooperative Chalcogen and Halogen Bonding. *J. Am. Chem. Soc.* **2012**, *134*, 4269–4279.

(14) Legon, A. C. Prereactive Complexes of Dihalogens XY with Lewis Bases B in the Gas Phase: A Systematic Case for the Halogen Analogue B···XY of the Hydrogen Bond B···HX. *Angew. Chem. Int. Ed.* **1999**, *38*, 2686–2714.

(15) Metrangolo, P.; Resnati, G. *Halogen Bonding: Fundamentals and Applications*; Springer, **2008**.

(16) Politzer, P.; S. Murray, J.; Clark, T. Halogen Bonding and Other σ-Hole Interactions: A Perspective. *Phys. Chem. Chem. Phys.* **2013**, *15*, 11178–11189.

(17) Bauzá, A.; Frontera, A. Aerogen Bonding Interaction: A New Supramolecular Force? *Angew. Chem. Int. Ed.* **2015**, *54*, 7340–7343.

(18) Latimer, W. M.; Rodebush, W. H. Polarity and Ionization from the Standpoint of the Lewis Theory of Valence. *J. Am. Chem. Soc.* **1920**, *42*, 1419–1433.

(19) Arunan, E. One Hundred Years After the Latimer and Rodebush Paper, Hydrogen Bonding Remains an Elephant! *J. Indian Inst. Sci.* **2020**, *100*, 249–255.

(20) Gibb, B. C. The Centenary (Maybe) of the Hydrogen Bond. *Nat. Chem.* **2020**, *12*, 665–667.

(21) Arunan, E.; Desiraju, G. R.; Klein, R. A.; Sadlej, J.; Scheiner, S.; Alkorta, I.; Clary, D. C.; Crabtree, R. H.; Dannenberg, J. J.; Hobza, P.; Kjaergaard, H. G.; Legon, A. C.; Mennucci, B.; Nesbitt, D. J. Definition of the Hydrogen Bond (IUPAC Recommendations 2011). *Pure Appl. Chem.* **2011**, *83*, 1637–1641.

(22) Das, A.; Mandal, P. K.; Lovas, F. J.; Medcraft, C.; Walker, N. R.; Arunan, E. The $H_2S$ Dimer Is Hydrogen-Bonded: Direct Confirmation from Microwave Spectroscopy. *Angew. Chem. Int. Ed.* **2018**, *57*, 15199–15203.

(23) Mundlapati, V. R.; Sahoo, D. K.; Bhaumik, S.; Jena, S.; Chandrakar, A.; Biswal, H. S. Noncovalent Carbon-Bonding Interactions in Proteins. *Angew. Chem. Int. Ed.* **2018**, *57*, 16496–16500.

(24) Grabowski, S. J. Tetrel Bond–σ-Hole Bond as a Preliminary Stage of the $S_N2$ Reaction. *Phys. Chem. Chem. Phys.* **2014**, *16*, 1824–1834.

(25) P. Thomas, S.; S. Pavan, M.; Row, T. N. G. Experimental Evidence for 'Carbon Bonding' in the Solid State from Charge Density Analysis. *Chem. Commun.* **2014**, *50*, 49–51.

(26) Southern, S. A.; Bryce, D. L. NMR Investigations of Noncovalent Carbon Tetrel Bonds. Computational Assessment and Initial Experimental Observation. *J. Phys. Chem. A* **2015**, *119*, 11891–11899.

(27) Legon, A. C. Tetrel, Pnictogen and Chalcogen Bonds Identified in the Gas Phase before They Had Names: A Systematic Look at Non-Covalent Interactions. *Phys. Chem. Chem. Phys.* **2017**, *19*, 14884–14896.

(28) Zhang, J.; Hu, Q.; Li, Q.; Scheiner, S.; Liu, S. Comparison of σ-Hole and π-Hole Tetrel Bonds in Complexes of Borazine with TH3F and F2TO/H2TO (T = C, Si, Ge). *Int. J. Quantum Chem.* **2019**, *119*, e25910.

(29) Juanes, M.; Saragi, R. T.; Caminati, W.; Lesarri, A. The Hydrogen Bond and Beyond: Perspectives for Rotational Investigations of Non-Covalent Interactions. *Chem. – Eur. J.* **2019**, *25*, 11402–11411.

(30) Gordy, W.; Cook, R. L. *Microwave Molecular Spectra*; Wiley-Interscience Pub., **1970**.

(31) Millen, D. J. Determination of Stretching Force Constants of Weakly Bound Dimers from Centrifugal Distortion Constants. *Can. J. Chem.* **1985**, *63*, 1477–1479.

# CHAPTER 2

# Experimental and computational methods

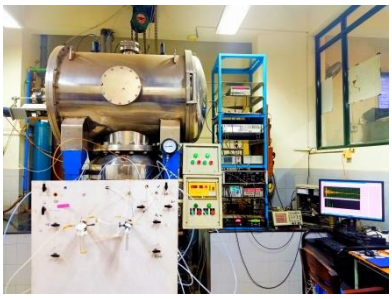

CHAPTER 2

# EXPERIMENTAL AND COMPUTATIONAL METHODS

## 2.1. Introduction

Rotational spectroscopy is an accurate technique to obtain structural information about molecules. Balle and Flygare's design of a Fabry-Perot cavity pulsed Fourier transform microwave spectrometer widened the scope of systems that could be investigated[1]. Rotational transitions of transient and short-lived species could be observed. The pulsed supersonic nozzle allows the adiabatic expansion of the high-pressure carrier gas seeded with molecules of interest into a vacuum chamber, leading to the formation of weakly bound complexes. This permits the study of the rotational spectra of non-covalently bonded complexes.

Modifications over the years especially those involving the nozzle design such as the heated nozzle and laser ablation techniques have expanded the scope of molecules whose rotational spectra can be studied. Though the cavity-based spectrometer has high sensitivity and resolution, it has a narrow bandwidth (~0.5MHz), this makes the time required to collect the spectra enormous. Pate and co-workers invented a broadband chirped pulse Fourier transform spectrometer (CP-FTMW)[2] that could collect broadband spectra >10 GHz. This invention has greatly reduced the time taken to obtain the spectra by several orders of magnitude. The CP-FTMW spectrometer has enabled a wide variety of experiments[3] such as obtaining the absolute configuration

of chiral molecular systems[4,5] and probing reaction dynamics[6]. We use a home-built spectrometer based on the Balle-Flygare design to record the spectra of weakly bound complexes. The details of our spectrometer are described in Reference 7. In this chapter the spectrometer and its functions will be discussed in brief. Our experiments are supplemented by theoretical studies and the computational methods used will be discussed in Section 2.3.

## 2.2. Pulsed Nozzle Fourier Transform Microwave Spectrometer

The pulsed nozzle Fourier transform microwave (PNFTMW) spectrometer can be categorized into two parts, mechanical and electrical.

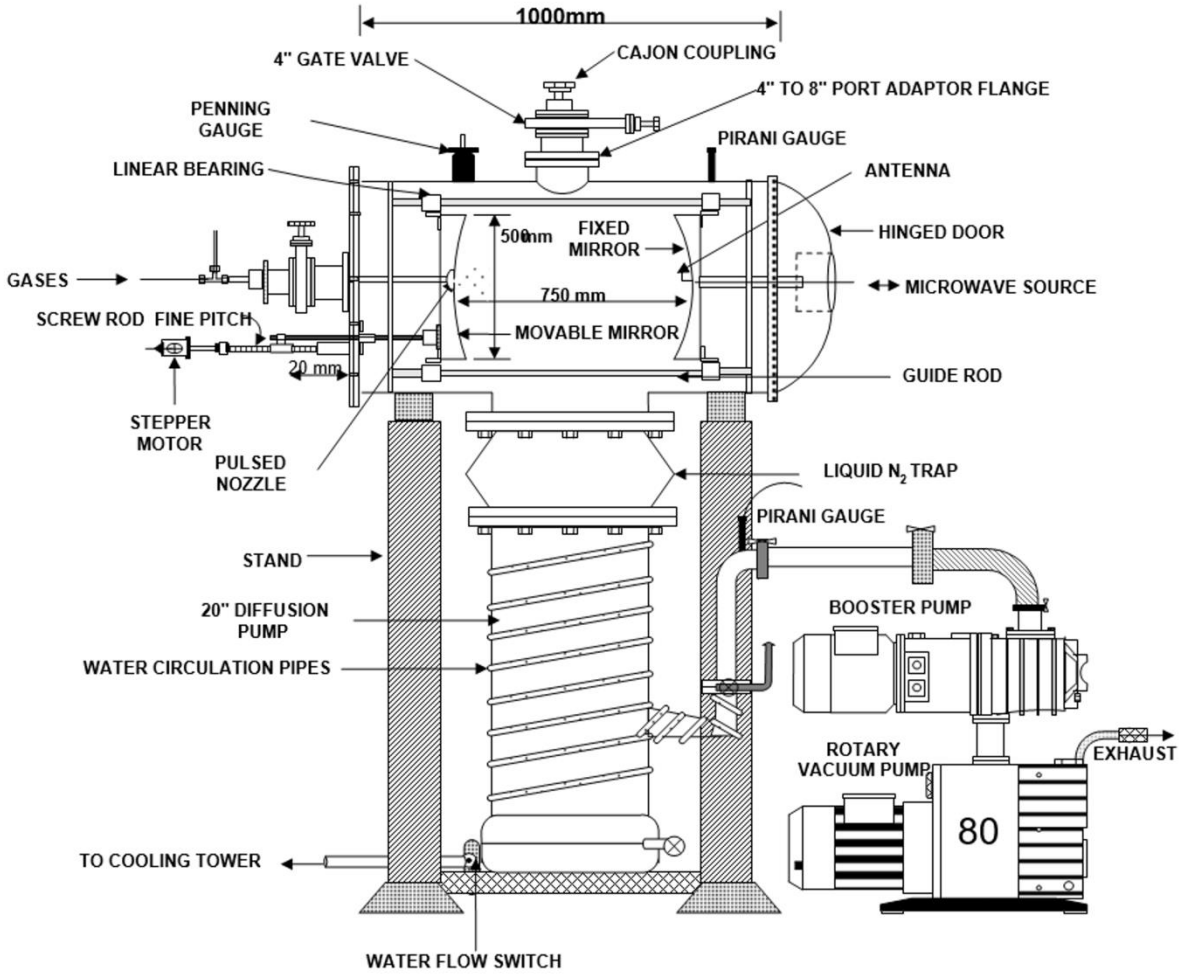


**Figure 2.1.** The mechanical design of the PNFTMW spectrometer. Figure taken from Reference 8.

### 2.2.1 Mechanical design of the PNFTMW spectrometer

The mechanical design of the vacuum chamber that contains the Fabry-Perot cavity is shown in Figure 2.1. The vacuum chamber is a cylindrical cavity made of stainless steel (SS304). The length of the chamber is 1000 mm and it has a diameter of 850 mm. The chamber encases two spherical aluminium mirrors that are made from 65 mm thick Al disks and have a diameter of 500 mm. These mirrors are mounted on three SS guide rods coaxially. The radius of curvature (R) of both these mirrors is 800 mm and they are highly polished to ensure that the surface roughness and the radius were good to 1 micron. One of these mirrors is fixed while the other is movable.

The fixed mirror contains a small hole at its centre. A coaxial cable running through the supporting rod for the mirror having an SMA female connector at one end goes through this hole. An L-shaped antenna is connected to the SMA connector, and can transmit and receive microwave radiation. The coaxial cable has a hermetically sealed SMA connector at the other end so that microwave power can be coupled in and out of the cavity at vacuum.

The other mirror is movable and is fixed with a micrometer controlled fine pitch screw rod that is driven by a synchronised stepper motor driver (*MicroLOGIX Driver MSB-403*). The linear screw rod has a pitch of 5 mm. A complete rotation (360°) moves the screw rod by a linear distance of 5 mm. In the high-resolution mode, the stepping motor (*103H8221-5041, Sanyo Denki, Japan*) takes 4000 steps for a complete rotation. Therefore, the mirror can move in steps of 1.25 micron. The mirror position can be varied from 630 mm to 730 mm to allow for the formation of standing waves at different MW frequencies. The resonant frequencies (ν) of the Fabry-Perot cavity for the $TEM_{mnq}$ modes[1] are

$$\nu = \nu_0(q+1) + \frac{1}{\pi}(m+n+1)\,cos^{-1}\left(1-\frac{d}{R}\right)$$

where $\nu_0$=c/2d, m, n, and q are the cavity modes, d is the distance of separation between the two mirrors, and R is the radius of curvature of the mirror. Many resonances are observed for a given frequency within the variation of distances between the mirrors. The $TEM_{00q}$ modes are used in our experiments. The movable mirror has a 10 mm hole at its centre. The backside of this mirror has a 25 mm cylinder

carved out such that a pulsed nozzle assembly can be placed. The nozzle (*General Valve, USA, Series 9*) has a diameter of 0.8 mm.

The chamber is evacuated by a 20" oil diffusion pump (*Vacuum Techniques, Bangalore, India*) which has a pumping speed of 10,000 $ls^{-1}$. The diffusion pump is water-cooled. To keep the water at room temperature the water circulation system includes a cooling tower. The diffusion pump is backed by a roots blower (*Boc Edward, EH 250*) and a belt-less rotary pump (*Boc Edward, E2M80*). These backing pumps have a combined pumping speed of ~4000 $ls^{-1}$. The pumps can evacuate the chamber to $10^{-6}$ mbar. To monitor the pressure of the cavity two gauges are employed. The Pirani gauge measures pressure up to $10^{-3}$ mbar and the Penning gauge measures pressure up to $10^{-6}$ mbar.

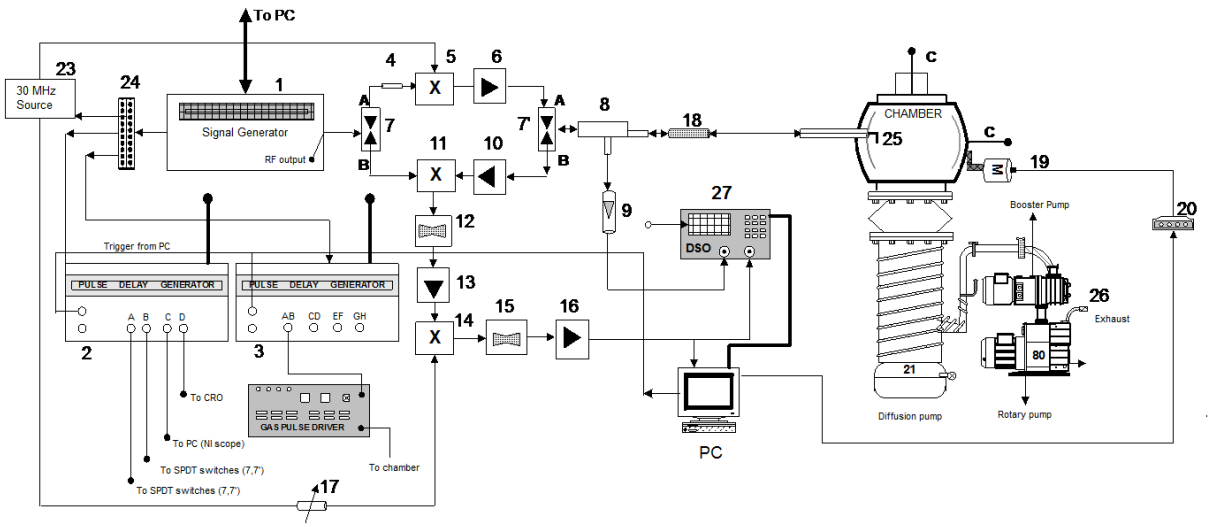


**Figure 2.2.** Electrical design of the PNFTMW spectrometer. **1.** Signal generator (*Agilent, MXG Analog Signal Generator, N5183A*); **2.** Delay generator (*BNC-575*); **3.** Delay generator (*SRS DG645*); **4.** Microwave attenuator (*HP, 8493C, 3dB*); **5.** SSBM (*Miteq,SMO-226LC1A*); **6.** Low noise amplifier (*Miteq, JS4-02002600-30-10P*); **7.** MW SPDT switch (*Sierra Microwave, 0.5-26.5 SFD0526-000*); **8.** Direction coupler (*Narda, 1.7-26.5–4227–16*); **9.** Diode detector (*Hewlett-Packard, 0.01-26.5 GHz, 8473C*); **10.** Low noise amplifier (*Miteq, JS4-02002600-30-10P*); **11.** IRM (*Miteq, IRO-0226LC1A*); **12.** Band pass filter (*Mini Circuits, BBP-30*); **13.** RF amplifier (*Mini Circuits, ZFL-500LN*); **14.** RF mixer (*Mini Circuits, ZAD-1*); **15.** Low pass filter (*Mini Circuits, BLP-5*); **16.** RF amplifier (*HD Communication Corp., HD 17153BB*); **17.** Attenuator (*Mini Circuits, ZAFT-51020*); **18.** Blocking capacitor (*HP, 11742A*); **19.** Stepper motor; **20.** Motor driver; **21.** Diffusion pump; **22.** Rotary pump; **23.** 30 MHz function generator (*Stanford Research System, DS345*); **24.** Distribution amplifier (*Stanford Research System, FS710*); **25.** Antenna; **26.** Exhaust; **27.** Digital storage oscilloscope (*Tektronix TDS 2022*).

### 2.2.2 Electrical design

The electrical circuit shown in Figure 2.2 is used to generate the microwave pulse which is sent to the cavity and also to detect the signals emitted by a molecule/complex. The model numbers for the various components are given in parentheses. Certain components had to be replaced during the course of this Thesis and are highlighted below. The frequency synthesizer (*Agilent, MXG Analog Signal Generator, N5183A*) is the microwave source and can generate any frequency between 100 kHz and 32 GHz to 0.01 Hz accuracy. The output from this synthesizer (frequency ν, power 13dBm) is directed to a Single Pole Double Throw (SPDT) switch (*Sierra Microwave, 0.5-26.5 SFD0526-00, isolation 60dB*). This switch powers either the single-sideband mixer (SSBM) (*Miteq, SMO-226LC1A*) during the polarization cycle or the image rejection mixer (IRM) (*Miteq, IRO-0226LC1A*) during the detection cycle. During the polarization cycle, the SSBM mixes the signal from the synthesizer with a synchronous 30 MHz (power 16 dBm) signal obtained from a function generator (*SRS, DS345*). The SSBM gives the upper band ν+30 MHz as an output. This signal is then amplified by a low noise amplifier (*Miteq, JS4-02002600-30-10P replaced the previous JS3-02002600-5-7A amplifier*) with a gain of 30 dB. The amplified signal is then sent to another identical SPDT switch. This switch works synchronously with the other SPDT switch connecting either the polarization circuit or the detection circuit. These SPDT switches are controlled by a delay generator (*BNC-555 was replaced with BNC-575*). The delay generator sends two pulses having the same time duration (typically 0.2-3.0 μs) but of opposite polarity to these switches. Since the pulses to the SPDT switches have a certain time span the ν+30 MHz signal has a certain width (~1 MHz for 1 μs time duration). The output of the switch is then sent through a direction coupler (*Narda, 1.7-26.5–4227–16*) which directs the signal to the antenna.

The antenna couples the signal to the cavity to form standing waves. The molecules are polarized by this ν+30 MHz signal. The polarizing signal is centred at ν+30 MHz and has a width, therefore if the molecule absorbs within this width a transition occurs and the molecules coherently emit microwave radiation of frequency ν+30±Δ MHz, where Δ is the offset from ν+30 MHz (typically ~1-2 MHz). This signal is detected by the same antenna which acts as a receiver. To ensure that a standing wave is formed, the cavity must be tuned. The cavity is said to be in tune if the distance between the two mirrors is an integral multiple of half the wavelength of the microwave radiation.

If the cavity is not tuned almost all the microwave power is reflected. The direction coupler sends 2.5% of this reflected power to a digital storage oscilloscope (*Tektronix TDS 2022*). This power is monitored while tuning the cavity. Figure 2.3 shows the power in the oscilloscope when the cavity is in tune and when it is not.

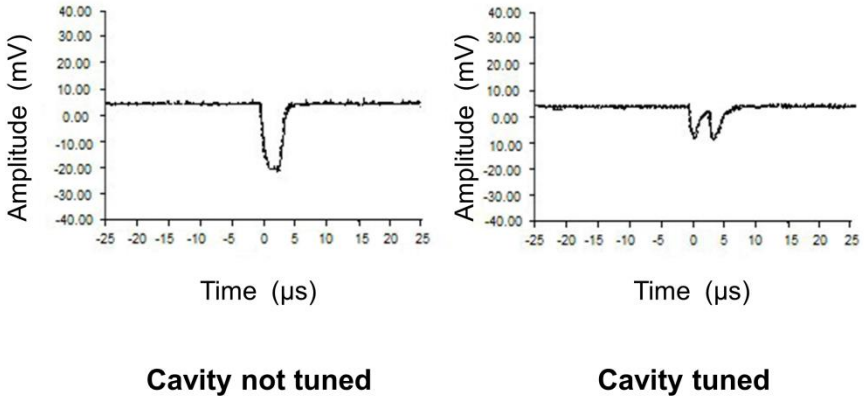


**Figure 2.3.** Reflected power signal on the oscilloscope, when the cavity is not tuned (V) and when the cavity is tuned (W).

The rest of the microwave signal from the direction coupler goes to a low noise amplifier (*Miteq JS4-02002600-3-5P, noise 2.8dB, gain 28 dB replaced by JS4-02002600-30-10P, gain 30 dB)* via the SPDT switch. The amplified signal is mixed with the frequency (ν) generated by the frequency synthesizer by an image rejection mixer (IRM). The IRM output then is the 30±Δ MHz signal which is routed to a band pass filter (*Mini Circuits, BBP-30*) and a low noise RF amplifier (*Mini Circuits, ZFL-500LN*). This signal is down converted to ±Δ MHz by mixing it with the output of the function generator (30 MHz) in an RF mixer (*Mini Circuits, ZAD-1*). The ±Δ signal is passed through a low pass filter (*Mini Circuits, BLP-5*) and then amplified by another RF amplifier (*HD Communication Corp., HD 17153BB*). This amplified signal is digitized by an NI-scope card (*National Instruments, PCI-5112 which was replaced by PCI-5114*). The PCI-5112 scope card has a maximum sampling speed of 100 MS/s whereas the PCI-5114 has a maximum sampling speed of 250 MS/s. The signal (±Δ) is typically <1 MHz and therefore, a sampling speed of 5 MHz is used. The external trigger input to the scope card is an analog trigger however the delay generator sends a digital trigger to the scope card. In the PCI-5112 this digital trigger was sent via the PFI 1 channel having a SMB jack connector. In the case of the PCI-5114 the PFI 1 channel could be accessed through

the AUX cable with a 9 pin DIN connector (pin 6 is the PFI 1 channel). The clock rate on the PCI-5114 is 25 MHz this means that the scope can detect only a 40 ns pulse whereas the trigger for the PCI-5112 was a 2 ns pulse; appropriate changes were made to digitize the observed signal correctly. The digitized time domain signal is Fourier transformed to obtain the signal in the frequency domain.

### 2.2.3 Software for the PNFTMW spectrometer

The operation of the spectrometer and the data acquisition is controlled by the computer. This is done using codes written in LabVIEW 7.1. The details of these codes are described in Reference 9. The codes control the frequency synthesizer via GPIB, and update the frequencies during the scanning process. The program also controls the timing of the pulse sequences and data acquisition. The time domain signal collected is Fourier transformed by these codes to give the frequency domain signal. The delay generator controlling the SPDT switches and hence the microwave pulses, is connected to the computer via a RS-232 connection. This delay generator is controlled by commands communicated through the HyperTerminal software.

### 2.2.4 Time sequences of the pulses

The microwave pulse is controlled by the *BNC-575* delay generator and the gas pulse is controlled by the *SRS-DG645* delay generator. A microwave pulse (typical pulse width 0.2-3.0 μs) is transmitted into the cavity. The pulse width of the microwave pulse is chosen based on the magnitude of the dipole moment under study. The microwave radiation forms a standing wave inside the tuned cavity and then decays after nearly 40 μs. The peak to peak amplitude of the standing wave formed is 6-8 V and it is therefore difficult to detect the molecular signal (mV) in the presence of such a high background. Thus, the digitisation begins only after the decay of this background signal, this is done by introducing a delay between the microwave pulse and the digitization pulse. This digitized signal is stored as noise. A gas pulse is then sent into the cavity. This gas pulse is polarised by another microwave pulse. There is a delay of a few microseconds between the gas pulse and the microwave pulse. This delay is called the 'start delay' and is taken care of by the processing time of the program. Multiple microwave pulses can be sent for a single gas pulse since the gas pulse takes nearly 2 ms to hit the other mirror while the typical data acquisition time is 100 μs. The signal is obtained by subtracting the record collected before sending the gas pulse from the corresponding

record after sending the gas pulse. A single shot is defined as the sequence of events starting from the first microwave pulse till the polarization of the molecules by multiple microwave pulses. The experiment is performed for *n* number of shots to improve the signal to noise ratio. The pulse sequence is given in the Figure 5.4.

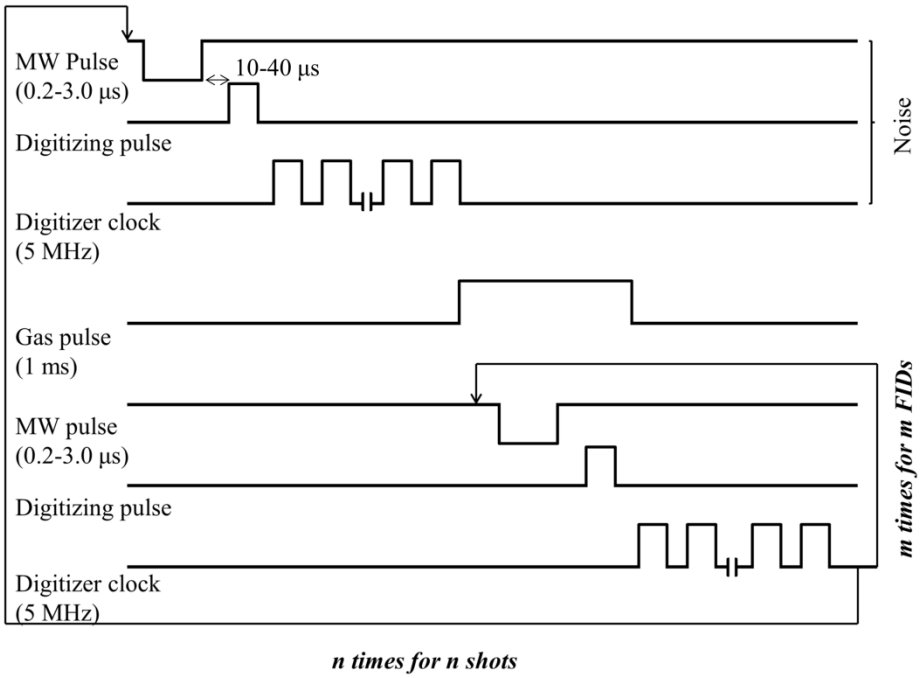


**Figure 5.4.** The pulse sequence for the experiment.

### 2.2.5 Sample preparation

In our experiments the pulsed nozzle produces a molecular beam. The molecules are introduced into the cavity by the supersonic expansion of the carrier gas (helium or argon) which contains the molecules to be investigated[1]. The flow of carrier gas (usually 1-5%) through a bubbler containing the liquid sample picks up the molecules. For complexes involving two or more liquid samples, the carrier gas is bubbled through each of the samples separately and then mixed at a four-way junction. The flow of gases is controlled by three different mass flow controllers (MKS, 1179). A 500 sccm mass flow controller is used to control the flow of the carrier gas which is usually 200 sccm for helium and 150 sccm for argon. Typically flow rates of less than 10 sccm are used for the sample molecules and therefore a 20-50 sccm mass flow controller is used. After mixing, the gas seeded with the molecules of interest is expanded against a back

pressure of 0.1-1.5 atm into the evacuated cavity ($10^{-6}$ mbar) through a pulsed nozzle having a diameter of 0.8 mm. This leads to a supersonic adiabatic expansion of the gases. The diameter (D) of the nozzle is much larger than the mean free path ($\lambda_0$) of the gases ($D \gg \lambda_0$). As the gas flows out of the nozzle many collisions between the molecules/atoms are possible. These two-body collisions lead to the cooling of the molecular beam[10]. This makes the environment conducive for the formation of weakly bound complexes which have low binding energies. The molecular complexes are formed by three-body collisions. The excess kinetic energy generated by the formation of the complex is carried away by the third body thus allowing the complex to stabilize.

## 2.3. Computational methods

### 2.3.1 Quantum chemical methods

The optimization of the molecular structures studied in this Thesis was done using various *ab initio* electronic structure methods as well as density functional methods (DFT). The 2nd order Møller-Plesset perturbation theory[11] and DFT methods were used for most of the systems studied. Single point calculations at the CCSD level were performed for a few systems. The optimized structures for a system are required to provide a starting point to search for the rotational transitions. Since a large number of conformations are possible for the weakly bound complexes the energy ordering is also important.

Harmonic frequency calculations are performed to confirm whether the optimized structures are minima structures at the potential energy surface or not. Centrifugal distortion constants were obtained from the vibrational-rotational coupling computed using the Freq=VibRot keyword. All computations were done using *Gaussian 09* software suite[12].

The binding energy for the complexes studied is calculated in the manner described below. The complex is considered to be a 'supermolecule', that is, separate subsystems (monomer units) are held together by non-covalent bonds to form the complex. The binding energy for the complex is calculated using the following expression; $\Delta E = E(\text{Complex}) - \Sigma E(\text{Monomer})$, where, $\Delta E$ is the binding energy for the complex and, E(complex) and E(monomer) are the energies of the complex and the monomer, respectively. In this approach, the basis sets of the subsystems are available to describe

the complex, but the monomer units are described by only their individual basis sets. Thus, the complex is more completely described by the 'borrowing' of the basis sets of all the subsystems. This leads to an artificial lowering of the energy calculated for the complex. This error can be corrected for by using infinite basis sets for the calculation, which is impractical for large systems. Therefore, the artificial lowering of the energy of the complex can be corrected for, either by using the basis sets of the whole 'supermolecule' to describe the subsystems or by extrapolating to the complete basis set limit. The first approach, developed by Boys and Bernardi is the counterpoise method and the error corrected for is known as the Basis Set Superposition Error (BSSE)[13]. The counterpoise correction is done by recalculating the energy of each subsystem using 'ghost orbitals' (basis set functions having no electrons or protons) in place of the other subsystems that form the complex. This method is therefore geometry dependent. We use the counterpoise method as implemented in *Gaussian 09*. The BSSE corrected binding energies are further corrected for the zero-point energy.

### 2.3.2 Atoms in Molecules (AIM) analysis

The geometrical parameters of a molecule such as bond distances and bond angles are accurately extracted from the rotational spectra. Molecular structure, which is the connectivity of the nuclei to each other by a network of bonds, is easily obtained from the electron density topology for the molecule. Bader's Atoms in Molecules theory[14,15] uses the charge density ($\varrho$) for the analysis. Any point in space where the first derivative of $\varrho$ vanishes is a critical point. The topological features of $\varrho$ (maxima, minima, and saddle points) are determined by the signs of the second derivatives of $\varrho$ along the three directions. A Hessian matrix of $\varrho$ is constructed and diagonalized to obtain the eigenvalues ($\lambda$). The trace of this diagonalized matrix is called the Laplacian ($\nabla^2\varrho$). The *rank* of the matrix is the number of non-zero eigenvalues. The *signature* is the algebraic sum of the sign of the eigenvalues. This helps to classify the critical points. Table 2.1 gives the critical points and the classification based on the rank and signature. Nuclear attractor represents positions of nuclei which are maxima along all three directions. Cage critical points are minima in all three directions. Bond/ring critical points are saddle points.

**Table 2.1.** The critical points classified on the basis of the eigenvalues of the Hessian of ϱ.

| Critical point | $\lambda_1$ | $\lambda_2$ | $\lambda_3$ | Rank | Signature |
|---|---|---|---|---|---|
| Nuclear attractor | - | - | - | 3 | -3 |
| Bond critical point | - | - | + | 3 | -1 |
| Ring critical point | - | + | + | 3 | +1 |
| Cage critical point | + | + | + | 3 | +3 |

Two nuclei are said to be bonded if there is a bond critical point (BCP) found between them. A bond path is defined as the line of maximum charge density that links the nuclei and the BCP. The molecular graph is a network of the bond paths that connect the nuclei and thus one can obtain structural information of the molecules and complexes.

The properties of the charge density help to quantify and understand the nature of the interactions present between atoms. The values of ϱ and $\nabla^2\varrho$ at the BCP help to identify the type of bond present between the atoms. Large values of ϱ and negative values of $\nabla^2\varrho$ are indicative of *shared interactions*, which are characteristic of a covalent bond, while low values of ϱ and positive values of $\nabla^2\varrho$ at the BCP indicates a *closed-shell interaction*, which is usually found in noble gas repulsive states, ionic bonds, hydrogen bonds, and van der Waals molecules[14].

### 2.3.3 Natural Bond Orbital (NBO) analysis

The NBO program developed by Weinhold and co-workers[16] performs an analysis of a many-electron wavefunction in terms of localised electron-pair bonding units. In this Thesis, NBO analysis was carried out to understand the nature of the orbitals in the intra/intermolecular bonds. It was also used to ascertain the presence of 3c-2e bonds. The natural resonance theory (NRT) module was used to obtain an analysis of the molecular electron density in terms of weighted resonance structures. This analysis was also used to calculate the bond orders. The calculations were performed using *NBO 6.0* as implemented in *Gaussian 09*.

## 2.4. References


(1) Balle, T. J.; Flygare, W. H. Fabry–Perot Cavity Pulsed Fourier Transform Microwave Spectrometer with a Pulsed Nozzle Particle Source. *Rev. Sci. Instrum.* **1981**, *52*, 33–45.

(2) Brown, G. G.; Dian, B. C.; Douglass, K. O.; Geyer, S. M.; Shipman, S. T.; Pate, B. H. A Broadband Fourier Transform Microwave Spectrometer Based on Chirped Pulse Excitation. *Rev. Sci. Instrum.* **2008**, *79*, 053103.

(3) Park, G. B.; Field, R. W. Perspective: The First Ten Years of Broadband Chirped Pulse Fourier Transform Microwave Spectroscopy. *J. Chem. Phys.* **2016**, *144*, 200901-1-200901-10.

(4) Patterson, D.; Schnell, M.; Doyle, J. M. Enantiomer-Specific Detection of Chiral Molecules via Microwave Spectroscopy. *Nature* **2013**, *497*, 475–477.

(5) Shubert, V. A.; Schmitz, D.; Patterson, D.; Doyle, J. M.; Schnell, M. Identifying Enantiomers in Mixtures of Chiral Molecules with Broadband Microwave Spectroscopy. *Angew. Chem. Int. Ed.* **2014**, *53*, 1152–1155.

(6) Abeysekera, C.; Joalland, B.; Ariyasingha, N.; Zack, L. N.; Sims, I. R.; Field, R. W.; Suits, A. G. Product Branching in the Low Temperature Reaction of CN with Propyne by Chirped-Pulse Microwave Spectroscopy in a Uniform Supersonic Flow. *J. Phys. Chem. Lett.* **2015**, *6*, 1599–1604.

(7) Arunan, E.; Tiwari, A. P.; Mandal, P. K.; Mathias, P. C. Pulsed Nozzle Fourier Transform Microwave Spectrometer: Ideal to Define Hydrogen Bond Radius. *Curr. Sci.* **2002**, *82*, 533–540.

(8) Mani, D. Microwave Spectroscopic and Atoms in Molecules Theoretical Investigations on Weakly Bound Complexes: From Hydrogen Bond to 'Carbon Bond'. PhD Thesis, Indian Institute of Science, Bangalore, **2013**.

(9) Goswami, M. Rotational Spectroscopic and Ab Initio Studies on The Weakly Bound Complexes Containing 0-H... π And SH... π Interactions. PhD Thesis, Indian Institute of Science, Bangalore, **2010**.

(10) Hayes, J. M.; Small, G. J. Supersonic Jets, Rotational Cooling, and Analytical Chemistry. *Anal. Chem.* **1983**, *55*, 565A-574A.

(11) Møller, Chr.; Plesset, M. S. Note on an Approximation Treatment for Many-Electron Systems. *Phys. Rev.* **1934**, *46*, 618–622.

(12) Frisch, M. J.; Trucks, G. W.; Schlegel, H. B.; Scuseria, G. E.; Robb, M. A.; Cheeseman, J. R.; Scalmani, G.; Barone, V.; Mennucci, B.; Petersson, G. A.; et al. *Gaussian 09,* Revision D. 01*,* Gaussian Inc: Wallingford, CT, **2009**.

(13) Boys, S. F.; Bernardi, F. de. The Calculation of Small Molecular Interactions by the Differences of Separate Total Energies. Some Procedures with Reduced Errors. *Mol. Phys.* **1970**, *19*, 553–566.

(14) Bader, R. F. W. *Atoms in Molecules: A Quantum Theory*; International Series of Monographs on Chemistry; Oxford University Press: Oxford, New York, **1994**.

(15) Bader, R. F. W.; Anderson, S. G.; Duke, A. J. Quantum Topology of Molecular Charge Distributions. 1. *J. Am. Chem. Soc.* **1979**, *101*, 1389–1395.

(16) Glendening, E. D.; Badenhoop, J. K.; Reed, A. E.; Carpenter, J. E.; Bohmann, J. A.; Morales, C. M.; Landis, C. R.; F. Weinhold. *NBO 6.0*; Theoretical Chemistry Institute, University of Wisconsin: Madison, WI, (nbo6.chem.wisc.edu), **2013**.

# CHAPTER 3

# Rotational spectra of a multifunctional alcohol-water complex: the propargyl alcohol···$H_2O$ dimer

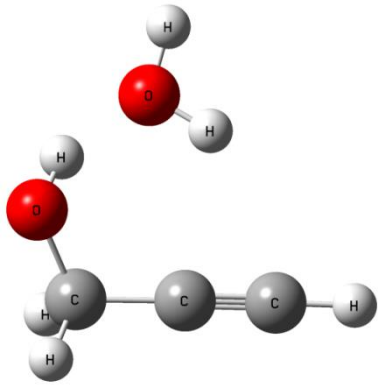

CHAPTER 3

# ROTATIONAL SPECTRA OF A MULTIFUNCTIONAL ALCOHOL-WATER COMPLEX: THE PROPARGYL ALCOHOL···$H_2O$ DIMER

## 3.1. Introduction

Molecules where multiple sites are available for hydrogen bonding offer a unique opportunity to study the propensity for various sites to act as H-bond donors or acceptors. Multiple sites could exist on one of the molecular fragments, or the monomer units that form the complex have functional groups that can act as either H-bond donors or acceptors, leading to varied binding possibilities.

The hydroxyl (-OH) group is one such group which can either donate or accept an H-bond. Alcohols and water both contain a hydroxyl group and it is of interest to note which of these fragments act as donors or acceptors of an H-bond when a complex is formed between the two species. Rotational spectroscopic studies helped resolve the debate about the donor-acceptor roles in the methanol···water complex[1]. It established that methanol acts as the H-bond acceptor and water as the donor, in the global minimum structure.

It is only in recent times that the structures of a number of small alcohol-water complexes have been investigated[2–9]. It is to be noted that saturated aliphatic alcohols

such as ethanol[2], n-propanol[3], iso-propanol[4], and t-butanol[5] form complexes with water where the alcohol acts as the hydrogen bond acceptor. Even the cyclic aliphatic alcohol, cyclohexanol[6] forms a complex with water where cyclohexanol acts as the H-bond acceptor. On the other hand, when the fluorinated counterparts of these saturated aliphatic alcohols (2-fluoroethanol[7], 2,2,2-trifluoroethanol[8], hexafluoroisopropanol[9], etc.) and the aromatic alcohol, phenol[10] form a complex with water, the alcohols act as H-bond donors. It seems that the electron donating or withdrawing characteristics of the groups attached to the hydroxyl group in the alcohols dictate if the OH group would act as an H-bond donor or acceptor. The R groups (R= $CH_3$, $C_2H_5$) on the saturated aliphatic alcohols are electron donating groups whereas, fluorine and the phenyl group are electron withdrawing groups. It is of interest then to see the role of propargyl alcohol when it forms a complex with water.

Propargyl alcohol (PA) is an unsaturated aliphatic alcohol. This multifunctional molecule contains a hydroxyl (-OH) group and an acetylenic moiety. The acetylenic group is weakly electron withdrawing and therefore provides an intriguing possibility to explore its H-bond donor-acceptor capabilities in a complex with water. One can visualize this molecule to be made up of two fragments — a substituted methanol and an acetylene unit. This leads to multiple binding sites in the molecule, with the hydroxyl group capable of donating or accepting an H-bond, and the acetylene group capable of accepting a weak H-bond with the π-cloud or donating an H-bond with the acidic acetylenic hydrogen. When a complex is formed with water, a number of donor-acceptor combinations are possible leading to many different structures. Would the structure be similar to that of the methanol···water complex[1] or that of the acetylene-water complex[11](where the acetylene donates an H-bond forming a C-H···O bond)? Is it possible that the H-bond sites compete to form a structure where multiple interactions could lead to further stabilization? It is interesting to note the preference for H-bonding in molecules with multiple binding sites and how competing interactions would influence the H-bonded structures of complexes formed by such molecules.

A couple of infrared spectroscopic investigations have been carried out on the PA···$H_2O$ complex. Saini and Viswanathan studied the hydrogen bonded PA···$H_2O$ complex using matrix isolation IR spectroscopy[12]. The experiments were done in both $N_2$ and Ar matrices, with comparable results. They have observed the global minimum

structure for the complex, where PA donates the H-bond to the water fragment, and the acetylenic moiety accepts an H-bond from the water forming a closed hydrogen bonded network. However, calculations show that another structure is possible which differs only in the position of the free hydrogen atom of water and is very close in energy to the global minimum structure. These IR spectroscopic results however offer no information about the position of the non-bonded free H of water, making it difficult to differentiate between these two structures.

The other IR study on the PA···$H_2O$ complex was done using helium droplets. Mani et al. formed the PA···$D_2O$ complex inside superfluid helium droplets and studied the IR spectrum[13]. Surprisingly, they did not find the global minimum structure but observed only local minima structures. They have observed two structures, one where water acts as the hydrogen bond donor and another structure where PA donates an H-bond to water from the acetylenic end (C-H···O). These two observed structures are similar to those expected, if we consider the multifunctional PA molecule to be made up of separate entities that is of a substituted methanol and an acetylenic moiety. Both these IR studies observe different structures for the PA···$H_2O$ complex. A rotational spectroscopic study of this complex would enable us to observe a structure that would be free from any effects of the environment. Also, the specificity of rotational spectroscopy allows for the determination of the position of the non-bonded hydrogen of water, thereby differentiating between similar structures.

Weakly bound complexes of small organic molecules with water have been the subject of numerous investigations[5]. Such studies are valuable as they help in the accurate modelling of interactions that are important in biological systems. These complexes of water with small molecules usually show some splitting in the rotational transitions due to the internal motions of water. These internal dynamics of water have been summarized by Caminati and coworkers[5] for different categories based on the various donor-acceptor possibilities and the symmetry of the species involved.

The PA···water complex offers the possibility to observe such internal dynamics of water in the presence of two different H-bonds. One expects these motions to be similar to those found in the 2-fluoroethanol···water complex[7]. This complex is bound by a strong O-H···O bond (alcohol is the donor) and a weak O-H···F bond (water is the donor). The tunneling splitting arises due to the interchange of the two equivalent

hydrogen atoms of water by a concerted motion of the OH wag (of water) along with the rotation of water about the O-H···O H-bond.

In the present study, we report the rotational spectra of the PA···$H_2O$ complex and its isotopologues. The isotopic substitution aids in ascertaining the position of the free hydrogen, thereby distinguishing between the two lowest energy structures. We also aim to understand the possible internal motions that give rise to the splitting observed for the rotational transitions.

## 3.2. Methods

### 3.2.1. Experimental details

The spectra of the PA···$H_2O$ complex and its isotopologues have been recorded using a Balle-Flygare type pulsed nozzle Fourier transform microwave (PNFTMW) spectrometer[14]. Details of this spectrometer have been described in *Chapter 2*. The propargyl alcohol (PA) was obtained from *Sigma-Aldrich*. The isotopes $H_2{}^{18}O$ and $D_2O$ were obtained from *Cambridge Isotope Laboratories* and used without further purification. $D_2O$ and $H_2O$ were mixed in a ratio of 3:1 to form the DOH isotopologue. This was done to form appreciable amounts of DOH in the system. $D_2O$ was used in a higher ratio because there was some amount of $H_2O$ always present in the gas lines. For the PA(OD) isotopologue, $D_2O$ was added to the bubbler containing PA to make a mixture of PA and $D_2O$ in a 9:4 ratio as prescribed by Hirota for the monomer spectrum of PA(OD)[15]. This same ratio was also used in previous studies for the PA(OD) isotopologues of the PA dimer[16] and PA···Ar spectra[17]. The PA···$H_2{}^{18}O$ spectrum was obtained by using a 10% solution of $H_2{}^{18}O$ in water because only 1ml of $H_2{}^{18}O$ was available. Helium was used as a carrier gas to avoid complexation of PA with argon and therefore reduce the congestion of the spectra. Helium was flown at a backing pressure of 1.4-1.6 atm. The flow through PA and water was kept as low as possible to ensure that not too much water was present in the gas lines. This was done to easily check the dependence of the observed signals on PA and $H_2O$. The signals for the complex were optimum when the flow of helium through PA and $H_2O$ were kept in a ratio of 2:1. The optimum pulse width for the *a*-, *b*-, and *c*- dipole lines was 0.8-1.0, 0.2, 0.4-0.6 μs, respectively. The spectra were collected using 256 points while scanning for transitions and the observed rotational lines were later averaged at 512 or 1024 points to obtain the high-resolution spectra.

### 3.2.2. Computational details

The structures of the PA···$H_2O$ complex were optimized at the MP2/6-311++G(d,p) level of theory using *Gaussian 09*[18]. The initial guess geometries that were used for the optimization, resembled known interactions such as the O-H···O bonds in water dimer and other alcohol-water complexes, and the O-H···π interactions in the acetylene···water and ethylene···water complexes. Harmonic frequency calculations were performed at the same level of theory to determine if the structures obtained were minima structures on the potential energy surface. The centrifugal distortion constants were calculated for all isotopologues by using the freq=vibrot keyword. The binding energies for the complexes were corrected for the basis set superposition error (BSSE) using Boys and Bernardi's counterpoise method[19]. The zero-point energy (ZPE) correction was done using the harmonic frequency calculations. The rotational transitions were predicted using the calculated rotational constants with the help of the programs, SPCAT[20,21] and ASROT[22,23]. The observed rotational transitions show splitting; these could be due to various internal motions of the monomers in the complex. To understand the possible motions involved, relaxed and rigid scans about various bonds and axes were carried out using opt=modredundant and scan keywords, respectively. The barriers determined from these scans would help determine the feasible pathways for internal motions which lead to the splitting of the observed spectra. The electron density topologies for the optimized geometries have been calculated using the *AIMAll* software[24]. The wavefunctions for this calculation were obtained from the *Gaussian 09* at MP2/6-311++G(d,p).

## 3.3. Results

### 3.3.1. Optimized structures

The PA monomer can exist in the gauche as well as trans conformations and the energy barrier[15] between them is reported to be around 8.2 kJmol$^{-1}$. The optimized structures for the PA···$H_2O$ complex are shown in Figures 3.1 and 3.2. Structures are labelled to indicate in which conformer PA is present (gauche or trans), and which species plays the role of the donor or acceptor. They are labelled in the order donor-acceptor according to the primary interaction, which is followed by a number to indicate the energy ordering of the complexes.

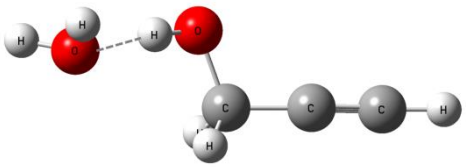

T-PW-1
(-13.7 kJmol$^{-1}$)

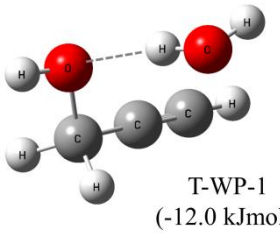

T-WP-1
(-12.0 kJmol$^{-1}$)

**Figure 3.1.** Structures of the trans-PA···$H_2O$ complex optimized at MP2/6-311++G(d,p).

The optimized structures for the trans-PA···$H_2O$ complex are shown in Figure 3.1 and the rotational constants and binding energies are given in Table 3.1. All previous IR[12,13] and rotational[15–17,25,26] spectroscopic studies on PA and its complexes found PA to be in the gauche conformation. Since there is no evidence for the existence of the trans conformer, all further discussions in this Chapter will consider only the gauche conformer of PA.

**Table 3.1.** The rotational constants (MHz), electric dipole moment components (debye), and the binding energy (ΔE) with BSSE and ZPE corrections (kJmol$^{-1}$) calculated at MP2/6-311++G(d,p) for the lowest energy optimized structures of the trans-PA···$H_2O$ complex.

| **Parameters** | **PA as donor** T-PW-1 | **$H_2O$ as donor** T-WP-1 |
|---|---|---|
| **Rotational Constants** (MHz) | | |
| A | 17423.6 | 5575.1 |
| B | 1500.8 | 2593.6 |
| C | 1479.7 | 1896.6 |
| **Dipole Moment** (D) | | |
| $\lvert\mu_a\rvert$ | 3.67 | 2.52 |
| $\lvert\mu_b\rvert$ | 1.38 | 1.45 |
| $\lvert\mu_c\rvert$ | 0.21 | 0.12 |
| **ΔE (BSSE+ZPE)** (kJmol$^{-1}$) | -13.7 | -12.0 |

The optimized structures for the gauche-PA···$H_2O$ complex are shown in Figure 3.2. Structures G-PW-1a and G-PW-1b are the lowest energy structures and have the hydroxyl (-OH) group of PA acting as the O-H···O hydrogen bond donor, these complexes are also bound by a weaker O-H···π secondary interaction. The position of the free H atom of water is the only difference between these two structures. Structure G-PW-2 has a structure similar to the acetylene···water dimer[11] having a C-H···O bond. Structures G-WP-1, G-WP-2a, and G-WP-2b are close in energy and are structures where $H_2O$ is the H-bond donor. Structures G-WP-2a and G-WP-2b differ only in the position of the non-bonded hydrogen of water. In structure G-WP-3 the $H_2O$ molecule approaches PA in the direction anti to the hydroxyl group and forms an O-H···π bond. The helium droplet IR study found structure G-PW-2 and G-WP-2; however, they cannot distinguish between G-WP-2a and 2b. The matrix isolation IR spectroscopic study found G-PW-1 and is unable to unambiguously assign the spectra to either G-PW-1a or 1b.

The calculated rotational constants, electric dipole moment components, and the BSSE and ZPE corrected binding energies for the optimized structures of the G-PA···$H_2O$ complex are given in Table 3.2. Structures G-PW-1a and G-PW-1b, the lowest energy structures are quite close in energy differing by only 0.7 $kJmol^{-1}$. Their rotational constants are also quite close as they only differ in the position of the non-bonded H of $H_2O$. A rotational spectrum could easily distinguish between them since the *c*-dipole moment components for both the structures are very different. These *ab initio* rotational constants were used to predict the spectra for a 1:1 complex of PA and water and to also study the isotopic substitutions which helped in determining the structure.

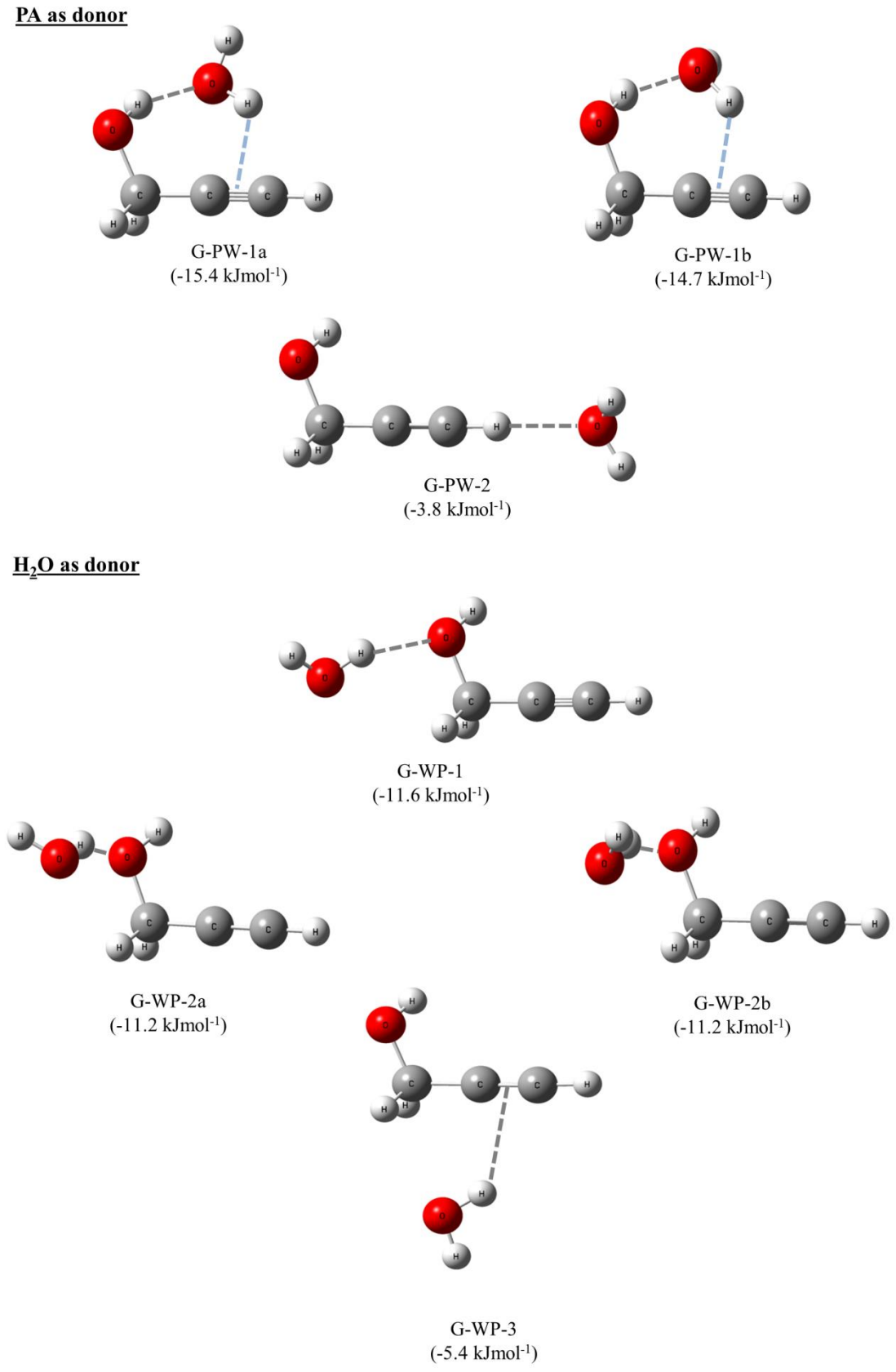


**Figure 3.2.** Structures of the gauche-PA···$H_2O$ complex optimized at MP2/6-311++G(d,p).

**Table 3.2.** The rotational constants (MHz), electric dipole moment components (debye), asymmetry parameter (κ), and the binding energy (ΔE) with the BSSE and ZPE corrections ($kJmol^{-1}$) calculated at MP2/6-311++G(d,p) for the optimized structures of the gauche-PA···$H_2O$ complex.

| **Parameters** | **PA as donor** | | |
|---|---|---|---|
| | **G-PW-1a** | **G-PW-1b** | **G-PW-2** |
| **Rotational Constants** (MHz) | | | |
| A | 4623.9 | 4579.1 | 23373.9 |
| B | 3814.8 | 3861.7 | 1056.0 |
| C | 2242.4 | 2252.6 | 1020.3 |
| **Dipole Moment** (D) | | | |
| $\lvert\mu_a\rvert$ | 0.07 | 0.21 | 3.50 |
| $\lvert\mu_b\rvert$ | 3.13 | 2.89 | 0.73 |
| $\lvert\mu_c\rvert$ | 0.20 | 2.27 | 0.02 |
| **Asymmetry Parameter** (κ) | 0.32 | 0.38 | -0.99 |
| **ΔE (BSSE+ZPE)** ($kJmol^{-1}$) | -15.4 | -14.7 | -3.8 |

| **Parameters** | **$H_2O$ as donor** | | | |
|---|---|---|---|---|
| | **G-WP-1** | **G-WP-2a** | **G-WP-2b** | **G-WP-3** |
| **Rotational Constants** (MHz) | | | | |
| A | 22909.5 | 7957.7 | 8277.4 | 5626.2 |
| B | 1549.8 | 2041.7 | 1988.3 | 2585.8 |
| C | 1471.7 | 1782.2 | 1760.3 | 1804.2 |
| **Dipole Moment** (D) | | | | |
| $\lvert\mu_a\rvert$ | 1.84 | 1.49 | 2.78 | 1.80 |
| $\lvert\mu_b\rvert$ | 1.30 | 2.09 | 0.36 | 2.28 |
| $\lvert\mu_c\rvert$ | 0.00 | 0.76 | 1.64 | 1.72 |
| **Asymmetry Parameter** (κ) | -0.99 | -0.92 | -0.93 | -0.59 |
| **ΔE (BSSE+ZPE)** ($kJmol^{-1}$) | -11.6 | -11.2 | -11.2 | -5.4 |

### 3.3.2. Search and assignment

The rotational transitions for the PA···$H_2O$ complex were searched for using helium as the carrier gas. Many of the optimized structures are quite close in energy to the lowest energy structures, and therefore using helium as a carrier gas allows for the possibility of observing these local minima structures as well. Initial searches for the dimer were carried out by flowing He through PA and $H_2O$ in a 1:1 ratio. A number of transitions were obtained. The dependence of these transitions was difficult to ascertain because they were of similar intensity even in the absence of $H_2O$. The flow through $H_2O$ was reduced to nearly half of that of PA and the search continued. A large region from 6-14 GHz was searched. We expected to observe the 0⟶1 and the

1→2 transitions in this range. However, the spectrum obtained could not be assigned satisfactorily.

The search was extended to the 15 GHz region, where the 2→3 transitions were predicted. The $3_{03}$-$2_{12}$, $3_{13}$-$2_{12}$, $3_{03}$-$2_{02}$, and $3_{13}$-$2_{02}$ quartet were predicted to be within a 500 MHz range of each other, and would therefore be easy to assign. Strong lines were soon obtained at 15125.5, 15170.9, 15359.8, and 15405.2 MHz. The pulse width and species dependence were confirmed and other transitions easily found based on these transitions. It was then realized that a number of transitions, especially the 1→2 transitions were overlooked as they were listed as unassigned transitions in a previous study of the PA···dimer[16]. These transitions were wrongly assigned as belonging to a PA···dimer structure; because they were found when only PA was used (in the absence of water). However, these lines were observed because PA is hygroscopic and there were always trace amounts of water in the gas lines, making it possible to form the PA···water complex even without flow through water.

A total of 27 transitions were observed for the PA···$H_2O$ complex, 20 of these are from the R-branch and 7 belong to the Q-branch. Only *b*-dipole transitions were observed for the Q-branch. All the *a*-type and *b*-type transitions show a doubling. Certain *b*-type transitions show hyperfine features and some are split into three lines instead of two. The *c*-type transitions are further split resulting in four lines. The intensities of some of the lines in the doublet were clearly in the ratio of 3:1. However, for most of the lines it was difficult to ascertain the intensity pattern.

The transitions were fit assuming that the lower frequency of the doublet arises from one state (State 1) and the higher frequency from the other state (State 2). The *c*-type transitions are split into four components. Therefore, an average was taken of the two lower frequency doublets and fit with the lower frequency set and the higher frequency doublet were fit in a similar manner. The doublets are split by around 105 kHz. Each state could be fit independently to a semi-rigid rotor Watson's A-reduced Hamiltonian in the $III^r$ representation.

While fitting it was noticed that a few transition frequencies had large observed-calculated values and the standard deviation of the fit was also large (nearly 50 kHz). Since it was the same transitions in both the states that were showing large deviations of opposite sign, we interchanged these frequencies and fitted the rotational constants.

This led to a better fit where the standard deviations are within experimental uncertainty. The standard deviation of the fit for State 1 is 3.2 kHz and for State 2 it is 2.8 kHz. For those transitions where the intensity pattern could be discerned, we notice that the higher intensity lines belong to State 1 and the lower intensity lines to State 2. For certain transitions in State 1 where the intensity was strong enough (mostly *b*-type transitions), hyperfine features could be observed in the high-resolution spectrum. Therefore, we suggest that State 1 has $H_2O$ in ortho (I=1) spin state and State 2 has $H_2O$ in the para (I=0) spin state. The observed transitions are given in Table 3.3 and the fitted parameters are given in Table 3.4.

**Table 3.3.** Observed transition frequencies for the PA···$H_2O$ complex.

| Transition | State 1 (MHz) | obs-calc (MHz) | State 2 (MHz) | obs-calc (MHz) |
|---|---|---|---|---|
| **R-branch** | | | | |
| $1_{01}$ -$0_{00}$ | 6016.7850 | -0.0004 | 6017.0190 | 0.0003 |
| $1_{11}$ -$0_{00}$ | 6813.1410 | 0.0045 | 6813.1215 | 0.0013 |
| $1_{10}$ -$0_{00}$[a] | 8386.7774 | 0.0008 | 8387.0557 | 0.0024 |
| $2_{02}$ -$1_{11}$ | 10225.5264 | 0.0022 | 10225.8584 | 0.0003 |
| $2_{12}$ -$1_{11}$ | 10459.8628 | 0.0037 | 10460.0337 | 0.0002 |
| $2_{02}$ -$1_{01}$ | 11021.8752 | 0.0000 | 11021.9582 | -0.0014 |
| $2_{12}$ -$1_{01}$ | 11256.2070 | -0.0032 | 11256.1337 | -0.0013 |
| $2_{11}$ -$1_{10}$ | 13606.9240 | -0.0058 | 13607.6930 | 0.0024 |
| $3_{03}$ -$2_{12}$ | 15125.4774 | 0.0003 | 15125.5995 | 0.0019 |
| $3_{13}$ -$2_{12}$ | 15170.9068 | -0.0002 | 15170.9801 | 0.0012 |
| $3_{03}$ -$2_{02}$ | 15359.8118 | -0.0003 | 15359.7728 | -0.0002 |
| $3_{13}$ -$2_{02}$ | 15405.2435 | 0.0015 | 15405.1556 | 0.0013 |
| $2_{11}$ -$1_{01}$[a] | 15976.9240 | 0.0030 | 15977.7285 | 0.0033 |
| $2_{21}$ -$1_{10}$ | 15996.1048 | 0.0038 | 15996.1048 | -0.0042 |
| $3_{12}$ -$2_{21}$ | 16986.4216 | -0.0003 | 16987.7862 | -0.0034 |
| $2_{20}$ -$1_{10}$[a] | 17007.5335 | -0.0047 | 17007.9266 | -0.0015 |
| $2_{21}$ -$1_{11}$[a] | 17569.7383 | -0.0029 | 17570.0410 | -0.0011 |
| **Q-branch** | | | | |
| $3_{12}$ -$3_{21}$ | 4764.3430 | 0.0023 | 4764.7950 | -0.0039 |
| $2_{11}$ -$2_{02}$ | 4955.0470 | 0.0012 | 4955.7640 | -0.0016 |
| $2_{12}$ -$2_{21}$ | 7109.8775 | -0.0046 | 7110.0093 | -0.0007 |
| $4_{13}$ -$4_{22}$ | 8121.1780 | 0.0006 | 8122.7760 | 0.0025 |
| $3_{31}$ -$3_{22}$ | 8434.2170 | 0.0029 | 8433.8660 | 0.0018 |
| $3_{12}$ -$3_{03}$ | 8970.8287 | 0.0018 | 8972.2208 | 0.0002 |
| $3_{13}$ -$3_{22}$ | 9988.7930 | -0.0028 | 9989.5508 | 0.0002 |
| $4_{32}$ -$4_{23}$ | 10537.8870 | -0.0024 | 10538.2970 | -0.0014 |
| $4_{13}$ -$4_{04}$ | 13201.0174 | -0.0021 | 13202.6744 | -0.0046 |
| $4_{14}$ -$4_{23}$ | 13494.6120 | 0.0017 | 13495.9760 | 0.0055 |

[a] the average frequency for the *c*-dipole transitions are reported.

**Table 3.4.** Experimental rotational constants and centrifugal distortion constants for the two states of the PA···$H_2O$ complex.

| Constant | State 1 | State 2 |
|---|---|---|
| **A (MHz)** | 4591.5418(8) | 4591.5536(7) |
| **B (MHz)** | 3795.2932(8) | 3795.5586(7) |
| **C (MHz)** | 2221.5572(7) | 2221.5269(6) |
| **$\Delta_J$ (kHz)** | 14.58(5) | 14.75(4) |
| **$\Delta_{JK}$ (kHz)** | -32.0(1) | - 32.8(1) |
| **$\Delta_K$ (kHz)** | 19.4(1) | 20.06(9) |
| **$\delta_J$ (kHz)** | -2.46(3) | - 2.37(2) |
| **$\delta_K$ (kHz)** | -20.7(2) | - 21.9(2) |
| **n** | 27 | 27 |
| **RMS (kHz)** | 3.2 | 2.8 |

### 3.3.3. Isotopic substitution

The spectra for the isotopologues were studied to ascertain the geometry of the experimentally observed structure and to confirm the position of the non-bonded H-atom of $H_2O$ in the PA···$H_2O$ complex.

**PA···$D_2O$**

It is expected that the splitting of the lines into doublets that was observed in the parent spectrum should reduce due to the substitution of H by D. Since the doublets are split by only few hundreds of kHz in the parent spectrum, we are not able to resolve the splitting of the transitions in the case of $D_2O$. The transitions however show hyperfine splitting due to the nuclear quadrupole coupling of the two D atoms. The hyperfine splitting could not be assigned and fitted, therefore only the strongest line for each frequency was used in the fit. Only one *c*-type line was observed and we note that it splits as a doublet instead of four lines as was observed in the parent spectrum. Surprisingly, we obtain two different sets of transitions for the PA···$D_2O$ complex. These two sets of transitions could be fit independently and the rotational constants obtained for the two sets differ by several MHz. The possible reason for this observation will be discussed later. The observed transitions for the PA···$D_2O$ complex are given in Table 3.5.

**Table 3.5.** Observed transition frequencies for the PA···$D_2O$ complex.

| Transition | Set-1 (MHz) | obs-calc (MHz) | Set-2 (MHz) | obs-calc (MHz) |
|---|---|---|---|---|
| $1_{11}$ -$0_{00}$ | 6526.7177 | 0.0064 | 6583.7424 | 0.0000 |
| $1_{10}$ -$0_{00}$ | 7971.5884 | -0.0025 | - | - |
| $2_{02}$ -$1_{11}$ | 9546.2726 | 0.0003 | 9606.7335 | -0.0050 |
| $2_{12}$ -$1_{11}$ | 9844.0726 | -0.0006 | 9914.3387 | 0.0007 |
| $2_{02}$ -$1_{01}$ | 10428.5142 | 0.0032 | 10507.5092 | 0.0071 |
| $2_{12}$ -$1_{01}$ | 10726.3056 | -0.0063 | 10815.0957 | -0.0059 |
| $3_{03}$ -$2_{12}$ | 14254.2654 | -0.0038 | 14357.2278 | 0.0078 |
| $3_{13}$ -$2_{12}$ | 14321.5629 | 0.0064 | 14427.6529 | -0.0115 |
| $3_{03}$ -$2_{02}$ | 14552.0654 | -0.0047 | 14664.8310 | 0.0115 |
| $3_{13}$ -$2_{02}$ | 14619.3602 | 0.0028 | 14735.2582 | -0.0057 |
| $2_{21}$ -$1_{10}$ | 15380.3775 | 0.0005 | - | - |
| $3_{12}$ -$2_{21}$ | 15616.3726 | 0.0002 | - | - |
| $2_{20}$ -$1_{11}$ | 17685.5752 | -0.0002 | - | - |

**PA···DOH**

As mentioned earlier, the parent PA···$H_2O$ complex shows a doubling of the rotational transitions. If this doubling of the transitions were due to the interchange of the equivalent H atoms of water, one expects that no doubling would be observed in the PA···DOH spectrum as the deuterium substitution breaks the symmetry of the $H_2O$ molecule. We do not observe any doubling in the spectrum. The spectrum shows no splitting in the transitions except for the hyperfine splitting due to the nuclear quadrupole coupling of deuterium. The *c*-type lines show a doublet instead of the four lines observed in the parent spectrum. An average of the doublet was used to obtain the fit. However, two different sets of spectra are observed for the PA···DOH complex as was observed in the case of the PA···$D_2O$ spectra. The *c*-type lines in both the sets are a doublet. The doublets were split by around 57 kHz for Set 1 and around 85 kHz for Set 2. We note that this splitting is reduced from the parent spectra, where the corresponding splitting was around 105 kHz.

The rotational constants obtained from the fit suggest that the observed spectra correspond to the structure where the deuterium atom of DOH is bound to the acetylenic moiety of PA. The spectrum for the complex where the H atom is bound to the π-cloud instead of D was not obtained despite careful searches. The observed transitions are given in Table 3.6 and the experimental fit for the constants of the PA···DOH and PA···$D_2O$ complexes are given in Table 3.7.

**Table 3.6.** Observed transition frequencies for the PA···DOH complex.

| Transition | Set-1 (MHz) | obs-calc (MHz) | Set-2 (MHz) | obs-calc (MHz) |
|---|---|---|---|---|
| $1_{11}$ -$0_{00}$ | - | - | 6701.7004 | -0.0008 |
| $1_{10}$ -$0_{00}$[a] | 8213.8665 | -0.0023 | 8279.5630 | 0.0011 |
| $2_{02}$ -$1_{11}$ | 10060.6457 | -0.0007 | 10151.2898 | -0.0031 |
| $2_{12}$ -$1_{11}$ | - | - | 10354.5508 | 0.0031 |
| $2_{02}$ -$1_{01}$ | 10799.4434 | -0.0038 | 10886.7506 | -0.0015 |
| $2_{12}$ -$1_{01}$ | 11006.0606 | 0.0065 | 11090.0093 | 0.0024 |
| $3_{03}$ -$2_{12}$ | 14836.5947 | 0.0028 | 14960.2359 | 0.0016 |
| $3_{13}$ -$2_{12}$ | 14874.4653 | 0.0006 | 14997.0125 | 0.0014 |
| $3_{13}$ -$2_{02}$ | 15081.0678 | -0.0038 | 15200.2627 | -0.0032 |
| $2_{21}$ -$1_{10}$ | 15605.4199 | -0.0039 | 15716.5752 | -0.0016 |
| $2_{11}$ -$1_{01}$[a] | 16634.0078 | 0.0001 | 15823.3906 | -0.0013 |
| $2_{20}$ -$1_{10}$[a] | - | - | 16762.0654 | 0.0005 |
| $3_{12}$ -$2_{21}$ | 16796.6484 | -0.0001 | 16966.6090 | 0.0003 |
| $2_{21}$ -$1_{11}$[a] | 17166.3655 | 0.0037 | 17294.4387 | 0.0013 |

[a] the average frequency for the *c*-dipole transitions are reported.

**Table 3.7.** Experimental rotational constants and centrifugal distortion constants for the two sets of the PA···DOH and PA···$D_2O$ complexes.

| Constant | PA···DOH (Set-1) | PA···DOH (Set-2) | PA···$D_2O$ (Set-1) | PA···$D_2O$ (Set-2)[a] |
|---|---|---|---|---|
| **A (MHz)** | 4476.321(8) | 4507.506(3) | 4426.903(6) | 4468.016(9) |
| **B (MHz)** | 3737.604(8) | 3772.108(3) | 3544.736(7) | 3567.341(8) |
| **C (MHz)** | 2176.583(3) | 2194.180(1) | 2099.756(4) | 2115.692(2) |
| **$\Delta_J$ (kHz)** | 14.0(6) | 13.1(2) | 12.0(7) | [11.89] |
| **$\Delta_{JK}$ (kHz)** | - 28(2) | -26.2(9) | - 60(3) | [-27.4] |
| **$\Delta_K$ (kHz)** | 16(2) | 15.0(8) | 56(4) | [17.19] |
| **$\delta_J$ (kHz)** | - 1.9(3) | -2.6(1) | 4.9(3) | [-2.19] |
| **$\delta_K$ (kHz)** | - 17(2) | - 10.2(9) | -28(2) | [-17.8] |
| **n** | 11 | 14 | 13 | 9 |
| **RMS (kHz)** | 6.2 | 2.9 | 6.1 | 8.8 |

[a] The centrifugal distortion constants are kept fixed at values calculated for the PA···$D_2O$ complex at MP2/6-311++G(d,p).

**PA(OD)···$H_2O$**

The hydrogen atom of the hydroxyl group on PA that forms the O-H···O bond was also substituted by deuterium. We recorded the spectrum for the PA(OD)···$H_2O$ isotopologue. The spectrum observed shows doubling of the rotational transitions, similar to the parent spectrum. However, in this case only six *b*-type transitions were observed. No *a*- or *c*-type transitions were observed despite a large number of gas pulses averaged in the predicted frequency range. These transitions show similar

splitting as observed for the parent dimer in addition to the hyperfine features due to deuterium. The observed transitions and the fit rotational constants are given in Tables 3.8 and 3.9, respectively. The centrifugal distortion constants were fixed to values that were obtained from *ab initio* calculations at MP2/6-311++G(d,p) for the PA(OD)···$H_2O$ dimer. This is a reasonable approximation since for the parent PA···$H_2O$ complex, experimental distortion constants were very close to the values calculated at this level.

**Table 3.8.** Observed transition frequencies for the PA(OD)···$H_2O$ complex.

| Transition | State 1 (MHz) | obs-calc (MHz) | State 2 (MHz) | obs-calc (MHz) |
|---|---|---|---|---|
| $1_{11}$ -$0_{00}$ | 6770.8616 | 0.0062 | 6770.8468 | 0.0104 |
| $2_{12}$ -$1_{01}$ | 11178.1336 | 0.0111 | 11178.0579 | 0.0135 |
| $3_{13}$ -$2_{02}$ | 15288.5665 | -0.0001 | 15288.4762 | -0.0019 |
| $2_{21}$ -$1_{10}$ | 15905.1070 | -0.0043 | 15905.1070 | -0.0060 |
| $4_{04}$ -$3_{13}$ | 19518.7410 | 0.0094 | 19518.7410 | -0.0159 |
| $4_{14}$ -$3_{03}$ | 19575.6469 | -0.0143 | 19575.5736 | 0.0110 |

**Table 3.9.** Experimental rotational constants of the two states for the PA(OD)···$H_2O$ complex. The centrifugal distortion constants are kept fixed at the values calculated for the PA(OD)···$H_2O$ complex at MP2/6-311++G(d,p).

| Constant | State 1 | State 2 |
|---|---|---|
| **A (MHz)** | 4567.173(4) | 4567.183(6) |
| **B (MHz)** | 3754.96(4) | 3755.23(5) |
| **C (MHz)** | 2203.648(3) | 2203.618(4) |
| **$\Delta_J$ (kHz)** | [12.26] | [12.26] |
| **$\Delta_{JK}$ (kHz)** | [-27.7] | [-27.7] |
| **$\Delta_K$ (kHz)** | [17.13] | [17.13] |
| **$\delta_J$ (kHz)** | [-2.18] | [-2.18] |
| **$\delta_K$ (kHz)** | [-18.3] | [-18.3] |
| **n** | 6 | 6 |
| **RMS (kHz)** | 12.5 | 16.0 |

**PA···$H_2{}^{18}O$**

We also recorded the spectrum for the PA···$H_2{}^{18}O$ and find that the splitting pattern is similar to the PA···$H_2O$ spectrum. However, the 3:1 intensity pattern observed for parent PA···$H_2O$ complex was not easily discernable for the transitions of the PA···$H_2{}^{18}O$. Only 11 transitions could be recorded due to the limited amount of the enriched $H_2{}^{18}O$ available (Table 3.10). The transitions were fit in a manner similar to that of the parent dimer. It was observed that the same transitions had large observed-

calculated values and so their frequencies were interchanged. Since, only 11 transitions were observed we kept the centrifugal distortion constants for reasons mentioned in the PA(OD)···$H_2O$ section. The fit parameters and the RMS deviation are given for both states in the Table 3.11.

**Table 3.10.** Observed transition frequencies for the PA···$H_2{}^{18}O$ complex.

| Transition | State 1 (MHz) | obs-calc (MHz) | State 2 (MHz) | obs-calc (MHz) |
|---|---|---|---|---|
| $1_{10}$ -$0_{00}$[a] | 8128.7211 | 0.0153 | 8128.9554 | 0.0108 |
| $2_{02}$ -$1_{11}$ | 9659.1848 | 0.0114 | 9659.4584 | 0.0093 |
| $2_{12}$ -$1_{11}$ | 9999.9027 | -0.0042 | 10000.0199 | -0.0085 |
| $2_{02}$ -$1_{01}$ | 10615.0812 | 0.0175 | 10615.1690 | 0.0194 |
| $2_{12}$ -$1_{01}$ | 10955.7996 | 0.0025 | 10955.7312 | 0.0023 |
| $3_{03}$ -$2_{12}$ | 14485.8140 | 0.0129 | 14485.9191 | 0.0129 |
| $3_{13}$ -$2_{12}$ | 14567.7508 | -0.0045 | 14567.7948 | -0.0046 |
| $3_{03}$ -$2_{02}$ | 14826.5322 | -0.0024 | 14826.4833 | -0.0022 |
| $3_{13}$ -$2_{02}$ | 14908.4678 | -0.0210 | 14908.3604 | -0.0183 |
| $2_{11}$ -$1_{01}$[a] | 15301.2710 | -0.0209 | 15301.9424 | -0.0168 |
| $2_{20}$ -$1_{10}$[a] | 16597.8674 | 0.0085 | 16598.1896 | 0.0071 |

[a] the average frequency for the *c*-dipole transitions are reported.

**Table 3.11.** Experimental rotational constants for the two states of the PA···$H_2{}^{18}O$ complex. The centrifugal distortion constants are kept fixed at the values calculated for the PA-$H_2{}^{18}O$ complex at MP2/6-311++G(d,p).

| Constant | State 1 | State 2 |
|---|---|---|
| **A (MHz)** | 4542.283(5) | 4542.308(5) |
| **B (MHz)** | 3586.470(4) | 3586.684(4) |
| **C (MHz)** | 2137.840(1) | 2137.809(1) |
| **$\Delta_J$ (kHz)** | [11.92] | [11.92] |
| **$\Delta_{JK}$ (kHz)** | [-26.4] | [-26.4] |
| **$\Delta_K$ (kHz)** | [16.24] | [16.24] |
| **$\delta_J$ (kHz)** | [-2.04] | [-2.04] |
| **$\delta_K$ (kHz)** | [-15.2] | [-15.2] |
| **n** | 11 | 11 |
| **RMS (kHz)** | 15.1 | 13.8 |

### 3.3.4. Structural analysis

The isotopologue spectra are essential in deriving the experimental structure of the complex. Kraitchman developed a set of equations which are based on the changes of the moments of inertia due to a single isotopic substitution of an atom[27]. The Kraitchman analysis helps to identify the coordinates of the substituted atoms. The

analysis works on the assumption that the bond distances and angles do not alter on isotopic substitution. We used the KRA program by Kisiel[28] to obtain the positions of the substituted atoms.

The PA···$H_2O$ dimer was considered to be the parent isotopologue in the analysis and the analysis was carried out for both the observed states. We discuss here the results pertaining to state 2 as this corresponds to the para state. To obtain the position of the H atom of water that is bound to the π-cloud of PA, the PA-DOH rotational constants of set 1 are used. Using rotational constants for set 2 of PA-DOH leads to large O-H distances (1.24Å) that are unreasonable. The PA-$H_2{}^{18}O$ rotational constants were used to obtain the position of the oxygen atom of water. The rotational constants for the PA(OD)···$H_2O$ isotopologue help to determine the position of the H atom involved in the strong O-H···O bond. The H/D substitution is less reliable as the zero-point amplitudes are significantly different between H and D. In this analysis only the magnitude of the coordinates is obtained for the substituted atoms. The sign of the coordinates is ambiguous and needs to be determined from the calculated structure. Table 3.12 shows the experimentally determined coordinates for the substituted atoms.

**Table 3.12.** Principal axis coordinates and distance from the center of mass (R) for the substituted atoms obtained experimentally and the corresponding coordinates theoretically calculated at MP2/6-311++G(d,p) for the G-PW-1a and G-PW-1b structures.

*a. For oxygen atom of water*

| O | G-PW-1a | G-PW-1b | experimental |
|---|---|---|---|
| **x** | 1.811 | 1.810 | ±1.939 |
| **y** | -1.079 | -1.089 | ±0.896 |
| **z** | -0.142 | -0.059 | ±0.103 |
| **R(Å)** | 2.113 | 2.113 | 2.139 |

*b. For hydroxyl hydrogen of PA*

| OH | G-PW-1a | G-PW-1b | experimental |
|---|---|---|---|
| **x** | 1.222 | 1.217 | ±1.151 |
| **y** | 0.712 | 0.726 | ±0.732 |
| **z** | 0.302 | 0.313 | ±0.294 |
| **R(Å)** | 1.446 | 1.452 | 1.395 |

*c. For H atom of water bound to the acetylenic moiety*

| H···π | G-PW-1a | G-PW-1b | experimental |
|---|---|---|---|
| **x** | 1.015 | 0.982 | ±1.320 |
| **y** | -1.602 | -1.573 | ±1.727 |
| **z** | 0.002 | -0.104 | ±0.322 |
| **R(Å)** | 1.896 | 1.859 | 2.198 |

These substitutions however do not help to distinguish between structure G-PW-1a and G-PW-1b. The structures differ only in the position of the free hydrogen of water. To obtain this position, we considered the PA···DOH dimer as the parent isotopologue and the PA···$D_2O$ as the isotopic substitution. The PA···DOH and PA···$D_2O$ dimer have two sets of rotational constants. Reasonable results are only obtained using the rotational constants of set 1 for both the dimers. The coordinates of the free H-atom of water in the calculated structures G-PW-1a and 1b can be differentiated based on the sign of the z-coordinate. The free hydrogen is on either side of the *x-y* plane for both these structures. Therefore, the sign of the z-coordinate for G-PW-1a is positive and for G-PW-1b it is negative. The sign of the coordinates is not obtained from the Kraitchman analysis. Hence, we consider both the signs and find that the positive sign coincides with the position expected for structure G-PW-1a. The negative sign on the other hand shows the position of the free H atom to be midway between that calculated for structures G-PW-1a and 1b (see Figure 3.3). Therefore, we can conclude that G-PW-1b is unlikely to be the experimentally observed structure.

**Table 3.13.** Principal axis coordinates and distance from the center of mass (R) for the non-bonded H-atom of water obtained experimentally and the corresponding coordinates theoretically calculated at MP2/6-311++G(d,p) for the G-PW-1a and G-PW-1b structures.

| H | G-PW-1a | G-PW-1b | experimental |
|---|---|---|---|
| **x** | 2.521 | 2.407 | -/+2.636 |
| **y** | -1.598 | -1.507 | -/+1.266 |
| **z** | 0.244 | -0.685 | -/+0.257 |
| **R(Å)** | 2.995 | 2.921 | 2.935 |

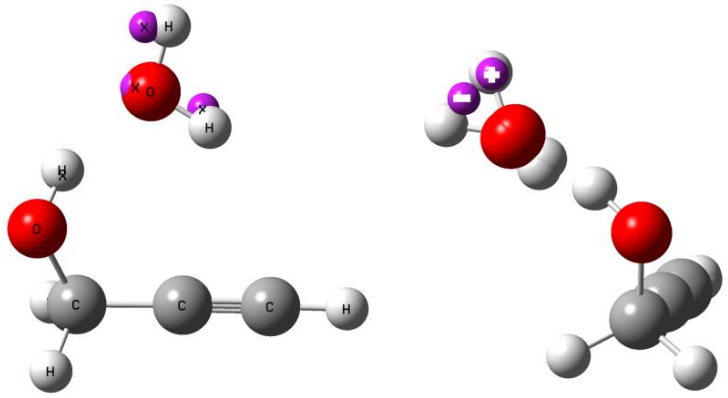


**Figure 3.3.** The purple spheres show the coordinates obtained from the Kraitchman analysis superimposed on G-PW-1a. The figure on the right shows the coordinates for the non-bonded hydrogen of water considering both the signs, superimposed on G-PW-1a and G-PW-1b.

Further evidence that G-PW-1a is the experimentally observe structure is obtained from the optimized pulse widths for the three different types of transitions. Pulse width dependence for the observed transitions shows that the optimum pulse widths for the *a*-, *b*-, and *c*-type lines are 0.8-1.0, 0.2, and 0.4-0.6 μs, respectively. The *c*-dipole component in G-PW-1a is low (0.2) and similar to the *a*-dipole component, whereas the *c*-dipole component in G-PW-1b is high (2.27) and similar to the *b*-dipole component (see Table 3.2). Thus, it can be concluded from the optimum pulse widths, that the observed transitions correspond to structure G-PW-1a.

## 3.4. Discussions

### 3.4.1. Internal motions

The observed splitting of the lines in the spectra for the PA···$H_2O$ dimer is indicative of the presence of some internal motions in the complex. The previously reported rotational spectrum for the PA monomer shows a splitting of lines due to tunneling between the two equivalent gauche conformers[15]. The two equivalent gauche conformers are connected via an internal motion involving the hydroxyl group rotating through the lower 'cis' barrier (1.1 $kJmol^{-1}$). A similar motion of the hydroxyl group of the PA unit in the PA···$H_2O$ complex converts structure G-PW-1a to G-PW-1b and the barrier for this conversion is 9.6 $kJmol^{-1}$. However, the PA(OD)···$H_2O$ spectrum shows no significant changes in the splitting pattern, and thus this motion can be ruled out.

It is to be noted that many small molecule complexes with water show a splitting of the rotational transitions having an intensity ratio of 3:1[5]. The H atoms are spin ½ systems and any tunneling motion that interchanges these equivalent H atoms in $H_2O$ leads to the two states of water, ortho (I=1) and para (I=0). The nuclear spin statistical weights for these two states are in the ratio 3:1 which leads to the observed intensity ratio. Since, we have observed many lines that follow this intensity pattern we can expect that an internal motion involving the interchange of the bonded and non-bonded H atoms of water causes the splitting. Also, we can consider State 1 to correspond to the ortho state since the lines are stronger and show hyperfine features (expected for an I=1 state). State 2, which is the higher frequency set consists of lines that are weaker. Therefore, State 2 could correspond to the para state (I=0).

The 2-fluoroethanol (2-F-EtOH)···$H_2O$ complex shows tunneling splitting of the lines, with the transitions split having an intensity ratio of 3:1[7]. The two lowest energy structures for the 2-F-EtOH···$H_2O$ complex differ only in the position of the non-bonded H atom of water. These two structures can easily interconvert via a low-barrier OH wagging motion (0.5 $kJmol^{-1}$) of the non-bonded H atom. A rotation of the water molecule about the strong O-H···O H-bond leads to the conversion of one structure to another, the barrier for this motion is 7.0 $kJmol^{-1}$. A concerted motion involving the low-barrier OH wag and the rotation of the $H_2O$ about the strong H-bond leads to the interchange of the equivalent hydrogen atoms which causes the tunneling splitting of the transitions.

We consider the similar motions for the PA···$H_2O$ complex to see if it could explain the observed splitting. The OH wagging motion of water in the PA···$H_2O$ system has a small barrier (0.9 $kJmol^{-1}$) to convert structure G-PW-1a to G-PW-1b. The internal motion of water rotating about the strong O-H···O hydrogen bond axis neither interconverts between two equivalent structures nor does it convert G-PW-1a to G-PW-1b. Therefore, it does not seem possible to interchange the H atoms of the $H_2O$ fragment via the same concerted motion possible for the 2-fluoroethanol···$H_2O$ complex. The OH-wag however could be important to understand the splitting of the *c*-type transitions into four lines. The splitting could be explained by the fact that the *c*-dipole moment changes during an OH wagging motion of the free hydrogen of water.

Phenylacetylene (PhAc) is a multifunctional molecule similar to PA that also shows a splitting of the transitions when it forms a complex with $H_2O$. The observed global

minimum structure for the PhAc···$H_2O$ dimer is a compromise between various possible interactions[29]. The water molecule lies in the plane of the phenylacetylene molecule bound by two weak hydrogen bonds forming a closed H-bonded network. The phenyl ring donates an H-bond forming a C-H···O bond with $H_2O$, and the water donates an H-bond to the acetylenic π-cloud forming an O-H···π interaction. The splitting of the lines is of the order of a few MHz. This is larger than that observed for the PA···$H_2O$ complex (few kHz). The reason for the splitting of the lines observed for the phenylacetylene···water complex is attributed to the rotation of water about its symmetry axis. This rotation of water about its $C_2$ axis interchanges the equivalent hydrogen atoms of water, splitting the lines with an intensity ratio of 3:1. The *ab initio* barrier calculated for this motion is 14.0 kJmol$^{-1}$. A rigid scan was performed to calculate the barrier for the rotation of water about its $C_2$ axis in the PA···$H_2O$ complex. The calculated barrier for this motion is 18.0 kJmol$^{-1}$. This motion causes the weak O-H···π bond to break and reform and has no effect on the strong O-H···O interaction. This barrier is higher than that calculated for the PhAc···$H_2O$ complex. This correlates with the fact that the splitting of the lines is smaller than that of the PhAc···$H_2O$ complex. Thus, the observed splitting for PA···$H_2O$ complex could be attributed to the internal motion of water about its $C_2$ axis.

The two sets of spectra obtained for the DOH and $D_2O$ have the same dipole moment strengths (optimized pulse widths are the same), which rules out the possibility that the two sets of spectra belong to the two different structures G-PW-1a and G-PW-1b. However, only one set of transitions were obtained for the other isotopologues (no deuterium substitution for the $H_2O$) of the PA···$H_2O$ complex. This suggests that this is caused by an internal motion of the complex where the splitting is reduced due to deuterium substitution allowing us to observe the two sets. This splitting could be much larger for the other isotopologues, since they do not contain deuterium in the water moiety making it difficult to observe the other set of transitions.

### 3.4.2. Atoms in Molecules (AIM) analysis

The experimentally observed structure, G-PW-1a is bound by two different hydrogen bonds. The AIM analysis has been carried out to understand these interactions in detail. The electron density topologies for all the different optimized structures have been computed and the molecular graphs are shown in Figure 3.4. Our

results match with those reported previously using wavefunctions obtained at the MP2/aug-cc-pVDZ level[12].

The molecular graphs for the structures G-PW-1a and 1b are very similar. There is a bond critical point (BCP) between the hydroxyl of PA and the oxygen atom of $H_2O$ (O-H···O). A BCP is also present between the H atom of water and the acetylenic carbon atom of PA (O-H···π). The presence of these two BCPs signifies that there is an interaction present between these two groups. Since these two interactions form a closed network, a ring critical point (RCP) is also observed. The $\varrho$ and $\nabla^2\varrho$ values at the BCPs of the O-H···O and the O-H···π bonds are given in Table 3.14. Low $\varrho$ values and positive $\nabla^2\varrho$ values at the BCP are indicative of a closed-shell interaction, such as hydrogen bonds[30]. These values of $\varrho$ and $\nabla^2\varrho$ for structures G-PW-1a and 1b are within the ranges prescribed by Koch and Popelier[31] for C-H···O hydrogen bonds, confirming that the PA···$H_2O$ complex is hydrogen bonded.

The multifunctional molecule, PA offered the opportunity to study the influence of multiple H-bond sites on the structure of a complex. Saini and Viswanathan have carried out detailed analysis on the PA···$H_2O$ complex based on the binding energies to show that the interactions do not show any synergistic effects[12]. They conclude that the two H-bonds do not stabilize the energy of the complex to the extent expected by adding the individual interaction energies. Both H-bonds do not have the optimum geometry and they are somewhat bent to accommodate the other H-bond.

**Table 3.14.** The electron density ($\varrho$) and Laplacian of electron density ($\nabla^2\varrho$) at the BCP (in au) and the distances between the atoms involved in the interaction (in Å).

| Structure | O-H···O | | | O-H···π | | | O···C2 | | |
|---|---|---|---|---|---|---|---|---|---|
| | $\varrho$ | $\nabla^2\varrho$ | rH···O | $\varrho$ | $\nabla^2\varrho$ | rH···C2 | $\varrho$ | $\nabla^2\varrho$ | rO···C2 |
| **G-PW-1a** | 0.0250 | +0.0946 | 1.937 | 0.0093 | +0.0318 | 2.570 | - | - | 3.074 |
| **G-PW-1b** | 0.0241 | +0.0927 | 1.945 | 0.0102 | +0.0348 | 2.518 | - | - | 3.067 |
| **T.S.$C_2$ rot.** | 0.0226 | +0.0960 | 1.937 | - | - | 3.048 | 0.0084 | +0.0275 | 3.074 |

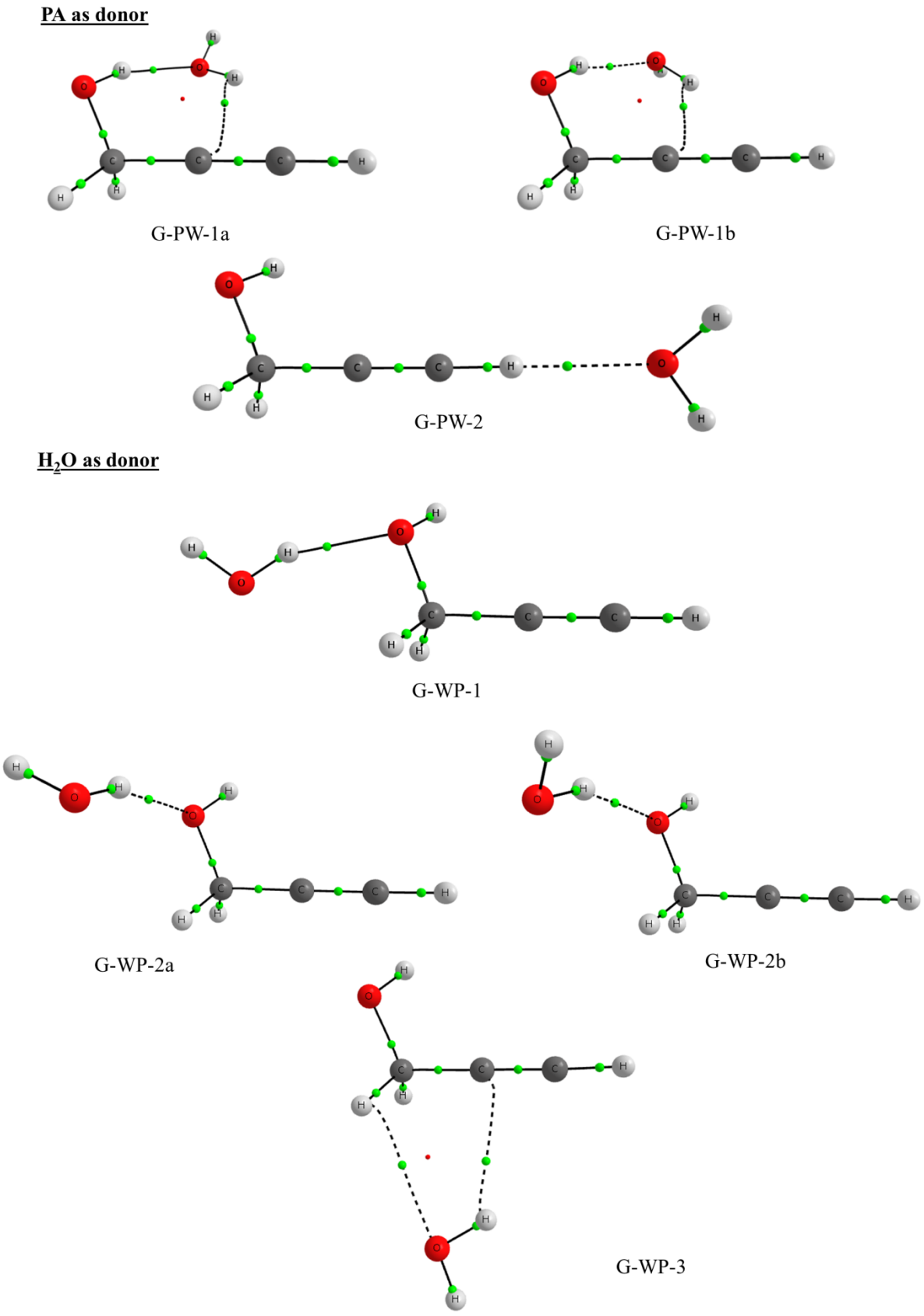


**Figure 3.4.** The molecular graphs for all the G-PA···$H_2O$ optimized structures.

We carried out an AIM analysis for the transition state structure obtained for the rotation of the water fragment about its $C_2$ axis in the PA···$H_2O$ complex. The molecular graph is shown in Figure 3.5. It is evident that the O-H···O bond does not break during the internal rotation. However, we find that the weak O-H···π bond has been replaced by an interaction between the oxygen of water and the acetylenic carbon of PA. The AIM and NCI (non-covalent index) analysis on the 2-F-EtOH···$H_2O$ complex shows that though the weak O-H···F bond breaks during the rotation of water about the O-H···O bond, it is replaced by two interactions of similar strength between the two H atoms of water and the F atom of 2-F-EtOH.

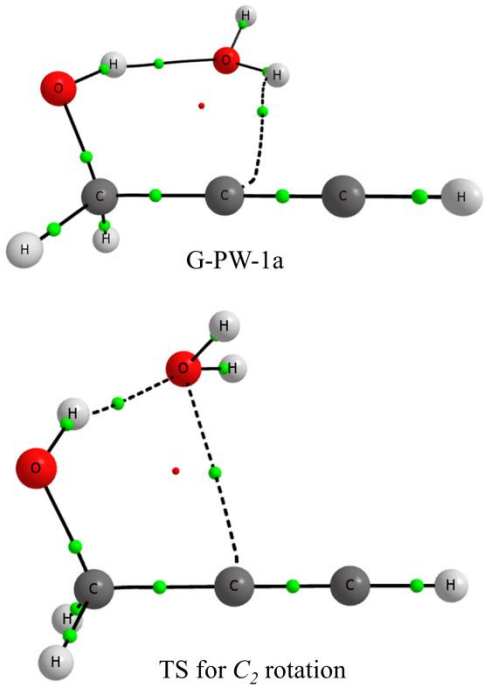


**Figure 3.5.** Molecular graphs for structure G-PW-1a and the transition state for the rotation of water about its $C_2$ axis.

### 3.4.3. Alcohol-Water interactions

As pointed out earlier alcohols and water both contain -OH groups. When a complex is formed between the two molecules it is interesting to note which of the hydroxyl groups donates an H-bond and which acts as the acceptor. The many alcohol-water complexes studied recently show that saturated aliphatic alcohols act as hydrogen bond acceptors with water and their fluorinated counterparts and phenol act as donors. It was surmised that these trends in the alcohol-water interaction could be understood based on the electron donating or withdrawing abilities of the group attached to the

hydroxyl functional group. Groups that withdraw electron density make the -OH hydrogen more acidic and therefore capable of acting as an H-bond donor in the alcohol-water complex. Electron donating groups on the other hand make the hydroxyl oxygen more negative and therefore it can easily accept an H-bond. This could be better understood if we take a look at the p*Ka* values of the alcohols. The p*Ka* values for some alcohols are tabulated below. Alcohols having p*Ka* values less than 14 can be considered to be more acidic than $H_2O$ (p*Ka*=14[32]). These alcohols act as H-bond donors, and those alcohols that have p*Ka* values greater than 14 act as H-bond acceptors. This explains why fluorinated alcohols and phenol act as H-bond donors and saturated aliphatic alcohols act as H-bond acceptors when they form a complex with water. Propargyl alcohol has a p*Ka* value of 13.55, this helps to understand why in the primary O-H···O interaction, PA acts as the H-bond donor. The p*Ka* values are calculated in the solution. We observe that the gas phase basicity values however show no correlation.

**Table 3.15.** The p*Ka* and gas phase basicity of some alcohols and their donor-acceptor capabilities in a complex with $H_2O$.

| alcohol | p*Ka* | Gas phase basicity[33] | Role of alcohol in the complex |
|---|---|---|---|
| methanol | 15.54[34] | 724.5 | acceptor |
| ethanol | 16.00[34] | 746.0 | acceptor |
| n-propanol | 16.10[35] | 756.1 | acceptor |
| Propargyl alcohol | 13.55[34] | - | donor |
| 2,2,2- trifluoroethanol | 12.43[34] | 669.9 | donor |
| hexafluoroisopropanol | 9.30[36] | 656.2 | donor |
| phenol | 9.98[35] | 786.3 | donor |

## 3.5. Conclusions

The rotational spectrum for the lowest energy structure (G-PW-1a) has been observed. The G-PW-1a structure has PA in the gauche conformer forming a hydrogen bonded ring structure with $H_2O$. The PA donates an H-bond to $H_2O$ forming a strong O-H···O bond and the dimer is further stabilized by a weak O-H···π interaction between the $H_2O$ and the acetylenic moiety. This structure shows that the PA···$H_2O$ complex neither resembles the methanol···water complex where the water donates an H-bond nor the acetylene···water complex where the acetylenic hydrogen donates an H-bond. The two structures found in the IR study of the PA···$H_2O$ dimer

trapped in helium nanodroplets resemble the methanol···water complex and the acetylene···water complex[13].

The matrix isolation IR spectrum[12] for the PA···$H_2O$ dimer finds the lowest energy structure but is unable to differentiate between G-PW-1a and G-PW-1b. These two structures differ only in the position of the non-bonded H atom of water. However, we are able to distinguish between the lowest energy structures G-PW-1a and G-PW-1b with the help of the deuterium substituted rotational spectra of the PA···$H_2O$ complex. The rotational spectra of the PA···$H_2O$ complex and its isotopic substituted spectra confirm that structure G-PW-1a is observed.

The rotational transitions for the complex show splitting and these can be attributed to the internal motions of $H_2O$. The rotation of water about its symmetry axis leads to the interchange of the equivalent hydrogen atoms of $H_2O$. This motion causes the observed splitting of the rotational transitions.

This study helps to understand alcohol-water interactions. The donor/acceptor capabilities of the OH groups in an alcohol-water complex could be generalized based on the electron donating and withdrawing abilities of the groups attached to the hydroxyl group. Thus, saturated aliphatic alcohols act as H-bond acceptors and their fluorinated counterparts as H-bond donors in a hydrogen bonded complex with $H_2O$.

## 3.6. References


(1) Stockman, P. A.; Blake, G. A.; Lovas, F. J.; Suenram, R. D. Microwave Rotation-Tunneling Spectroscopy of the Water–Methanol Dimer: Direct Structural Proof for the Strongest Bound Conformation. *J. Chem. Phys.* **1997**, *107*, 3782–3790.

(2) Finneran, I. A.; Carroll, P. B.; Allodi, M. A.; Blake, G. A. Hydrogen Bonding in the Ethanol–Water Dimer. *Phys. Chem. Chem. Phys.* **2015**, *17*, 24210–24214.

(3) Mead, G. J.; Alonso, E. R.; Finneran, I. A.; Carroll, P. B.; Blake, G. A. Identification of Two Conformationally Trapped n -Propanol-Water Dimers in a Supersonic Expansion. *J. Mol. Spectrosc.* **2017**, *335*, 68–73.

(4) Evangelisti, L.; Gou, Q.; Feng, G.; Caminati, W.; Mead, G. J.; Finneran, I. A.; Carroll, P. B.; Blake, G. A. Conformational Equilibrium and Internal Dynamics in the Iso-Propanol–Water Dimer. *Phys. Chem. Chem. Phys.* **2017**, *19*, 568–573.

(5) Evangelisti, L.; Caminati, W. Internal Dynamics in Complexes of Water with Organic Molecules. Details of the Internal Motions in Tert-Butylalcohol–Water. *Phys. Chem. Chem. Phys.* **2010**, *12*, 14433–14441.

(6) Juanes, M.; Li, W.; Spada, L.; Evangelisti, L.; Lesarri, A.; Caminati, W. Internal Dynamics of Cyclohexanol and the Cyclohexanol–Water Adduct. *Phys. Chem. Chem. Phys.* **2019**, *21*, 3676–3682.

(7) Huang, W.; Thomas, J.; Jäger, W.; Xu, Y. Tunnelling and Barrier-Less Motions in the 2-Fluoroethanol–Water Complex: A Rotational Spectroscopic and Ab Initio Study. *Phys. Chem. Chem. Phys.* **2017**, *19*, 12221–12228.

(8) Thomas, J.; Xu, Y. Structure and Tunneling Dynamics in a Model System of Peptide Co-Solvents: Rotational Spectroscopy of the 2,2,2-Trifluoroethanol···water Complex. *J. Chem. Phys.* **2014**, *140*, 234307-1-234307-5.

(9) Shahi, A.; Arunan, E. Microwave Spectroscopic and Theoretical Investigations of the Strongly Hydrogen Bonded Hexafluoroisopropanol···water Complex. *Phys. Chem. Chem. Phys.* **2015**, *17*, 24774–24782.

(10) Gerhards, M.; Schmitt, M.; Kleinermanns, K.; Stahl, W. The Structure of Phenol ($H_2O$) Obtained by Microwave Spectroscopy. *J. Chem. Phys.* **1996**, *104*, 967–971.

(11) Peterson, K. I.; Klemperer, W. Water–Hydrocarbon Interactions: Rotational Spectroscopy and Structure of the Water–Acetylene Complex. *J. Chem. Phys.* **1984**, *81*, 3842–3845.

(12) Saini, J.; Viswanathan, K. S. Does a Hydrogen Bonded Complex with Dual Contacts Show Synergism? A Matrix Isolation Infrared and Ab-Initio Study of Propargyl Alcohol–Water Complex. *J. Mol. Struct.* **2016**, *1118*, 147–156.

(13) Mani, D.; Pal, N.; Smialkowski, M.; Beakovic, C.; Schwaab, G.; Havenith, M. Accessing Different Binding Sites of a Multifunctional Molecule: IR Spectroscopy of Propargyl Alcohol···water Complexes in Helium Droplets. *Phys. Chem. Chem. Phys.* **2019**, *21*, 20582–20587.

(14) Arunan, E.; Tiwari, A. P.; Mandal, P. K.; Mathias, P. C. Pulsed Nozzle Fourier Transform Microwave Spectrometer: Ideal to Define Hydrogen Bond Radius. *Curr. Sci.* **2002**, *82*, 533–540.

(15) Hirota, E. Internal Rotation in Propargyl Alcohol from Microwave Spectrum. *J. Mol. Spectrosc.* **1968**, *26*, 335–350.

(16) Mani, D.; Arunan, E. Rotational Spectra of Propargyl Alcohol Dimer: A Dimer Bound with Three Different Types of Hydrogen Bonds. *J. Chem. Phys.* **2014**, *141*, 164311-1-164311-8.

(17) Mani, D.; Arunan, E. Microwave Spectroscopic and Atoms in Molecules Theoretical Investigations on the Ar···Propargyl Alcohol Complex: Ar···H-O, Ar···π, and Ar···C Interactions. *ChemPhysChem* **2013**, *14*, 754–763.

(18) Frisch, M. J.; Trucks, G. W.; Schlegel, H. B.; Scuseria, G. E.; Robb, M. A.; Cheeseman, J. R.; Scalmani, G.; Barone, V.; Mennucci, B.; Petersson, G. A.; et al. *Gaussian 09* Revision D. 01; Gaussian, Inc. Wallingford, CT, **2009**.

(19) Boys, S. F.; Bernardi, F. de. The Calculation of Small Molecular Interactions by the Differences of Separate Total Energies. Some Procedures with Reduced Errors. *Mol. Phys.* **1970**, *19*, 553–566.

(20) JPL Molecular Spectroscopy https://spec.jpl.nasa.gov/ (accessed Aug 26, 2020).

(21) Pickett, H. M. The Fitting and Prediction of Vibration-Rotation Spectra with Spin Interactions. *J. Mol. Spectrosc.* **1991**, *148*, 371–377.

(22) Asymmetric Rotor Programs http://www.ifpan.edu.pl/~kisiel/asym/asym.htm#crib (accessed Aug 26, 2020).

(23) Kisiel, Z.; Białkowska-Jaworska, E. Sextic Centrifugal Distortion in Fluorobenzene and Phenylacetylene from Cm-Wave Rotational Spectroscopy. *J. Mol. Spectrosc.* **2019**, *359*, 16–21.

(24) Keith, T. A. *AIMAll*, Version 16.05.18; TK Gristmill Software: Overland Park, KS, (aim.tkgristmill.com), **2016**.

(25) Pearson, J. C.; Drouin, B. J. The Ground State Torsion–Rotation Spectrum of Propargyl Alcohol (HCCCH2OH). *J. Mol. Spectrosc.* **2005**, *234*, 149–156.

(26) Bolton, K.; Owen, N. L.; Sheridan, J. Molecular Structures of Propargyl Alcohol and Propargyl Amine from Microwave Spectra. *Nature* **1968**, *217,* 164–164.

(27) Kraitchman, J. Determination of Molecular Structure from Microwave Spectroscopic Data. *Am. J. Phys.* **1953**, *21*, 17–24.

(28) Structural calculations http://www.ifpan.edu.pl/~kisiel/struct/struct.htm#kra (accessed Aug 26, 2020).

(29) Goswami, M.; Arunan, E. Microwave Spectroscopic and Theoretical Studies on the Phenylacetylene···H2O Complex: C–H···O and O–H···π Hydrogen Bonds as Equal Partners. *Phys. Chem. Chem. Phys.* **2011**, *13* (31), 14153-14162.

(30) Bader, R. F. W. *Atoms in Molecules: A Quantum Theory*; International Series of Monographs on Chemistry; Oxford University Press: Oxford, New York, **1994**.

(31) Koch, U.; Popelier, P. L. Characterization of CHO Hydrogen Bonds on the Basis of the Charge Density. *J. Phys. Chem.* **1995**, *99*, 9747–9754.

(32) Silverstein, T. P.; Heller, S. T. P $K_a$ Values in the Undergraduate Curriculum: What Is the Real p $K_a$ of Water? *J. Chem. Educ.* **2017**, *94*, 690–695.

(33) Hunter, E. P. L.; Lias, S. G. Evaluated Gas Phase Basicities and Proton Affinities of Molecules: An Update. *J. Phys. Chem. Ref. Data* **1998**, *27*, 413–656.

(34) pKa Table data compiled by R. Williams. https://organicchemistrydata.org/hansreich/resources/pka/#pka_water_compilation_williams (accessed Sep 14, 2020).

(35) Phenols, alcohols and carboxylic acids - pKa values https://www.engineeringtoolbox.com/paraffinic-benzoic-hydroxy-dioic-acids-structure-pka-carboxylic-dissociation-constant-alcohol-phenol-d_1948.html (accessed Sep 14, 2020).

(36) Chambers, M. ChemIDplus - 920-66-1 Hexafluoroisopropanol https://chem.nlm.nih.gov/chemidplus/rn/920-66-1 (accessed Sep 14, 2020).

## 3.7. Supplementary Information

**Table S3.1.** Cartesian coordinates for the G-PW-1a structure of the PA···$H_2O$ complex calculated at MP2/6-311++G(d,p).

| atom | x | y | z |
|---|---|---|---|
| **O** | 0.400329000 | -1.502314000 | -0.456027000 |
| **H** | 1.114535000 | -0.861521000 | -0.327910000 |
| **O** | 1.908659000 | 0.831938000 | 0.174282000 |
| **H** | 1.181589000 | 1.449476000 | 0.042572000 |
| **H** | 2.678608000 | 1.274268000 | -0.191315000 |
| **C** | -0.664203000 | -1.070214000 | 0.368709000 |
| **H** | -1.493514000 | -1.761607000 | 0.200603000 |
| **H** | -0.394755000 | -1.119667000 | 1.432054000 |
| **C** | -1.117063000 | 0.299512000 | 0.062278000 |
| **C** | -1.502688000 | 1.432306000 | -0.180413000 |
| **H** | -1.854642000 | 2.412438000 | -0.405488000 |

**Table S3.2.** Cartesian coordinates for the G-PW-1b structure of the PA···$H_2O$ complex calculated at MP2/6-311++G(d,p).

| atom | x | y | z |
|---|---|---|---|
| **O** | 0.391430000 | -1.515838000 | -0.453024000 |
| **H** | 1.107970000 | -0.871258000 | -0.363874000 |
| **O** | 1.908032000 | 0.857267000 | 0.031072000 |
| **H** | 1.140889000 | 1.430765000 | 0.131145000 |
| **H** | 2.555339000 | 1.193360000 | 0.655491000 |
| **C** | -0.650948000 | -1.066784000 | 0.389457000 |
| **H** | -1.485899000 | -1.758304000 | 0.252751000 |
| **H** | -0.357931000 | -1.101240000 | 1.447460000 |
| **C** | -1.107773000 | 0.299222000 | 0.073157000 |
| **C** | -1.493488000 | 1.429163000 | -0.182640000 |
| **H** | -1.842813000 | 2.405644000 | -0.427195000 |

**Table S3.3.** Cartesian coordinates for the G-PW-2 structure of the PA···$H_2O$ complex calculated at MP2/6-311++G(d,p).

| atom | x | y | z |
|---|---|---|---|
| **O** | -2.750639000 | 0.718649000 | 0.067844000 |
| **C** | -2.368703000 | 1.280402000 | -0.613010000 |
| **O** | 3.856114000 | 0.198821000 | -0.053074000 |
| **H** | 4.453914000 | -0.550914000 | -0.108914000 |
| **H** | 4.268081000 | 0.770818000 | 0.599425000 |
| **C** | -2.051604000 | -0.522381000 | 0.014074000 |
| **H** | -2.358051000 | -1.076340000 | 0.904020000 |
| **H** | -2.354969000 | -1.103049000 | -0.866266000 |
| **C** | -0.594176000 | -0.354862000 | 0.002809000 |
| **C** | 0.618401000 | -0.218765000 | -0.016662000 |
| **H** | 1.680201000 | -0.084624000 | -0.034737000 |

**Table S3.4.** Cartesian coordinates for the G-WP-1 structure of the PA···$H_2O$ complex calculated at MP2/6-311++G(d,p).

| atom | x | y | z |
|---|---|---|---|
| **O** | -0.425606000 | -0.844079000 | -0.066327000 |
| **H** | -0.040838000 | -1.451793000 | 0.573304000 |
| **O** | -3.019085000 | 0.315552000 | 0.048517000 |
| **H** | -2.270052000 | -0.289467000 | -0.037369000 |
| **H** | -3.680385000 | -0.050271000 | -0.541713000 |
| **C** | 0.274363000 | 0.400084000 | 0.056695000 |
| **H** | -0.071059000 | 1.017589000 | -0.774050000 |
| **H** | -0.001171000 | 0.904530000 | 0.989582000 |
| **C** | 1.728150000 | 0.227178000 | -0.004423000 |
| **C** | 2.935795000 | 0.067602000 | -0.048928000 |
| **H** | 3.991178000 | -0.071550000 | -0.087338000 |

**Table S3.5.** Cartesian coordinates for the G-WP-2a structure of the PA···$H_2O$ complex calculated at MP2/6-311++G(d,p).

| atom | x | y | z |
|---|---|---|---|
| **O** | -2.535828000 | 0.869208000 | 0.058288000 |
| **H** | -1.981906000 | 0.201930000 | -0.367911000 |
| **H** | -3.427422000 | 0.541207000 | -0.072267000 |
| **O** | -0.493719000 | -1.026822000 | -0.488171000 |
| **H** | 0.062344000 | -1.329551000 | -1.212736000 |
| **C** | 0.370440000 | -0.663594000 | 0.595148000 |
| **H** | -0.255082000 | -0.109691000 | 1.298167000 |
| **H** | 0.748224000 | -1.561475000 | 1.096831000 |
| **C** | 1.493849000 | 0.168064000 | 0.155691000 |
| **C** | 2.441381000 | 0.841414000 | -0.211219000 |
| **H** | 3.256197000 | 1.443182000 | -0.540739000 |

**Table S3.6.** Cartesian coordinates for the G-WP-2b structure of the PA···$H_2O$ complex calculated at MP2/6-311++G(d,p).

| atom | x | y | z |
|---|---|---|---|
| **O** | 0.483435000 | 1.017367000 | -0.498689000 |
| **H** | -0.078028000 | 1.411670000 | -1.173050000 |
| **O** | 2.634356000 | -0.736872000 | 0.112104000 |
| **H** | 2.053271000 | -0.130768000 | -0.365423000 |
| **H** | 2.775422000 | -1.453583000 | -0.509340000 |
| **C** | -0.355734000 | 0.627756000 | 0.593353000 |
| **H** | 0.282503000 | 0.042041000 | 1.257888000 |
| **H** | -0.708468000 | 1.510524000 | 1.138232000 |
| **C** | -1.501813000 | -0.174626000 | 0.155170000 |
| **C** | -2.469522000 | -0.823765000 | -0.203201000 |
| **H** | -3.304610000 | -1.400037000 | -0.527558000 |

**Table S3.7.** Cartesian coordinates for the G-WP-3 structure of the PA···$H_2O$ complex calculated at MP2/6-311++G(d,p).

| atom | x | y | z |
|---|---|---|---|
| **C** | 0.722978000 | -0.617428000 | 0.123707000 |
| **H** | 0.486547000 | -1.020704000 | 1.115293000 |
| **H** | 0.200098000 | -1.227395000 | -0.613539000 |
| **C** | 0.245495000 | 0.771982000 | 0.044016000 |
| **C** | -0.151220000 | 1.924393000 | -0.023893000 |
| **H** | -0.462845000 | 2.941476000 | -0.084575000 |
| **O** | 2.111972000 | -0.729317000 | -0.166902000 |
| **H** | 2.573128000 | -0.122956000 | 0.420026000 |
| **O** | -2.391199000 | -0.812196000 | -0.066801000 |
| **H** | -2.160710000 | 0.121265000 | -0.053028000 |
| **H** | -3.305924000 | -0.833267000 | 0.222464000 |

**Table S3.8.** Cartesian coordinates for the T-PW-1 structure of the PA···$H_2O$ complex calculated at MP2/6-311++G(d,p).

| atom | x | y | z |
|---|---|---|---|
| **C** | 0.419409000 | -0.204041000 | 0.590992000 |
| **H** | -0.041261000 | 0.701038000 | 1.005953000 |
| **H** | 0.507194000 | -0.936036000 | 1.404633000 |
| **C** | 1.765030000 | 0.132012000 | 0.113694000 |
| **C** | 2.902006000 | 0.382247000 | -0.247396000 |
| **H** | 3.884532000 | 0.613862000 | -0.585663000 |
| **O** | -0.363166000 | -0.728707000 | -0.471655000 |
| **H** | -1.263678000 | -0.409164000 | -0.329738000 |
| **O** | -2.960975000 | 0.397655000 | -0.001302000 |
| **H** | -3.712275000 | -0.149699000 | 0.241869000 |
| **H** | -3.300055000 | 0.967104000 | -0.697135000 |

**Table S3.9.** Cartesian coordinates for the T-WP-1 structure of the PA···$H_2O$ complex calculated at MP2/6-311++G(d,p).

| atom | x | y | z |
|---|---|---|---|
| **C** | 0.627920000 | 1.008307000 | -0.409606000 |
| **H** | 0.253377000 | 0.957557000 | -1.438742000 |
| **H** | 1.306513000 | 1.864657000 | -0.324501000 |
| **C** | 1.357554000 | -0.219150000 | -0.096883000 |
| **C** | 1.955102000 | -1.250507000 | 0.153948000 |
| **H** | 2.483939000 | -2.147988000 | 0.375935000 |
| **O** | -0.461138000 | 1.137400000 | 0.513552000 |
| **H** | -0.821471000 | 2.024316000 | 0.411311000 |
| **O** | -2.404369000 | -0.882830000 | -0.181102000 |
| **H** | -1.754267000 | -0.260815000 | 0.171505000 |
| **H** | -2.187490000 | -1.706190000 | 0.260143000 |

**Table S3.10.** Normal modes of vibrations for the structures G-PW-1a, 1b, and 2 of the PA···$H_2O$ complex calculated at MP2/6-311++G(d,p). Frequency in $cm^{-1}$ and IR intensity in km/mol.

| G-PW-1a | | G-PW-1b | | G-PW-2 | |
|---|---|---|---|---|---|
| **Frequency** | **IR intensity** | **Frequency** | **IR intensity** | **Frequency** | **IR intensity** |
| 76.1 | 29.7 | 86.7 | 13.6 | 24.0 | 41.5 |
| 101.6 | 7.4 | 105.7 | 1.0 | 52.8 | 2.2 |
| 152.1 | 85.5 | 160.2 | 101.8 | 68.9 | 14.2 |
| 176.9 | 1.3 | 174.7 | 25.8 | 114.6 | 1.2 |
| 217.7 | 9.9 | 211.8 | 24.0 | 186.8 | 23.1 |
| 270.6 | 152.2 | 235.9 | 58.0 | 234.5 | 142.9 |
| 314.1 | 11.3 | 314.0 | 8.0 | 253.4 | 132.9 |
| 337.8 | 56.1 | 362.0 | 118.9 | 302.7 | 42.6 |
| 557.0 | 6.0 | 556.8 | 6.2 | 394.1 | 122.3 |
| 649.6 | 52.9 | 651.7 | 58.0 | 562.0 | 19.4 |
| 674.8 | 44.6 | 675.0 | 51.4 | 882.6 | 43.9 |
| 684.5 | 176.9 | 694.4 | 166.1 | 913.3 | 25.4 |
| 924.2 | 18.8 | 923.4 | 17.0 | 934.0 | 53.7 |
| 1013.4 | 14.7 | 1011.9 | 15.6 | 1017.7 | 17.6 |
| 1098.9 | 107.5 | 1100.3 | 106.1 | 1080.6 | 109.1 |
| 1267.1 | 10.6 | 1262.8 | 12.1 | 1232.7 | 13.4 |
| 1401.0 | 10.9 | 1398.3 | 7.7 | 1372.4 | 1.5 |
| 1484.5 | 55.7 | 1471.2 | 62.4 | 1436.8 | 61.7 |
| 1512.6 | 2.1 | 1512.6 | 1.6 | 1522.5 | 0.9 |
| 1631.0 | 68.2 | 1626.1 | 60.8 | 1641.4 | 62.6 |
| 2119.4 | 1.0 | 2119.4 | 1.2 | 2126.2 | 20.6 |
| 3063.3 | 34.5 | 3058.8 | 38.6 | 3068.6 | 39.6 |
| 3146.9 | 11.7 | 3146.4 | 11.5 | 3151.9 | 10.7 |
| 3497.1 | 56.4 | 3496.6 | 57.8 | 3436.3 | 230.7 |
| 3767.0 | 274.1 | 3774.1 | 246.4 | 3874.4 | 18.4 |
| 3849.4 | 42.1 | 3846.4 | 54.0 | 3884.9 | 38.7 |
| 3975.5 | 116.8 | 3976.2 | 119.5 | 3990.7 | 78.7 |

**Table S3.11.** Normal modes of vibrations for the structures G-WP-1 and 3 of the PA···$H_2O$ complex calculated at MP2/6-311++G(d,p). Frequency in $cm^{-1}$ and IR intensity in km/mol.

| G-WP-1 | | G-WP-3 | |
|---|---|---|---|
| **Frequency** | **IR intensity** | **Frequency** | **IR intensity** |
| 23.0 | 7.1 | 26.4 | 12.5 |
| 32.4 | 10.3 | 59.6 | 50.2 |
| 131.9 | 135.6 | 96.9 | 141.0 |
| 142.6 | 9.3 | 107.2 | 11.3 |
| 225.8 | 2.2 | 167.6 | 110.2 |
| 281.4 | 52.1 | 198.3 | 7.5 |
| 331.7 | 136.5 | 242.1 | 82.9 |
| 387.9 | 35.4 | 285.9 | 30.6 |
| 559.4 | 15.8 | 406.3 | 132.2 |
| 619.1 | 189.1 | 560.3 | 15.5 |
| 662.3 | 46.5 | 658.9 | 49.3 |
| 695.6 | 40.1 | 685.3 | 51.2 |
| 934.4 | 31.6 | 923.0 | 25.2 |
| 1008.0 | 16.6 | 1005.6 | 21.5 |
| 1067.4 | 113.4 | 1081.8 | 112.5 |
| 1228.9 | 19.6 | 1235.2 | 17.9 |
| 1373.3 | 3.7 | 1376.2 | 1.9 |
| 1438.4 | 59.6 | 1432.8 | 47.5 |
| 1519.9 | 3.4 | 1512.2 | 2.7 |
| 1656.9 | 41.8 | 1628.8 | 59.4 |
| 2136.8 | 4.3 | 2123.3 | 1.0 |
| 3091.1 | 18.7 | 3084.9 | 24.9 |
| 3169.2 | 3.2 | 3178.6 | 1.9 |
| 3501.1 | 58.8 | 3497.2 | 58.2 |
| 3779.9 | 297.7 | 3860.7 | 24.6 |
| 3878.3 | 46.9 | 3885.4 | 38.7 |
| 3967.9 | 117.8 | 3985.7 | 102.6 |

**Table S3.12.** Normal modes of vibrations for the structures G-WP-2a and 2b of the PA···$H_2O$ complex calculated at MP2/6-311++G(d,p). Frequency in $cm^{-1}$ and IR intensity in km/mol.

| G-WP-2a | | G-WP-2b | |
|---|---|---|---|
| **Frequency** | **IR intensity** | **Frequency** | **IR intensity** |
| 28.7 | 2.3 | 26.3 | 2.7 |
| 55.5 | 34.7 | 67.1 | 60.3 |
| 117.0 | 121.4 | 129.9 | 89.3 |
| 174.0 | 6.2 | 172.8 | 6.3 |
| 199.1 | 3.3 | 200.2 | 10.5 |
| 281.4 | 12.4 | 275.9 | 25.9 |
| 318.3 | 127.0 | 314.5 | 93.2 |
| 377.8 | 91.5 | 382.7 | 150.1 |
| 548.6 | 4.5 | 553.5 | 11.7 |
| 595.7 | 167.1 | 563.9 | 170.5 |
| 670.4 | 51.3 | 674.4 | 48.0 |
| 691.9 | 40.9 | 692.9 | 39.3 |
| 934.4 | 37.5 | 933.8 | 29.4 |
| 1020.9 | 13.7 | 1016.6 | 16.6 |
| 1069.3 | 110.3 | 1071.0 | 107.2 |
| 1234.9 | 23.5 | 1233.4 | 25.0 |
| 1364.4 | 3.4 | 1368.4 | 2.1 |
| 1443.3 | 50.9 | 1442.8 | 49.0 |
| 1523.8 | 2.1 | 1523.1 | 2.4 |
| 1659.9 | 45.6 | 1657.9 | 34.3 |
| 2137.0 | 4.4 | 2135.5 | 3.8 |
| 3087.2 | 28.2 | 3087.9 | 26.7 |
| 3163.4 | 1.4 | 3165.5 | 1.1 |
| 3501.4 | 57.5 | 3501.0 | 57.2 |
| 3792.2 | 231.5 | 3801.0 | 199.7 |
| 3882.5 | 44.9 | 3884.7 | 45.4 |
| 3968.6 | 110.2 | 3968.9 | 100.9 |

**Table S3.13.** Normal modes of vibrations for the structures T-PW-1 and T-WP-1 of the PA···$H_2O$ complex calculated at MP2/6-311++G(d,p). Frequency in $cm^{-1}$ and IR intensity in km/mol.

| T-PW-1 | | T-WP-1 | |
|---|---|---|---|
| **Frequency** | **IR intensity** | **Frequency** | **IR intensity** |
| 5.6 | 3.2 | 20.5 | 5.8 |
| 57.0 | 13.2 | 34.1 | 3.6 |
| 92.3 | 42.8 | 115.8 | 130.3 |
| 157.5 | 4.1 | 175.0 | 42.9 |
| 184.0 | 7.3 | 181.4 | 61.0 |
| 221.9 | 8.6 | 213.1 | 123.7 |
| 294.3 | 248.4 | 266.4 | 2.4 |
| 307.3 | 5.2 | 411.0 | 46.9 |
| 554.8 | 15.9 | 540.8 | 18.7 |
| 653.5 | 29.9 | 605.0 | 105.0 |
| 684.5 | 100.4 | 640.6 | 50.3 |
| 691.8 | 93.9 | 680.3 | 32.8 |
| 935.1 | 13.6 | 928.3 | 10.9 |
| 1020.7 | 5.6 | 1034.0 | 7.1 |
| 1094.1 | 114.8 | 1068.3 | 118.9 |
| 1283.0 | 9.8 | 1254.2 | 68.2 |
| 1365.9 | 70.7 | 1292.0 | 7.9 |
| 1478.5 | 13.8 | 1459.8 | 21.8 |
| 1523.5 | 1.9 | 1526.3 | 2.1 |
| 1645.1 | 62.6 | 1666.8 | 34.4 |
| 2138.3 | 1.6 | 2146.6 | 5.8 |
| 3053.1 | 42.0 | 3070.8 | 30.5 |
| 3099.0 | 20.6 | 3118.9 | 13.4 |
| 3505.7 | 51.8 | 3502.4 | 55.5 |
| 3794.7 | 489.7 | 3788.0 | 275.7 |
| 3873.1 | 9.1 | 3875.9 | 52.9 |
| 3986.5 | 95.1 | 3967.1 | 92.2 |

# CHAPTER 4

# Rotational spectra of the acetonitrile···carbon dioxide complex

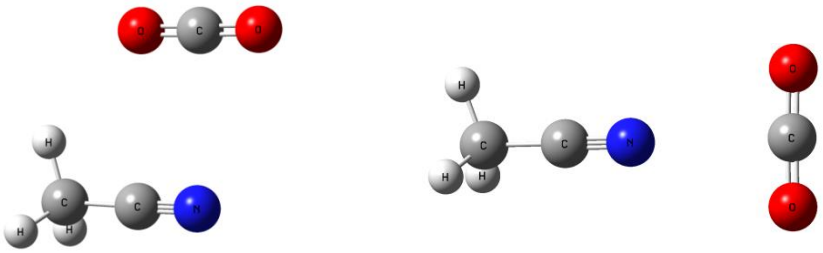

CHAPTER 4

# ROTATIONAL SPECTRA OF THE ACETONITRILE···CARBON DIOXIDE COMPLEX

## 4.1. Introduction

Non-covalent interactions analogous to the hydrogen bond have been described for the elements of group 14[1,2]. They are named as tetrel bonds[2]. Since the conception of this interaction a large number of computational studies have been carried out to understand the tetrel bonds. However, experimental studies involving tetrel bonds have been few and far between. Rotational spectroscopic studies provide valuable structural information about complexes bound by such an interaction. Legon pointed out that many rotational spectroscopic studies have investigated such interactions before, but never identified them as tetrel bonds[3]. The complexes of acetonitrile and methyl fluoride with molecules such as $CO_2$ and $H_2O$ are ideal to investigate tetrel bonding. In this Chapter, we report the rotational spectra $CH_3CN\cdots CO_2$ complex. The rotational spectrum of the $CH_3F\cdots H_2O$ complex is discussed in *Chapter 6* of this Thesis.

Mani and Arunan studied a number of $CH_3X$ complexes with various electron rich donors and found that the positive methyl face can accept electron density forming an X-C···Y carbon/tetrel bond, where Y is the electron rich donor moiety[1]. It has been pointed out[3,4] that the T-shaped $HCN\cdots CO_2$ complex can be considered as a tetrel bonded complex, where the nitrogen of HCN interacts with the positively charged central carbon atom of $CO_2$. Therefore, the higher homologue $CH_3CN\cdots CO_2$ complex offers the possibility to study various tetrel bonded interactions since it can either form

a T-shaped complex like the HCN···$CO_2$ complex or the methyl face of $CH_3CN$ can accept electron density from the oxygen end of $CO_2$ forming a NC-C···O tetrel bond.

$CO_2$ is a greenhouse gas and there have been attempts to develop methods for its sequestration in order contain global warming. Supramolecular assemblies such as metal organic frameworks (MOFs)[5] and zeolites[6] and other recent technologies[7] often use nitrogen-based compounds to capture $CO_2$. Studying the N···$CO_2$ interactions could be relevant to the modelling and understanding of such supramolecular assemblies.

The rotational spectra of a number of complexes of $CO_2$ with nitrogen containing compounds have been investigated. Complexes with $CO_2$ of molecules such as $N_2$[8], $NH_3$[9], HCN[10], HCCCN[11], pyridine[12] and many others have been studied. All these complexes have the same structural motif, that is a T-shaped structure with the nitrogen interacting with the central positively charged carbon atom in $CO_2$. Two structures are possible for the HCN···$CO_2$ complex. One is the carbon/tetrel bonded structure which is T-shaped[10] and the other is the linear H-bonded structure[13]. The T-shaped structure is observed in an Ar beam whereas the linear structure was only observed in a first run Ne beam (70% Ne, 30% He). Theoretical studies on $CH_3CN$···$CO_2$ predict four different structures for this complex[14].

In this chapter, the rotational spectra of the $CH_3CN$···$CO_2$ complex and its isotopologues are studied. Two different structures for the $CH_3CN$···$CO_2$ complex are observed, a π-stacked structure and the T-shaped one. We have used the Atoms in Molecules (AIM) analysis to understand the tetrel bonding interactions present in this system.

## 4.2. Methods

### 4.2.1. Experimental details

The rotational spectra of the $CH_3CN$···$CO_2$ complex and its isotopologues have been recorded using a Balle-Flygare type pulsed nozzle Fourier transform microwave (PNFTMW) spectrometer[15]. The details of this spectrometer have been described in Chapter 2. The acetonitrile ($CH_3CN$) was obtained from *Sigma Aldrich*, carbon dioxide ($CO_2$) and helium were obtained from *Bhuruka Gases*. Helium was used as a carrier gas. Helium was selected instead of argon, to avoid complexation of $CH_3CN$ with argon

thereby reducing the congestion of the spectra. The $CH_3CN\cdots CO_2$ dimers were formed by supersonically expanding the gases through a 0.8 mm nozzle into the evacuated cavity against backing pressures of 1.4-1.6 atm. The spectra were collected using 256 points while scanning for transitions and the observed rotational frequencies were later averaged at 512 or 1024 points to obtain the high-resolution spectra. The isotopes of $CH_3CN$; $CD_3CN$, and $CH_3{}^{13}CN$ were obtained from *Cambridge Isotope Laboratories* and used without further purification. The $CH_3{}^{13}CN\cdots CO_2$ spectrum was obtained by using a 10% mixture of $CH_3{}^{13}CN$ in $CH_3CN$ since only 1 ml of $CH_3{}^{13}CN$ was available.

### 4.2.2. Computational details

The structures for the $CH_3CN\cdots CO_2$ dimer were optimized at various levels of theory with similar results. Herein, we report the results obtained at the MP2/aug-cc-pVDZ level of theory. The molecular electrostatic potential surfaces for the monomer units, $CH_3CN$ and $CO_2$, helped to visualize the possible interactions that could stabilize the dimer. Plausible structures based on these interactions were constructed to be used as the initial guess geometries for the optimization. Harmonic frequency calculations at the same level of theory give no imaginary frequencies, confirming that the structures obtained are minima structures on the potential energy surface. The centrifugal distortion constants were calculated by using the freq=vibrot keyword. The binding energies for the dimers were corrected for both the zero-point energy (ZPE), and for the basis set superposition error (BSSE). The BSSE was computed using Boys and Bernardi's counterpoise method[16]. All these calculations were performed using the *Gaussian 09* software[17]. The rotational constants obtained for the optimized structures were used to predict the rotational spectra. This was done using SPCAT[18,19] and ASROT[20,21] programs. The electron density topologies for the optimized geometries were calculated using the *AIMAll* software[22].

## 4.3. Structure optimization

The molecular electrostatic potential (MESP) surfaces plotted for the $CH_3CN$ and $CO_2$ are shown in Figure 4.1. The red regions indicate regions of higher electron density (relatively negative) and the blue regions indicate regions of lower electron density (relatively positive). The methyl face of $CH_3CN$ is positive and can accept electron density, while the cyano nitrogen end is negative and can donate electron density. In the $CO_2$ molecule the central carbon is positive and the oxygen ends are

negative. Guess structures based on the electrostatic attraction between the two moieties were used as starting geometries to obtain the optimized structures of the $CH_3CN\cdots CO_2$ complex.

The optimized structures obtained at MP2/aug-cc-pVDZ are shown in Figure 4.2. The rotational constants, the electric dipole moment components, and the binding energies for these structures are given in Table 4.1. The MESP surfaces show that the cyano C is positive and the N is negative for $CH_3CN$, while the O is negative and C is positive in the $CO_2$ moiety. Therefore, a π-stacked structure is formed when the C≡N and O=C π-bonds align due to the electrostatic attraction. The T-shaped structure is formed when the nitrogen end of $CH_3CN$ donates its electron density to the C-center of $CO_2$. This structural motif (T-shaped) has been observed for many N-containing compounds[8–12] that form a complex with $CO_2$. The other two structures, linear and L-shaped, have very similar interactions and differ in the orientation of the $CO_2$ molecule. For these two structures the oxygen end of $CO_2$ interacts with the positive methyl face of $CH_3CN$. All four minima structures have very distinct rotational constants and these structures are the same as those reported in a theoretical study of the $CH_3CN\cdots CO_2$ complex[14]. We note that the π-stacked and T-shaped structures have nearly equal binding energies and therefore, both these structures could possibly be observed in the molecular beam.

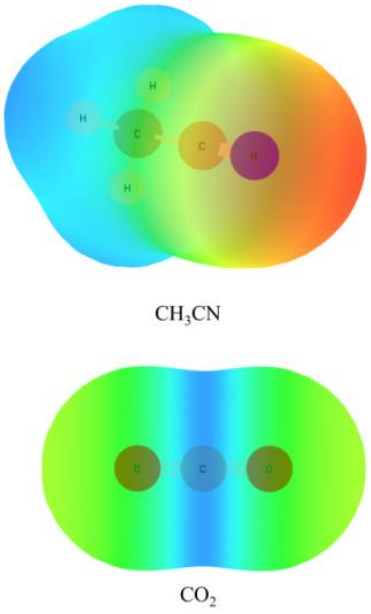


**Figure 4.1.** The molecular electrostatic potential (MESP) surface for $CH_3CN$ and $CO_2$. The blue regions are positively charged and red regions are negatively charged.

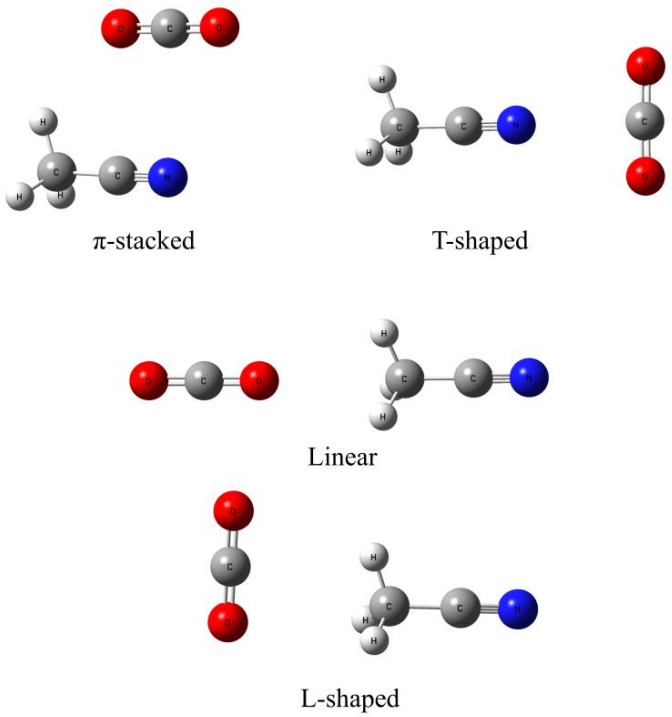


**Figure 4.2.** The optimised structures of the $CH_3CN\cdots CO_2$ complex calculated at MP2/aug-cc-pVDZ.

**Table 4.1.** The rotational constants (MHz), electric dipole moment components (debye), and the binding energies (ΔE) with the BSSE and ZPE corrections ($kJmol^{-1}$) calculated at MP2/aug-cc-pVDZ for the optimized structures of the $CH_3CN\cdots CO_2$ complex.

| | **π-stacked** | **T-shaped** | **Linear** | **L-shaped** |
|---|---|---|---|---|
| **Rotational Constants** (MHz) | | | | |
| A | 6501.19 | 10581.97 | 156752.66 | 10516.68 |
| B | 1857.69 | 1130.33 | 659.08 | 964.99 |
| C | 1458.31 | 1027.96 | 659.08 | 888.89 |
| **Dipole Moment** (D) | | | | |
| $\lvert\mu_a\rvert$ | 2.17 | 4.40 | 4.26 | 3.94 |
| $\lvert\mu_b\rvert$ | 3.08 | 0.02 | 0.00 | 0.64 |
| $\lvert\mu_c\rvert$ | 0.00 | 0.00 | 0.02 | 0.00 |
| **ΔE (BSSE)** ($kJmol^{-1}$) | -9.6 | -9.1 | -3.8 | -0.9 |
| **ΔE (BSSE+ZPE)** ($kJmol^{-1}$) | -7.7 | -7.6 | -2.6 | 0.1 |

## 4.4. T-shaped structure

### 4.4.1. Rotational spectra

As noted earlier most nitrogen containing molecules form a T-shaped complex with $CO_2$. Therefore, the initial searches were done based on the predictions for the T-shaped structure. Searches for the $4_{04}$-$3_{03}$ rotational transition of this structure were carried out in the region, 8.5-9.5 GHz. A signal was observed at 8727 MHz, we assumed that this signal is the $4_{04}$-$3_{03}$ transition expected for the T-shaped structure. We then continued to search for transitions based on the B+C pattern expected for a nearly prolate asymmetric top, T-shaped structure. Frequencies corresponding to six rotational transitions from $3_{03}$-$2_{02}$ to $8_{08}$-$7_{07}$ having a B+C value of ~2183 MHz were observed. However, no K=1 transitions based on this assignment were found despite careful searches. All observed transitions show a hyperfine structure expected for the nuclear quadrupole coupling due to N-14. However, the number of transitions observed was more than what was expected from hyperfine splitting. We matched the observed lines with the predicted hyperfine splitting and we realized that there were two sets of lines in the spectrum. The hyperfine splitting for one set (higher frequency) corresponds to K=0 and for the other (lower frequency set) the hyperfine pattern is that expected for K=1 transitions. Though the hyperfine pattern matches those expected for the K=1 lines the frequencies observed are far from those predicted for the m=0 state and therefore these set of lines could correspond to the K=1 levels for the m=1 state. The K=0 lines were fit keeping the 'A' rotational constant fixed at the predicted value. The rotational transitions were fit using Pickett's program, SPFIT[18,19].

The rotational spectrum for the $CD_3CN\cdots CO_2$ isotopologue was also recorded. The spectral pattern observed for this isotopologue was similar to the parent complex but with a B+C value of 1989 MHz. The hyperfine splitting for the higher frequency set matches well with that expected for the K=0 transitions and the lower frequency set matches with the K=1 transitions. One expects a larger number of lines due to the nuclear quadrupole coupling of the three deuterium nuclei of $CD_3CN$ and the nitrogen, however only the hyperfine splitting due of the nitrogen could be observed and assigned. The observed transitions for $CH_3CN\cdots CO_2$ and its isotopologue $CD_3CN\cdots CO_2$ are given in Table 4.2. The assigned transitions and the experimental rotational constants are given in Table 4.3 and 4.4, respectively. The uncertainty for

the fitted B and C rotational constants is larger than expected and this is probably because the effects of the free methyl rotor have not been accounted for.

**Table 4.2.** Observed transition frequencies for the T-shaped complex of $CH_3CN\cdots CO_2$ and $CD_3CN\cdots CO_2$.

| **Transitions** | **Frequency (MHz)** | |
|---|---|---|
| **J"-J'** | **$CH_3CN\cdots CO_2$** | **$CD_3CN\cdots CO_2$** |
| **3-2** | 6547.0122 | - |
| | 6547.5785 | - |
| | 6547.9300 | - |
| | 6548.3304 | - |
| **4-3** | 8726.6564 | 7949.1880 |
| | 8726.7125 | 7949.3468 |
| | 8727.3009 | 7949.8253 |
| | 8727.3302 | 7949.8546 |
| **5-4** | 10902.2046 | - |
| | 10902.2486 | - |
| | 10902.2924 | - |
| | 10903.0688 | - |
| | 10903.1128 | - |
| | 10903.1372 | - |
| **6-5** | 13073.8044 | 11912.8213 |
| | 13073.8240 | 11912.8408 |
| | 13073.8582 | 11912.8799 |
| | 13074.9128 | 11913.6953 |
| | 13074.9422 | 11913.7197 |
| | 13074.9568 | 11913.7392 |
| **7-6** | 15240.5934 | 13889.9262 |
| | 15240.6276 | 13889.9604 |
| | - | 13890.9931 |
| | - | 13891.0150 |
| | - | 13891.0272 |
| **8-7** | 17401.8250 | 15863.1895 |
| | 17401.8518 | 15863.2188 |
| | 17403.5560 | 15864.5078 |
| | 17403.5706 | - |

**Table 4.3.** Assigned rotational transitions (K=0) for the T-shaped complex of $CH_3CN\cdots CO_2$ and $CD_3CN\cdots CO_2$. Frequencies and observed-calculated values are in MHz.

| Transitions | | $CH_3CN\cdots CO_2$ | | $CD_3CN\cdots CO_2$ | |
|---|---|---|---|---|---|
| J'K$_1$'K$_1$'F'←J"K$_1$"K$_1$"F" | | Frequency | obs-calc | Frequency | obs-calc |
| 3034 | 2023 | 6548.3304 | 0.0015 | - | - |
| 4044 | 3033 | 8727.3009 | 0.0003 | 7949.8253 | 0.0003 |
| 4045 | 3034 | 8727.3302 | 0.0002 | 7949.8546 | 0.0001 |
| 5054 | 4043 | 10903.0688 | -0.0009 | - | - |
| 5055 | 4044 | 10903.1128 | -0.0034 | - | - |
| 5056 | 4045 | 10903.1372 | 0.0006 | - | - |
| 6065 | 5054 | 13074.9128 | 0.0009 | 11913.6953 | 0.0016 |
| 6066 | 5055 | 13074.9422 | 0.0007 | 11913.7197 | -0.0036 |
| 6067 | 5056 | 13074.9568 | 0.0004 | 11913.7392 | 0.0009 |
| 7076 | 6065 | - | - | 13890.9931 | -0.0008 |
| 7077 | 6066 | - | - | 13891.0150 | 0.0004 |
| 7078 | 6067 | - | - | 13891.0272 | 0.0013 |
| 8087 | 7076 | 17403.5560 | 0.0046 | - | -0.0002 |
| 8089 | 7078 | 17403.5706 | -0.0047 | 15864.5078 | - |

**Table 4.4.** Experimental rotational constants, centrifugal distortion constant, and nuclear quadrupole coupling constant of the T-shaped $CH_3CN\cdots CO_2$ complex and its isotopologue.

| | Predicted [a] | Experimental | |
|---|---|---|---|
| **Constant** | **$CH_3CN\cdots CO_2$** | **$CH_3CN\cdots CO_2$** | **$CD_3CN\cdots CO_2$** |
| **A (MHz)** | 10766.0 | [10766.0][b] | [10087.7][b] |
| **B (MHz)** | 1150.1 | 1139.8(5) | 1032.5(5) |
| **C (MHz)** | 1045.9 | 1044.0(5) | 956.3(5) |
| **$D_J$ (kHz)** | - | 3.8(6) | 3.0(6) |
| **$3/2\chi_{aa}$** | -5.7 | -5.8(2) | -5.8(3) |
| **n** | | 11 | 9 |
| **RMS (kHz)** | | 2.4 | 1.5 |

[a] the constants are predicted at MP2/aug-cc-pVTZ
[b]values in [ ] are fixed at the calculated values at MP2/aug-cc-pVTZ

### 4.4.2. Structural analysis

The spectra indicate that the methyl group of acetonitrile is a free rotor. In such a case, the effective symmetry of the T-shaped structure would be $C_{2v}$. This would make the two oxygen atoms of $CO_2$ equivalent. The nuclear spin statistics then dictates that only even |K-m| levels would be observed. Which explains why no K=1 lines were observed for the m=0 internal rotor state. The second set of lines obtained could correspond to the K=1 lines for the m=1 state.

The angle (θ) that the molecular axis of acetonitrile makes with the line joining the center of masses of the two molecules could be found using the following relation[23]

$$\frac{\chi_{aa}}{\chi_0} = \frac{3}{2}\left(\cos^2\theta - \frac{1}{2}\right)$$

where $\chi_{aa}$ is the nuclear quadrupole coupling constant obtained for the $CH_3CN\cdots CO_2$ complex and the $\chi_0$ is the coupling constant for the free $CH_3CN$. Using the above equation, we find that for the $CH_3CN\cdots CO_2$ complex the angle (θ) is 16.2°. This is similar to the angles reported for the other T-shaped complexes[8–12] of nitrogen containing complexes with $CO_2$. The corresponding bending angle for the T-shaped complex of $HCN\cdots CO_2$ is reported[10] to be 17.4(2)°.

## 4.5. π-stacked structure

### 4.5.1. Rotational spectra

A number of additional lines were observed that did not belong to the T-shaped structure but were stronger in intensity than the lines assigned to the T-shaped structure. It was realized that these lines could belong to the π-stacked structure following which other lines based on the predictions were easily found and assigned. The description of π-stacked should only be taken as a geometric one and does not imply attractive interactions between the two π-electron clouds. A total of 31 rotational transitions were observed. Only *a*-type and *b*-type transitions were observed. The spectra show hyperfine structure due to the nuclear quadrupole coupling of the N-14 nucleus. This leads to a total of 81 lines being observed. The rotational transitions were assigned and fit using a Watson's A-reduced Hamiltonian. The observed transitions are given in Table 4.5. The experimentally observed rotational, distortion, and quadrupole coupling constants are given in Table 4.8 and are close to the *ab initio* predicted values.

### 4.5.2. Isotopic substitutions

The rotational spectra for the isotopologues were recorded to ascertain the structure obtained. Two isotopologues were studied, the $CD_3CN\cdots CO_2$ and the $CH_3{}^{13}CN\cdots CO_2$. The $CD_3CN$ isotopic substitution confirms the assignment of the rotational transitions and thus, the observed structure. The three deuterium nuclei are also expected to show hyperfine splitting due to nuclear quadrupole coupling. However, the splitting caused

by N and D are quite different from each other and the observed hyperfine splitting suggests that only the splitting due to nitrogen could be resolved. A total of 26 lines were observed for the $CD_3CN\cdots CO_2$ isotopologue (Table 4.6). The transitions for $CH_3{}^{13}CN\cdots CO_2$ were too weak to obtain the spectrum in natural abundance. Therefore, an enriched sample of 99% $CH_3{}^{13}CN$ was diluted to a 10% mixture in $CH_3CN$ and used. Only a few lines (Table 4.7) were observed because of the small quantity of enriched sample available. Since, only 12 lines were observed the centrifugal distortion constants were kept fixed at the values obtained for the parent isotopologues while fitting. The rotational constants as well as the quadrupole coupling constants were fit. The observed rotational transitions and the fit parameters for the isotopologues are given in Table 4.8.

**Table 4.5.** The assigned transition frequencies for the π-stacked $CH_3CN\cdots CO_2$ complex.

| J'K$_1$'K$_l$'F' | ← | J"K$_1$"K$_l$"F" | Frequency (MHz) | obs-calc (MHz) |
|---|---|---|---|---|
| 2 0 2 1 | | 1 0 1 1 | 6432.3324 | 0.0024 |
| 2 0 2 3 | | 1 0 1 2 | 6432.3788 | 0.0009 |
| 2 0 2 1 | | 1 0 1 0 | 6432.4496 | -0.0041 |
| 2 1 1 3 | | 1 1 0 2 | 6828.9834 | 0.0019 |
| 2 1 1 2 | | 1 1 0 1 | 6829.0811 | 0.0005 |
| 1 1 1 1 | | 0 0 0 1 | 8228.0015 | 0.0048 |
| 1 1 1 2 | | 0 0 0 1 | 8228.6655 | -0.0006 |
| 1 1 1 0 | | 0 0 0 1 | 8229.6714 | -0.0003 |
| 4 0 4 5 | | 3 1 3 4 | 8552.5835 | 0.0062 |
| 4 0 4 4 | | 3 1 3 3 | 8553.0889 | -0.0028 |
| 3 1 3 2 | | 2 1 2 1 | 9102.3019 | -0.0022 |
| 3 1 3 3 | | 2 1 2 2 | 9102.4045 | -0.0006 |
| 3 1 3 4 | | 2 1 2 3 | 9102.4338 | 0.0020 |
| 3 0 3 3 | | 2 0 2 2 | 9597.5288 | 0.0004 |
| 3 0 3 4 | | 2 0 2 3 | 9597.6070 | 0.0014 |
| 3 0 3 2 | | 2 0 2 1 | 9597.6314 | 0.0005 |
| 3 2 2 2 | | 2 2 1 1 | 9679.3164 | 0.0046 |
| 3 2 2 4 | | 2 2 1 3 | 9679.3409 | -0.0004 |
| 3 2 2 3 | | 2 2 1 2 | 9679.3897 | -0.0044 |
| 3 2 1 2 | | 2 2 0 2 | 9760.5458 | -0.0005 |
| 3 2 1 4 | | 2 2 0 3 | 9760.5897 | 0.0004 |
| 3 2 1 3 | | 2 2 0 2 | 9760.7166 | -0.0046 |
| 3 1 2 4 | | 2 1 1 3 | 10229.9920 | 0.0001 |
| 3 1 2 3 | | 2 1 1 2 | 10230.0164 | 0.0010 |
| 3 1 2 2 | | 2 1 1 1 | 10230.1311 | 0.0001 |
| 2 1 2 2 | | 1 0 1 1 | 11078.2476 | 0.0002 |
| 2 1 2 3 | | 1 0 1 2 | 11078.9605 | -0.0006 |
| 2 1 2 1 | | 1 0 1 1 | 11079.2876 | 0.0059 |
| 4 1 4 3 | | 3 1 3 2 | 12113.8310 | -0.0011 |
| 4 1 4 4 | | 3 1 3 3 | 12113.8531 | -0.0014 |

| | | | |
|---|---|---|---|
| 4 1 4 5 | 3 1 3 4 | 12113.8873 | -0.0005 |
| 5 0 5 4 | 4 1 4 3 | 12177.2620 | -0.0058 |
| 5 0 5 6 | 4 1 4 5 | 12177.3980 | 0.0049 |
| 4 0 4 4 | 3 0 3 3 | 12703.8835 | -0.0002 |
| 4 0 4 5 | 3 0 3 4 | 12703.9861 | -0.0005 |
| 4 0 4 3 | 3 0 3 2 | 12704.0056 | -0.0003 |
| 4 2 3 5 | 3 2 2 4 | 12889.3290 | -0.0011 |
| 4 3 2 5 | 3 3 1 4 | 12944.7680 | -0.0066 |
| 4 3 2 3 | 3 3 1 3 | 12944.8270 | 0.0045 |
| 4 3 1 5 | 3 3 0 4 | 12948.9240 | -0.0012 |
| 4 3 1 3 | 3 3 0 3 | 12948.9820 | 0.0117 |
| 7 2 5 7 | 7 1 6 7 | 12978.4680 | 0.0015 |
| 7 2 5 6 | 7 1 6 6 | 12978.5160 | -0.0001 |
| 4 2 2 3 | 3 2 1 2 | 13089.8139 | -0.0087 |
| 4 2 2 5 | 3 2 1 4 | 13089.8384 | -0.0009 |
| 4 2 2 4 | 3 2 1 3 | 13089.9604 | 0.0076 |
| 6 2 4 6 | 6 1 5 6 | 13154.7820 | -0.0072 |
| 6 2 4 7 | 6 1 5 7 | 13154.9970 | 0.0058 |
| 5 2 3 6 | 5 1 4 6 | 13535.2440 | -0.0064 |
| 5 2 3 4 | 5 1 4 4 | 13535.3220 | -0.0002 |
| 4 1 3 5 | 3 1 2 4 | 13613.7737 | 0.0004 |
| 4 1 3 3 | 3 1 2 2 | 13613.8420 | -0.0004 |
| 3 1 3 3 | 2 0 2 2 | 13748.3191 | -0.0013 |
| 3 1 3 3 | 2 0 2 3 | 13748.3288 | 0.0050 |
| 3 1 3 4 | 2 0 2 3 | 13749.0172 | 0.0022 |
| 3 1 3 2 | 2 0 2 1 | 13749.2516 | -0.0042 |
| 4 2 2 5 | 4 1 3 5 | 14032.1700 | -0.0032 |
| 4 2 2 3 | 4 1 3 3 | 14032.3060 | 0.0049 |
| 3 2 1 3 | 3 1 2 3 | 14555.4980 | 0.0022 |
| 3 2 1 4 | 3 1 2 4 | 14556.1150 | 0.0079 |
| 5 1 5 5 | 4 1 4 4 | 15107.8727 | -0.0021 |
| 5 1 5 6 | 4 1 4 5 | 15107.9118 | 0.0000 |
| 5 0 5 5 | 4 0 4 4 | 15738.5826 | 0.0011 |
| 5 0 5 6 | 4 0 4 5 | 15738.7046 | 0.0009 |
| 5 0 5 4 | 4 0 4 3 | 15738.7193 | 0.0003 |
| 6 0 6 5 | 5 1 5 4 | 15767.9740 | -0.0038 |
| 6 0 6 7 | 5 1 5 6 | 15768.0620 | 0.0020 |
| 6 0 6 6 | 5 1 5 5 | 15768.3940 | 0.0031 |
| 4 1 4 4 | 3 0 3 3 | 16264.6428 | -0.0038 |
| 4 1 4 5 | 3 0 3 4 | 16265.2946 | -0.0027 |
| 4 1 4 3 | 3 0 3 2 | 16265.4558 | -0.0012 |
| 5 2 3 4 | 4 2 2 3 | 16476.0433 | 0.0051 |
| 5 2 3 5 | 4 2 2 4 | 16476.1605 | -0.0029 |
| 3 2 2 4 | 3 1 3 4 | 16710.2103 | -0.0123 |
| 3 2 2 3 | 3 1 3 4 | 16710.2298 | 0.0070 |
| 5 1 4 5 | 4 1 3 4 | 16972.9458 | -0.0025 |
| 5 1 4 6 | 4 1 3 5 | 16972.9702 | -0.0013 |
| 5 1 4 4 | 4 1 3 3 | 16973.0141 | -0.0029 |
| 6 1 6 6 | 5 1 5 5 | 18082.4310 | 0.0007 |
| 6 1 6 5 | 5 1 5 4 | 18082.4505 | 0.0018 |
| 6 1 6 7 | 5 1 5 6 | 18082.4701 | -0.0001 |

**Table 4.6.** The assigned transition frequencies for the π-stacked $CD_3CN\cdots CO_2$ complex.

| J'K$_1$'K$_1$'F' ← | J"K$_1$"K$_1$"F" | Frequency(MHz) | obs-calc (MHz) |
|---|---|---|---|
| 3 1 3 4 | 2 1 2 3 | 8460.9068 | 0.0045 |
| 3 0 3 3 | 2 0 2 2 | 8901.6726 | 0.0031 |
| 3 0 3 2 | 2 0 2 1 | 8901.7459 | -0.0042 |
| 2 1 2 3 | 1 0 1 2 | 10346.4339 | -0.0025 |
| 2 1 2 1 | 1 0 1 1 | 10346.7705 | -0.0033 |
| 2 1 2 1 | 1 0 1 2 | 10346.8022 | 0.0059 |
| 4 1 4 4 | 3 1 3 3 | 11262.1998 | -0.0053 |
| 4 1 4 5 | 3 1 3 4 | 11262.2389 | -0.0001 |
| 4 0 4 4 | 3 0 3 3 | 11791.3564 | 0.0035 |
| 4 0 4 3 | 3 0 3 2 | 11791.4541 | -0.0064 |
| 4 2 3 5 | 3 2 2 4 | 11945.6750 | 0.0001 |
| 4 1 3 4 | 3 1 2 3 | 12587.1566 | -0.0035 |
| 4 1 3 5 | 3 1 2 4 | 12587.1688 | 0.0011 |
| 4 1 3 3 | 3 1 2 2 | 12587.2323 | 0.0025 |
| 5 1 5 5 | 4 1 4 4 | 14048.8750 | -0.0007 |
| 5 1 5 6 | 4 1 4 5 | 14048.9116 | 0.0000 |
| 5 0 5 5 | 4 0 4 4 | 14620.4956 | 0.0008 |
| 5 0 5 6 | 4 0 4 5 | 14620.6128 | 0.0067 |
| 5 1 4 5 | 4 1 3 4 | 15697.2822 | 0.0035 |
| 5 1 4 6 | 4 1 3 5 | 15697.2994 | 0.0017 |
| 5 1 4 4 | 4 1 3 3 | 15697.3384 | -0.0056 |
| 6 1 6 6 | 5 1 5 5 | 16819.0532 | 0.0013 |
| 6 1 6 5 | 5 1 5 4 | 16819.0678 | 0.0024 |
| 6 1 6 7 | 5 1 5 6 | 16819.0922 | -0.0017 |
| 6 0 6 6 | 5 0 5 5 | 17385.2081 | 0.0012 |
| 6 0 6 5 | 5 0 5 4 | 17385.3326 | -0.0050 |

**Table 4.7.** The assigned transition frequencies for the π-stacked $CH_3{}^{13}CN\cdots CO_2$ complex.

| J'K$_1$'K$_1$'F' ← | J"K$_1$"K$_1$"F" | Frequency(MHz) | obs-calc (MHz) |
|---|---|---|---|
| 3 1 3 3 | 2 1 2 2 | 9022.5725 | -0.0039 |
| 3 1 3 4 | 2 1 2 3 | 9022.6018 | 0.0009 |
| 3 0 3 3 | 2 0 2 3 | 9511.0870 | -0.0033 |
| 3 0 3 4 | 2 0 2 3 | 9511.1560 | 0.0014 |
| 3 1 2 4 | 2 1 1 3 | 10132.8780 | -0.0049 |
| 3 1 2 3 | 2 1 1 2 | 10132.9160 | 0.0069 |
| 4 1 4 4 | 3 1 3 3 | 12008.0730 | 0.0058 |
| 4 0 4 5 | 3 0 3 4 | 12591.3840 | -0.0021 |
| 5 0 5 5 | 4 0 4 4 | 15601.6930 | 0.0015 |
| 5 0 5 6 | 4 0 4 5 | 15601.8100 | -0.0028 |
| 2 1 2 2 | 1 0 1 1 | 11023.4880 | -0.0019 |
| 2 1 2 2 | 1 0 1 2 | 11023.5490 | 0.0021 |

**Table 4.8.** Experimental rotational constants, centrifugal distortion constants, and nuclear quadrupole coupling constants for the π-stacked $CH_3CN\cdots CO_2$ complex and its isotopologues.

| | Predicted [a] | Experimental | | |
|---|---|---|---|---|
| **Constant** | **$CH_3CN\cdots CO_2$** | **$CH_3CN\cdots CO_2$** | **$CD_3CN\cdots CO_2$** | **$CH_3{}^{13}CN\cdots CO_2$ [b]** |
| **A (MHz)** | 6689.8 | 6803.528(2) | 6359.9(2) | 6784.55(2) |
| **B (MHz)** | 1774.7 | 1801.3811(5) | 1661.14(3) | 1783.6861(10) |
| **C (MHz)** | 1415.1 | 1425.1040(5) | 1328.83(3) | 1413.178(1) |
| **$\Delta_J$ (kHz)** | 4.4 | 5.559(5) | 5.0(2) | 5.43(2) |
| **$\Delta_K$ (kHz)** | 110.2 | 136.1(4) | 129.(157) | [136.1] |
| **$\Delta_{JK}$ (kHz)** | -15.2 | -20.75(4) | -7.2(3) | [-20.75] |
| **$\delta_J$ (kHz)** | 1.1 | 1.507(4) | 1.44(2) | [1.507] |
| **$\delta_K$ (kHz)** | 10.5 | 16.8(2) | 19.(13) | [16.8] |
| **$3/2\chi_{aa}$ (MHz)** | 0.3 | 0.247(6) | 0.12(3) | 0.29(3) |
| **$1/4(\chi_{bb}-\chi_{cc})$ (MHz)** | -0.9 | -1.075(2) | -1.02(2) | -1.08(5) |
| **$\chi_{ab}$ (MHz)** | 2.5 | 4.(1) | 8.(2) | [4.] |
| **n** | | 81 | 26 | 12 |
| **RMS (kHz)** | | 3.9 | 3.6 | 3.6 |

[a] the constants predicted at MP2/6-311++g(d,p)
[b] values in [ ] are kept fixed at the values obtained for the parent isotopologue.

### 4.5.3. Structural analysis

The rotational constants obtained experimentally match well with those computed for the π-stacked structure at the MP2/6-311++G(d,p) level. The structure is nearly planar with all the heavy atoms in a plane with only the methyl hydrogen atoms out of plane. The isotopic substitution helps to obtain the position of the substituted atom in the observed structure using the Kraitchman equations[24]. The equations help to get the coordinates based on the difference in the moments of inertia of the parent and substituted isotopologue. The equations are formulated for a single atom substitution and assume that the bond distances and angles do not change on isotopic substitution. The $CH_3{}^{13}CN\cdots CO_2$ isotopologue helps to identify the position of the cyano carbon atom. The experimentally observed coordinates show excellent agreement with the *ab initio* coordinates (see Table 4.9).

**Table 4.9.** Principal axis coordinates and distance from the centre of mass (R) for the cyano carbon atom of $CH_3CN$ obtained experimentally and the corresponding coordinates calculated at MP2/aug-cc-pVDZ for the π-stacked $CH_3CN\cdots CO_2$ complex.

| | Predicted | Experimental |
|---|---|---|
| **x** | 1.692 | -/+1.675 |
| **y** | 0.460 | -/+0.462 |
| **z** | 0.000 | -/+0.029i |
| **R(Å)** | 1.737 | 1.737 |

## 4.6. Atoms in Molecules (AIM) analysis

We could observe and assign the rotational spectra of the $CH_3CN\cdots CO_2$ complex corresponding to the π-stacked and T-shaped structures and their isotopologues. The weak interactions that bind $CH_3CN$ and $CO_2$ are investigated by studying the electron density topology of the four optimized structures. The molecular graphs obtained for the four structures are shown in Figure 4.3. The π-stacked structure shows a weak C-H···O H-bond, with the methyl C-H bond interacting with the oxygen atom of the $CO_2$. The same oxygen atom also interacts with the carbon atom of the cyano group. A closed network of bonds is formed by these two weak interactions and is indicated by the presence of a ring critical point (RCP). It is surprising that there is no interaction between the carbon center of $CO_2$ and the nitrogen of $CH_3CN$ as might be expected from the MESP surfaces shown in Figure 4.1. The molecular graph for the T-shaped structure shows a bond critical point (BCP) between the nitrogen and the carbon center of $CO_2$. This interaction between the two units is indicative of a tetrel bond and is similar to those observed for the other T-shaped complexes bound via $N\cdots CO_2$ interaction. The linear and L-shaped structures show similar interaction where the methyl face of $CH_3CN$ accepts electron density from the oxygen end of $CO_2$. These interactions are tetrel bonds, where the electron density is donated to the σ-hole on the $CH_3CN$, unlike the T-shaped structure where the electron density is donated to the π-hole.

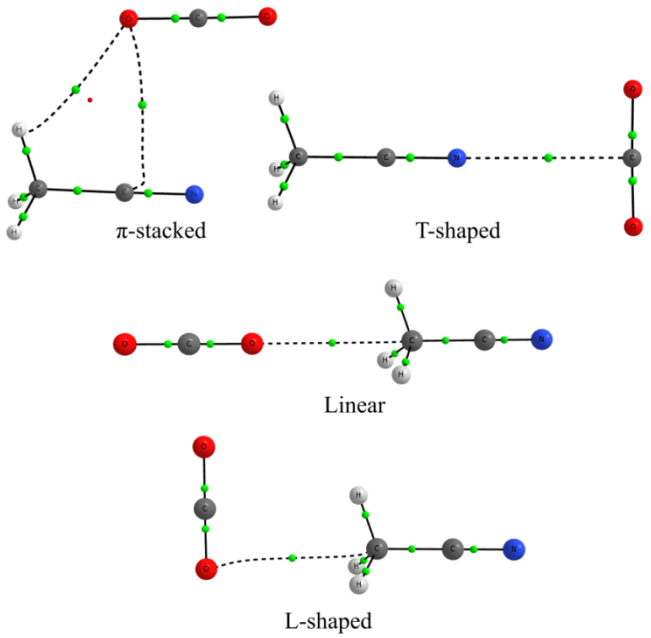


**Figure 4.3.** The molecular graphs for the $CH_3CN\cdots CO_2$ complex calculated from wavefunctions obtained using the MP2/aug-cc-pVDZ calculations.

All the three different carbon atoms present in the complex, take part in different tetrel bonded interactions. Thus, the $CH_3CN\cdots CO_2$ complex offers an opportunity to study different tetrel bonded complexes involving carbon. The properties of the electron density are tabulated in Table 4.10 and help to quantify the interactions present. Koch and Popelier have proposed a set of ranges for various properties to help identify the weak C-H···O hydrogen bond[25]. The $\varrho$ value is between 0.002-0.034 au and the $\nabla^2\varrho$ is between 0.024-0.139 au for the weak C-H···O hydrogen bond. In general, when the $\varrho$ at the BCP has a low value and the $\nabla^2\varrho$ is positive the bond can be considered to be a closed-shell interaction. Hydrogen bonds and other van der Waals interactions are examples of closed-shell interactions. Sosa and co-workers[26] have proposed that for a closed-shell interaction the $|\lambda_1| / \lambda_3$ ratio must be less than 1. From the tabulated values, it can be considered that the weak C-H···O interaction present in the π-stacked structure of $CH_3CN\cdots CO_2$ complex is an H-bond. The $\varrho$ and the $\nabla^2\varrho$ values at the BCP suggest that the C···O interaction between the oxygen end of $CO_2$ and the carbon atom of the cyano group in the π-stacked structure is also a closed-shell interaction. The values for the T-shaped structure clearly indicate that the complex is bound by an N-C tetrel bond. The linear and L-shaped structures have $\varrho$ values that are similar to the C-H···O bond but lower than the tetrel interactions in the π-stacked and T-shaped structures. The $\nabla^2\varrho$ value for the L-shaped complex is not within the range suggested by Koch and Popelier, this correlates with the fact that the binding energy for this complex is low and the BSSE+ZPE corrected binding energy is positive.

**Table 4.10**. Analysis of the non-covalent bond critical points in the optimized structures of the $CH_3CN$-$CO_2$ complex.

| System | Interaction | $\varrho$ | $\nabla^2\varrho$ | $\lambda_1$ | $\lambda_2$ | $\lambda_3$ | $\lvert\lambda_1\rvert / \lambda_3$ |
|---|---|---|---|---|---|---|---|
| **π-stacked** | C-H···O | 0.006 | 0.024 | -0.005 | -0.002 | 0.031 | 0.158 |
| | C···O | 0.008 | 0.027 | -0.005 | -0.003 | 0.035 | 0.156 |
| **T-shaped** | C···N | 0.009 | 0.038 | -0.008 | -0.002 | 0.048 | 0.159 |
| **Linear** | NC-C···O | 0.005 | 0.025 | -0.002 | -0.002 | 0.029 | 0.067 |
| **L-shaped** | NC-C···O | 0.004 | 0.017 | -0.002 | -0.001 | 0.020 | 0.081 |

## 4.7. Discussions

The rotational spectra observed indicate that both the lowest energy conformers are found. The π-stacked and the T-shaped structure have similar binding energies and both these structures are observed in a helium molecular beam. The rotational transitions observed for the π-stacked structure are stronger than the transitions observed for the T-shaped structure. This suggests that the calculated energy ordering matches well with the observed intensities (see Table 4.1). Both the structures have all the heavy atoms lying in a plane with only the methyl hydrogen atoms out of plane. The inertial defect $\Delta=I_c-I_a-I_b$ calculated at MP2/aug-cc-pVDZ is -3.23 amuÅ$^2$ for both the structures.

The T-shaped motif is the most commonly observed structure in the complexes of nitrogen containing molecules with $CO_2$. As mentioned earlier, the HCN···$CO_2$ dimer has two different conformers (a linear H-bonded structure[13] and the T-shaped structure[10]) both of which have been observed, albeit in different expansion conditions. One of the exceptions to the T-shaped motif for complexes of N-containing molecules with $CO_2$ is the $N_2O$···$CO_2$ complex[27,28]. The observed structure for the $N_2O$···$CO_2$ complex is similar to that of the π-stacked structure we found for the $CH_3CN$···$CO_2$ complex. It is an approximately slipped parallel structure where the O atom of $N_2O$ is closer to the C atom of $CO_2$. The $N_2O$ is slightly tilted such that the O end of $N_2O$ is closer to the C atom of $CO_2$. A T-shaped structure for the $N_2O$···$CO_2$ complex has not been observed as yet.

Millen derived an expression to obtain the stretching force constant ($k_s$) for a non-covalent bond from the rotation and centrifugal distortion constants[29]. This is done assuming a pseudo-diatomic model where the monomer units of the weakly bound complex are considered to be point masses. The $k_s$ for the T-shaped complexes of HCN···$CO_2$[10] and HCCCN···$CO_2$[11] are 4.9 Nm$^{-1}$ and 3.9 Nm$^{-1}$, respectively. The rotational transitions observed for the T-shaped $CH_3CN$···$CO_2$ complex need to be fitted taking into account the effects of the free methyl rotor to obtain accurate rotational and centrifugal constants, before deriving the experimental stretching force constant. However, one can obtain the stretching force constant from the calculated stretching frequency using the expression,

$$\nu_s = \frac{1}{2\pi}\sqrt{\frac{k_s}{\mu}}$$

where, $\nu_s$ is the stretching frequency and $\mu$ is the reduced mass of the pseudo-diatomic system. Harmonic frequency calculations at MP2/aug-cc-pVDZ give a normal mode (whose frequency is 83 $cm^{-1}$) which corresponds to the stretching of the weak N···$CO_2$ tetrel bond. Using this value for the stretching frequency we obtain a $k_s$ value of 5.2 $Nm^{-1}$. This value is slightly higher than the values reported for the HCN···$CO_2$ and HCCCN···$CO_2$ complexes. This is in agreement with the fact that the electron donating methyl group in $CH_3CN$ would make the N···$CO_2$ bond stronger.

The angle (θ) that the molecular axis of $CH_3CN$ makes with the *a*-axis can be obtained from the nuclear quadrupole coupling constants and is 16.2° for the $CH_3CN$···$CO_2$ complex. This bending angle is similar to that obtained for other N···$CO_2$ T-shaped complexes (see Table 4.11.). It was found that this bending angle θ for HCN in the weakly bound complexes of HCN on an average remained constant. For complexes where HCN donates electron density from the N end[10], the bending angle was around 17° and in hydrogen bonded complexes[30], it was around 12°. Complexes of $CH_3CN$ with various H-bond donors and Lewis acids are mostly symmetric tops with the nitrogen end interacting with either hydrogen or a Lewis acid center. The exception is the $CH_3CN$···Ar[31,32] complex which forms a T-shaped structure similar to the $CH_3F$···Ar complex discussed in *Chapter 6* of this Thesis. The bending angle of $CH_3CN$ in different complexes tabulated below shows that the angle θ is fairly constant with the exception of the $CH_3CN$···HCl complex.

**Table 4.11.** The bending angle (θ) for various T-shaped complexes of N-containing molecules with carbon dioxide.

| Complex | θ(°) |
|---|---|
| $CH_3CN$···$CO_2$ [a] | 16.2 |
| HCN···$CO_2$ [10] | 17.4 |
| HCCCN···$CO_2$ [11] | 10.0 |
| $NH_3$···$CO_2$ [9] | 22.7 |
| $N_2$···$CO_2$ [8] | 19.5 |
| Pyridine···$CO_2$ [12] | 9.0 |

[a] this work

**Table 4.12.** The bending angle (θ) for various complexes of $CH_3CN$.

| Complex | θ (°) |
|---|---|
| $CH_3CN\cdots HCl$ [33] | 7.0 |
| $CH_3CN\cdots HCN$ [34] | 13.0 |
| $CH_3CN\cdots HCCH$ [35] | 12.0 |
| $CH_3CN\cdots H_2O$ [32] | 15.4 |
| $CH_3CN\cdots BF_3$ [36] | 12.4 |
| $CH_3CN\cdots F_2$ [37] | 13.18 |

The T-shaped complexes of nitrogen containing molecules with $CO_2$ are bound by an N···C tetrel bond involving a π-hole. Recent theoretical investigations show that π-hole tetrel bonds are stronger than σ-hole bonds[38]. The linear and L-shaped structures of $CH_3CN\cdots CO_2$ complex show a tetrel bonding interaction, where the electron density is donated to the σ-hole. The binding energies seem to suggest that the π-hole tetrel bond in the T-shaped structure is stronger than the σ-hole interactions in the linear and L-shaped structures. However, these interactions do not involve the same donor/acceptor groups and therefore, the strength of these two different tetrel bonding interactions cannot be compared.

## 4.8. Conclusions

We investigated the rotational spectra of the $CH_3CN\cdots CO_2$ dimer using helium as a carrier gas. We observe two structures that are very close in energy: a π-stacked structure and a T-shaped structure. The assignments for both these structures are confirmed by the rotational spectra of the isotopologues. The absence of K=1 lines for the m=0 state of the T-shaped structure proves its $C_{2v}$ symmetry. Bader's Atoms in Molecules analysis for these two structures show that the π-stacked structure is bound by a weak C-H···O hydrogen bond and an interaction between the oxygen end of $CO_2$ and the cyano carbon atom of $CH_3CN$ while the T-shaped structure is stabilized by an N···C tetrel bonded interaction, where the nitrogen of $CH_3CN$ interacts with the π-hole over the carbon atom of $CO_2$.

## 4.9. References


(1) Mani, D.; Arunan, E. The X–C···Y (X = O/F, Y = O/S/F/Cl/Br/N/P) 'Carbon Bond' and Hydrophobic Interactions. *Phys. Chem. Chem. Phys.* **2013**, *15*, 14377–14383.

(2) Bauzá, A.; Mooibroek, T. J.; Frontera, A. Tetrel-Bonding Interaction: Rediscovered Supramolecular Force? *Angew. Chem. Int. Ed.* **2013**, *52*, 12317–12321.

(3) Legon, A. C. Tetrel, Pnictogen and Chalcogen Bonds Identified in the Gas Phase before They Had Names: A Systematic Look at Non-Covalent Interactions. *Phys. Chem. Chem. Phys.* **2017**, *19*, 14884–14896.

(4) Gnanasekar, S. P.; Arunan, E. Molecular Beam and Spectroscopic Techniques: Towards Fundamental Understanding of Intermolecular Interactions/Bonds. In *Intermolecular Interactions in Crystals: Fundamentals of Crystal Engineering*; Novoa, J. J., Ed.;Royal Society of Chemistry, **2017**.

(5) Ye, Y.; Zhang, H.; Chen, L.; Chen, S.; Lin, Q.; Wei, F.; Zhang, Z.; Xiang, S. Metal–Organic Framework with Rich Accessible Nitrogen Sites for Highly Efficient $CO_2$ Capture and Separation. *Inorg. Chem.* **2019**, *58*, 7754–7759.

(6) Phan, A.; Doonan, C. J.; Uribe-Romo, F. J.; Knobler, C. B.; O'Keeffe, M.; Yaghi, O. M. Synthesis, Structure, and Carbon Dioxide Capture Properties of Zeolitic Imidazolate Frameworks. *Acc. Chem. Res.* **2010**, *43*, 58–67.

(7) Kou, J.; Sun, L.-B. Nitrogen-Doped Porous Carbons Derived from Carbonization of a Nitrogen-Containing Polymer: Efficient Adsorbents for Selective $CO_2$ Capture. *Ind. Eng. Chem. Res.* **2016**, *55*, 10916–10925.

(8) Frohman, D. J.; Contreras, E. S.; Firestone, R. S.; Novick, S. E.; Klemperer, W. Microwave Spectra, Structure, and Dynamics of the Weakly Bound Complex, $N_2$-$CO_2$. *J. Chem. Phys.* **2010**, *133*, 244303-1-244303-6.

(9) Fraser, G. T.; Leopold, K. R.; Klemperer, W. The Rotational Spectrum, Internal Rotation, and Structure of $NH_3$ –$CO_2$. *J. Chem. Phys.* **1984**, *81*, 2577–2584.

(10) Leopold, K. R.; Fraser, G. T.; Klemperer, W. Rotational Spectrum and Structure of the Complex HCN-$CO_2$. *J. Chem. Phys.* **1984**, *80*, 1039–1046.

(11) Kang, L.; Davis, P.; Dorell, I.; Li, K.; Oncer, O.; Wang, L.; Novick, S. E.; Kukolich, S. G. Rotational Spectrum and Structure of the T-Shaped Cyanoacetylene Carbon Dioxide Complex, HCCCN···$CO_2$. *J. Mol. Spectrosc.* **2017**, *342*, 62–72.

(12) Doran, J. L.; Hon, B.; Leopold, K. R. Rotational Spectrum and Structure of the Pyridine–$CO_2$ van Der Waals Complex. *J. Mol. Struct.* **2012**, *1019*, 191–195.

(13) Klots, T. D.; Ruoff, R. S.; Gutowsky, H. S. Rotational Spectrum and Structure of the Linear $CO_2$–HCN Dimer: Dependence of Isomer Formation on Carrier Gas. *J. Chem. Phys.* **1989**, *90*, 4216–4221.

(14) Williams, H. L.; Rice, B. M.; Chabalowski, C. F. Investigation of the $CH_3CN-CO_2$ Potential Energy Surface Using Symmetry-Adapted Perturbation Theory. *J. Phys. Chem. A* **1998**, *102*, 6981–6992.

(15) Arunan, E.; Tiwari, A. P.; Mandal, P. K.; Mathias, P. C. Pulsed Nozzle Fourier Transform Microwave Spectrometer: Ideal to Define Hydrogen Bond Radius. *Curr. Sci.* **2002**, *82*, 533–540.

(16) Boys, S. F.; Bernardi, F. de. The Calculation of Small Molecular Interactions by the Differences of Separate Total Energies. Some Procedures with Reduced Errors. *Mol. Phys.* **1970**, *19*, 553–566.

(17) Frisch, M. J.; Trucks, G. W.; Schlegel, H. B.; Scuseria, G. E.; Robb, M. A.; Cheeseman, J. R.; Scalmani, G.; Barone, V.; Mennucci, B.; Petersson, G. A.; et al. *Gaussian 09,* Revision D. 01; Gaussian Inc: Wallingford, CT, **2009**.

(18) JPL Molecular Spectroscopy https://spec.jpl.nasa.gov/ (accessed Aug 26, 2020).

(19) Pickett, H. M. The Fitting and Prediction of Vibration-Rotation Spectra with Spin Interactions. *J. Mol. Spectrosc.* **1991**, *148*, 371–377.

(20) Asymmetric Rotor Programs http://www.ifpan.edu.pl/~kisiel/asym/asym.htm#crib (accessed Aug 26, 2020).

(21) Kisiel, Z.; Białkowska-Jaworska, E. Sextic Centrifugal Distortion in Fluorobenzene and Phenylacetylene from Cm-Wave Rotational Spectroscopy. *J. Mol. Spectrosc.* **2019**, *359*, 16–21.

(22) Keith, T. A. *AIMAll,* Version 16.05.18; TK Gristmill Software: Overland Park, KS, (aim.tkgristmill.com), **2016**.

(23) Gordy, W.; Cook, R. L. *Microwave Molecular Spectra*; Wiley-Interscience Pub., **1984**.

(24) Kraitchman, J. Determination of Molecular Structure from Microwave Spectroscopic Data. *Am. J. Phys.* **1953**, *21*, 17–24.

(25) Koch, U.; Popelier, P. L. Characterization of C-H-O Hydrogen Bonds on the Basis of the Charge Density. *J. Phys. Chem.* **1995**, *99*, 9747–9754.

(26) Amezaga, N. J. M.; Pamies, S. C.; Peruchena, N. M.; Sosa, G. L. Halogen Bonding: A Study Based on the Electronic Charge Density. *J. Phys. Chem. A* **2010**, *114*, 552–562.

(27) Leung, H. O. The Rotational Spectrum and Nuclear Quadrupole Hyperfine Structure of $CO_2$–$N_2O$. *J. Chem. Phys.* **1998**, *108*, 3955–3961.

(28) Marshall, M. D.; Leung, H. O. The Molecular Structure of $CO_2$-$N_2O$. *J. Mol. Spectrosc.* **1999**, *196*, 149–153.

(29) Millen, D. J. Determination of Stretching Force Constants of Weakly Bound Dimers from Centrifugal Distortion Constants. *Can. J. Chem.* **1985**, *63*, 1477–1479.

(30) Aldrich, P. D.; Kukolich, S. G.; Campbell, E. J. The Structure and Molecular Properties of the Acetylene–HCN Complex as Determined from the Rotational Spectra. *J. Chem. Phys.* **1983**, *78*, 3521–3530.

(31) Ford, R. S.; Suenram, R. D.; Fraser, G. T.; Lovas, F. J.; Leopold, K. R. Rotational Spectrum and Structure of the Complex Ar–$CH_3CN$. *J. Chem. Phys.* **1991**, *94*, 5306–5312.

(32) Lovas, F. J.; Sobhanadri, J. Microwave Rotational Spectral Study of $CH_3CN$–$H_2O$ and Ar–$CH_3CN$. *J. Mol. Spectrosc.* **2015**, *307*, 59–64.

(33) Legon, A. C.; Millen, D. J.; North, H. M. Rotational Spectrum of the Hydrogen-Bonded Dimer Acetonitrile···hydrogen Chloride. *J. Phys. Chem.* **1987**, *91*, 5210–5213.

(34) Howard, N. W.; Legon, A. C. Rotational Spectrum and Properties of the Hydrogen-Bonded Dimer $CH_3CN$···HCN. *J. Chem. Soc. Faraday Trans. 2* **1987**, *83*, 991–999.

(35) Howard, N. W.; Legon, A. C. Pulsed-nozzle, Fourier-transform Microwave Spectroscopy of the Methyl Cyanide–Acetylene Dimer. *J. Chem. Phys.* **1986**, *85*, 6898–6904.

(36) Dvorak, M. A.; Ford, R. S.; Suenram, R. D.; Lovas, F. J.; Leopold, K. R. Van Der Waals vs. Covalent Bonding: Microwave Characterization of a Structurally Intermediate Case. *J. Am. Chem. Soc.* **1992**, *114*, 108–115.

(37) Cotti, G.; Cooke, S. A.; Evans, C. M.; Holloway, J. H.; Legon, A. C. A Complex of Molecular Fluorine with an Organic Compound Detected in the Gas Phase: The Rotational Spectrum of $CH_3CN$···$F_2$. *Chem. Phys. Lett.* **1996**, *260*, 388–394.

(38) Zhang, J.; Hu, Q.; Li, Q.; Scheiner, S.; Liu, S. Comparison of σ-Hole and π-Hole Tetrel Bonds in Complexes of Borazine with $TH_3F$ and $F_2TO$/$H_2TO$ (T = C, Si, Ge). *Int. J. Quantum Chem.* **2019**, *119*, e25910.

## 4.10. Supplementary Information

**Table S4.1.** Cartesian coordinates for the π-stacked structure of the $CH_3CN\cdots CO_2$ complex calculated at MP2/aug-cc-pVDZ.

| atom | x | y | z |
|---|---|---|---|
| **C** | 2.383307000 | -0.639419000 | 0.000051000 |
| **H** | 1.741053000 | -1.531146000 | -0.000059000 |
| **H** | 3.020303000 | -0.648205000 | -0.895458000 |
| **H** | 3.020153000 | -0.648319000 | 0.895665000 |
| **C** | 1.537554000 | 0.562822000 | 0.000057000 |
| **N** | 0.839938000 | 1.521729000 | 0.000062000 |
| **C** | -1.686326000 | -0.329254000 | -0.000056000 |
| **O** | -0.955153000 | -1.258534000 | -0.000061000 |
| **O** | -2.428383000 | 0.584867000 | -0.000051000 |

**Table S4.2.** Cartesian coordinates for the T-shaped structure of the $CH_3CN\cdots CO_2$ complex calculated at MP2/aug-cc-pVDZ.

| atom | x | y | z |
|---|---|---|---|
| **C** | -3.396969000 | -0.002923000 | -0.000182000 |
| **H** | -3.771157000 | 0.424176000 | 0.940769000 |
| **H** | -3.771649000 | 0.596291000 | -0.841829000 |
| **H** | -3.764431000 | -1.033881000 | -0.099544000 |
| **C** | -1.926579000 | 0.003805000 | 0.000096000 |
| **N** | -0.742008000 | 0.009536000 | 0.000344000 |
| **C** | 2.188798000 | -0.002595000 | -0.000051000 |
| **O** | 2.200521000 | -1.182438000 | -0.000060000 |
| **O** | 2.213203000 | 1.177055000 | -0.000063000 |

**Table S4.3.** Cartesian coordinates for the linear structure of the $CH_3CN\cdots CO_2$ complex calculated at MP2/aug-cc-pVDZ.

| atom | x | y | z |
|---|---|---|---|
| **C** | -1.548063000 | 0.002218000 | -0.006325000 |
| **H** | -1.173722000 | 0.902515000 | -0.512421000 |
| **H** | -1.173004000 | -0.884455000 | -0.535341000 |
| **H** | -1.166142000 | -0.010948000 | 1.023555000 |
| **C** | -3.018895000 | 0.001709000 | 0.000366000 |
| **N** | -4.204398000 | 0.001376000 | 0.005732000 |
| **C** | 2.744054000 | -0.001828000 | 0.000907000 |
| **O** | 3.922622000 | 0.009378000 | 0.002296000 |
| **O** | 1.562513000 | -0.013045000 | -0.000496000 |

**Table S4.4.** Cartesian coordinates for the L-shaped structure of the $CH_3CN\cdots CO_2$ complex calculated at MP2/aug-cc-pVDZ.

| atom | x | y | z |
|---|---|---|---|
| **C** | 1.110380000 | -0.204599000 | -0.000057000 |
| **H** | 0.579958000 | 0.758841000 | 0.000523000 |
| **H** | 0.824080000 | -0.777207000 | 0.893303000 |
| **H** | 0.824024000 | -0.776169000 | -0.894065000 |
| **C** | 2.561929000 | 0.032177000 | 0.000016000 |
| **N** | 3.731933000 | 0.222923000 | 0.000035000 |
| **C** | -2.293829000 | 0.011906000 | 0.000005000 |
| **O** | -2.101190000 | -1.152988000 | 0.000023000 |
| **O** | -2.476619000 | 1.177634000 | 0.000002000 |

**Table S4.5.** Harmonic frequencies (in $cm^{-1}$) of the normal modes of vibration for the $CH_3CN\cdots CO_2$ complex calculated at MP2/aug-cc-pVDZ. IR intensity in km/mol.

| **π-stacked** | | **T-shaped** | |
|---|---|---|---|
| **frequency** | **IR intensity** | **frequency** | **IR intensity** |
| 28.0 | 4.5 | 6.3 | 0.0 |
| 48.3 | 0.3 | 16.9 | 6.8 |
| 64.9 | 1.3 | 28.2 | 8.6 |
| 67.8 | 12.8 | 83.3 | 0.2 |
| 103.6 | 0.1 | 108.9 | 0.8 |
| 353.7 | 0.4 | 353.6 | 0.3 |
| 354.3 | 0.8 | 355.3 | 0.2 |
| 646.3 | 31.3 | 643.4 | 42.7 |
| 654.8 | 19.2 | 658.3 | 19.8 |
| 930.6 | 1.7 | 933.5 | 1.7 |
| 1048.1 | 2.4 | 1048.4 | 1.1 |
| 1051.2 | 0.7 | 1048.5 | 1.1 |
| 1307.8 | 0.7 | 1308.3 | 0.2 |
| 1387.3 | 3.1 | 1391.0 | 0.4 |
| 1464.9 | 7.8 | 1465.8 | 9.6 |
| 1467.6 | 8.4 | 1465.9 | 9.7 |
| 2178.2 | 0.2 | 2186.2 | 0.0 |
| 2382.3 | 517.1 | 2382.2 | 530.7 |
| 3087.8 | 3.5 | 3089.3 | 3.1 |
| 3188. 9 | 0.6 | 3190.2 | 0.4 |
| 3190.6 | 0.0 | 3190.4 | 0.4 |

**Table S4.6.** Harmonic frequencies (in $cm^{-1}$) of the normal modes of vibration for the $CH_3CN\cdots CO_2$ complex calculated at MP2/aug-cc-pVDZ. IR intensity in km/mol.

| **Linear** | | **L-shaped** | |
|---|---|---|---|
| **frequency** | **IR intensity** | **frequency** | **IR intensity** |
| 21.8 | 3.9 | 12.4 | 0.3 |
| 21.9 | 3.9 | 24.6 | 5.9 |
| 44.8 | 6.4 | 38.4 | 10.0 |
| 45.1 | 6.4 | 44.8 | 3.7 |
| 62.2 | 0.1 | 60.6 | 0.0 |
| 357.9 | 0.3 | 355.4 | 0.3 |
| 358.0 | 0.3 | 357.8 | 0.2 |
| 654.8 | 21.3 | 652.1 | 18.9 |
| 654.8 | 21.3 | 652.9 | 29.9 |
| 931.2 | 2.8 | 932.9 | 1.4 |
| 1045.2 | 1.2 | 1047.0 | 1.3 |
| 1045.3 | 1.2 | 1057.7 | 2.2 |
| 1306.3 | 0.2 | 1304.9 | 0.1 |
| 1384.9 | 3.4 | 1391.7 | 1.8 |
| 1462.6 | 8.1 | 1464.9 | 5.9 |
| 1462.8 | 8.1 | 1467.6 | 6.4 |
| 2178.7 | 0.0 | 2179.1 | 0.0 |
| 2379.5 | 668.4 | 2378.2 | 502.2 |
| 3093.5 | 5.1 | 3083.4 | 5.7 |
| 3194.3 | 0.6 | 3182.6 | 0.4 |
| 3194.6 | 0.6 | 3187.7 | 0.4 |

# CHAPTER 5

# Inter/intramolecular bonds in $TH_5^+$ (T = C/Si/Ge): $H_2$ as tetrel bond acceptor and classification of the 3c-2e bonds

(most of this chapter has been published in, *J. Phys. Chem. A*, **2019**, *123,* 1168-1178. and, *Aust. J. Chem.,* **2020**, *73,* 767-774)

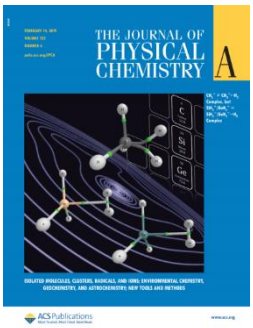

CHAPTER 5

# INTER/INTRAMOLECULAR BONDS IN $TH_5^+$ (T = C/Si/Ge): $H_2$ AS TETREL BOND ACCEPTOR AND CLASSIFICATION OF THE 3c-2e BONDS

## 5.1. Introduction

The structure of a molecule provides valuable insights into its properties. $CH_5^+$ though, has gained notoriety for eluding a formal definition of its structure. Since its discovery in 1952 in mass spectrometric experiments[1], attempts at assigning this molecule with a definite structure have proved to be futile. This is because $CH_5^+$ is highly fluxional with theoretical investigations revealing that the potential energy surface (PES) is quite shallow[2,3]. The PES of $CH_5^+$ is characterized by 120 equivalent minima which are easily accessible via low lying saddle point structures[4–6]. The difference in energy between these saddle point structures and the $C_s$ symmetry minima is small and decreases with increasing levels of theory[7,8]. Though there is a consensus that the molecule is highly fluxional and the ground state minimum has $C_s$ symmetry, results regarding the $C_s$ symmetry minimum veer between a structure having a pentacoordinated carbon center with no interaction between the H atoms[9,10] and a structure where $CH_5^+$ is made up of a methyl cation ($CH_3^+$) complexed with $H_2$.[4,11–13] The crux of the matter then is, whether $H_2$ retains its identity in the molecule or not.

The nature of bonding in $CH_5^+$ can also be studied by examining the possible non-covalent interactions that could lead to its formation. It is known that the hydrogen bonded structures are intermediates in proton transfer reactions. The hydronium ion ($H_3O^+$) and ammonium ion ($NH_4^+$) are formed by the protonation of $H_2O$ and $NH_3$, respectively. These are often mediated by a hydrogen bonded complex such as $H_2O\cdots HX$ or $H_3N\cdots HX$. Rotational spectroscopic investigations on several $CH_4\cdots HX$ (X= F, Cl, CN, and OH) dimers[14–16] reveal that the global minimum structure is the one where HX is the hydrogen bond donor and $CH_4$ is the acceptor. The H atom of HX forms a hydrogen bond with the carbon center through the tetrahedral face of $CH_4$. It has been pointed out[17] that this hydrogen bonded structure having a 'pentacoordinate carbon' could be a precursor to the formation of $CH_5^+$. The three O-H bond lengths in $H_3O^+$ are equal and the same is true for the four N-H bonds in $NH_4^+$. If one were to guess the geometry of $CH_5^+$, without any prior knowledge, a trigonal bipyramidal would be a reasonable choice. Even in this structure, one would expect two long C-H bonds on the opposite directions and three short C-H bonds in a plane, such as in $Fe(CO)_5$ which is also a fluxional molecule. However, the established structure for $CH_5^+$ has $C_s$ symmetry with three short C-H bonds on one side (not in the same plane) and two long C-H bonds in the opposite side. It appears as though the $H_2$ moiety is separated from the $CH_3^+$ tripod. This arrangement then is reminiscent of a 'carbon (tetrel) bond'[18,19].

That sigma bonding electrons of $H_2$ can act as an acceptor of an intermolecular bond has been recognized and $FX\cdots H_2$ (X = H/Li/Cl) complexes exhibiting hydrogen/lithium/halogen bonds have been discussed earlier[20]. Structures of complexes such as $H_2\cdots HF$[21] and $H_2\cdots OCS$[22]($H_2$ interacting with the C) are known experimentally where $H_2$ donates its σ electron density to the electron deficient H/C, respectively. Tetrel bonded complexes with π-electron donors[23] and radical species as single electron donors[24] have been reported. It appears that tetrel bonding with $H_2$ acceptor has not been discussed so far. If $CH_5^+$ were indeed $CH_3^+$ complexed with $H_2$, the positively charged central carbon can accept electron density from the sigma electrons of $H_2$ forming a tetrel bonded complex. If such is the case then, a normal mode analysis on $CH_5^+$ could reveal H-H vibration and the vibrational frequency would show a red-shift. Moreover, Atoms in Molecules (AIM) and Natural Bond Orbital (NBO) theoretical methods could yield evidence for the carbon/tetrel bond.

The infrared spectrum obtained by Oka and coworkers[9] was an important step towards solving the structure of $CH_5^+$. The spectrum is complicated, with nearly 900 lines that depend on $CH_5^+$. However, none of these spectral lines could be assigned. In subsequent years, efforts were made to decipher this spectrum by obtaining another extended spectrum[12], by computing the spectrum using quantum calculations,[5] and by obtaining the spectrum at low temperatures[25]. However, recent tentative assignments using combination differences by Asvany et al.[25] from the low temperature spectra and the calculated rotation-bending energy levels which were compared with this spectra[26] are the closest one has come to solving the structure. This study could not give any information about H-H vibration in $CH_5^+$.

Bader[27] opines that distinction must be made between molecular geometry and structure, as molecular geometry is a non-generic property of the molecule defined by a set of nuclear coordinates, whereas, structure is a generic property defined by the network of bonds between atoms in a molecule. He notes that "difficulties ascribed to the notion of molecular structure are the inabilities to assign a single geometrical structure…to a molecule in a 'floppy' state wherein the nuclear excursions cover a wide range of geometrical parameters". Bader proposed the use of the charge density topology of a molecule, to determine linkages of the atoms present. This is used to assign a molecular graph which defines the molecular structure. Therefore, the structure of $CH_5^+$ could be defined by performing a topological analysis of the electron density. Okulik et al. have in fact carried out a topological analysis of the electron density on the $CH_5^+$ molecule and concluded that it is a pentacoordinated carbocation with no interaction present between the H atoms[10] thereby providing evidence against the structure of $CH_5^+$ being a complex between $CH_3^+$ and $H_2$. Earlier studies by Marx and Savin, subjected $CH_5^+$ to a similar analysis, using the electron localization function (ELF), which is a local measure of the Pauli repulsion[28]. This helps locate regions having a pair of electrons. Their findings lead to four basins, three for the 2c-2e C-H bonds and one for the 3c-2e bond involving the $H_2$ moiety. This does not answer the question about whether or not there is an H-H bond. Asvany et al. depict the structure of $CH_5^+$ with a 3c-2e bond with the H atoms of the $H_2$ moiety connected[25], whereas the molecular graph for $CH_5^+$ clearly shows no interaction between the H atoms (Figure 5.1). The question we then ask is, what does the molecular graph for the congeners of $CH_5^+$, $SiH_5^+$ and $GeH_5^+$ look like? Would this comparison help in choosing the right structure for $CH_5^+$?

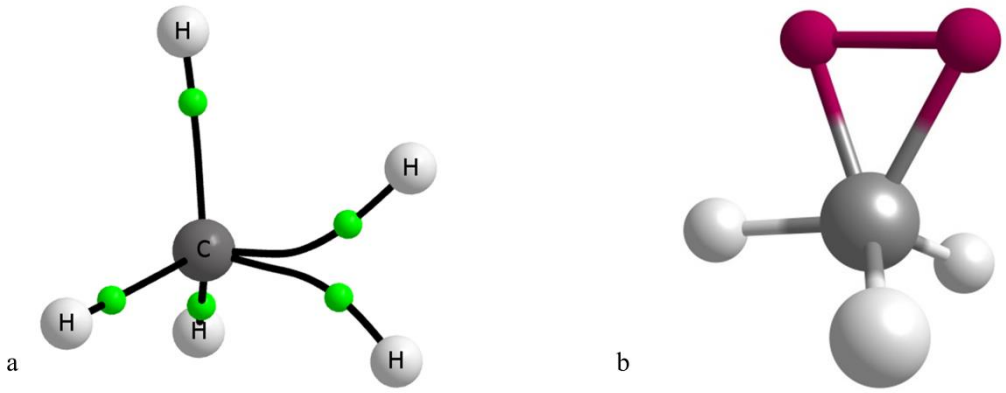


**Figure 5.1.** (a) Molecular graph for $CH_5^+$; (b) $CH_5^+$as depicted in Reference 25.

The 2c-2e bonds are traditionally represented by a solid line connecting the two atoms. How are 3c-2e bonds represented? In his article in the *Journal of Chemical Education*, Jensen[29] uses Y-shaped polyethylene tubing to represent 3c-2e bonds in molecular modelling kits. DeKock and Bosma's [30] article in the same journal notes that these bonds are usually represented by curved lines and suggest that an appropriate way to symbolize 3c-2e bonds would be a 'Y' notation. This 'Y' notation to denote 3c-2e bonds implies that the bridging atom interacts with the other two atoms and makes no mention of the interaction between the terminal atoms in the three atom bridge.

It has been reported that 3c-2e bonds could be of two types: 'open' or 'closed'. It is considered to be 'open' if there is no interaction between the terminal atoms in the bridge, and 'closed' if there is an interaction between them[31]. DeKock and Bosma[30] have classified the 3c-2e bonds into an 'unsupported' and a 'supported' type. The 'unsupported' types are usually 'open' structures; linear or bent and with no interaction with the other bonds. The 'supported' types are 3c-2e bonds where these bonds are entangled with other bonds. The 3c-2e bonds have been categorized based on the number of atoms providing the two electrons in the 3c-2e bond, as an extension of the Covalent Bond Classification. Three-centre two-electron bonds of Class I are those where two atoms contribute one electron each, and Class II are those where a single atom provides the pair of electrons[32,33].

Jemmis et al.[34] have shown that the 3c-2e bonds in $CH_3M_2^+$ systems could either be bent or linear, and are model systems to understand the stereochemistry of aliphatic electrophilic substitution reactions. The transition states that resemble the bent 3c-2e

bond show retention of configuration and those that are linear show inversion of configuration. It is evident that the properties of the 3c-2e bonds differ based on their arrangements. One realises that three points could be linked in a number of ways in space. The possible arrangements are V, L, Δ, Y, T, and I (linear). In this Chapter we also explore the possibility of classifying the 3c-2e bonds into these arrangements.

Considering the difficulty in defining a structure for $CH_5^+$ it is interesting to examine the structures of $SiH_5^+$ and $GeH_5^+$. Are they similar, considering they belong to the same group or different? $SiH_5^+$ was first observed in ionized silane-methane mixtures using mass spectrometry by Beggs and Lampe[35]. The optimized geometries and the heats of hydrogenation for $SiH_3^+$ led Schleyer et al. to surmise that $SiH_5^+$ is a weakly bound complex of $SiH_3^+$ and $H_2$[36]. The rovibrational spectrum of $SiH_5^+$ obtained by Boo and Lee provides evidence for the $H_2$ moiety rotating freely with respect to the $SiH_3^+$ frame[37]. $GeH_5^+$ on the other hand was difficult to obtain and was first observed in ion beam scattering experiments by Senzer and coworkers[38]. Kohda-Sudoh et al. described the shape of $GeH_5^+$ to be a loose complex between the germyl cation ($GeH_3^+$) and $H_2$[39]. The comprehensive study of all the structures of the $GeH_5^+$ by Schreiner et al. concluded that the geometry having $C_s$ symmetry was the global minimum on the potential energy surface[40]. It is evident that the ground state minimum structure for the $TH_5^+$ molecule has $C_s$ symmetry.

Theoretical and spectroscopic results for $SiH_5^+$ and $GeH_5^+$ suggest that these are weakly bound complexes of the $TH_3^+$ (T= Si, and Ge) cation with $H_2$. The topological analysis of the charge density would then allow us to observe a tetrel bonded interaction between the $TH_3^+$ cation and the $H_2$ moiety. This has not been carried out so far to the best of our knowledge. In this Chapter we compare the electron density topologies of $SiH_5^+$ and $GeH_5^+$ with $CH_5^+$and investigate if there is any evidence for a tetrel bond. Natural bond orbital theory and normal mode analysis on these structures have been carried out as well. This has helped in arriving at unambiguous conclusions about the structure of $CH_5^+$. We also investigate a set of molecules that contain 3c-2e bonds using Natural Bond Orbital (NBO), Natural Resonance Theory (NRT), and Atoms in Molecules (AIM) analysis to categorize the 3c-2e bonds formed in these and similar molecules based on their connectivity.

## 5.2. Computational methods

The geometries of the $TH_5^+$ species (T = C, Si, and Ge) were optimized at the MP2 level of theory with the aug-cc-pVTZ basis set. The geometry of the molecules investigated for the 3c-2e bonds was optimized at both MP2 and B3LYP levels of theory using the 6-311++G(d,p) and aug-cc-pVTZ basis sets. The results are consistent at all four levels of theory and we report only the results obtained from calculations at MP2/6-311++G(d,p) and B3LYP/ aug-cc-pVTZ for these molecules. Frequency calculations were also performed to ascertain the nature of the optimized geometries. The absence of an imaginary frequency confirms a structure to be a minimum and its presence indicates that the structure is a saddle point on the potential energy surface. The harmonic frequencies were also calculated for the molecules at the MP2 level as well as using the B3LYP functional. Relaxed potential energy scans for the $TH_5^+$ were carried out by varying the distance between the $TH_3^+$ moiety and $H_2$. This was computed using the keyword opt=modredundant. This allows all the parameters defining the molecule to alter during a scan. All calculations were performed using the *Gaussian 09* suite of programs[41].

To establish the nature of bonding, the topological analysis of the electron density for the optimized structures of the $TH_5^+$ was done using the *AIMAll* software[42]. It was also analyzed at select points of the potential energy scans to study the appearance or disappearance of various weak interactions and their role in the formation of the $TH_5^+$ species. The wavefunction required for this calculation was obtained from the *Gaussian 09* computation at MP2/aug-cc-pVTZ level. The AIM calculations for the molecules with 3c-2e bonds were done using wavefunctions obtained at the MP2/6-311++G(d,p) level of theory. The molecular graphs obtained for the molecules containing the 3c-2e bonds helped to understand the connectivity between atoms in a 3c-2e bond. The green, red, blue, and pink dots in the molecular graph represent a bond critical point (BCP), ring critical point (RCP), cage critical point (CCP), and a non-nuclear attractor (NNA), respectively.

To understand the nature of orbital interaction and confirm the presence of a 3c-2e bond a Natural Bond Orbital (NBO) analysis was carried out. This was done using *NBO 6.0*[43] as implemented in *Gaussian 09*. The Natural Resonance Theory (NRT) calculations were carried out using the *.47 file* on the standalone NBO program *gennbo*.

## 5.3. $TH_5^+$ (T= C, Si, and Ge)

### 5.3.1. Optimized geometries

**$CH_5^+$**

Methane distorts to accommodate the presence of the added proton to form $CH_5^+$. The $CH_5^+$ molecule was optimized at MP2/aug-cc-pVTZ. The three lowest energy stationary structures obtained are shown in Figure 5.2. The energies we obtained at MP2/aug-cc-pVTZ agree well with those obtained by Schreiner et al. using high level *ab initio* theory (CCSD(T)/ TZ2P+f)[7]. We repeated the calculations at the CCSD(T) level with the same basis, aug-cc-pVTZ, and these results are in close agreement with the results by Schreiner et al. The structure with $C_s$(I) symmetry is a minimum on the potential energy surface which is confirmed by the vibrational frequency analysis. The $CH_3$ unit of the molecule is more pyramidal than planar. Thus, $CH_5^+$ bears resemblance to a protonated methane structure rather than to a planar methyl cation ($CH_3^+$) interacting with an elongated $H_2$ molecule.

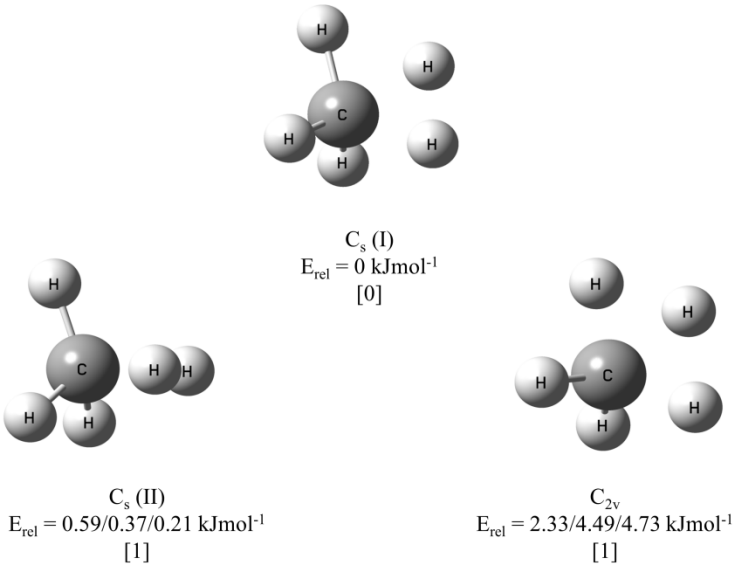


**Figure 5.2.** Optimized geometries and relative energies of the three lowest energy stationary structures of $CH_5^+$. First entry calculated at MP2/aug-cc-pVTZ, second at CCSD(T)/aug-cc-pVTZ (single point calculation on optimized geometries obtained at MP2/aug-cc-pVTZ), and third at CCSD(T)/TZ2P+f (obtained from Ref.7). Number in brackets denotes number of imaginary frequencies.

A quantitative evaluation of the bond lengths reveals the presence of three short C-H bonds comprising the $CH_3$ tripod and two long C-H bonds which make up the $H_2$ moiety. These two C-H bonds are about 0.1 Å longer than the three other C-H bonds.

Therefore, it appears as though the H-atoms involved in the long C-H bonds are a separate entity with respect to the $CH_3$ tripod. One of the three short C-H bonds is slightly longer (marked b in Figure 5.3) and it is with respect to this unique bond that the $H_2$ unit is eclipsed in the $C_s$(I) geometry. The distance between the H atoms of the two long C-H bonds is 0.975 Å. When compared to the H-H distance in free $H_2$, which is 0.737 Å, it seems that this bond is quite elongated with possibly no interaction between the H atoms. The C-H and H-H bond lengths are summarized in Tables 5.1 and 5.2.

The second stationary structure is a saddle point on the potential energy surface, confirmed by the presence of an imaginary frequency. This structure has $C_s$(II) symmetry with the $H_2$ moiety staggered with respect to the unique C-H bond (b). The $C_s$(II) saddle point is the transition state for the rotation of the $H_2$ unit about the pseudo $C_3$ axis in the methanium ion as noted in earlier works[4–8]. The energies computed at MP2/aug-cc-pVTZ level indicate that this structure is only 0.59 $kJmol^{-1}$ higher in energy with respect to the minimum $C_s$(I) structure. Therefore, the rotation of the $H_2$ moiety about the pseudo $C_3$ axis would be facile.

The third structure is also a saddle point on the potential energy surface. Three of the C-H bonds in this structure are in a plane and equidistant from each other. This $C_{2v}$ symmetry structure is the transition state on the reaction coordinate where the H atom flips between the $H_2$ moiety and the $CH_3$ unit. This structure is nearly 4.7 $kJmol^{-1}$ higher in energy than the minimum $C_s$(I) structure. Thus, hydrogen scrambling via these two saddle point structures is quite facile. $CH_5^+$ therefore, easily interconverts between its 120 equivalent minima, supporting the established fact that it is a highly fluxional molecule.

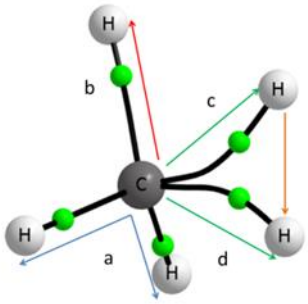


**Figure 5.3.** The different T-H bonds in $TH_5^+$.

**Table 5.1.** Bond lengths calculated for $TH_5^+$.

| System | a(Å) | b(Å) | c(Å) | d(Å) | H-H (Å) |
|---|---|---|---|---|---|
| $CH_5^{+a}$ | 1.085 | 1.107 | 1.184 | 1.182 | 0.975 |
| $CH_5^{+b}$ | 1.085 | 1.101 | 1.202 | 1.201 | 0.927 |
| $SiH_5^{+a}$ | 1.460 | 1.463 | 1.879 | 1.884 | 0.773 |
| $SiH_5^{+c}$ | 1.458 | 1.460 | 1.910 | 1.915 | 0.774 |
| $GeH_5^{+a}$ | 1.498 | 1.500 | 1.948 | 1.953 | 0.770 |
| $GeH_5^{+d}$ | 1.519 | 1.520 | 2.031 | 2.034 | 0.770 |

[a] calculated at MP2/aug-cc-pVTZ
[b] calculated at CCSD/TZ2P Ref. 7
[c] calculated at CCSD/TZ2P Ref.44
[d] calculated at CCSD/TZP+f Ref.40

**Table 5.2.** Bond lengths calculated for $TH_4$, $TH_3^+$ and $H_2$ at MP2/aug-cc-pVTZ.

| Molecule | T-H (Å) | Molecule | T-H (Å) | Molecule | H-H(Å) |
|---|---|---|---|---|---|
| $CH_4$ | 1.086 | $CH_3^+$ | 1.087 | | |
| $SiH_4$ | 1.479 | $SiH_3^+$ | 1.462 | $H_2$ | 0.737 |
| $GeH_4$ | 1.512 | $GeH_3^+$ | 1.501 | | |

### $SiH_5^+$ and $GeH_5^+$

The congeners of $CH_5^+$, $SiH_5^+$and $GeH_5^+$ were also optimized at MP2/aug-cc-pVTZ level. The optimized geometries of $TH_5^+$ (T= Si and Ge) resemble a planar $TH_3^+$ moiety complexed with an elongated $H_2$ unit. The $C_s$(I) structure has the $H_2$ unit eclipsed with the T-H bond (b) and is the minimum on the potential energy surface. The $C_s$(II) structure has the $H_2$ unit staggered with respect to the T-H bond (b). It is

energetically quite close to the $C_s$(I) structure and is a first order saddle point having one imaginary frequency. This $C_s$(II) symmetry saddle point is the transition state via which rotation of the $H_2$ moiety about the $TH_3^+$ frame occurs. However, in the case of $SiH_5^+$ and $GeH_5^+$ the $C_{2v}$ structure is energetically higher than the dissociation energy of the complex and thus complete hydrogen scrambling is not facile[44,40].

The $TH_3^+$ unit is nearly planar though the T-H bonds are not all equal. The tabulated bond distances (Tables 5.1 and 5.2) show that the T-H bonds in the $TH_5^+$ molecule are slightly distorted from those computed for $TH_3^+$. Comparing the H-H bond distances for the $H_2$ moiety in $TH_5^+$ with the free $H_2$ molecule, it seems that the $H_2$ unit in $TH_5^+$ is slightly elongated. The H-H distance in $SiH_5^+$ is 0.773 Å and in $GeH_5^+$ it is 0.770 Å. These are only slightly longer than the H-H distance in the free $H_2$ molecule which is 0.737 Å. Therefore, the $H_2$ moiety in $TH_5^+$ seems to retain its identity in the molecule. For comparison, in $CH_5^+$, this distance is 0.975 Å.

### 5.3.2. Atoms in Molecules (AIM) analysis

Bader's Atoms in Molecules (AIM) theory examines the topology of the electron density to understand the nature of bonding in molecules[26]. The interaction between two atoms is confirmed by the presence of a bond critical point (BCP). The properties of the electron density at the BCP provide further insights about the bond. These topological properties for the $TH_5^+$ (T= C, Si, and Ge) and $C_2H_7^+$ are tabulated in Tables 5.3 and 5.4. The molecular graphs obtained from the AIM analysis are shown in Figures 5.4 and 5.5.

**$CH_5^+$**

The molecular graphs for the three lowest lying stationary structures of $CH_5^+$ are shown in Figure 5.4. The $C_s$(I) symmetry minimum structure is characterized by the presence of the five bond critical points (BCPs) which connect each of the H atoms to the C center. The value of the electron density ($\varrho$) at the five BCPs ranges from 0.2174 to 0.2911 au and the Laplacian of electron density ($\nabla^2\varrho$) from -0.5017 to -1.2082 au. When $\nabla^2\varrho$ at the BCP is negative and the $\varrho$ is large in magnitude, these interactions are referred to as shared interactions, which is characteristic of a covalent bond. Therefore, $CH_5^+$ is pentacoordinated with five covalent C-H bonds. The most striking observation however, is the absence of a bond critical point between the H atoms of

the $H_2$ moiety. The two long C-H bonds that make up the $H_2$ moiety have very high ellipticity values (2.1739 and 1.3412) which suggests that these bonds are unstable. Ellipticity is defined as $[(\lambda_1/ \lambda_2) -1]$. It is a measure of the anisotropy of the curvature of electron density in the directions perpendicular to the bond path. It has been observed that bonds with high ellipticity are associated with structural changes; therefore, the bond can be considered to be unstable. It is quite evident that $CH_5^+$ cannot be considered as a weakly bound complex of $CH_3^+$ and $H_2$. These results agree with those obtained previously by Okulik et al. using the 6-311++G** basis set[10].

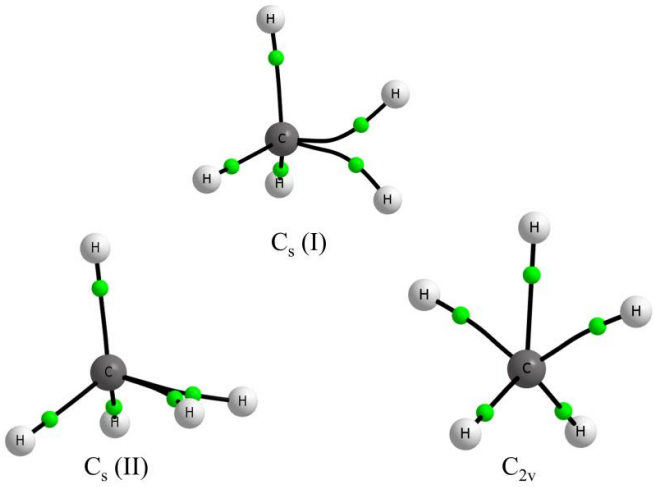


**Figure 5.4.** Molecular graphs for the three lowest energy stationary structures of $CH_5^+$calculated at MP2/aug-cc-pVTZ.

### $SiH_5^+$ and $GeH_5^+$

The molecular graphs for $SiH_5^+$ and $GeH_5^+$ are quite different from that of $CH_5^+$ (Figure 5.5). It is evident that the slightly elongated $H_2$ moiety retains its identity. A bond critical point (BCP) is present between the two H atoms. The large magnitude of $\varrho$ and the negative sign of $\nabla^2\varrho$ at the BCP (Table 5.4) indicate that a covalent bond is present between the two H atoms. The $\varrho$ value in $GeH_5^+$ is larger than in $SiH_5^+$ which correlates well with the computed $H_2$ bond lengths (Table 5.4).

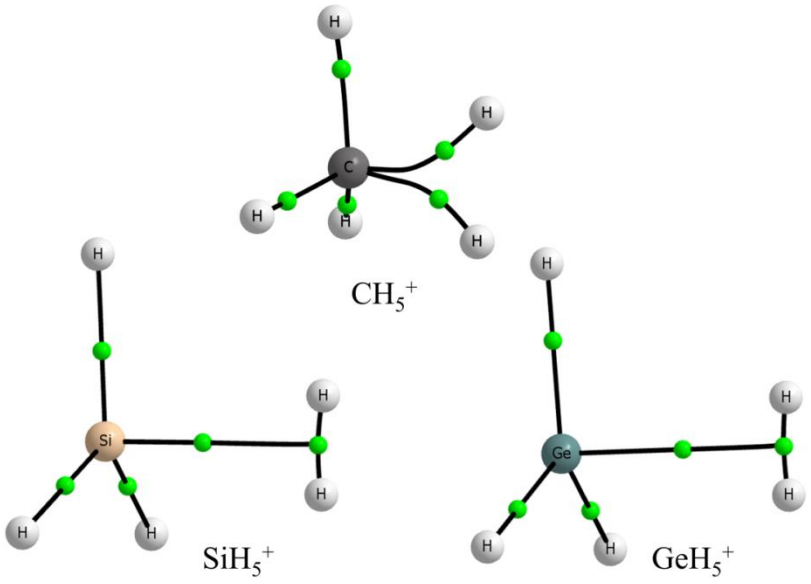


**Figure 5.5.** Molecular graphs for the $TH_5^+$ molecule calculated at MP2/aug-cc-pVTZ.

**Table 5.3.** Properties of the electron density at the BCP between the central atom (T) and the $H_2$ moiety.

| system | ϱ(au) | $\nabla^2\varrho$(au) | ellipticity | $\lvert\lambda_1\rvert / \lambda_3$ |
|---|---|---|---|---|
| $CH_5^+$ | 0.2174 | -0.5017 | 2.1739 | 2.4190 |
| | 0.2229 | -0.5586 | 1.3412 | 2.5094 |
| $SiH_5^+$ | 0.0465 | +0.1194 | 0.3878 | 0.2255 |
| $GeH_5^+$ | 0.0527 | +0.1267 | 0.3907 | 0.2643 |
| $C_2H_7^+$ | 0.2156 | -0.4653 | 32.2703 | 9.1543 |

**Table 5.4.** Properties of the electron density at the BCP between the H-H atoms of the $H_2$ moiety.

| system | ϱ(au) | $\nabla^2\varrho$(au) | ellipticity | $\lvert\lambda_1\rvert / \lambda_3$ |
|---|---|---|---|---|
| $SiH_5^+$ | 0.2506 | -1.0639 | 0.0753 | 1.4918 |
| $GeH_5^+$ | 0.2517 | -1.0745 | 0.0627 | 1.4722 |
| $C_2H_7^+$ | 0.2159 | -0.5173 | 6.7925 | 5.5024 |

The other prominent difference is the interaction between the planar cation and the $H_2$ moiety. The molecular graphs for $SiH_5^+$ and $GeH_5^+$ are best described as conflict structures. This is because the bond critical point between the two moieties connects the central T atom not with another atom but with the BCP between the two H atoms. This could be viewed as a bond between the σ-bond electrons of $H_2$ and the positive

central T atom. Low values of ρ at BCP and $\nabla^2\rho$ at BCP being positive indicates a closed-shell interaction. Such an interaction is usually found in noble gas repulsive states, ionic bonds, hydrogen bonds, and van der Waals molecules.

The BCPs and bond paths clearly indicate the presence of the silyl/germyl cation interacting with an $H_2$ moiety. This interaction is indicative of a tetrel bonded interaction. The ρ values for $SiH_5^+$(0.0465 au) and $GeH_5^+$(0.0527 au) are slightly higher than the range given by Koch and Popelier's criterion for a C-H···O hydrogen bond[45] (0.002-0.034 au). Clearly, the tetrel bonds in these cations are stronger than the strongest C-H···O hydrogen bond discussed in Koch and Popelier's work. The Laplacian on the other hand for $SiH_5^+$ and $GeH_5^+$ is 0.1194 and 0.1267, respectively. These values are within the range for the criterion proposed by Koch and Popelier (0.024-0.139). Sosa and coworkers have suggested that the $|\lambda_1|/\lambda_3$ ratio must be less than 1 for a closed-shell interaction[46]. This ratio for $SiH_5^+$ and $GeH_5^+$ satisfy this criterion. The ellipticity values for these BCPs are quite large which is indicative of an unstable bond between these two units.

Would the cations of a larger alkane reveal a tetrel bond? In order to address this question, AIM analysis for $C_2H_7^+$ was carried out. The result is shown in Figure 5.6. There is a BCP between the two H atoms in $C_2H_7^+$, though the bond path is curved. This BCP appears very close to another BCP, connecting the $H_2$ to the C atom. A look at the bond ellipticity value at both these BCPs indicates that they are highly unstable (32.27 and 6.79) and therefore the molecular graph for this structure is highly unstable. In any case, this result indicates that there could be a tetrel bond between C and $H_2$ in favorable cases.

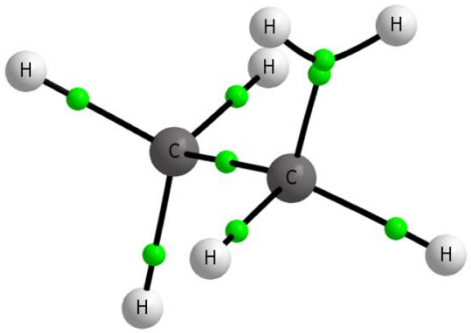


**Figure 5.6.** Molecular graph for $C_2H_7^+$.

### 5.3.3. Natural Bond Orbital (NBO) analysis

$TH_5^+$ (T= C, Si, and Ge) shows the presence of a 3c-2e H-T-H bond in the Natural Bond Orbital (NBO) analysis. In combination with the molecular graphs obtained from the AIM analysis, the 3c-2e bond in the case of $CH_5^+$ can be considered to be 'open' or 'V' type since there is no interaction between the two H atoms. Whereas in the case of $SiH_5^+$ and $GeH_5^+$ we can consider it to be a 'closed' or 'T' type 3c-2e interaction since there is an H-H bond. A comprehensive study of classifying 3c-2e bonds based on their connectivity is detailed in Section 5.4. A look at the nature of the orbitals reveals that the long C-H bonds in $CH_5^+$ use $sp^3$ orbitals from C and the equivalent bonds in $SiH_5^+$ and $GeH_5^+$ use an empty p orbital from the central atom which interacts with the $H_2$ unit. The charge analyses in both AIM and NBO reveal some interesting observations. The charge on the C atom in $CH_5^+$ is negative and the H atoms carry the positive charge. This therefore reinforces the idea that $CH_5^+$ is more like protonated methane than a $CH_3^+\cdots H_2$ complex. The charge analysis for $SiH_5^+$ and $GeH_5^+$ on the other hand reveals that the central T atom is positively charged and the hydrogen atoms are negatively charged, indicating that it is $TH_3^+$ and $H_2$. Table 5.5 reports the charges on the atoms obtained from NBO calculations.

**Table 5.5.** Charges on the atoms in $TH_5^+$ calculated at MP2/aug-cc-pVTZ.

| | **Natural** | **Mulliken** | **AIM** |
|---|---|---|---|
| **Ge** | 1.13784 | 0.91818 | 1.73715 |
| **H** | -0.10788 | -0.01234 | -0.27640 |
| **H** | -0.10719 | -0.01977 | -0.27620 |
| **H** | -0.10725 | -0.02035 | -0.27623 |
| **H*** | 0.09377 | -0.00146 | 0.04832 |
| **H*** | 0.09071 | 0.13574 | 0.04354 |
| | | | |
| **Si** | 1.21569 | 0.79104 | 2.89541 |
| **H** | -0.13911 | 0.04032 | -0.64711 |
| **H** | -0.14003 | 0.04325 | -0.64564 |
| **H** | -0.13928 | 0.03775 | -0.64721 |
| **H*** | 0.10404 | 0.05542 | 0.02767 |
| **H*** | 0.09868 | 0.03222 | 0.01726 |
| | | | |
| **C** | -0.81970 | -1.10023 | -0.35387 |
| **H** | 0.31256 | 0.43595 | 0.23590 |
| **H** | 0.35425 | 0.41383 | 0.27039 |
| **H** | 0.31248 | 0.43595 | 0.23583 |
| **H*** | 0.43839 | 0.36654 | 0.33777 |
| **H*** | 0.40204 | 0.44796 | 0.27320 |

### 5.3.4. Vibrational frequency analysis

Both AIM and NBO analyses do not give any evidence for the H---H bond in $CH_5^+$ and both do give evidence for the same in $TH_5^+$ (T= Si and Ge). Would the normal mode analysis on these three cations provide additional evidence about the bonding? Clearly $TH_5^+$ has been considered as a weakly bound complex, with the central T atom tetrel bonded to the $H_2$ moiety. The positively charged central T atom can therefore accept electron density from the σ electrons of the $H_2$ moiety. This donation of electron density should lead to the weakening of the $H_2$ bond. The electron density (ϱ) obtained from the AIM analysis shows that the $H_2$ bond is weakened more for $SiH_5^+$ than for $GeH_5^+$. An elongation of the $H_2$ bond length is expected as a consequence of the donation of electron density to the T center. The tabulated bond lengths show that the $H_2$ bond lengths in $TH_5^+$ are elongated compared to free $H_2$. The $H_2$ bond in $SiH_5^+$ is longer than in $GeH_5^+$, and this correlates well with the computed electron density. It is evident that the $H_2$ unit retains its identity in the molecule. We therefore expect to find a normal mode in $TH_5^+$ which comprises of the $H_2$ stretch. We then anticipate that the weakening and elongation of the bond would cause this $H_2$ stretch frequency to be red shifted. The computed harmonic frequencies are tabulated in Table 5.6. The $H_2$ stretch is red shifted by 466.65 $cm^{-1}$ in $SiH_5^+$ and by 440.23 $cm^{-1}$ in $GeH_5^+$. Boo and Lee obtained the infrared spectrum of the H–H stretching mode in $SiH_5^+$ and it appears between 3650 and 3740 $cm^{-1}$,[37] reasonably close to the predicted value of 3800 $cm^{-1}$. In contrast there is no normal mode in $CH_5^+$ which can be classified as $H_2$ stretch. There are two normal modes which involve the two H atoms and the central C atom. These are symmetric and antisymmetric stretches for the H-C-H unit. This provides further evidence that $CH_5^+$ has two long and equivalent bonds and it is not a weak complex between $CH_3^+$and $H_2$.

**Table 5.6.** Harmonic frequencies of the H-H stretch calculated at MP2/aug-cc-pVTZ and at B3LYP/aug-cc-pVTZ, the scaled frequencies are also reported. All values are reported in $cm^{-1}$.

| system | MP2 | Scaled[a] | B3LYP | Scaled[b] | Experimental |
|---|---|---|---|---|---|
| **$CH_5^+$** | No normal mode comprising of a H-H stretch | | | | |
| **$SiH_5^+$** | 4026.4 | 3825.1 | 3940.4 | 3802.5 | 3650-3740 [37] |
| **$GeH_5^+$** | 4054.2 | 3851.5 | 4006.9 | 3866.7 | - |
| **$H_2$** | 4517.6 | 4291.8 | 4417.7 | 4315.2 | 4401.21 [47] |

[a]scaling factor is 0.95 [b]scaling factor is 0.965.
Scaling factors taken from "CCCBDB listing of precalculated vibrational scaling factors" (https://cccbdb.nist.gov/vibscale.asp accessed on November, 2018)

### 5.3.5. Potential energy scans

As discussed earlier, $CH_5^+$ is commonly considered as protonated methane and the $H_4C\cdots HX$ complex could be thought of as the hydrogen bonded complex leading to it. However, the structure at the global minimum shows similarities with a weakly bound complex between $CH_3^+$ and $H_2$. All the results presented above clearly indicate that $CH_5^+$ neither has a tetrel bond nor a bond between the two H atoms which are at a longer distance from C compared to the other three H atoms. Would the reaction path between $CH_5^+$ and $CH_3^+ + H_2$ indicate the presence of a tetrel bond anywhere along the reaction coordinate? To address this question, the potential energy scan was done at MP2/aug-cc-pVDZ level by varying the distance between the $TH_3^+$ unit and the $H_2$ moiety. The AIM analysis was carried out at various points along the reaction coordinate. The results for $CH_5^+$ are shown in Figure 5.7 and the results for $SiH_5^+$ and $GeH_5^+$ are shown in Figures 5.8 and 5.9, respectively.

In all these cases the AIM analysis indicates that there is no tetrel bond formation between $H_2$ and $TH_3^+$ as the $H_2$ approaches $TH_3^+$ until very close to the minimum. In the $CH_5^+$ case the tetrel bond is not found anywhere along this coordinate and for $SiH_5^+$ and $GeH_5^+$, only at the minimum a tetrel bond is seen. In all cases one of the hydrogen atoms is interacting with the central atom along the reaction coordinate and this interaction is likely the driving force for the reaction. There is a bond path connecting one hydrogen atom to the central atom which may be considered as a tetrel bond.

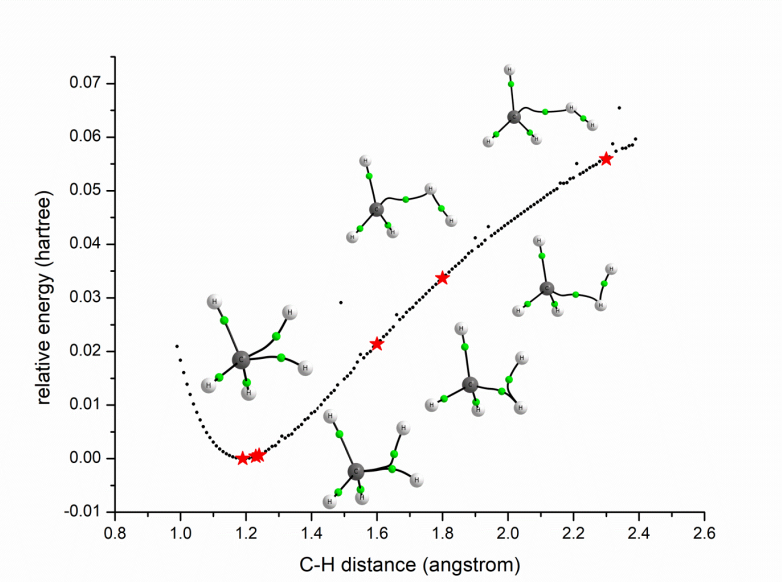


**Figure 5.7.** Potential energy scan for changing the distance between the $CH_3^+$ and $H_2$ moieties.

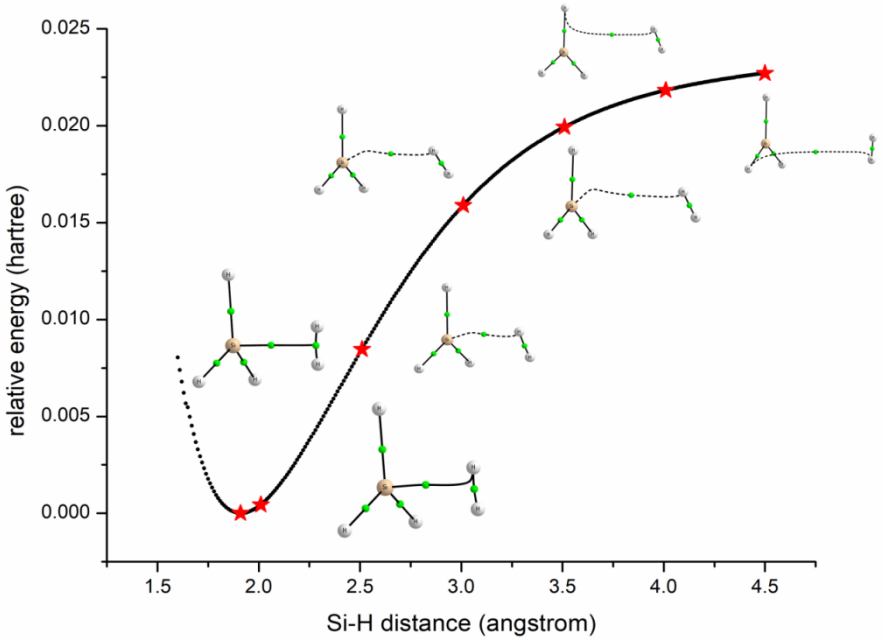


**Figure 5.8.** Potential energy scan obtained by changing the distance between the $SiH_3^+$ and $H_2$ moieties. Calculation done at MP2/aug-cc-pVDZ.

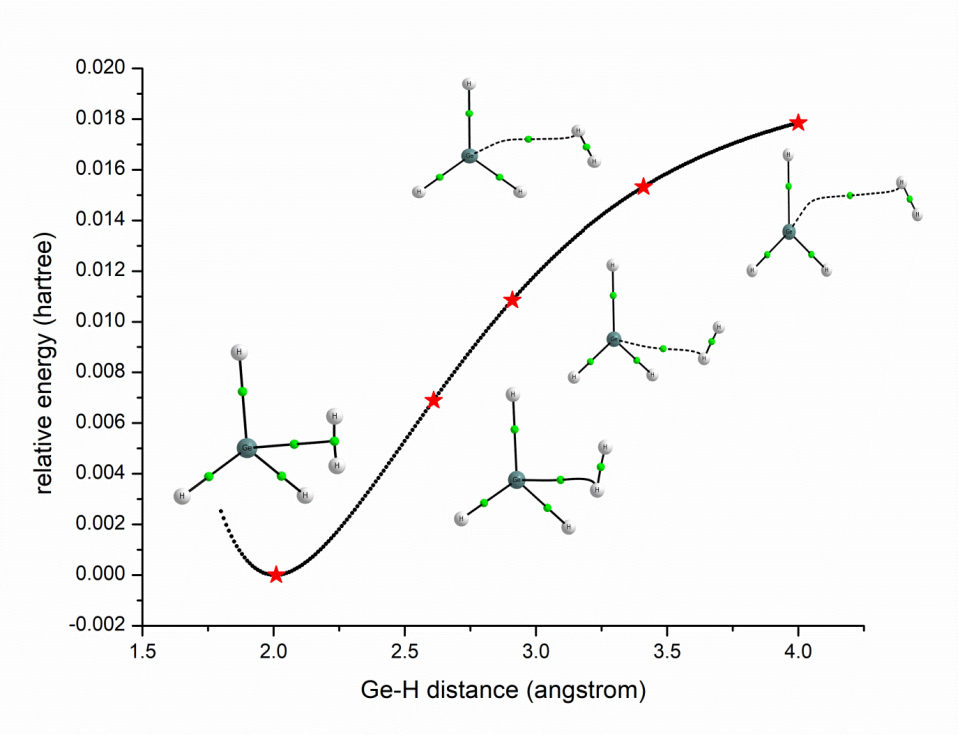


**Figure 5.9.** Potential energy scan obtained by changing the distance between the $GeH_3^+$ and $H_2$ moieties. Calculation done at MP2/aug-cc-pVDZ.

## 5.4. Three-center two-electron bonds

### 5.4.1. Geometry optimization

The molecular systems studied here are notable for having three-center two-electron bonding patterns. Figure 5.10 shows the optimized geometries of the molecular systems investigated. The bonds are drawn by the visualization software based on some in-built criteria for the distances between two atoms and they may or may not represent the real existence of bonds, *vide infra*. The structural parameters for the optimized geometries are given in Table 5.7.

Considering that a pair of electrons are shared between three centers in a 3c-2e bond, one expects these bonds to be weaker compared to their 2c-2e counterparts. This implies that the 3c-2e bond would be longer compared to a conventional 2c-2e bond between the same atoms or groups.

**$B_2H_6$:** To explain the structure and bonding of the electron deficient diborane, Pitzer[48] suggested that $B_2H_6$ is formed by a two proton attack on the double bond of $B_2H_4^{2-}$. This structure then has two electrons being shared among the three centres (BHB). The electron deficient $BH_3$ dimerizes to form $B_2H_6$ with a hydrogen atom from each unit, forming a bridge between the two boron centers. The two 3c-2e bonds formed share the two boron atoms, making a four centered ring. The two bridging B-H-B bonds are in a plane perpendicular to the four terminal B-H bonds. The B-H bond length in the 3c-2e bridging bond (1.31 Å) is longer than the terminal B-H bonds (1.18 Å). The B-H-B angle is around 84°. The two boron atoms seem to be brought closer by the 3c-2e bridge. The B-B distance is nearly 1.76 Å, which is only slightly longer than the B-B bond length (1.59 Å)[49] in $B_2$. The visualization software draws a bond between the two boron atoms in $B_2H_6$, but is there really any bond between them? This question about the B-B bond will be discussed later.

**$CH_5^+$:** The structure has been discussed in section 5.3.1. Three short C-H bonds make up the $CH_3$ tripod and two long C-H bonds forms the 3c-2e (H-C-H) bond. We see that the C-H bond lengths involved in the 3c-2e bond (1.18 Å) are longer than the other three C-H bonds (1.11 Å, 1.09 Å). It is also much longer compared to the C-H bond in $CH_4$ (1.086 Å) (see Table 5.2). This 3c-2e H-C-H bond is bent with an angle of 49.6°. There seems to be no interaction between the two terminal hydrogen atoms in the 3c-2e bond. The H-H distance of the $H_2$ moiety is considerably longer (0.99 Å)

compared to H-H bond length in that of free $H_2$ (0.74 Å) making this an *'open-V-shaped'* 3c-2e bond.

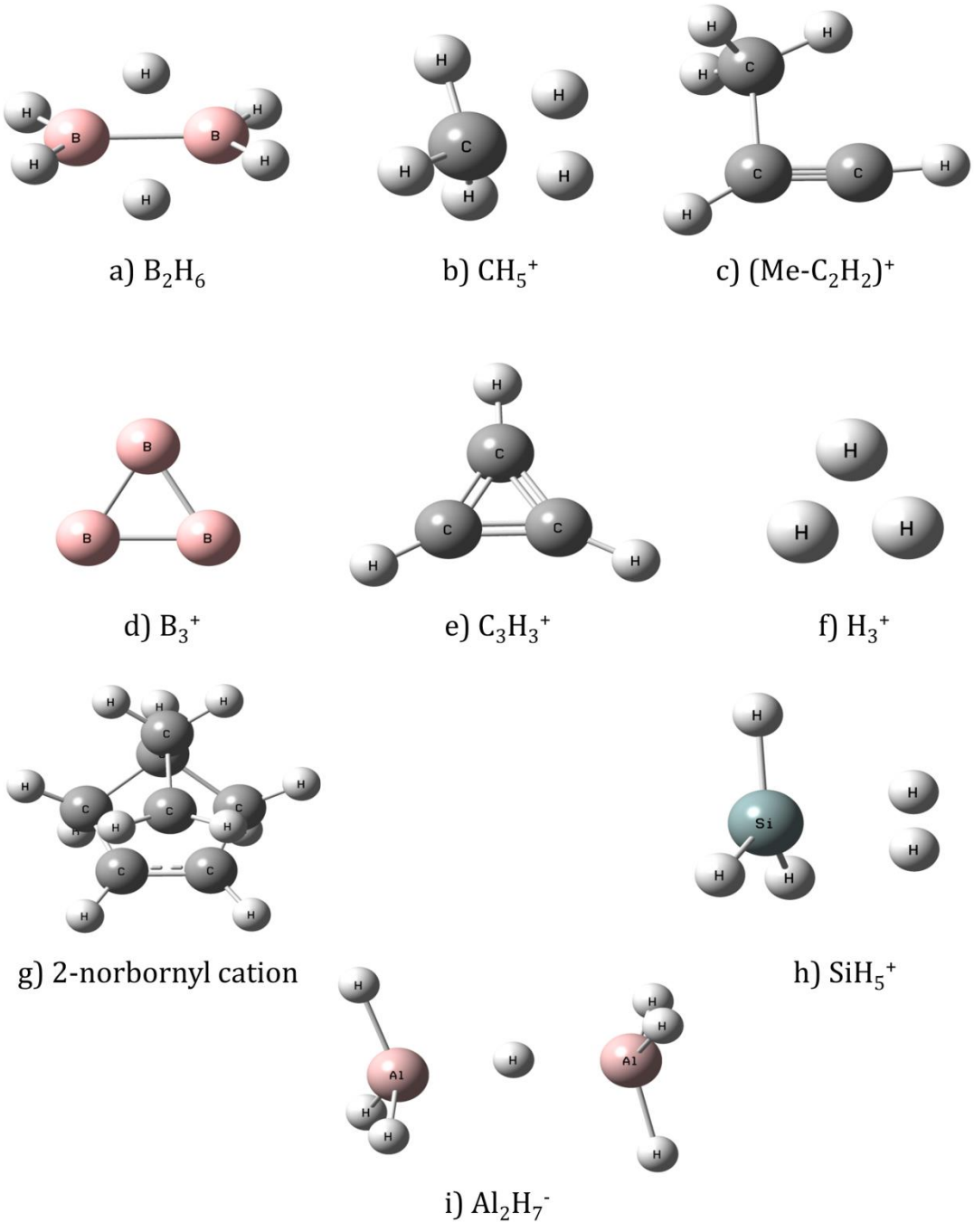


**Figure 5.10.** The optimized geometries at B3LYP/aug-cc-pVTZ level.

**Table 5.7.** Structural parameters for the optimized geometries. Bond lengths are in Å and bond angles in °.

| | Parameters | MP2/6-311++G(d,p) | B3LYP/aug-cc-pVTZ |
|---|---|---|---|
| **$B_2H_6$** | B-$H_t$ | 1.187 | 1.185 |
| | B-$H_b$ | 1.316 | 1.312 |
| | B-B | 1.770 | 1.758 |
| | ∠B-$H_b$-B | 84.4 | 84.2 |
| **$CH_5^+$** | C-$H_t$ | 1.089 | 1.088 |
| | | 1.111 | 1.110 |
| | C-$H_h$ | 1.188 | 1.185 |
| | | 1.186 | 1.181 |
| | H-H | 0.976 | 0.993 |
| | ∠H-C-H | 48.5 | 49.6 |
| **$Me^+$-$C_2H_2$** | C-Me | 1.695 | 1.611 |
| | C=C | 1.240 | 1.238 |
| | ∠C-C-C | 77.6 | 91.5 |
| **$B_3^+$** | B-B | 1.619 | 1.559 |
| | ∠B-B-B | 60.0 | 60.0 |
| **$C_3H_3^+$** | C-C | 1.373 | 1.358 |
| | C-H | 1.083 | 1.080 |
| | ∠C-C-C | 60.0 | 60.0 |
| **$H_3^+$** | H-H | 0.874 | 0.880 |
| | ∠H-H-H | 60.0 | 60.0 |
| **2-norbornyl$^+$** | C-C | 1.836 | 1.893 |
| | C=C | 1.399 | 1.388 |
| **$SiH_5^+$** | Si-$H_t$ | 1.458 | 1.469 |
| | | 1.456 | 1.467 |
| | Si-$H_h$ | 1.881 | 1.898 |
| | | 1.885 | 1.904 |
| | H-H | 0.771 | 0.777 |
| **$Al_2H_7^-$** | Al-$H_t$ | 1.60 | 1.611 |
| | Al$H_b$ | 1.699 | 1.703 |
| | ∠Al-H-Al | 146.8 | 170.5 |

**$R^+$--$C_2H_2$:** An interesting L-shaped 3c-2e bond has been reported in complexes between carbenium ions ($R^+$) and acetylene ($C_2H_2$)[50]. This complex forms a substituted vinyl cation structure with a 3c-2e bond between the two acetylene carbon atoms and the carbenium ion. When $R^+$ is an alkyl group an *'open, L-shaped'* 3c-2e bond is formed. We have examined here, the methyl substituted vinyl cation. The 3c-2e bond in this case is unsymmetrical, one side being shorter than the other. The C-C bond length between the acetylene carbons (1.24 Å) is shorter than that of the C-C bond between the acetylene carbon and the methyl group (1.61 Å). The optimized geometry bond angles (∠C-C-C) vary between 77°-91° depending on the level of theory.

**$C_3H_3^+$:** The cyclopropenyl cation forms a 3c-2e π-bond and is stabilized by the (4n+2) π aromaticity. The three carbon atoms form an equilateral triangle (60°) with a bond length of (1.36 Å). In this case all the three atoms interact with each other forming a *'closed, Δ-shaped'* 3c-2e bond.

**$B_3^+$:** The smallest boron cluster also forms an equilateral triangular structure with all three boron atoms interacting with each other. This motif is found in higher boron clusters as well, for example $B_5H_9$. The three B-B bonds are equal, and the bond length is 1.56Å. Thus, $B_3^+$ has a *'closed, Δ-shaped'* 3c-2e bond.

**$H_3^+$:** The simplest 3c-2e bound molecule would be the $H_3^+$. The cation was observed in 1912[51] much before the 3c-2e bond was conceptualized. However, it was only in 1978 that the triangular shape was experimentally confirmed[52]. The equilateral triangle structure gives three equal bonds of length 0.88 Å which is longer compared to the H-H bond length in free $H_2$ molecule (0.74 Å). Clearly, the *Gaussview* software[53] is non-committal about the type of 3c-2e bond in $H_3^+$. The AIM calculations help in characterizing this and that will be discussed in the Section 5.4.4.

**2-norbornyl cation**: This non-classical cation structure provoked a well-known debate in chemistry. The arguments against the structure were mainly that the properties could be explained by a rapidly equilibrating pair of cations without the need to invoke a 3c-2e bond. With various proofs over the years regarding the presence of a 3c-2e bond in the 2-norbornyl cation, the debate was resolved in 2013[54] with the crystal structure showing evidence for a 3c-2e bond. The bridgehead carbon has a double bond which donates electrons to the cation forming a *T-shaped* 3c-2e bond.

**$SiH_5^+$:** $SiH_5^+$ and its higher analogue $GeH_5^+$ have similar *T-shaped* structures. They can be considered as complexes of the $TH_3^+$ (T=Si, Ge) cation with $H_2$. The $H_2$ donates its sigma electrons to the central cation (Si/Ge) forming a 3c-2e bond. The H-H bond length is slightly longer (0.78 Å) than the free $H_2$ (0.74 Å). The identity of the $H_2$ moiety is retained as demonstrated by the red shift in the H-H stretch frequency.

**$Al_2H_7^-$** : The $Al_2H_7^-$ anion has a hydrogen atom bridging two $AlH_3$ units. The $AlH_3$ units are trans to each other, and the Al-H bonds (1.61Å) in the $AlH_3$ unit are slightly shorter than the bridging Al-H bond (1.7 Å). The geometries optimized with the DFT functional B3LYP using 6-311++G(d,p) and aug-cc-pVTZ have an Al-H-Al angle of 179 and 170 degrees, respectively. The MP2 calculations with the same basis sets have an Al-H-Al angle of close to 140 degrees. This is an example of a linear, *I-shaped* 3c-2e bond.

### 5.4.2. Natural Bond Orbital (NBO) analysis

The NBO calculation identifies 3c-2e bonds present in a structure and gives information about the type of orbitals involved in the bond. All the molecules investigated here show a 3c-2e bond. The 3c-2e bond in $B_2H_6$ and $CH_5^+$ involve the $sp^3$ orbitals of B and C and the s orbitals of H. In $C_3H_3^+$ and $B_3^+$ the 3c-2e bonds involve only p orbitals. $H_3^+$ involves only the s orbitals of the three H atoms. The L-shaped methyl vinyl cation has one p orbital and two $sp^3$ orbitals. The 3c-2e bond in the 2-norbornyl cation involves one nearly $sp^5$ type orbital of the carbocation and two p-type ($sp^{16}$) orbitals of the other two carbon atoms. This is essentially the cation center interacting with the double bond forming a π-complex. The 3c-2e bond in $SiH_5^+$ involves a p type orbital of Si interacting with the s orbitals of both the H atoms. The nearly linear 3c-2e bonds in $Al_2H_7^-$ involve nearly p type orbitals ($sp^{12.6}$) of Al interacting with the s orbital of hydrogen.

### 5.4.3. Natural Resonance Theory (NRT)

NRT calculations were performed using the *.47* files. This gives us information about the most weighted resonance structures that would represent these 3c-2e bonded structures if they were to be represented only by 2c-2e bonds. This in turn gives us the bond order for the bonds present between the two atoms. The bond orders calculated at MP2/6-311++G(d,p) are given in Table 5.8.

**Table 5.8.** The natural bond orders obtained from the NRT calculations.

| System | Bond | Natural Bond Order (MP2/6-311++G(d,p)) | Natural Bond Order (B3LYP/aVTZ) | Wiberg Bond Index (B3LYP/aVTZ)* |
|---|---|---|---|---|
| **$B_2H_6$** | B-$H_t$ | 0.9960 | 0.9996 | 0.9877 |
| | B-$H_b$ | 0.4124 | 0.3866 | 0.4791 |
| | B-B | 0.3568 | 0.4550 | 0.6528 |
| **Me-$C_2H_2^+$** | C-Me | 0.5737 | 0.6166 | 0.7934 |
| | C=C | 2.2086 | 2.2208 | 2.2310 |
| **$B_3^+$** | B-B | 1.3239 | 1.3333 | 1.6160 |
| | | 1.3242 | | |
| | | 1.3245 | | |
| **$C_3H_3^+$** | C-C | 1.3244 | 1.3300 | 1.4311 |
| | | 1.3292 | 1.3273 | 1.4312 |
| | | 1.3292 | 1.3255 | 1.4314 |
| **2-norbornyl$^+$** | C-C | 0.3999 | 0.4049 | |
| | | 0.4000 | 0.4053 | |
| | C=C | 1.2290 | 1.2344 | |
| **$SiH_5^+$** | Si-$H_t$ | 0.9836 | 0.9777 | 0.9452-0.9511 |
| | Si-$H_h$ | 0.0516 | 0.0576 | 0.2069 |
| | H-H | 0.8865 | 0.8724 | 0.7611 |
| **$Al_2H_7^-$** | Al-$H_t$ | 0.9885 | 0.9843 | 0.8234 |
| | Al-$H_b$ | 0.4956 | 0.4955 | 0.3802 |
| **$H_3^+$ [A]** | H-H | - | 0.33 | 0.4446 |
| **$CH_5^+$ [A]** | C-$H_t$ | - | 1.0000-0.8162 | 0.8747-0.7906 |
| | C-$H_h$ | | 0.6030-0.5809 | 0.6093-0.5774 |

* The Wiberg bond index in the NAO basis calculated at B3LYP/aug-cc-pVTZ.
[A] These results are based on NBO 7.0 calculations by an anonymous referee of Reference 55.

It can be seen that for $B_2H_6$ the bond order is close to 0.5 for each B-H bond in the 3c-2e bond. The B-B bond order is of similar magnitude indicating that there might be some interaction between the boron atoms. For both $CH_5^+$ and $H_3^+$ the calculations fail to find any resonance structures and therefore the bond orders are not obtained. Since completing this work, it has come to our notice that, with an improved algorithm,

the *NBO 7.0* version[56,57] can handle these two systems well and provide bond orders that look reasonable. For $H_3^+$, it gives uniform bond order of 0.33 between all three pairs of H and for $CH_5^+$, the bond orders range from 0.58 to 1.00 for the five C-H bonds. For the L-shaped Me-$C_2H_2^+$ the asymmetry is visible with the Me-C bond having a nearly 'half' bond and the acetylene carbons having a bond order slightly greater than 2. In the case of the triangular structures of $C_3H_3^+$ and $B_3^+$ the bond order for each bond is 1.33 which indicates 1 sigma bond and a total of *2e* shared between the three centers. For $SiH_5^+$ it is evident that the $H_2$ moiety is separate with the H-H bond having a bond order of 0.8 and the central Si has weak interactions with this $H_2$ moiety with a bond order of 0.05.

### 5.4.4. Atoms in Molecules (AIM) analysis

A molecular structure is defined when atoms are connected with each other in a specific pattern. Information about this connectivity can be obtained from the Molecular Graph (MG). An AIM calculation of the electron density topology gives rise to the MG. Atoms are considered to be bonded when they are connected via a bond path through a bond critical point (BCP).

In a 3c-2e bond the electron density is delocalized over three centers. One then expects that the value of the electron density ($\varrho$) at the BCP of the bonds involved in a 3c-2e bond to be less than that of a typical 2c-2e bond involving similar atoms. This decrease in $\varrho$ correlates well with the longer bond lengths obtained for the 3c-2e bonds. The ring critical point (RCP) provides valuable information regarding the 3c-2e bonds. Often when all the three centers involved in the bond interact with each other a closed ring structure is formed characterized by an RCP. This can help us to differentiate between *'open'* and *'closed'* 3c-2e bonds. In addition to the density at these critical points, the Laplacian and ellipticity provide useful information about the bond in consideration. Our results calculated at the MP2/6-311++G(d,p) are summarized in Table 5.9 and the MG are shown in Figure 5.11. One can see a different perspective about the bonds in MG compared to what is displayed in Figure 5.10, where the bonds are drawn if the distance between two atoms is less than the sum of pre-defined covalent radii of the two atoms.

In diborane ($B_2H_6$), the value of $\varrho$ at the BCPs for the bridging B-H bonds is 0.1202 au; this is lower compared to that of the terminal B-H bonds (0.1802 au). This

correlates with the fact that the longer bridging B-H bonds are longer compared to the terminal B-H bonds. Since the two 3c-2e B-H-B bonds involve the same boron atoms, a closed 4-membered ring structure is formed; this is confirmed by the presence of an RCP. Though the optimized geometry shows a bond between the B atoms, there is no BCP found between them. This indicates that there is no interaction between the boron atoms in $B_2H_6$. The electron density topology for $CH_5^+$ has been discussed in detail in the Section 5.3.2. It is to be noted that there is no BCP obtained between the two hydrogens in the 3c-2e bond and that the structure is not a complex between $CH_3^+$ and $H_2$ but has a *V* type 3c-2e (H-C-H) bond.

The 3c-2e bonds discussed in this work are all symmetrical, that is the central atom in the 3c-2e bond bridges two similar groups except that found in the $CH_3^+$-$C_2H_2$ cation. In this case, the C-C distance between the C in $CH_3^+$ and the C in $C_2H_2$ which are both 'bonded' is significantly larger than the C-C distance in $C_2H_2$. We denote the 3c-2e bond in this case as an *L* type. Though, both *V* and *L* type 3c-2e bonds have acute angles, the significant difference between them is in the symmetry.

The molecular graphs obtained for $B_2H_6$ and $CH_5^+$ show that the 3c-2e bonds are bent but there is no interaction present between the two terminal atoms. They are examples of an '*open*' 3c-2e bond, though for $B_2H_6$, the presence of two such bonds leads to a closed structure. The 3c-2e π-bonded molecules $C_3H_3^+$ and $B_3^+$ show a ring critical point with all the three (carbon or boron) atoms bonded to each other forming an equilateral triangle. In this case all the three centers interact with each other forming a *'closed-Δ type'* 3c-2e bond.

One then expects that the simplest 3c-2e bonded structure, $H_3^+$ to also have a similar closed structure. However, the electron density topology finds a Non-Nuclear Attractor (NNA) at the centroid of the equilateral triangle at all four levels of theory investigated here and in Bader's work[58]. The three H atoms have bond paths terminating at the NNA forming a *Y*-shaped structure, similar to Jensen's notation for 3c-2e bonds. Clearly, Jensen's model cannot be used for all 3c-2e bonds.

**Table 5.9.** Electron density, Laplacian, and Ellipticity at the BCP based on AIM analysis at MP2/6-311++G(d,p) level.

| System | Parameter | $\varrho$ | $\nabla^2\varrho$ | $\varepsilon$ |
|---|---|---|---|---|
| $\mathbf{B_2H_6}$ | B-$H_t$ | 0.1802 | -0.2392 | 0.1054 |
| | B-$H_b$ | 0.1202 | 0.1459 | 0.7408 |
| $\mathbf{CH_5^+}$ | C-$H_t$ | 0.2788 | -1.0002 | 0.0286 |
| | C-$H_t$ | 0.2561 | -0.8418 | 0.0318 |
| | C-$H_h$ | 0.2096 | -0.4269 | 2.3094 |
| | C-$H_h$ | 0.2151 | -0.4772 | 1.3781 |
| $\mathbf{Me\text{-}C_2H_2^+}$ | C-Me | 0.1522 | -0.1076 | 0.5536 |
| | C=C | 0.3872 | -1.1673 | 0.2890 |
| $\mathbf{B_3^+}$ | B-B | 0.1267 | -0.1316 | 0.0767 |
| | B-B | 0.1268 | -0.1319 | 0.0779 |
| | B-B | 0.1268 | -0.1322 | 0.0791 |
| $\mathbf{C_3H_3^+}$ | C-C | 0.3059 | -0.6726 | 0.1698 |
| | C-H | 0.2819 | -1.0596 | 0.0241 |
| $\mathbf{H_3^+}$ | H-NNA[A] | 0.2337 | 0.8448 | 1.580 |
| **2-norbornyl$^+$** | C-C | 0.1263 | 0.01342 | 6.6416 |
| | C=C | 0.3068 | -0.8474 | 0.1560 |
| $\mathbf{SiH_5^+}$ | Si-$H_t$ | 0.1319 | 0.2591 | 0.0008 |
| | | 0.1326 | 0.2605 | 0.0074 |
| | Si-$H_h$ | 0.0451 | 0.1123 | 0.5220 |
| | H-H | 0.2465 | -0.9636 | 0.0480 |
| $\mathbf{Al_2H_7^-}$ | Al-$H_t$ | 0.0735 | 0.2725 | 0.0026 |
| | Al-$H_b$ | 0.0497 | 0.2053 | 0.0081 |

[A] NNA indicates non-nuclear attractor, which is a critical point in electron density having a maximum in all three directions.

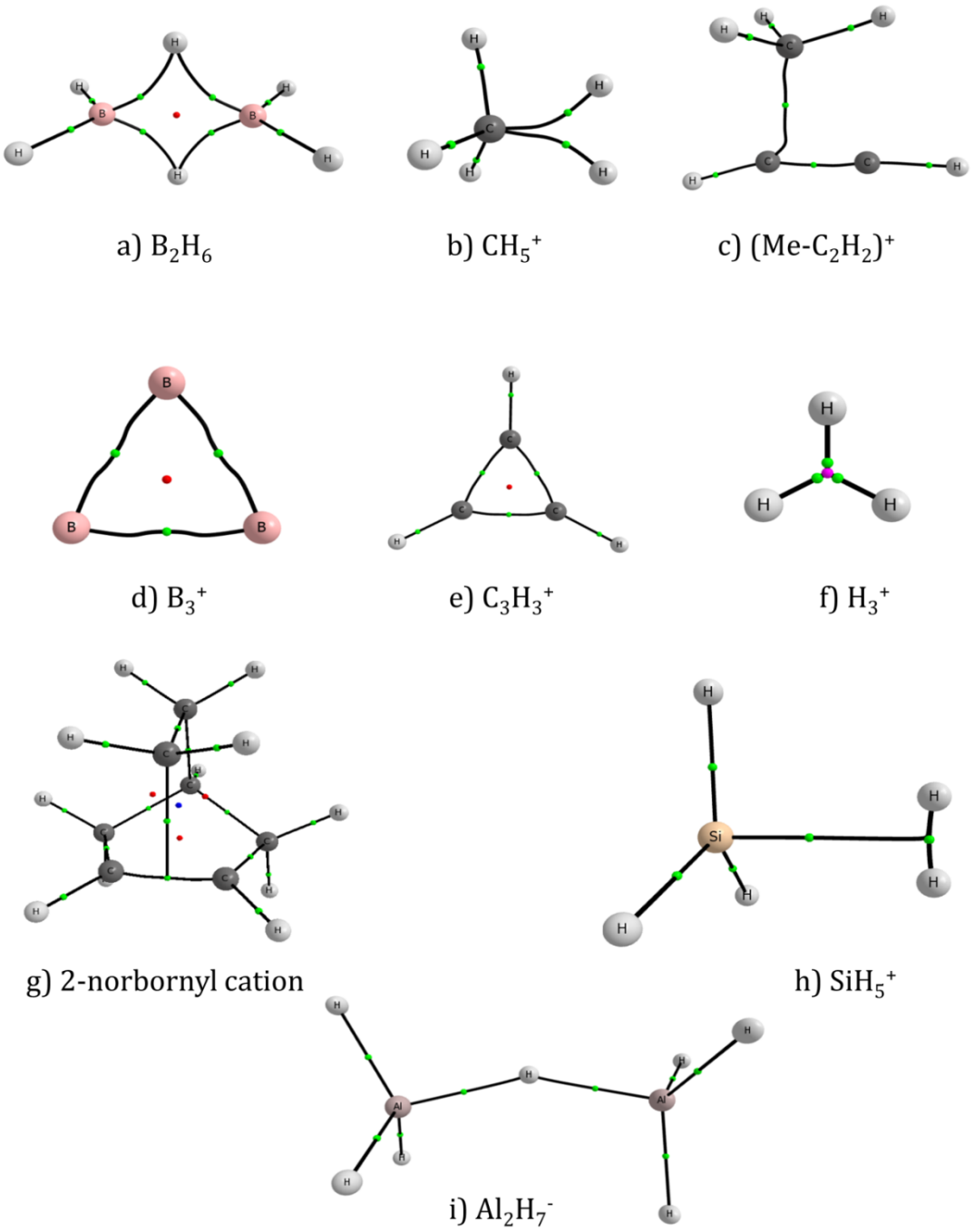


**Figure 5.11**. The molecular graphs obtained at MP2/6-311++g (d,p)

The MG for the 2-norbornyl cation is *T*-shaped and appears to be a π-complex formed by the carbocation and the C-C π-bond. This is similar to one of the three molecular graphs of the 2-norbornyl cation investigated by Werstiuk and Muchall[59]. A bond critical point is found between the cation and the π-bond. This type of a MG is

referred to as a conflict structure because a BCP is connected to another BCP and not an atom. This is a highly unstable configuration, for a slight deviation could shift the bond path to either atom. The bond ellipticity value at the BCP is 6.6 confirming that this is a highly unstable bond. The $\varrho$ value at the BCP for the C-C double bond is 0.3068 au which is similar to that in benzene and lower than that of ethylene[60]. This is indicative of the fact that this bond has a partial double bond character implying that the electron density is shared with the carbocation to form a 3c-2e bond. The electron density topology of $SiH_5^+$ and its higher homologue $GeH_5^+$ have also been discussed in the Section 5.3.2; both these cations form a *T*-shaped 3c-2e with the central cation interacting with the $H_2$ moiety.

The molecular graph for the H-bridged $Al_2H_7^-$ anion has a 3c-2e bond that is nearly linear. The $\varrho$ values at the BCP for the Al-H bridge bonds (0.0497 au) are lower than that of the Al-H terminal bonds (0.0729 au). The Laplacian of electron density $\nabla^2\varrho$ at the BCPs are positive, however the $\varrho$ values are high and therefore these are not indicative of *closed-shell* interactions[27].

The molecular graphs clearly show the connectivity between the atoms and it is evident that all the 3c-2e bonds are not the same. A variety of arrangements are possible for a 3c-2e bond and we have identified at least six types; *V, L, ⊿, Y, T* and *I*. The molecular graphs in conjunction with the NBO and NRT analysis show that the 3c-2e could be classified into one of these six arrangements. Except for the $H_3^+$ case, NBO and AIM results lead to similar conclusions.

## 5.5. Discussions

The $C_s$ (I) symmetry is the global minimum structure for $TH_5^+$. The $H_2$ moiety retains its identity in $SiH_5^+$and $GeH_5^+$ though the $H_2$ bond is slightly elongated. In the case of $CH_5^+$ the $H_2$ moiety is elongated to such an extent that it can no longer be considered as a separate unit. The two long C-H bonds that make up the $H_2$ moiety are similar to the other C-H bonds of the $CH_3^+$ tripod and the AIM parameters at all their BCPs clearly show that all five C-H bonds are covalent, though two of them are slightly weaker than the other three.

The harmonic frequencies for the $TH_5^+$ molecules show that the $H_2$ moiety retains its identity in $SiH_5^+$and $GeH_5^+$. The $H_2$ stretching frequency in these molecules is red

shifted from the free $H_2$ frequency because of the elongation in the $H_2$ bond. $CH_5^+$ is distinctly different with no pure $H_2$ vibration. $C_2H_7^+$ which is the higher homologue of $CH_5^+$ has an H-H interaction as is evident from its molecular graph, but the frequency analysis shows that there is no normal mode which corresponds to a pure H-H stretch. Although it seems on examining the molecular graphs that only $CH_5^+$ is different from its congeners and its homologues, the frequency analysis provides evidence that the carbocations ($CH_5^+$ and $C_2H_7^+$) are different from their congeners ($SiH_5^+$ and $GeH_5^+$).

Why is the structure of $CH_5^+$ distinctly different from that of its congeners, $SiH_5^+$ and $GeH_5^+$? This question can be answered by analyzing all the bond energies involved as well as the dissociation energies for the $TH_5^+$ molecules. The relevant bond energies are given in Tables 5.10 and 5.11. If we consider the formation of the $CH_5^+$ molecule to be the hydrogenation of the $CH_3^+$ species, it is evident that two C-H bonds are formed at the expense of one H-H bond. The C-H and H-H bond energies are nearly equal and the two weak C-H bonds can be easily formed by cleaving the H-H bond in $H_2$. This arrangement is more stable than having a slightly weaker H-H bond and a tetrel bond with the C atom in $CH_3^+$. This is not the case with $SiH_5^+$ and $GeH_5^+$, as the Si-H and Ge-H bonds are significantly weaker than H-H bond. The formation of two weak T-H bonds cannot compensate for the cleavage of the H-H bond and therefore $SiH_5^+$/$GeH_5^+$ prefers to form a tetrel bonded complex of the $TH_3^+$ species with $H_2$. In general, Si and Ge form a stronger tetrel bond than C[19]. The combination of the tetrel bond and H-H bond is energetically more preferred than having two weak T-H bonds, when T = Si/Ge. The difference between the structures of $CH_5^+$ and $SiH_5^+$ has been rationalized on the basis of their bond energies by Schleyer et al.[36]. Our analysis includes the bond energies of the T-H bonds and that of the tetrel bond between $T^+$ and $H_2$, which is discussed next.

The proton affinities of $TH_4$ are given in Table 5.10 as well. At first look, it appears counterintuitive to find the order $CH_4 < SiH_4 < GeH_4$ given the reverse order for the T-H bond energy. The proton affinity of $CH_4$ is about 100 $kJmol^{-1}$ less than that of $SiH_4$, which is about 40 $kJmol^{-1}$ less than that of $GeH_4$. This in a way provides further evidence to the structure of $TH_5^+$. While the protonation of $CH_4$ results in the formation of two relatively weaker C-H bonds, protonation of $SiH_4$ and $GeH_4$ results in the formation of a stronger H-H bond and a tetrel bond.

**Table 5.10.** T-H bond energies and proton affinities for the $TH_4$ molecule in $kJmol^{-1}$.

| Bond | Bond Energy ($kJmol^{-1}$) [61] | Molecule | Proton Affinity ($kJmol^{-1}$) |
|---|---|---|---|
| **C-H** | 423 | **$CH_4$** | -546.01 ± 8.4 [62] |
| **Si-H** | 398.3 | **$SiH_4$** | -640.15 ± 12.6 [63] |
| **Ge-H** | 365 | **$GeH_4$** | -682.15 ±3.9 [38] |
| **H-H** | 432 | | |

The dissociation energies calculated for the $TH_5^+$ molecules going to $TH_3^+$ and $H_2$ are given in Table 5.11. The $CH_5^+$ requires the most energy (183.0 $kJmol^{-1}$) to dissociate into a methyl cation and $H_2$. According to the calculations, it is higher by nearly 133 $kJmol^{-1}$ when compared with $SiH_5^+$ and the available experimental results show this difference to be about 96 $kJmol^{-1}$. However, this is not the 'tetrel bond energy' between $CH_3^+$ and $H_2$ as it does not exist in $CH_5^{+\cdot}$ This high energy is due to the fact that the two C-H bonds need to be broken before forming the H-H bond. The $SiH_5^+$ and $GeH_5^+$ have nearly equal dissociation energies (49.7 and 43.8 $kJmol^{-1}$, respectively) and these can be readily identified as the tetrel bond energy. In these cases, basis set superposition errors (BSSE) could affect these energies, and so BSSE correction[64] was done using the counterpoise method within *Gaussian 09* and results included in Table 5.11. For $SiH_5^+$, the error is only 1.2 $kJmol^{-1}$, but for $GeH_5^+$, it is about 8 $kJmol^{-1}$. Thus, the difference in hydrogenation energies between $SiH_5^+$ and $GeH_5^+$ increases to about 12 $kJmol^{-1}$ after BSSE correction. After BSSE correction, the tetrel bond energies are 48.4 $kJmol^{-1}$ and 35.9 $kJmol^{-1}$ for $SiH_5^+$ and $GeH_5^+$, respectively. The dissociation energies for $SiH_5^+$ and $GeH_5^+$ are 43.1 $kJmol^{-1}$ and 40.4 $kJmol^{-1}$ respectively as predicted by Archibong and Leszczynski[65], these values are calculated at CCSD(T)/TZP+f with ZPE corrections at MP2/TZP+f. These values are larger than the typical tetrel bond energies for neutral molecules, typically less than 16 $kJmol^{-1}$ [18,19]. Our results are compared with previous calculated and experimental values in Table 5.11 and the trends are similar.

**Table 5.11.** Hydrogenation energies for the $TH_3^+$ molecules.

| $TH_3^+ + H_2 \rightarrow TH_5^+$ | Calculated hydrogenation energy ($kJmol^{-1}$) | | | Experimental hydrogenation energy[e] |
|---|---|---|---|---|
| | MP2[a] | | CCSD(T) | |
| $CH_3^+ + H_2 \rightarrow CH_5^+$ | -183.0 | | -159.4 [c] | -175.7 ± 8.4 |
| $SiH_3^+ + H_2 \rightarrow SiH_5^+$ | -49.7 | -48.4[b] | -43.1[d 65] | -79.5 ± 12.5 |
| $GeH_3^+ + H_2 \rightarrow GeH_5^+$ | -43.8 | -35.9[b] | -40.4[d 65] | - |

[a] calculated at MP2/aug-cc-pVTZ with Zero Point Energy (ZPE) corrections.
[b] BSSE corrected.
[c] calculated at CCSD(T)/aug-cc-pVTZ for the geometry optimized at MP2/aug-cc-pVTZ with ZPE corrections at MP2/aug-cc-pVTZ.
[d] calculated at CCSD(T)/TZP+f with ZPE corrections at MP2/TZP+f from Ref. 65;
[e] Reference 36 and references therein.

The molecules investigated here possess a 3c-2e bond as confirmed by the NBO analysis. The NBO results give evidence for the presence of the 3c-2e bonds as well as the type of orbitals involved in these bonds. One expects that the 3c-2e bonds must have either two or three fractional bonds connecting the three centers. The bond order then for each of these bonds is expected to be less than one. The NRT results give the natural bond orders for the bonds present in these molecules. The bond orders obtained from the NRT calculations also lead to an understanding of *'open'* and *'closed'* 3c-2e bonds. In ring structures where the two electrons are shared between three centers the three connecting bonds have a bond order of 0.33. In the case of the triangular structures of $C_3H_3^+$ and $B_3^+$ the bond order for each bond is nearly 1.33. Each bond consists of a sigma C-C bond and a 3c-2e π-bond which leads to one 'bond' (2e) being shared by 3 atoms and therefore a bond order of 0.33. In contrast the 'open' 3c-2e bonds in $B_2H_6$ and $Al_2H_7^-$ have bond orders of nearly 0.5. It could then be considered that *'closed'* structures would have a bond order of 0.33 and *'open'* structures have bond orders that are nearly 0.5. The use of the AIM molecular graphs helps categorize these 3c-2e bonds into six different shapes *V, L, ⊿, Y, T*, and *I*, going beyond the traditional *'open'* and *'closed'* structures. There could be some ambiguity in differentiating between the *V, L,* and *I* types since they are all *'open'* structures with small differences in their angles. As pointed out in the previous section, the 3c-2e bonds can be defined as *V* when the bonds are symmetrical and of equal lengths, whereas they would be defined as *L* when the bonds involved in the 3c-2e are of

unequal lengths. The difference between *V* and *I* type 3c-2e bonds, we propose is, that the *V*-type has an acute angle or angles less than 135° and the *I*-type has an obtuse angle with angles greater than 135°.

Linear 3c-2e bonds are extremely rare. The 'corrected' Walsh diagram by Mulliken for the $AH_2$ systems predicts for two electrons the structures must be bent[66]. DeKock and Bosma note that often nuclear-nuclear repulsion could override the electronic effects and a linear 3c-2e bond is possible[30]. They mention a few systems such as $\{Al_2(CH_3)_6H\}^-$, $Al_2H_7^-$ (studied here also), $LiHLi^+$ and $NaHNa^+$ where such linear bonds are possible. The $Al_2H_7^-$ has an Al-H-Al *3c-2e* bond that is nearly linear. Depending on the level of theory of the calculation the Al-H-Al angle in the *3c-2e* bond ranges from 140° at MP2 calculations to 179° using the B3LYP functional. The methyl substituted anion $\{(CH_3)_3Al\text{-}(\mu\text{-}H)\text{-}Al\ (CH_3)_3\}^-$ has a similar bonding motif as the $Al_2H_7^-$ anion. The X-ray crystal structure gives an Al-H-Al angle of 180° but *ab initio* calculations at various levels of theory give an angle of 140°[67]. The NBO analysis on the $Li\text{-}H\text{-}Li^+$ finds no 3c-2e bond. DuPré reported a strong 3c-2e bond in the cage structure of in-bicyclo[4.4.4]-1-tetradecyl cation that is linear[68]. The linearity is induced by the constraints of the ring structure and the charge redistribution to prevent a bridgehead cation from forming.

We find that the nature of the 3c-2e bond in the $TH_5^+$ systems is quite different. The $CH_5^+$ forms a bent '*V*'-shaped 3c-2e bond while $SiH_5^+$ and $GeH_5^+$ form a T-shaped 3c-2e bond. The 3c-2e bond (H-C-H) in $CH_5^+$ shows no interaction between the two H atoms forming five covalent C-H bonds whereas the T-shaped 3c-2e bond is a weak tetrel interaction between the $SiH_3^+/GeH_3^+$ units and the $H_2$ moiety. Jemmis and coworkers investigated a number of $CH_3M_2^+$ systems (M being elements from group 1 and 2), having 3c-2e bonds[34]. Two possible structures are found, one with $C_s$ symmetry and the other with either $D_{3h}$ or $C_{3v}$ symmetry. As mentioned earlier, these are model systems for studying the stereochemistry of aliphatic electrophilic substitution reactions. The $C_s$ symmetry structures at the transition states for these reactions would undergo retention of configuration and the $D_{3h}$ linear structures (TS) would undergo inversion of configuration. Thus, it can be seen how important the shape and connectivity of the 3c-2e bond is in influencing the stereochemistry of the reaction. The $D_{3h}$ symmetry structures are saddle points at higher levels of theory whereas the $C_{3v}$ symmetry structures are minima. However, the NBO analyses for both

these linear symmetry structures do not give a 3c-2e bond as expected. The lithium (M) ions become positively charged and the central C atom becomes negatively charged forming a complex between the lithium cation and the carbon center.

## 5.6. Conclusions

The structures of $TH_5^+$ (T = C/Si/Ge) have been analyzed based on AIM, NBO, and normal coordinate analysis. All these results give a consistent picture. The $CH_5^+$ has a pentacoordinate carbon, having three shorter C-H bonds and two longer C-H bonds. Both $SiH_5^+$ and $GeH_5^+$ have a structure in which the $TH_3^+$ is tetrel bonded to $H_2$. Bond energies, proton affinities and hydrogenation energies are all consistent with these structures. We conclude that the common description of $CH_5^+$ as a complex between $CH_3^+$ and $H_2$ is not consistent with all the results presented here. Thus, $CH_5^+$ has no hydrogen bond or carbon bond, and $SiH_5^+$ and $GeH_5^+$ have a tetrel bond.

We have also investigated a set of molecular systems that possess a 3c-2e bonding pattern. We have used NBO, NRT, and AIM analyses to classify these 3c-2e bonds according to their connectivity. It can be seen that the 3c-2e bonds can be depicted in a number of ways beyond the usual '*Y*'-shaped or curved line connecting the three atoms involved. Moreover, the conventional descriptions as *'closed'* and *'open'* are not enough for accurate description of the bonds between the three centers. The different connectivity patterns of the 3c-2e bonds have different properties and reactivity. We find that these 3c-2e bonds can be classified as *V, L, ⊿, Y, T* and *I* (linear) arrangements and propose that 3c-2e bonds be classified further in to one of these six types.

## 5.7. References


(1) Tal'roze, V.; Lyubimova, A. *Dokl. Akad. Nauk SSSR* **1952**, *86*, 909.

(2) McCoy, A. B.; Braams, B. J.; Brown, A.; Huang, X.; Jin, Z.; Bowman, J. M. Ab Initio Diffusion Monte Carlo Calculations of the Quantum Behavior of $CH_5^+$ in Full Dimensionality. *J. Phys. Chem. A* **2004**, *108*, 4991–4994.

(3) Jin, Z.; Braams, B. J.; Bowman, J. M. An Ab Initio Based Global Potential Energy Surface Describing $CH_5^+ \rightarrow CH_3^+ + H_2^+$. *J. Phys. Chem. A* **2006**, *110*, 1569–1574.

(4) Kolbuszewski, M.; Bunker, P. R. Potential Barriers, Tunneling Splittings, and the Predicted $J = 1 \leftarrow 0$ Spectrum of $CH_5^+$. *J. Chem. Phys.* **1996**, *105*, 3649–3653.

(5) Huang, X.; McCoy, A. B.; Bowman, J. M.; Johnson, L. M.; Savage, C.; Dong, F.; Nesbitt, D. J. Quantum Deconstruction of the Infrared Spectrum of $CH_5^+$. *Science* **2006**, *311*, 60–63.

(6) Tian, S. X.; Yang, J. Driving Energies of Hydrogen Scrambling Motions in $CH_5^+$. *J. Phys. Chem. A* **2007**, *111*, 415–418.

(7) Schreiner, P. R.; Kim, S.; Schaefer, H. F.; von Ragué Schleyer, P. $CH_5^+$: The Never-ending Story or the Final Word? *J. Chem. Phys.* **1993**, *99*, 3716–3720.

(8) Müller, H.; Kutzelnigg, W.; Noga, J.; Klopper, W. $CH_5^+$: The Story Goes on. An Explicitly Correlated Coupled-Cluster Study. *J. Chem. Phys.* **1997**, *106*, 1863–1869.

(9) White, Edmund. T.; Tang, J.; Oka, T. $CH_5^+$: The Infrared Spectrum Observed. *Science* **1999**, *284*, 135–137.

(10) Okulik, N. B.; Peruchena, N. M.; Jubert, A. H. Three-Center−Two-Electron and Four-Center−Four-Electron Bonds. A Study by Electron Charge Density over the Structure of Methonium Cations. *J. Phys. Chem. A* **2006**, *110*, 9974–9982.

(11) Marx, D.; Parrinello, M. Structural Quantum Effects and Three-Centre Two-Electron Bonding in $CH_5^+$. *Nature* **1995**, *375*, 216–218.

(12) Asvany, O.; P, P. K.; Redlich, B.; Hegemann, I.; Schlemmer, S.; Marx, D. Understanding the Infrared Spectrum of Bare $CH_5^+$. *Science* **2005**, *309*, 1219–1222.

(13) Kubas, G. J. *Metal Dihydrogen and σ-Bond Complexes: Structure, Theory, and Reactivity*; Springer Science & Business Media, **2001**.

(14) Legon, A. C.; Roberts, B. P.; Wallwork, A. L. Rotational Spectra and Geometries of the Gas-Phase Dimers ($CH_4$, HF) and ($CH_4$, HCl). *Chem. Phys. Lett.* **1990**, *173*, 107–114.

(15) Legon, A. C.; Wallwork, A. L. The Pairwise Interaction of Methane with Hydrogen Cyanide: A Surprising Result from Rotational Spectroscopy. *J. Chem. Soc. Chem. Commun.* **1989**, 9, 588-590.

(16) Suenram, R. D.; Fraser, G. T.; Lovas, F. J.; Kawashima, Y. The Microwave Spectrum of $CH_4$ – $H_2O$. *J. Chem. Phys.* **1994**, *101*, 7230–7240.

(17) Raghavendra, B.; Arunan, E. Hydrogen Bonding with a Hydrogen Bond: The Methane–Water Complex and the Penta-Coordinate Carbon. *Chem. Phys. Lett.* **2008**, *467*, 37–40.

(18) Mani, D.; Arunan, E. The X–C···Y (X= O/F, Y= O/S/F/Cl/Br/N/P) 'Carbon Bond' and Hydrophobic Interactions. *Phys. Chem. Chem. Phys.* **2013**, *15*, 14377–14383.

(19) Grabowski, S. J. Tetrel Bond–σ-Hole Bond as a Preliminary Stage of the $S_N2$ Reaction. *Phys. Chem. Chem. Phys.* **2014**, *16*, 1824–1834.

(20) Raghavendra, B.; Arunan, E. Unpaired and σ Bond Electrons as H, Cl, and Li Bond Acceptors: An Anomalous One-Electron Blue-Shifting Chlorine Bond. *J. Phys. Chem. A* **2007**, *111*, 9699–9706.

(21) Lovejoy, C. M.; Nelson, D. D.; Nesbitt, D. J. Hindered Internal Rotation in Jet Cooled $H_2$-HF Complexes. *J. Chem. Phys.* **1987**, *87*, 5621–5628.

(22) Yu, Z.; Higgins, K. J.; Klemperer, W.; McCarthy, M. C.; Thaddeus, P.; Liao, K.; Jäger, W. Rotational Spectra of the van Der Waals Complexes of Molecular Hydrogen and OCS. *J. Chem. Phys.* **2007**, *127*, 054305-1-054305-8.

(23) Mani, D.; Arunan, E. The X–C···π (X = F, Cl, Br, CN) Carbon Bond. *J. Phys. Chem. A* **2014**, *118*, 10081–10089.

(24) Li, Q.; Guo, X.; Yang, X.; Li, W.; Cheng, J.; Li, H.-B. A σ-Hole Interaction with Radical Species as Electron Donors: Does Single-Electron Tetrel Bonding Exist? *Phys. Chem. Chem. Phys.* **2014**, *16*, 11617–11625.

(25) Asvany, O.; Yamada, K. M. T.; Brunken, S.; Potapov, A.; Schlemmer, S. Experimental Ground-State Combination Differences of $CH_5^+$. *Science* **2015**, *347*, 1346–1349.

(26) Wang, X.-G.; Carrington, T. Calculated Rotation-Bending Energy Levels of $CH_5^+$ and a Comparison with Experiment. *J. Chem. Phys.* **2016**, *144*, 204304-1-204304-12.

(27) Bader, R. F. W. *Atoms in Molecules: A Quantum Theory*; International Series of Monographs on Chemistry; Oxford University Press: Oxford, New York, **1994**.

(28) Marx, D.; Savin, A. Topological Bifurcation Analysis: Electronic Structure of $CH_5^+$. *Angew. Chem. Int. Ed. Engl.* **1997**, *36*, 2077–2080.

(29) Jensen, W. B. Extending Ball and Stick Models by Using Three-Center, Two-Electron Bonding Components. *J. Chem. Educ.* **1980**, *57*, 637–638.

(30) DeKock, R. L.; Bosma, W. B. The Three-Center, Two-Electron Chemical Bond. *J. Chem. Educ.* **1988**, *65*, 194–197.

(31) Bau, R.; Teller, R. G.; Kirtley, S. W.; Koetzle, T. F. Structures of Transition-Metal Hydride Complexes. *Acc. Chem. Res.* **1979**, *12*, 176–183.

(32) Green, J. C.; Green, M. L. H.; Parkin, G. The Occurrence and Representation of Three-Centre Two-Electron Bonds in Covalent Inorganic Compounds. *Chem. Commun.* **2012**, *48*, 11481–11503.

(33) Green, M. L. H.; Parkin, G. The Covalent Bond Classification Method and Its Application to Compounds That Feature 3-Center 2-Electron Bonds. In *The Chemical Bond III: 100 years old and getting stronger*; Mingos, D. M. P., Ed.; Structure and Bonding; Springer International Publishing: Cham, **2017**; pp 79–139.

(34) Jemmis, E. D.; Chandrasekhar, J.; Schleyer, P. von R. Stabilization of D3h Pentacoordinate Carbonium Ions. Linear Three-Center-Two-Electron Bonds. Implications for Aliphatic Electrophilic Substitution Reactions. *J. Am. Chem. Soc.* **1979**, *101*, 527–533.

(35) Beggs, D.; Lampe, F. $SiH_5^+$ Formation in Ionized Silane–Methane Mixtures. *J. Chem. Phys.* **1968**, *49*, 4230–4231.

(36) Schleyer, P. von R.; Apeloig, Y.; Arad, D.; Luke, B. T.; Pople, J. A. The Structure and Energy of $SiH_5^+$. Comparisons with $CH_5^+$ and $BH_5$. *Chem. Phys. Lett.* **1983**, *95*, 477–482.

(37) Boo, D. W.; Lee, Y. T. Infrared Spectroscopy of the Siliconium Ion, $SiH_5^+$. *J. Chem. Phys.* **1995**, *103*, 514–519.

(38) Senzer, S. N.; Abernathy, R. N.; Lampe, F. W. $GeH_5^+$ and the Proton Affinity of Monogermane. *J. Phys. Chem.* **1980**, *84*, 3066–3067.

(39) Kohda-Sudoh, S.; Ikuta, S.; Nomura, O.; Katagiri, S.; Imamura, M. Proton Affinity of $GeH_4$ and the Shape of $GeH_5^+$. *J. Phys. B At. Mol. Phys.* **1983**, *16*, L529–L531.

(40) Schreiner, P. R.; Schaefer, H. F.; Schleyer, P. von R. The Structures, Energies, Vibrational, and Rotational Frequencies, and Dissociation Energy of $GeH_5^+$. *J. Chem. Phys.* **1994**, *101*, 2141–2147.

(41) Frisch, M. J.; Trucks, G. W.; Schlegel, H. B.; Scuseria, G. E.; Robb, M. A.; Cheeseman, J. R.; Scalmani, G.; Barone, V.; Mennucci, B.; Petersson, G. A.; et al. *Gaussian 09*, Revision D. 01; Gaussian Inc: Wallingford, CT, **2009**.

(42) Keith, T. A. *AIMAll,* Version 16.05.18; TK Gristmill Software: Overland Park, KS, (aim.tkgristmill.com), **2016**.

(43) Glendening, E. D.; Badenhoop, J. K.; Reed, A. E.; Carpenter, J. E.; Bohmann, J. A.; Morales, C. M.; Landis, C. R.; F. Weinhold. *NBO 6.0.*; Theoretical Chemistry Institute, University of Wisconsin: Madison, WI, (nbo6.chem.wisc.edu), **2013**.

(44) Hu, C.-H.; Shen, M.; Schaefer, H. F. Toward the Infrared Spectroscopic Observation of $SiH_5^+$: The Silanium Ion. *Chem. Phys. Lett.* **1992**, *190*, 543–550.

(45) Koch, U.; Popelier, P. L. Characterization of C-H-O Hydrogen Bonds on the Basis of the Charge Density. *J. Phys. Chem.* **1995**, *99*, 9747–9754.

(46) Amezaga, N. J. M.; Pamies, S. C.; Peruchena, N. M.; Sosa, G. L. Halogen Bonding: A Study Based on the Electronic Charge Density. *J. Phys. Chem. A* **2010**, *114*, 552–562.

(47) Huber, K. P.; Herzberg, G. Constants of Diatomic Molecules, Hydrogen. In *NIST ChemistryWebBook*; NIST Standard Reference Database Number 69; National Institute of Standards and Technology: Gaithersberg, MD https://webbook.nist.gov/cgi/cbook.cgi?ID=C1333740&Mask=1000 (accessed Sep 10, 2018).

(48) Pitzer, K. S. Electron Deficient Molecules. i. the Principles of Hydroboron Structures. *J. Am. Chem. Soc.* **1945**, *67*, 1126–1132.

(49) Huber, K. P.; Herzberg, G.,*Molecular Spectra and Molecular Structure: IV. Constants of Diatomic Molecules*, Springer Science & Business Media, **1979**, 716

(50) Yoshikai, N.; Ammal, S. C.; Nakamura, E. L-Shaped Three-Center Two-Electron $(C-C-C)^+$ Bonding Array. *J. Am. Chem. Soc.* **2004**, *126*, 12941–12948.

(51) Thomson, J. J. XIX. Further Experiments on Positive Rays. *Lond. Edinb. Dublin Philos. Mag. J. Sci.* **1912**, *24*, 209–253.

(52) Gaillard, M. J.; Gemmell, D. S.; Goldring, G.; Levine, I.; Pietsch, W. J.; Poizat, J. C.; Ratkowski, A. J.; Remillieux, J.; Vager, Z.; Zabransky, B. J. Experimental Determination of the Structure of $H_3^+$. *Phys. Rev. A* **1978**, *17*, 1797–1803.

(53) Dennington, R.; Keith, T. A.; Millam, J. M. *GaussView,* Version 5; Semichem Inc: Shawnee Mission, KS, **2009**.

(54) Scholz, F.; Himmel, D.; Heinemann, F. W.; Schleyer, P. v. R.; Meyer, K.; Krossing, I. Crystal Structure Determination of the Nonclassical 2-Norbornyl Cation. *Science* **2013**, *341*, 62–64.

(55) Gnanasekar, S. P.; Arunan, E. Inter/Intramolecular Bonds in $TH_5^+$ (T= C/Si/Ge): H2 as Tetrel Bond Acceptor and the Uniqueness of Carbon Bonds. *J. Phys. Chem. A* **2019**, *123*, 1168–1176.

(56) Glendening, E. D.; Wright, S. J.; Weinhold, F. Efficient Optimization of Natural Resonance Theory Weightings and Bond Orders by Gram-Based Convex Programming. *J. Comput. Chem.* **2019**, *40*, 2028–2035.

(57) Glendening, E. D.; Landis, C. R.; Weinhold, F. Resonance Theory Reboot. *J. Am. Chem. Soc.* **2019**, *141*, 4156–4166.

(58) Bader, R. F. W.; Anderson, S. G.; Duke, A. J. Quantum Topology of Molecular Charge Distributions. 1. *J. Am. Chem. Soc.* **1979**, *101*, 1389–1395.

(59) Werstiuk, N. H.; Muchall, H. M. The Structure of the 2-Norbornyl Cation: The π-Complex and Beyond. *J. Phys. Chem. A* **2000**, *104*, 2054–2060.

(60) Bader, R. F. W.; Slee, T. S.; Cremer, D.; Kraka, E. Description of Conjugation and Hyperconjugation in Terms of Electron Distributions. *J. Am. Chem. Soc.* **1983**, *105*, 5061–5068.

(61) Darwent, B. deB. Bond Dissociation Energies in Simple Molecules. *Nat. Stand. Ref. Data Ser.*, **1970**, 31.

(62) Bohme, D. K.; Mackay, G. I.; Schiff, H. I. Determination of Proton Affinities from the Kinetics of Proton Transfer Reactions. VII. The Proton Affinities of $O_2$, $H_2$, Kr, O, $N_2$, Xe, $CO_2$, $CH_4$, $N_2O$, and CO. *J. Chem. Phys.* **1980**, *73*, 4976–4986.

(63) Cheng, T. M. H.; Lampe, F. W. $SiH_5^+$ and the Proton Affinity of Monosilane. *Chem. Phys. Lett.* **1973**, *19*, 532–534.

(64) Boys, S. F.; Bernardi, F. de. The Calculation of Small Molecular Interactions by the Differences of Separate Total Energies. Some Procedures with Reduced Errors. *Mol. Phys.* **1970**, *19*, 553–566.

(65) Archibong, E. F.; Leszczynski, J. Structures and Properties of $GeH_5^+$ Ions As Revealed by Post-Hartree-Fock Calculations. *J. Phys. Chem.* **1994**, *98*, 10084–10088.

(66) Mulliken, R. S. Bond Angles in Water-Type and Ammonia-Type Molecules and Their Derivatives. *J. Am. Chem. Soc.* **1955**, *77*, 887–891.

(67) Atwood, J. L.; Hrncir, D. C.; Rogers, R. D.; Howard, J. A. K. Novel Linear Al-H-Al Electron-Deficient Bond in $Na[(CH_3)_3Al\text{-}H\text{-}Al(CH_3)_3]$. *J. Am. Chem. Soc.* **1981**, *103*, 6787–6788.

(68) DuPré, D. B. Bonding Patterns in a Strong 3c2e C−H···C Hydrogen Bond. *J. Phys. Chem. A* **2005**, *109*, 622–628.

## 5.8. Supplementary Information

**Table S5.1.** Coordinates of the optimized geometry of $CH_5^+$ calculated at MP2/aug-cc-pVTZ.

| atom | x | y | z |
|---|---|---|---|
| **C** | -0.115764000 | -0.011463000 | 0.000032000 |
| **H** | -0.510846000 | -0.387023000 | -0.938354000 |
| **H** | -0.195563000 | 1.092843000 | -0.000671000 |
| **H** | -0.510591000 | -0.386038000 | 0.938903000 |
| **H** | 1.008258000 | 0.359068000 | -0.000022000 |
| **H** | 0.903323000 | -0.610072000 | -0.000051000 |

**Table S5.2.** Coordinates of the optimized geometry of $SiH_5^+$ calculated at MP2/aug-cc-pVTZ.

| atom | x | y | z |
|---|---|---|---|
| **Si** | 0.173904000 | 0.003360000 | -0.000211000 |
| **H** | -1.659941000 | -0.429283000 | 0.003157000 |
| **H** | 0.333466000 | -0.741721000 | -1.246320000 |
| **H** | 0.227230000 | 1.464584000 | -0.034053000 |
| **H** | 0.338675000 | -0.683861000 | 1.277955000 |
| **H** | -1.674087000 | 0.343243000 | 0.002218000 |

**Table S5.3.** Coordinates of the optimized geometry of $GeH_5^+$ calculated at MP2/aug-cc-pVTZ.

| atom | x | y | z |
|---|---|---|---|
| **Ge** | 0.094330000 | 0.001194000 | -0.000039000 |
| **H** | 0.148766000 | 1.500274000 | -0.015912000 |
| **H** | 0.232847000 | -0.749720000 | -1.289420000 |
| **H** | 0.234768000 | -0.722427000 | 1.304612000 |
| **H** | -1.821605000 | 0.351660000 | 0.000619000 |
| **H** | -1.813326000 | -0.417997000 | 0.001341000 |

**Table S5.4.** Normal modes of vibration for the $TH_5^+$ (T=C, Si, and Ge) molecules calculated at MP2/aug-cc-pVTZ. Frequency in $cm^{-1}$ and IR intensity in km/mol.

| $CH_5^+$ | | $SiH_5^+$ | | $GeH_5^+$ | |
|---|---|---|---|---|---|
| **frequency** | **IR intensity** | **frequency** | **IR intensity** | **frequency** | **IR intensity** |
| 254.5 | 45.0 | 46.5 | 0.3 | 109.3 | 0.3 |
| 752.5 | 200.0 | 655.3 | 1.9 | 610.3 | 0.1 |
| 1287.8 | 35.7 | 672.4 | 0.6 | 613.4 | 1.9 |
| 1301.7 | 52.2 | 773.5 | 102.6 | 671.0 | 74.5 |
| 1472.3 | 0.2 | 904.2 | 77.1 | 862.7 | 26.3 |
| 1501.9 | 0.2 | 940.3 | 58.9 | 883.7 | 34.3 |
| 1582.7 | 14.0 | 943.1 | 60.5 | 883.9 | 33.5 |
| 2514.9 | 64.5 | 1138.1 | 24.5 | 1026.6 | 24.8 |
| 2714.1 | 34.8 | 2354.2 | 0.0 | 2329.2 | 0.0 |
| 3029.7 | 108.8 | 2410.8 | 0.3 | 2369.0 | 0.2 |
| 3165.1 | 72.4 | 2419.3 | 0.7 | 2374.8 | 0.4 |
| 3266.0 | 77.3 | 4026.4 | 164.4 | 4054.2 | 189.5 |

**Table S5.5.** Coordinates of the optimized geometry of $CH_5^+$ $C_s$(I) saddle point calculated at MP2/aug-cc-pVTZ.

| atom | x | y | z |
|---|---|---|---|
| **C** | 0.115823000 | -0.000625000 | 0.014308000 |
| **H** | 0.358338000 | -0.854875000 | -0.629307000 |
| **H** | 0.534546000 | -0.015720000 | 1.010846000 |
| **H** | 0.346538000 | 0.885124000 | -0.591315000 |
| **H** | -0.965124000 | -0.486867000 | 0.059866000 |
| **H** | -0.969238000 | 0.476090000 | 0.064062000 |

**Table S5.6.** Coordinates of the optimized geometry of $CH_5^+$ $C_{2v}$ saddle point calculated at MP2/aug-cc-pVTZ.

| atom | x | y | z |
|---|---|---|---|
| **C** | 0.000000000 | 0.000000000 | 0.107706000 |
| **H** | 0.000000000 | 0.948440000 | 0.633390000 |
| **H** | 1.001291000 | 0.000000000 | -0.430927000 |
| **H** | 0.000000000 | -0.948440000 | 0.633390000 |
| **H** | 0.000000000 | 0.000000000 | -1.051162000 |
| **H** | -1.001291000 | 0.000000000 | -0.430927000 |

**Table S5.7.** Normal modes of vibration for the saddle point structures of $CH_5^+$ calculated at MP2/aug-cc-pVTZ. Frequency in $cm^{-1}$ and IR intensity in km/mol.

| $CH_5^+$ ($C_s$(II)) | | $CH_5^+$ ($C_{2v}$) | |
|---|---|---|---|
| **frequency** | **IR intensity** | **frequency** | **IR intensity** |
| -232.4 | 74.0 | -589.6 | 303.0 |
| 952.7 | 146.9 | 480.9 | 61.0 |
| 1138.2 | 69.1 | 1249.9 | 53.5 |
| 1331.2 | 28.2 | 1319.2 | 45.1 |
| 1478.5 | 0.9 | 1413.4 | 1.5 |
| 1504.1 | 1.1 | 1451.7 | 0.1 |
| 1610.0 | 15.8 | 1480.4 | 0.0 |
| 2490.5 | 67.6 | 2677.5 | 67.5 |
| 2731.4 | 33.0 | 2740.1 | 8.0 |
| 3070.4 | 75.2 | 2902.7 | 179.2 |
| 3128.1 | 122.2 | 3162.0 | 74.0 |
| 3273.6 | 63.9 | 3277.4 | 90.0 |

**Table S5.8.** Coordinates of the optimized geometry of $B_2H_6$.

| $B_2H_6$ | atom | x | y | z |
|---|---|---|---|---|
| **MP2/6-311++G(d,p)** | B | 0.884983000 | -0.000001000 | 0.000016000 |
| | H | 1.456492000 | -1.040890000 | 0.000783000 |
| | H | -0.000060000 | -0.002048000 | -0.975257000 |
| | H | 1.455587000 | 1.041402000 | -0.000843000 |
| | B | -0.884975000 | -0.000011000 | -0.000023000 |
| | H | -1.456210000 | -1.041067000 | 0.000844000 |
| | H | -0.000038000 | 0.001412000 | 0.975277000 |
| | H | -1.455811000 | 1.041250000 | -0.000770000 |
| **B3LYP/ aug-cc-pVTZ** | B | 0.879060000 | 0.000002000 | 0.000000000 |
| | H | 1.456440000 | -1.035011000 | 0.000165000 |
| | H | 0.000002000 | -0.000482000 | -0.973617000 |
| | H | 1.456195000 | 1.035150000 | -0.000164000 |
| | B | -0.879060000 | 0.000001000 | 0.000001000 |
| | H | -1.456421000 | -1.035024000 | 0.000166000 |
| | H | 0.000003000 | 0.000221000 | 0.973610000 |
| | H | -1.456219000 | 1.035135000 | -0.000166000 |

**Table S5.9.** Coordinates of the optimized geometry of $CH_5^+$.

| $CH_5^+$ | atom | x | y | z |
|---|---|---|---|---|
| **MP2/6-311++G(d,p)** | C | -0.117225000 | -0.010424000 | 0.000029000 |
| | H | -0.522944000 | -0.374575000 | -0.942459000 |
| | H | -0.165147000 | 1.099610000 | -0.000620000 |
| | H | -0.522646000 | -0.373640000 | 0.942993000 |
| | H | 1.018554000 | 0.339584000 | -0.000053000 |
| | H | 0.895533000 | -0.628433000 | -0.000033000 |
| **B3LYP/ aug-cc-pVTZ** | C | -0.111686000 | -0.015102000 | -0.000018000 |
| | H | -0.506616000 | -0.394768000 | -0.939702000 |
| | H | 0.915281000 | -0.598295000 | -0.000080000 |
| | H | -0.233975000 | 1.087875000 | 0.000496000 |
| | H | -0.506303000 | -0.395374000 | 0.939574000 |
| | H | 1.001729000 | 0.391172000 | -0.000181000 |

**Table S5.10.** Coordinates of the optimized geometry of $CH_3$-$C_2H_2^+$.

| $CH_3$-$C_2H_2^+$ | atom | x | y | z |
|---|---|---|---|---|
| **MP2/6-311++G(d,p)** | C | -0.496561000 | 0.696938000 | 0.000024000 |
| | H | -0.523646000 | 1.772848000 | 0.000010000 |
| | C | -0.849223000 | -0.491806000 | -0.000021000 |
| | H | -1.205995000 | -1.506866000 | -0.000029000 |
| | C | 0.987048000 | -0.122231000 | -0.000050000 |
| | H | 1.429771000 | 0.228849000 | 0.929854000 |
| | H | 1.429708000 | 0.228216000 | -0.930185000 |
| | H | 1.022577000 | -1.220453000 | 0.000632000 |
| **B3LYP/ aug-cc-pVTZ** | C | 0.325875000 | 0.673075000 | -0.000006000 |
| | H | 0.310449000 | 1.749789000 | 0.000008000 |
| | C | 1.035155000 | -0.341979000 | 0.000009000 |
| | H | 1.565189000 | -1.276948000 | -0.000015000 |
| | C | -1.018319000 | -0.214196000 | 0.000000000 |
| | H | -1.524715000 | 0.063292000 | -0.921828000 |
| | H | -1.524816000 | 0.063435000 | 0.921730000 |
| | H | -0.882371000 | -1.300961000 | 0.000089000 |

**Table S5.11.** Coordinates of the optimized geometry of $B_3^+$.

| $B_3^+$ | atom | x | y | z |
|---|---|---|---|---|
| **MP2/6-311++G(d,p)** | B | 0.809859000 | 0.467574000 | 0.467574000 |
| | B | -0.809859000 | 0.467268000 | 0.467268000 |
| | B | 0.000000000 | -0.934842000 | -0.934842000 |
| **B3LYP/ aug-cc-pVTZ** | B | 0.779388000 | -0.449986000 | 0.000000000 |
| | B | -0.779388000 | -0.449952000 | 0.000000000 |
| | B | 0.000000000 | 0.899938000 | 0.000000000 |

**Table S5.12.** Coordinates of the optimized geometry of $C_3H_3^+$.

| $C_3H_3^+$ | atom | x | y | z |
|---|---|---|---|---|
| **MP2/6-311++G(d,p)** | C | -0.686124000 | 0.396575000 | -0.000013000 |
| | C | 0.686501000 | 0.395923000 | -0.000013000 |
| | C | -0.000377000 | -0.792484000 | -0.000006000 |
| | H | -1.623730000 | 0.938430000 | -0.000029000 |
| | H | 1.624621000 | 0.936886000 | -0.000028000 |
| | H | -0.000892000 | -1.875401000 | 0.000242000 |
| **B3LYP/ aug-cc-pVTZ** | C | -0.723081000 | 0.302946000 | -0.000015000 |
| | C | 0.623895000 | 0.474738000 | -0.000015000 |
| | C | 0.099181000 | -0.777673000 | -0.000013000 |
| | H | -1.719062000 | 0.720188000 | -0.000004000 |
| | H | 1.483285000 | 1.128586000 | -0.000003000 |
| | H | 0.235809000 | -1.848842000 | 0.000267000 |

**Table S5.13.** Coordinates of the optimized geometry of $H_3^+$.

| $H_3^+$ | atom | x | y | z |
|---|---|---|---|---|
| **MP2/6-311++G(d,p)** | H | 0.000000000 | -0.504607000 | 0.000000000 |
| | H | -0.437019000 | 0.252295000 | 0.000000000 |
| | H | 0.437019000 | 0.252312000 | 0.000000000 |
| **B3LYP/ aug-cc-pVTZ** | H | 0.440091000 | -0.254046000 | 0.000000000 |
| | H | -0.440091000 | -0.254071000 | 0.000000000 |
| | H | 0.000000000 | 0.508117000 | 0.000000000 |

**Table S5.14.** Coordinates of the optimized geometry of 2-norbornyl$^+$.

| 2-norbornyl$^+$ | atom | x | y | z |
|---|---|---|---|---|
| **MP2/6-311++G(d,p)** | C | -0.159592000 | -1.395414000 | -0.000301000 |
| | C | -1.125629000 | 0.001038000 | -0.699744000 |
| | C | 0.975841000 | 0.677280000 | 0.000031000 |
| | C | 1.259575000 | -0.834173000 | -0.000368000 |
| | H | -0.476331000 | -1.976742000 | 0.873001000 |
| | H | -0.476486000 | -1.976054000 | -0.874018000 |
| | H | 1.806803000 | -1.152782000 | 0.889636000 |
| | H | 1.806594000 | -1.152421000 | -0.890628000 |
| | C | 0.020721000 | 0.849442000 | -1.195141000 |
| | H | -0.339709000 | 1.882227000 | -1.291409000 |
| | H | 0.427640000 | 0.519021000 | -2.153382000 |
| | C | -1.125382000 | 0.000584000 | 0.700023000 |
| | H | -1.944306000 | -0.376659000 | 1.305372000 |
| | C | 0.021068000 | 0.848793000 | 1.195570000 |
| | H | -0.339377000 | 1.881509000 | 1.292505000 |
| | H | 0.428295000 | 0.517870000 | 2.153505000 |
| | H | -1.944727000 | -0.375870000 | -1.305071000 |
| | H | 1.851993000 | 1.324601000 | 0.000063000 |
| **B3LYP/ aug-cc-pVTZ** | C | -0.474700000 | 1.355535000 | -0.002554000 |
| | C | 1.042039000 | 0.456227000 | -0.693087000 |
| | C | -0.599978000 | -1.020444000 | 0.000247000 |
| | C | -1.500109000 | 0.232025000 | -0.002960000 |
| | H | -0.433542000 | 2.006329000 | 0.868989000 |
| | H | -0.430418000 | 2.003700000 | -0.875894000 |
| | H | -2.135704000 | 0.278565000 | 0.878599000 |
| | H | -2.132742000 | 0.276301000 | -0.886778000 |
| | C | 0.345765000 | -0.779562000 | -1.194580000 |
| | H | 1.089087000 | -1.575375000 | -1.300974000 |
| | H | -0.151542000 | -0.647522000 | -2.152721000 |
| | C | 1.039107000 | 0.458632000 | 0.695175000 |
| | H | 1.615864000 | 1.142061000 | 1.301993000 |
| | C | 0.340819000 | -0.775716000 | 1.198093000 |
| | H | 1.083479000 | -1.571285000 | 1.310371000 |
| | H | -0.160624000 | -0.640445000 | 2.153640000 |
| | H | 1.620685000 | 1.138010000 | -1.299984000 |
| | H | -1.122202000 | -1.970526000 | 0.000757000 |

**Table S5.15.** Coordinates of the optimized geometry of $SiH_5^+$.

| $SiH_5^+$ | atom | x | y | z |
|---|---|---|---|---|
| **MP2/6-311++G(d,p)** | Si | 0.173865000 | 0.003461000 | -0.000220000 |
| | H | -1.660427000 | -0.429703000 | 0.003307000 |
| | H | 0.335597000 | -0.738909000 | -1.242081000 |
| | H | 0.226063000 | 1.459705000 | -0.034291000 |
| | H | 0.341017000 | -0.680654000 | 1.273879000 |
| | H | -1.676364000 | 0.341102000 | 0.002265000 |
| **B3LYP/ aug-cc-pVTZ** | Si | 0.176314000 | 0.003534000 | -0.000200000 |
| | H | -1.676098000 | -0.435333000 | 0.003219000 |
| | H | 0.336761000 | -0.740019000 | -1.254640000 |
| | H | 0.220348000 | 1.471679000 | -0.030808000 |
| | H | 0.341860000 | -0.687758000 | 1.283005000 |
| | H | -1.691270000 | 0.341956000 | 0.002021000 |

**Table S5.16.** Coordinates of the optimized geometry of $Al_2H_7^-$.

| $Al_2H_7^-$ | atom | x | y | z |
|---|---|---|---|---|
| **MP2/6-311++G(d,p)** | Al | 1.628085000 | -0.000147000 | -0.001235000 |
| | H | 2.336666000 | -0.727411000 | -1.250949000 |
| | H | 1.682029000 | -0.837602000 | 1.366354000 |
| | H | 1.998670000 | 1.556810000 | 0.143025000 |
| | Al | -1.628107000 | 0.000134000 | -0.001219000 |
| | H | -2.329279000 | 0.783636000 | -1.220662000 |
| | H | -2.014655000 | -1.557572000 | 0.081344000 |
| | H | -1.673102000 | 0.782786000 | 1.398673000 |
| | H | -0.000044000 | -0.000486000 | -0.485894000 |
| **B3LYP/ aug-cc-pVTZ** | Al | -1.697354000 | 0.000006000 | -0.000168000 |
| | H | -2.177254000 | 0.724866000 | -1.358492000 |
| | H | -1.995006000 | 0.839840000 | 1.341887000 |
| | H | -2.085003000 | -1.561927000 | 0.088842000 |
| | Al | 1.697382000 | -0.000005000 | -0.000181000 |
| | H | 2.175900000 | -0.838385000 | -1.291988000 |
| | H | 2.087479000 | 1.563253000 | -0.043957000 |
| | H | 1.993523000 | -0.723183000 | 1.408462000 |
| | H | -0.000002000 | -0.004481000 | -0.140217000 |

# CHAPTER 6

# Rotational spectra and structures of weakly bound complexes of $CH_3F$: $CH_3F\cdots H_2O$, $CH_3F\cdots Ar$, and $CH_3F\cdots CH_3F$

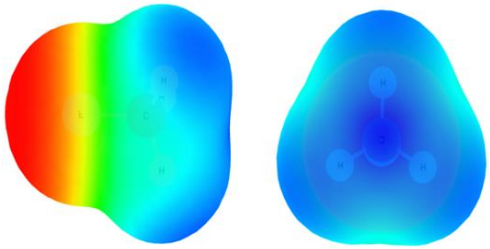

CHAPTER 6

# ROTATIONAL SPECTRA AND STRUCTURES OF WEAKLY BOUND COMPLEXES OF $CH_3F$: $CH_3F\cdots H_2O$, $CH_3F\cdots Ar$, AND $CH_3F\cdots CH_3F$

## 6.1. Introduction

A comprehensive study of weakly bound complexes of $CH_3X$ (X= O, F, Cl, Br, $NO_2$, $NF_2$) with a variety of electron rich donor moieties led to the proposal of the carbon bond[1]. This study showed that the $CH_3F\cdots H_2O$ complex would be an ideal candidate to investigate the tetrel interaction. The σ-hole over the methyl face of $CH_3F$ can accept electron density to form a tetrel bond. The $CH_3F$ molecule can also form a hydrogen bonded $CH_3F\cdots H_2O$ complex where the fluorine atom accepts an H-bond from water. Hydrogen bonds involving the C-F bond are not so common. A matrix isolation infrared spectroscopic study of $CH_3F\cdots H_2O$ found that the complex is bound by a bent O-H···F-C hydrogen bond[2]. This result helped dispel doubts about the existence of hydrogen bonds involving fluorine containing organic molecules. Thus, the complexes, $CH_3F\cdots H_2O$, $CH_3F\cdots Ar$, and $CH_3F\cdots CH_3F$ provide an opportunity to experimentally investigate both the hydrogen bond as well as the tetrel bond.

Monat et al. performed *ab initio* calculations on the structures of the $CH_3F\cdots H_2O$ complex to obtain a model potential for the system[3]. They found the structure having a bent O-H···F-C hydrogen bond to be the global minimum structure. Rosenberg[4] questioned whether the $CH_3F\cdots H_2O$ complex forms a hydrogen bond or not because of the prevalent ideas about the nonexistence of C-F H-bonds. The matrix isolation

infrared spectroscopic studies by Futami et al.[2] confirmed the presence of a hydrogen bonded structure. Rosenberg later studied the microsolvation of $CH_3F$ in order to understand the solubility of $CH_3F$ in water[5]. He did so by investigating structures of $CH_3F\cdots(H_2O)_n$ (n= 1-6). All the structures reported in his work bears a resemblance to the structures of the corresponding $(H_2O)_{n+1}$ cluster. Structures where the $H_2O$ donates electron density to the positively charged methyl face of $CH_3F$ forming an F-C···O carbon bond were not considered. He concludes that the limited solubility of methyl fluoride in water is because $CH_3F$ does not effectively bind to a growing water cluster. However, it is known that the solubility of methyl fluoride in water is nearly 100 times more than that of methane in water.

Futami et al. also recorded a matrix isolation infrared spectrum of the $CH_3F\cdots CH_3F$ dimer[2]. The DFT calculations they performed, found two structures, an antiparallel one and a linear one. From these calculations they conclude that the antiparallel structure "seems to be stabilized by the dipole-dipole interaction of $CH_3F$ rather than the intermolecular hydrogen bonding between H and F atoms"[2]. The matrix isolation IR spectrum indicates the presence of an antiparallel structure. This antiparallel structure has no permanent electric dipole moment and therefore would have no observable rotational spectrum. The linear structure of the $(CH_3F)_2$ dimer where the dipoles are arranged in a head to tail manner would be tetrel bonded.

In this Chapter, we discuss the rotational spectra and structures of the $CH_3F\cdots H_2O$, $CH_3F\cdots Ar$, and $CH_3F\cdots CH_3F$ complexes. We have tentatively assigned and observed the rotational spectra of the hydrogen bonded $CH_3F\cdots H_2O$ complex, the T-shaped $CH_3F\cdots Ar$ complex, and possibly the tetrel bonded linear structure of the $CH_3F\cdots CH_3F$ dimer. These are preliminary results and none of the isotopologues for these complexes have been studied to ascertain the geometrical parameters. Detailed Atoms in Molecules (AIM) analysis has been carried out to understand the non-covalent interactions that bind these complexes. Some of these complexes are bound by hydrogen bonds involving the fluorine atom and some are carbon/tetrel bonded.

## 6.2. Method

### 6.2.1. Experimental details

The rotational spectra of the $CH_3F\cdots H_2O$, $CH_3F\cdots Ar$, and $CH_3F\cdots CH_3F$ complexes have been recorded using the pulsed supersonic jet Fourier transform microwave spectrometer of the PhLAM Laboratory in Lille. Details of this spectrometer have been described by Kassi et al.[6] The complexes were formed by expanding a mixture of $CH_3F$ in a carrier gas via a 0.8 mm nozzle into a vacuum chamber. The $H_2O$ was introduced through an injector just before expansion. The mixture of $CH_3F$ in 2-3 atm of either neon or argon was prepared in a steel cylinder. Signals were optimum when a 10% mixture of $CH_3F$ in the carrier gas was used. Water was kept in the injector at room temperature and heating the injector produced no significant changes in the intensity of the lines obtained. The rotational transitions for the $CH_3F\cdots H_2O$ complex were identified by their dependence on both $CH_3F$ and $H_2O$ and the fact that they could be observed using both Ar and Ne as carrier gas. The $CH_3F\cdots Ar$ lines were identified by their disappearance when Ne was used as carrier gas and the fact that they required only $CH_3F$. The signals which do not require $H_2O$ and appeared in both Ar and Ne beams were identified as belonging to the $CH_3F$ dimer. The spectra were collected using low resolution while scanning for transitions and the observed rotational lines were later averaged at a higher number of points to obtain the high-resolution spectra.

### 6.2.2. Computational details

The structures of the $CH_3F$ complexes were optimized at the various levels of theory using *Gaussian 09*[7]. Herein, we report the results obtained at MP2/aug-cc-pVDZ and MP2/aug-cc-pVQZ levels of theory. Harmonic frequency calculations were performed to determine if the structures obtained were true minima on the potential energy surface. The centrifugal distortion constants for the complexes were calculated using the freq=vibrot keyword. The binding energies of the complexes corrected for the basis set superposition error (BSSE) were obtained using Boys and Bernardi's counterpoise method[8]. The binding energies for the complexes were also obtained by extrapolating to the complete basis set (CBS) limit. The following expression was used for the extrapolation[9,10].

$$E_X = E_{CBS} + \alpha e^{-(X-1)} + \beta e^{-(X-1)^2}$$

Here, X= 2, 3, 4 for the calculations done at aug-cc-pVDZ, aug-cc-pVTZ, and aug-cc-pVQZ, respectively. The rotational transitions were predicted from the calculated rotational constants using Pickett's SPCAT program[11,12]. The electron density topologies for the optimized geometries of all the three complexes have been calculated using the *AIMAll* software[13]. This was done using the wavefunctions obtained from the *Gaussian 09* calculations at MP2/aug-cc-pVDZ. This provides an understanding of the non-covalent interactions present in the system.

## 6.3. Methyl fluoride···water complex

### 6.3.1. Optimized structures

Two structures were optimized for the $CH_3F\cdots H_2O$ complex and are shown in Figure 6.1. The first one is the hydrogen bonded structure where the water donates an H-bond to the F atom of $CH_3F$ forming a bent O-H···F hydrogen bond. The hydrogen bonded structure can be envisaged as two dipoles ($CH_3F$ and $H_2O$) arranged in an antiparallel manner. It seems like a weak C-H···O hydrogen bond is also possible as a secondary interaction, forming a cyclic hydrogen bonded network. The second structure is a carbon/tetrel bonded structure where the electron rich $H_2O$ moiety donates electron density via the O atom to the σ-hole over the methyl face of $CH_3F$ forming a linear F-C···O tetrel bond. The calculated rotational constants, electric dipole moment components, and the binding energies are given in Table 6.1. Both the structures are nearly prolate asymmetric tops, and one expects the predominantly *a*-type spectra to follow a B+C pattern.

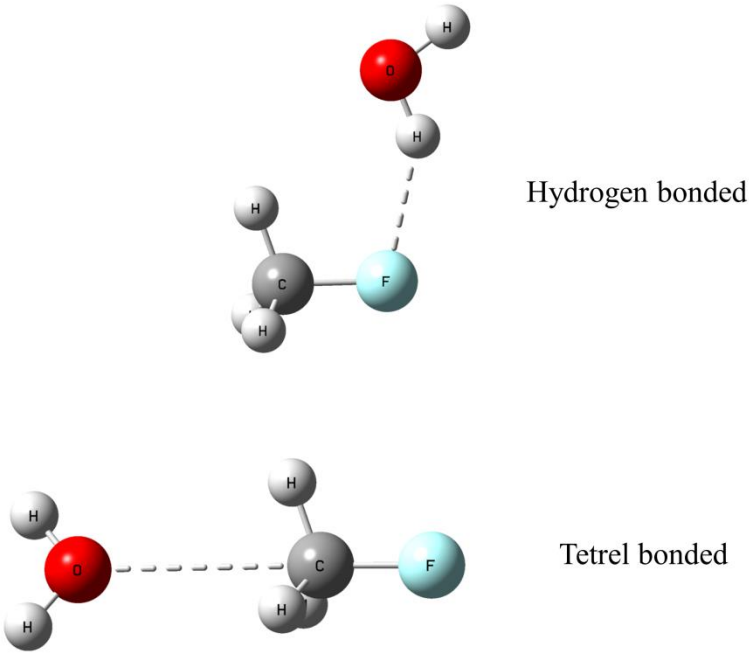


**Figure 6.1.** Structures of the $CH_3F\cdots H_2O$ complex optimized at MP2/aug-cc-pVQZ.

**Table 6.1.** The rotational constants (MHz), electric dipole moment components (debye), and the binding energy (ΔE) with BSSE corrections calculated at MP2/aug-cc-pVQZ, and the binding energy at the CBS limit ($kJmol^{-1}$) for the optimized structures of the $CH_3F\cdots H_2O$ complex.

| | **Hydrogen bonded** | **Tetrel bonded** |
|---|---|---|
| **Rotational constants (MHz)** | | |
| **A** | 26638.2 | 116271.6 |
| **B** | 4703.2 | 2578.4 |
| **C** | 4101.4 | 2563.4 |
| **Dipole moments (D)** | | |
| $\mu_a$ | 0.79 | 4.06 |
| $\mu_b$ | 0.05 | 0.00 |
| $\mu_c$ | 0.00 | 0.02 |
| **Binding energy ($kJmol^{-1}$)** | | |
| **ΔE (BSSE)** | -16.2 | -7.7 |
| **ΔE (CBS)** | -16.9 | -8.0 |

### 6.3.2. Rotational spectra

Search for the rotational transitions was started by using a 5% $CH_3F$ mixture in 2.5 atm of neon, with the $H_2O$ in the injector at room temperature. We searched the regions predicted for the $K_a$=0 lines corresponding to 1←0 and 2←1 transitions for

the hydrogen bonded structure (7950-8450 MHz, 8550-8800 MHz, and 17150-18000 MHz). However, only rotational transitions pertaining to the water dimer could be observed. The concentration was then changed to 10% $CH_3F$ mixture in 3 atm of Ne which led to observation of the lines corresponding to 1←0 and 2←1 transitions at 8400.5 MHz and 16788.2 MHz, respectively. Based on this assignment, the $K_a$=1 lines for the 2←1 transition was found at 16181.1 MHz and 17418.9 MHz. The observed B+C value is 8400 MHz which is in agreement with the predicted B+C for the H-bonded structure. The optimum power is -6 dBm and correlates well with the calculated *a*-dipole moment of the H-bonded structure. Transitions corresponding to higher J levels were beyond the range of the spectrometer and *b*-type lines could not be found despite careful searches at the predicted regions. A number of lines that depend on both $CH_3F$ and $H_2O$ are observed but could not be assigned; these are listed in Table 6.2.

**Table 6.2.** Observed rotational transitions (MHz) that depend on both $CH_3F$ and $H_2O$.

| Observed frequency (MHz) | Optimum power (dBm) |
|---|---|
| 8400.57 | -6 |
| 8400.68 | -6 |
| 11546.99 | -12 |
| 12916.22 | 0 |
| 14092.82 | -6 |
| 15199.99 | -9 |
| 15203.28 | 5 |
| 15203.95 | 5 |
| 15236.19 | -3 |
| 15439.98 | -9 |
| 15457.83 | -9 |
| 16181.09 | -6 |
| 16181.13 | -6 |
| 16788.03 | -6 |
| 16788.25 | -6 |
| 16959.93 | 0 |
| 17031.33 | 3 |
| 17097.49 | -6 |
| 17106.94 | 0 |
| 17184.40 | -12 |
| 17418.42 | -6 |
| 17418.88 | -6 |
| 17557.24 | 3 |

The observed transitions are split in to two. This could either be due to the internal rotation of the methyl rotor about the $C_3$ axis which could lead to A/E states or the internal rotation of the $H_2O$ moiety about its $C_2$ axis which interchanges the equivalent hydrogen atoms leading to two states that correspond to the ortho and para states of water. We fit the lower and higher frequency sets separately. They are fit to a Watson's S-reduced Hamiltonian using Pickett's SPFIT program[11,12]. The A rotational constant is kept fixed at the calculated value while the B and C rotational constants and the $D_J$ centrifugal distortion constant are fitted. The RMS deviation of the fit is quite large and this is because only four *a*-type transitions are being fit (see Table 6.3 and 6.4).

**Table 6.3.** Assigned transition frequencies for the $CH_3F\cdots H_2O$ complex.

| Transition | Lower frequency (MHz) | obs-calc (MHz) | Higher frequency (MHz) | obs-calc (MHz) |
|---|---|---|---|---|
| $1_{10}$ -$0_{00}$ | 8400.5665 | 0.0002 | 8400.6745 | 0.0002 |
| $2_{12}$ -$1_{11}$ | 16181.0950 | -0.3694 | 16181.1250 | -0.3324 |
| $2_{02}$ -$1_{01}$ | 16788.0317 | 0.7094 | 16788.2449 | 0.6935 |
| $2_{11}$ -$1_{10}$ | 17418.4223 | -0.3400 | 17418.8843 | -0.3324 |

**Table 6.4.** Experimental rotational and distortion constants for the hydrogen bonded $CH_3F\cdots H_2O$ complex.

| Constant | Lower frequency set | Higher frequency set |
|---|---|---|
| **A (MHz)** | [26638.17] | [26638.17] |
| **B (MHz)** | 4509.7(7) | 4509.9(6) |
| **C (MHz)** | 3891.0(7) | 3891.0(6) |
| **$D_J$ (kHz)** | 42.(76) | 42.(74) |
| **n** | 4 | 4 |
| **RMS (kHz)** | 434.5 | 424.8 |

We were interested in finding the tetrel bonded structure of the $CH_3F\cdots H_2O$ complex. Extensive searches were conducted in the regions predicted for the tetrel bonded structure by attenuating the power to -30 dBm, since the *a*-dipole moment is quite large (4D). However, no transitions were found in these regions corresponding to a nearly prolate asymmetric top tetrel bonded structure.

### 6.3.3. Atoms in Molecules (AIM) analysis

The electron density topologies for the two structures of the $CH_3F\cdots H_2O$ complex are shown in Figure 6.2. The hydrogen bonded structure shows two weak interactions forming a closed network which is indicated by the presence of a ring critical point (RCP). A bond critical point (BCP) is found, where the $H_2O$ donates an H-bond to the F atom of $CH_3F$ forming a bent O-H···F-C bond. A weak C-H···O hydrogen bond is also present, where the C-H bond of the methyl fluoride interacts with the O atom of water. However, the angle for this interaction is calculated to be 116.7°. The $\varrho$ and $\nabla^2\varrho$ values of the O-H···F bond suggest that this is a much stronger interaction than the C-H···O bond. The tetrel bonded structure shows a BCP between the electron rich O atom of $H_2O$ and the positive C atom of $CH_3F$. The values for the $\varrho$ and $\nabla^2\varrho$ at the BCPs for both these complexes are within the ranges suggested by Koch and Popelier[14] for a C-H···O hydrogen bond.

**Table 6.5.** The electron density ($\varrho$) and Laplacian of electron density ($\nabla^2\varrho$) at the BCP (in au) and the calculated geometrical parameters (MP2/aug-cc-pVDZ) involved in the non-covalent interaction.

| $CH_3F\cdots H_2O$ | BCP | $\varrho$ | $\nabla^2\varrho$ | bond | R (Å) | angle | deg. (°) |
|---|---|---|---|---|---|---|---|
| **Hydrogen bonded** | O-H···F | 0.0193 | +0.0731 | H···F | 1.99 | ∠OHF | 146.5 |
| | C-H···O | 0.0071 | +0.0336 | H···O | 2.58 | ∠CHO | 116.7 |
| **Tetrel bonded** | F-C···O | 0.0063 | +0.0312 | C···O | 3.02 | ∠FCO | 179.4 |

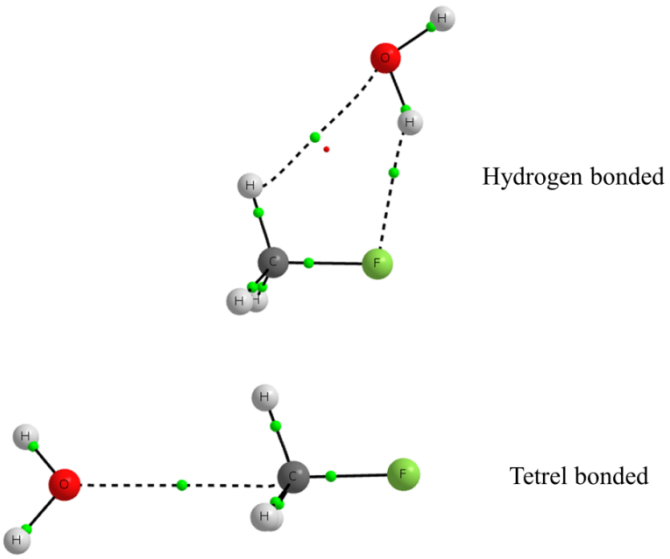


**Figure 6.2.** Molecular graphs for the structures of the $CH_3F\cdots H_2O$ complex obtained using wavefunctions calculated at MP2/aug-cc-pVDZ.

## 6.4. Methyl fluoride···argon complex

### 6.4.1. Optimized structures

Three different structures are optimized for the $CH_3F$···Ar complex. The structures optimized at MP2/aug-cc-pVQZ are shown in Figure 6.3. The T-shaped structure has the Ar atom positioned nearly perpendicular to the C-F bond axis much like the structures observed for the other $CH_3X$···Ar complexes[15–17]. The tetrel bonded structure has the Ar approaching the positive methyl face of $CH_3F$ in a linear arrangement. This structure resembles the pre-transition state for an $S_N2$ reaction where the Ar can be considered to be equivalent to $Cl^-$. The linear structure has Ar approaching from the fluorine end of the C-F bond axis. The calculated rotational constants and electric dipole moment components and the binding energies for all three complexes are tabulated in Table 6.6. All the three structures are very close in energy. These structures are similar to those calculated for the $CH_3F$···He complex[18]. The rotational constants and electric dipole moment components for the tetrel bonded and the linear structures are very similar and could possibly be differentiated only by isotopic substitution.

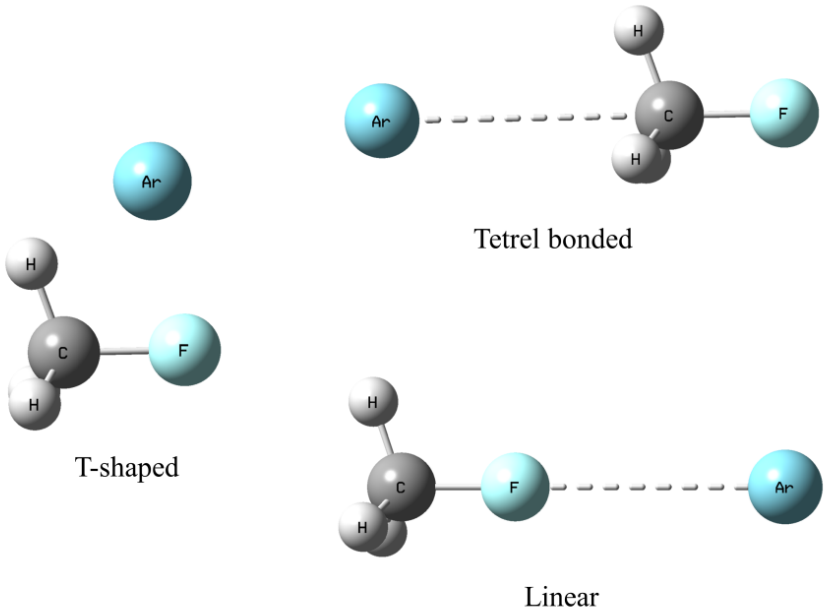


**Figure 6.3.** Structures of the $CH_3F$···Ar complex optimized at MP2/aug-cc-pVQZ.

**Table 6.6.** The rotational constants (MHz), electric dipole moment components (debye), and the binding energy (ΔE) with BSSE corrections calculated at MP2/aug-cc-pVQZ, and the binding energy at the CBS limit ($kJmol^{-1}$) for the optimized structures of the $CH_3F\cdots Ar$ complex.

| | T-shaped | Tetrel bonded | Linear |
|---|---|---|---|
| **Rotational constants (MHz)** | | | |
| **A** | 25907.9 | 158182.5 | 158137.0 |
| **B** | 2312.7 | 1465.8 | 1664.6 |
| **C** | 2152.0 | 1465.8 | 1664.6 |
| **Dipole moments (D)** | | | |
| $\mu_a$ | 0.2 | 2.0 | 2.0 |
| $\mu_b$ | 1.8 | 0.0 | 0.0 |
| $\mu_c$ | 0.0 | 0.0 | 0.0 |
| **Binding energy ($kJmol^{-1}$)** | | | |
| **ΔE (BSSE)** | -2.2 | -2.1 | -1.4 |
| **ΔE (CBS)** | -3.1 | -3.2 | -2.2 |

### 6.4.2. Rotational spectra

A number of lines that do not depend on the presence of water were observed while searching for the *b*-type rotational transitions of the $CH_3F\cdots H_2O$ complex (See Table 6.7). These lines disappeared when the carrier gas was changed from argon to neon. It was concluded that these lines could belong to the $CH_3F\cdots Ar$ complex. Listed in Table 6.8 are the seven lines that could be assigned to rotational transitions of the T-shaped $CH_3F\cdots Ar$ complex. These lines are fitted to a semi-rigid rotor Hamiltonian. Since the high-resolution spectra is yet to be recorded, and dedicated searches for other lines based on these assignments yet to be made, the RMS deviation for the fit is quite large. However, the fitted rotational constants (See Table 6.9) indicate that the T-shaped $CH_3F\cdots Ar$ complex is observed. The many unassigned lines could belong to the other two structures optimized for the $CH_3F\cdots Ar$ complex since they are all very close in energy.

**Table 6.7.** Observed rotational transitions (MHz) that depend on both $CH_3F$ and Ar.

| Observed frequency (MHz) | Optimum power (dBm) |
|---|---|
| 8076.13 | 0 |
| 8212.32 | -3 |
| 8244.24 | -6 |
| 9119.30 | -12 |
| 11887.72 | -12 |
| 12097.82 | -9 |
| 12112.07 | 0 |
| 13578.05 | -9 |
| 13733.05 | -6 |
| 14464.96 | -6 |
| 14579.79 | -9 |
| 14604.48 | -9 |
| 14613.08 | -3 |
| 14624.98 | -9 |
| 14693.48 | -3 |
| 14750.13 | -9 |
| 15173.05 | -6 |
| 15225.35 | -6 |
| 15236.19 | -3 |
| 15697.18 | -3 or 0 |
| 15753.03 | -3 or 0 |
| 16145.46 | 0 |
| 16936.48 | 0 |
| 17026.85 | -12 |
| 17106.94 | 0 |
| 17593.53 | -9 |
| 17720.51 | -6 |
| 17762.96 | -6 |
| 17770.34 | -3 |

**Table 6.8.** Assigned transition frequencies for the $CH_3F\cdots Ar$ complex.

| Transition | Frequency (MHz) | obs-calc (MHz) |
|---|---|---|
| $2_{12}$ -$1_{11}$ | 8076.1300 | 0.1840 |
| $2_{02}$ -$1_{01}$ | 8244.2400 | -0.1577 |
| $3_{13}$ -$2_{12}$ | 12112.0100 | 0.0588 |
| $3_{03}$ -$2_{02}$ | 12362.6500 | -0.0884 |
| $4_{14}$ -$3_{13}$ | 16145.4600 | -0.1403 |
| $4_{04}$ -$3_{03}$ | 16476.6000 | 0.1494 |
| $7_{07}$ -$6_{16}$ | 9119.3000 | 0.0002 |

**Table 6.9.** Experimental rotational and distortion constants for the T-shaped $CH_3F\cdots Ar$ complex.

| Constant | T-shaped |
|---|---|
| **A (MHz)** | 23441.(2) |
| **B (MHz)** | 2146.26(8) |
| **C (MHz)** | 1976.80(5) |
| **$D_J$ (kHz)** | 22.(1) |
| **n** | 7 |
| **RMS (kHz)** | 126.5 |

### 6.4.3. Atoms in Molecules (AIM) analysis

The electron density topologies for the structures of the $CH_3F\cdots Ar$ complex were calculated at MP2/aug-cc-pVDZ. The molecular graphs are shown in Figure 6.4. Bond critical points (BCP) are found between the Ar atom and $CH_3F$ molecule. In the T-shaped structure two BCPs are found, one between Ar and C and the other between Ar and F. In the tetrel bonded structure a BCP is found between the Ar and C atom. For the linear structure a BCP is found between the Ar atom and the fluorine. The electron density ($\varrho$) and the Laplacian of electron density ($\nabla^2\varrho$) are given along with pertinent geometrical parameters in Table 6.10. The values for the $\varrho$ and $\nabla^2\varrho$ at the BCPs are indicative of a closed shell interaction. However, the values are just out of the ranges suggested by Koch and Popelier[14] for a weak C-H···O bond ($\varrho$= 0.002-0.034 and $\nabla^2\varrho$=0.024-0.139). The values obtained for the $CH_3F\cdots Ar$ complex are similar to those seen in other complexes of Ar such as the Propargyl alcohol···Ar complex[19]. One can compare the values of $\varrho$ and $\nabla^2\varrho$ at the Ar···C and Ar···F BCPs for the T-shaped with the tetrel bonded and linear structures. One can see that despite the interaction being perpendicular in the T-shaped and linear in the other two structures the $\varrho$ and $\nabla^2\varrho$ values are similar, indicating that this interaction has no directional preference.

**Table 6.10.** The electron density ($\varrho$) and Laplacian of electron density ($\nabla^2\varrho$) at the BCP (in au) and the calculated geometrical parameters (MP2/aug-cc-pVDZ) involved in the non-covalent interaction.

| $CH_3F\cdots Ar$ | BCP | $\varrho$ | $\nabla^2\varrho$ | bond | R (Å) | angle | deg. (°) |
|---|---|---|---|---|---|---|---|
| **T-shaped** | C···Ar | 0.0035 | +0.0141 | C···Ar | 3.57 | ∠ArCF | 74.1 |
| | F···Ar | 0.0036 | +0.0172 | F···Ar | 3.46 | ∠ArFC | 82.9 |
| **Tetrel bonded** | F-C···Ar | 0.0039 | +0.0170 | C···Ar | 3.45 | ∠ArCF | 180.0 |
| **Linear** | C-F···Ar | 0.0036 | +0.0174 | F···Ar | 3.35 | ∠ArFC | 180.0 |

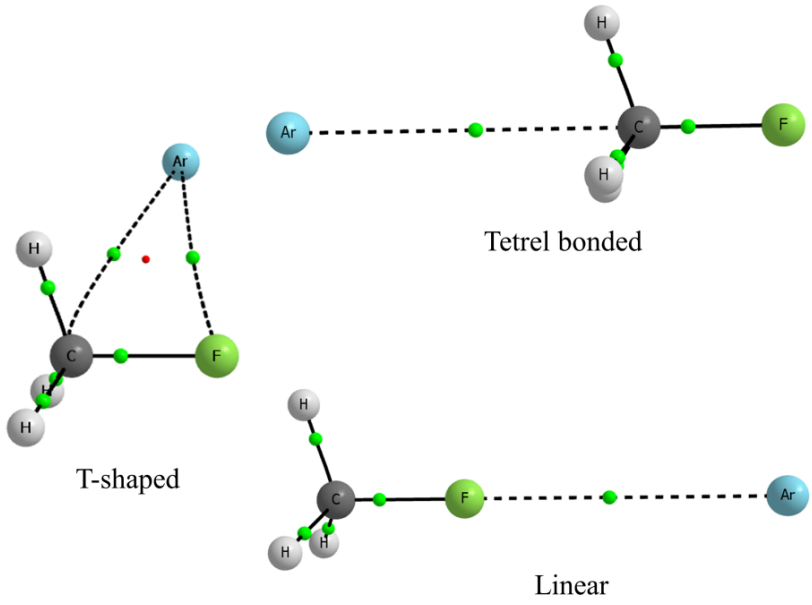


**Figure 6.4.** Molecular graphs for the structures of the $CH_3F\cdots Ar$ complex obtained from wavefunctions at MP2/aug-cc-pVDZ.

## 6.5. Methyl fluoride dimer

### 6.5.1. Optimized structures

The possible structures for the $(CH_3F)_2$ dimer were optimized at MP2/aug-cc-pVDZ and are shown in Figure 6.5. The antiparallel structure is formed by the antiparallel arrangement of the dipoles of two $CH_3F$ molecules and is also stabilized by two symmetrical C-H···F hydrogen bonds. This antiparallel arrangement of the dipoles leads to a zero net electric dipole moment for the complex and therefore, the pure rotational spectrum for this structure cannot be observed. The linear and the skewed-linear structures are similar, with the electron rich fluorine atom pointing towards the positive methyl face of $CH_3F$ forming a carbon/tetrel bond. These two structures differ only in the orientation of the donor methyl fluoride moiety. The skewed-linear structure is a saddle point structure at other levels of theory. The rotational constants, dipole moment components, and binding energies are tabulated below (see Table 6.11).

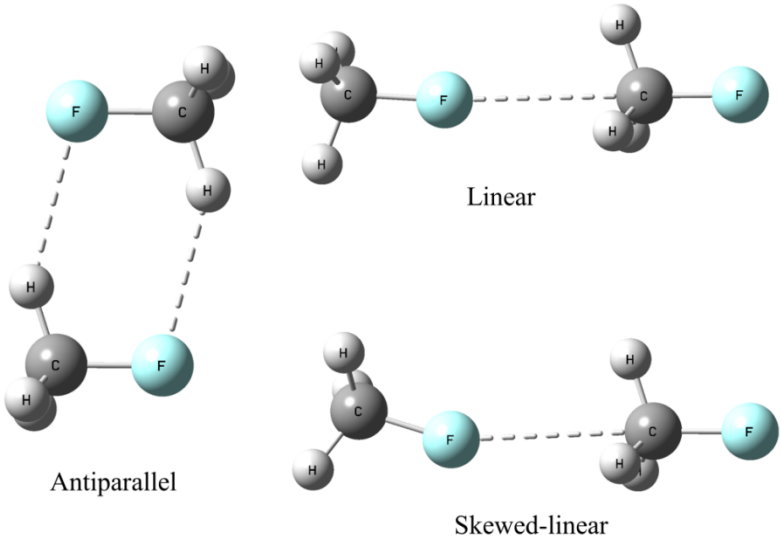


**Figure 6.5.** Structures of the $CH_3F$ dimer optimized at MP2/aug-cc-pVDZ.

**Table 6.11.** The rotational constants (MHz), electric dipole moment components (debye), and the binding energy (ΔE) with BSSE corrections ($kJmol^{-1}$) calculated at MP2/aug-cc-pVDZ, for the optimized structures of the $CH_3F$ dimer.

| | Antiparallel | Linear | Skewed-linear |
|---|---|---|---|
| **Rotational constants (MHz)** | | | |
| **A** | 12407.1 | 76092.2 | 64590.4 |
| **B** | 2500.7 | 1388.4 | 1408.0 |
| **C** | 2139.1 | 1388.2 | 1403.1 |
| **Dipole moments (D)** | | | |
| $\mu_a$ | 0.0 | 4.2 | 4.2 |
| $\mu_b$ | 0.0 | 0.1 | 0.4 |
| $\mu_c$ | 0.0 | 0.0 | 0.0 |
| **Binding energy ($kJmol^{-1}$)** | | | |
| **ΔE (BSSE)** | -8.7 | -5.9 | -5.8 |

### 6.5.2. Rotational spectra

Several lines were observed while searching for the $CH_3F\cdots H_2O$ and $CH_3F\cdots Ar$ complexes which do not depend on $H_2O$ and had similar intensities both in neon and argon beams. These lines could possibly belong to the $CH_3F\cdots CH_3F$ dimer. Since the antiparallel structure has no net dipole moment and hence no rotational spectrum, it is possible that these lines arise from either the linear or the skewed-linear structures. The $CH_3F$ dimer has two methyl groups and internal rotations involving the two

methyl rotors could possibly lead to a complicated rotational spectrum. The observed frequencies are yet to be assigned (Table 6.12) and dedicated searches for this dimer need to be carried out.

**Table 6.12.** Observed rotational transitions (MHz) that depend only on $CH_3F$. Optimum power is in dBm.

| Frequency | Optimum power | Frequency | Optimum power |
|---|---|---|---|
| 9172.35 | -9 or -12 | 14573.27 | -12 |
| 11113.90 | -15 | 14575.92 | -12 |
| 11146.94 | -15 | 14576.69 | -12 |
| 11157.74 | -15 | 14591.68 | -12 |
| 11177.51 | -15 | 14638.72 | -12 |
| 11190.10 | -15 | 14676.69 | -6 |
| 11242.48 | -9 or -12 | 14859.07 | -9 |
| 11338.60 | -6 | 14884.26 | -9 |
| 11367.86 | -6 | 15363.36 | -6 |
| 11407.40 | -6 | 15439.98 | -9 |
| 12171.98 | -6 | 15457.83 | -9 |
| 13492.30 | -12 or -15 | 16213.33 | -12 |
| 13500.30 | -12 or -15 | 16225.49 | -12 |
| 13505.97 | -12 | 16228.23 | -12 |
| 14522.35 | -12 | 16232.75 | -12 |
| 14525.39 | -9 | 16235.00 | -12 |
| 14529.58 | -12 | 16919.90 | -3 |
| 14542.16 | -12 | 16920.10 | -3 |
| 14558.93 | -9 or-12 | 16929.91 | -6 |
| 14566.20 | -12 | 17064.56 | 3 |
| 14569.02 | -12 | | |

### 6.5.3. Atoms in Molecules (AIM) analysis

Electron density topological analysis was carried out for the $CH_3F$ dimer. The molecular graphs for the dimer are shown in Figure 6.6. The antiparallel structure shows two symmetrical interactions between the F atoms of one of the $CH_3F$ moieties with the H atom of the other $CH_3F$ unit. These two C-H···F hydrogen bonds form a closed network indicated by the ring critical point. Both the linear and skewed-linear structures show an interaction between the F atoms of the donor $CH_3F$ moiety with the positive methyl face of the acceptor $CH_3F$. The low values of $\rho$ and positive values for the $\nabla^2\rho$ at the BCPs are indicative of a closed shell interaction and are given in Table 6.13. These values are within the ranges suggested by Koch and Popelier[14] for the C-H···O bond. Thus, the antiparallel structure is bound by two symmetrical C-H···F hydrogen bonds contrary to the geometrical results obtained from DFT calculations

by Futami et al[2]. Based on the ϱ and $\nabla^2\varrho$ values, it can be concluded that the linear and skewed-linear structures are tetrel bonded structures where the F atom donates electron density to the σ-hole over the methyl face of $CH_3F$.

**Table 6.13.** The electron density (ϱ) and Laplacian of electron density ($\nabla^2\varrho$) at the BCP (in au) and the calculated geometrical parameters (MP2/aug-cc-pVDZ) involved in the non-covalent interaction.

| $CH_3F\cdots CH_3F$ | BCP | ϱ | $\nabla^2\varrho$ | bond | R (Å) | angle | deg. (°) |
|---|---|---|---|---|---|---|---|
| **Antiparallel** | C-H···F | 0.0091 | +0.0344 | H···F | 2.42 | ∠CHF | 147.8 |
| **Linear** | F-C···F | 0.0055 | +0.0315 | C···F | 2.95 | ∠FCF | 179.4 |
| **Skewed-linear** | F-C···F | 0.0056 | +0.0319 | C···F | 2.95 | ∠FCF | 177.4 |

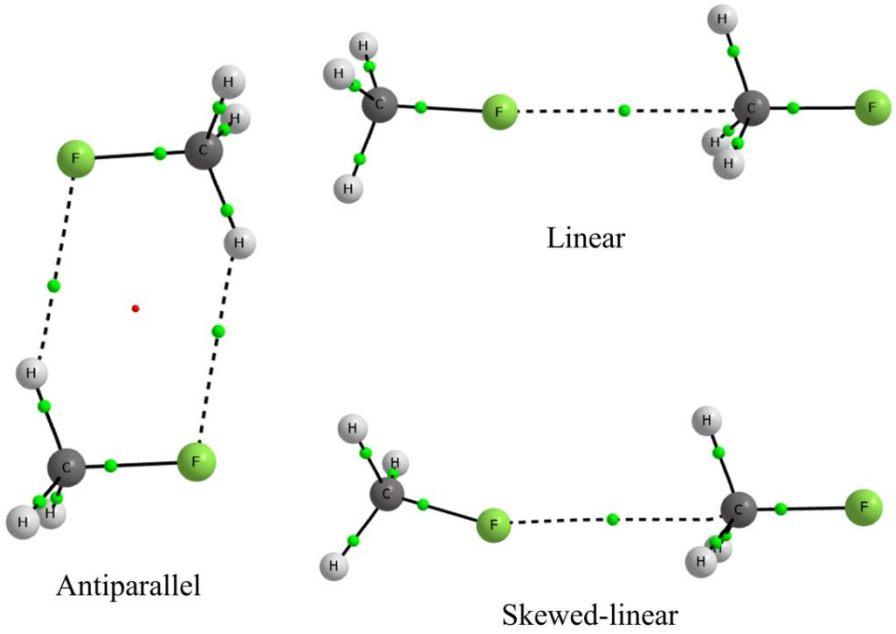


**Figure 6.6.** Molecular graphs for the structures of the $CH_3F$ dimer obtained from wavefunctions at MP2/aug-cc-pVDZ.

## 6.6. Summary

Microwave spectroscopic results are reported for the complexes, $CH_3F\cdots H_2O$, $CH_3F\cdots Ar$, and $CH_3F\cdots CH_3F$. We find evidence for the O-H···F hydrogen bonded $CH_3F\cdots H_2O$ structure but the tetrel bonded structure is yet to be found. The tetrel bonded structure could possibly be observed under different expansion conditions such as using a helium beam. A few lines could be tentatively fit to the T-shaped $CH_3F\cdots Ar$ complex. A large number of lines remain unassigned and could possibly correspond to the other structures of the $CH_3F\cdots Ar$ complex, since they are very close in energy. The observed lines corresponding to the $(CH_3F)_2$ dimer suggest that either the linear or skewed-linear structures is present as the antiparallel structure would not have a rotational spectrum.

## 6.7. References


(1) Mani, D.; Arunan, E. The X–C⋯Y (X= O/F, Y= O/S/F/Cl/Br/N/P) 'Carbon Bond' and Hydrophobic Interactions. *Phys. Chem. Chem. Phys.* **2013**, *15*, 14377–14383.

(2) Futami, Y.; Kudoh, S.; Takayanagi, M.; Nakata, M. Structures of $CH_3F\cdots CH_3F$ and $CH_3F\cdots H_2O$ Complexes in a Supersonic Jet Studied by Matrix-Isolation Infrared Spectroscopy and Density-Functional-Theory Calculation. *Chem. Phys. Lett.* **2002**, *357*, 209–216.

(3) Monat, J. E.; Toczyłowski, R. R.; Cybulski, S. M. Ab Initio Study of the $CH_3F\cdots H_2O$ Complex. *J. Phys. Chem. A* **2001**, *105*, 9004–9013.

(4) Rosenberg, R. E. Does Fluoromethane Form a Hydrogen Bond with Water? *J. Phys. Chem. A* **2012**, *116*, 10842–10849.

(5) Rosenberg, R. E. Microsolvation of Fluoromethane. *J. Phys. Chem. A* **2016**, *120*, 7519–7528.

(6) Kassi, S.; Petitprez, D.; Wlodarczak, G. Microwave Fourier Transform Spectroscopy of t-Butylchloride and t-Butylbromide Isotopic Species. *J. Mol. Struct.* **2000**, *517–518*, 375–386.

(7) Frisch, M. J.; Trucks, G. W.; Schlegel, H. B.; Scuseria, G. E.; Robb, M. A.; Cheeseman, J. R.; Scalmani, G.; Barone, V.; Mennucci, B.; Petersson, G. A.; et al. *Gaussian 09,* Revision D. 0; Gaussian Inc: Wallingford, CT, **2009**.

(8) Boys, S. F.; Bernardi, F. de. The Calculation of Small Molecular Interactions by the Differences of Separate Total Energies. Some Procedures with Reduced Errors. *Mol. Phys.* **1970**, *19*, 553–566.

(9) Peterson, K. A.; Woon, D. E.; Dunning, T. H. Benchmark Calculations with Correlated Molecular Wave Functions. IV. The Classical Barrier Height of the $H+H_2 \rightarrow H_2+H$ Reaction. *J. Chem. Phys.* **1994**, *100*, 7410–7415.

(10) Woon, D. E.; Dunning, T. H. Benchmark Calculations with Correlated Molecular Wave Functions. VI. Second Row A $_2$ and First Row/Second Row AB Diatomic Molecules. *J. Chem. Phys.* **1994**, *101*, 8877–8893.

(11) JPL Molecular Spectroscopy https://spec.jpl.nasa.gov/ (accessed Aug 26, 2020).

(12) Pickett, H. M. The Fitting and Prediction of Vibration-Rotation Spectra with Spin Interactions. *J. Mol. Spectrosc.* **1991**, *148*, 371–377.

(13) Keith, T. A. *AIMAll,* Version 16.05.18; TK Gristmill Software: Overland Park, KS, (aim.tkgristmill.com), **2016.**

(14) Koch, U.; Popelier, P. L. Characterization of C-H-O Hydrogen Bonds on the Basis of the Charge Density. *J. Phys. Chem.* **1995**, *99*, 9747–9754.

(15) Fraser, G. T.; Suenram, R. D.; Lovas, F. J. Nearly Free Internal Rotation in Ar–$CH_3Cl$. *J. Chem. Phys.* **1987**, *86*, 3107–3114.

(16) Ford, R. S.; Suenram, R. D.; Fraser, G. T.; Lovas, F. J.; Leopold, K. R. Rotational Spectrum and Structure of the Complex Ar–$CH_3CN$. *J. Chem. Phys.* **1991**, *94*, 5306–5312.

(17) Lovas, F. J.; Sobhanadri, J. Microwave Rotational Spectral Study of $CH_3CN$–$H_2O$ and Ar–$CH_3CN$. *J. Mol. Spectrosc.* **2015**, *307*, 59–64.

(18) Higgins, K. J.; Klemperer, W. Structure and Energy Difference of Two Isomers of He–$CH_3F$. *J. Chem. Phys.* **2005**, *122*, 244309-1-244309-12.

(19) Mani, D.; Arunan, E. Microwave Spectroscopic and Atoms in Molecules Theoretical Investigations on the Ar···Propargyl Alcohol Complex: Ar···H-O, Ar···π, and Ar···C Interactions. *ChemPhysChem* **2013**, *14*, 754–763.

## 6.8. Supplementary Information

**Table S6.1.** Cartesian coordinates for the H-bonded structure of the $CH_3F\cdots H_2O$ complex calculated at MP2/aug-cc-pVQZ.

| atom | x | y | z |
|---|---|---|---|
| **C** | -1.302332000 | -0.537110000 | -0.000002000 |
| **H** | -1.908479000 | -0.653359000 | -0.891719000 |
| **H** | -0.477691000 | -1.241600000 | -0.000046000 |
| **H** | -1.908413000 | -0.653392000 | 0.891755000 |
| **F** | -0.773176000 | 0.755552000 | 0.000001000 |
| **O** | 1.895408000 | -0.219411000 | 0.000006000 |
| **H** | 2.709503000 | 0.285850000 | -0.000044000 |
| **H** | 1.194388000 | 0.440481000 | 0.000005000 |

**Table S6.2.** Cartesian coordinates for the tetrel bonded structure of the $CH_3F\cdots H_2O$ complex calculated at MP2/aug-cc-pVQZ.

| atom | x | y | z |
|---|---|---|---|
| **C** | -0.722570000 | 0.003107000 | -0.015172000 |
| **H** | -0.350010000 | -0.058601000 | 1.001067000 |
| **H** | -0.380726000 | -0.849890000 | -0.591067000 |
| **H** | -0.385827000 | 0.922810000 | -0.480968000 |
| **F** | -2.112067000 | -0.002502000 | 0.013060000 |
| **O** | 2.328264000 | -0.000358000 | 0.001582000 |
| **H** | 2.912839000 | -0.760788000 | 0.015330000 |
| **H** | 2.921636000 | 0.753204000 | 0.016474000 |

**Table S6.3.** Normal modes of vibration for the $CH_3F\cdots H_2O$ complex calculated at MP2/aug-cc-pVQZ. Frequency in $cm^{-1}$ and IR intensity in km/mol.

| Hydrogen bonded | | Tetrel bonded | |
|---|---|---|---|
| **frequency** | **IR intensity** | **frequency** | **IR intensity** |
| 46.2 | 1.0 | 3.8 | 0.1 |
| 84.7 | 136.8 | 68.0 | 2.2 |
| 98.4 | 30.4 | 69.8 | 7.9 |
| 159.5 | 13.2 | 85.4 | 0.3 |
| 306.9 | 112.2 | 114.3 | 69.8 |
| 388.4 | 73.1 | 116.7 | 221.6 |
| 1045.8 | 110.9 | 1060.8 | 130.2 |
| 1210.4 | 1.3 | 1203.5 | 1.4 |
| 1221.2 | 0.6 | 1204.2 | 1.3 |
| 1502.8 | 0.1 | 1485.9 | 0.4 |
| 1521.9 | 5.8 | 1518.6 | 4.8 |
| 1525.6 | 5.1 | 1520.4 | 4.4 |
| 1641.5 | 77.2 | 1636.4 | 73.4 |
| 3100.5 | 28.1 | 3102.5 | 31.9 |
| 3210.8 | 15.9 | 3208.7 | 21.5 |
| 3214.5 | 7.3 | 3212.9 | 18.4 |
| 3799.3 | 79.5 | 3835.5 | 9.2 |
| 3943.8 | 130.2 | 3959.0 | 84.3 |

**Table S6.4.** Cartesian coordinates for the T-shaped structure of the $CH_3F\cdots Ar$ complex calculated at MP2/aug-cc-pVQZ.

| atom | x | y | z |
|---|---|---|---|
| **C** | -0.629620000 | -1.795522000 | 0.000000000 |
| **H** | -0.847519000 | -2.859039000 | 0.000000000 |
| **H** | -1.039511000 | -1.328194000 | 0.890108000 |
| **H** | -1.039511000 | -1.328194000 | -0.890108000 |
| **F** | 0.744918000 | -1.623696000 | 0.000000000 |
| **Ar** | 0.000000000 | 1.716768000 | 0.000000000 |

**Table S6.5.** Cartesian coordinates for the tetrel bonded structure of the $CH_3F\cdots Ar$ complex calculated at MP2/aug-cc-pVQZ.

| atom | x | y | z |
|---|---|---|---|
| **C** | 0.000000000 | 0.000000000 | -1.414741000 |
| **H** | 0.000000000 | 1.027960000 | -1.065343000 |
| **H** | 0.890239000 | -0.513980000 | -1.065343000 |
| **H** | -0.890239000 | -0.513980000 | -1.065343000 |
| **F** | 0.000000000 | 0.000000000 | -2.799824000 |
| **Ar** | 0.000000000 | 0.000000000 | 2.049050000 |

**Table S6.6.** Cartesian coordinates for the linear structure of the $CH_3F\cdots Ar$ complex calculated at MP2/aug-cc-pVQZ.

| atom | x | y | z |
|---|---|---|---|
| **C** | 0.000000000 | 0.000000000 | -2.654130000 |
| **H** | 0.000000000 | 1.028108000 | -3.002493000 |
| **H** | -0.890368000 | -0.514054000 | -3.002493000 |
| **H** | 0.890368000 | -0.514054000 | -3.002493000 |
| **F** | 0.000000000 | 0.000000000 | -1.268555000 |
| **Ar** | 0.000000000 | 0.000000000 | 2.019403000 |

**Table S6.7.** Normal modes of vibration for the $CH_3F\cdots Ar$ complex calculated at MP2/aug-cc-pVQZ. Frequency in $cm^{-1}$ and IR intensity in km/mol.

| **T-shaped** | | **Tetrel bonded** | | **Linear** | |
|---|---|---|---|---|---|
| **frequency** | **IR intensity** | **frequency** | **IR intensity** | **frequency** | **IR intensity** |
| 41.0 | 2.5 | 47.6 | 0.0 | 15.9 | 6.8 |
| 53.4 | 0.0 | 49.8 | 6.8 | 15.9 | 6.8 |
| 58.9 | 5.9 | 49.8 | 6.8 | 38.9 | 0.1 |
| 1075.2 | 99.9 | 1075.6 | 119.0 | 1074.4 | 115.8 |
| 1211.9 | 1.2 | 1213.1 | 0.8 | 1212.2 | 1.4 |
| 1212.3 | 1.2 | 1213.1 | 0.8 | 1212.2 | 1.4 |
| 1501.7 | 0.8 | 1499.3 | 0.7 | 1501.6 | 1.9 |
| 1522.1 | 7.1 | 1522.1 | 4.0 | 1523.7 | 5.2 |
| 1522.9 | 6.7 | 1522.1 | 4.0 | 1523.7 | 5.2 |
| 3089.9 | 28.8 | 3089.2 | 37.8 | 3091.0 | 34.3 |
| 3194.8 | 19.6 | 3194.9 | 18.4 | 3196.1 | 20.6 |
| 3195.0 | 24.8 | 3194.9 | 18.4 | 3196.1 | 20.6 |

**Table S6.8.** Cartesian coordinates for the antiparallel structure of the $CH_3F\cdots CH_3F$ complex calculated at MP2/aug-cc-pVDZ.

| atom | x | y | z |
|---|---|---|---|
| **C** | 1.785520000 | -0.608302000 | 0.000207000 |
| **H** | 2.351205000 | -0.876557000 | -0.901837000 |
| **H** | 0.794968000 | -1.079887000 | -0.001026000 |
| **H** | 2.348797000 | -0.876287000 | 0.903838000 |
| **F** | 1.604312000 | 0.796121000 | -0.000246000 |
| **C** | -1.785603000 | 0.608290000 | 0.000210000 |
| **H** | -0.795107000 | 1.079995000 | 0.000160000 |
| **H** | -2.349939000 | 0.876072000 | 0.903240000 |
| **H** | -2.350289000 | 0.876619000 | -0.902438000 |
| **F** | -1.604216000 | -0.796108000 | -0.000247000 |

**Table S6.9.** Cartesian coordinates for the linear structure of the $CH_3F\cdots CH_3F$ complex calculated at MP2/aug-cc-pVDZ.

| atom | x | y | z |
|---|---|---|---|
| **C** | -2.827469000 | 0.034204000 | 0.000058000 |
| **H** | -3.127757000 | 0.721670000 | 0.801744000 |
| **H** | -3.233526000 | -0.970338000 | 0.177248000 |
| **H** | -3.147108000 | 0.415419000 | -0.978706000 |
| **F** | -1.417971000 | -0.054036000 | -0.000130000 |
| **C** | 1.531101000 | 0.001487000 | 0.000111000 |
| **H** | 1.187124000 | -0.258493000 | 1.009122000 |
| **H** | 1.190481000 | -0.746146000 | -0.727217000 |
| **H** | 1.177730000 | 1.001464000 | -0.281447000 |
| **F** | 2.943667000 | 0.012066000 | -0.000065000 |

**Table S6.10.** Cartesian coordinates for the skewed-linear structure of the $CH_3F\cdots CH_3F$ complex calculated at MP2/aug-cc-pVDZ.

| atom | x | y | z |
|---|---|---|---|
| **C** | -1.516178000 | 0.004839000 | 0.001902000 |
| **H** | -1.138248000 | 1.034620000 | -0.031010000 |
| **H** | -1.185052000 | -0.555289000 | -0.881491000 |
| **H** | -1.187858000 | -0.496740000 | 0.920829000 |
| **F** | -2.928207000 | 0.049564000 | -0.001594000 |
| **C** | 2.791374000 | 0.142350000 | -0.000210000 |
| **H** | 3.385337000 | -0.751719000 | -0.230727000 |
| **H** | 3.042733000 | 0.529648000 | 0.996016000 |
| **H** | 2.940011000 | 0.915119000 | -0.765924000 |
| **F** | 1.427307000 | -0.222761000 | -0.000389000 |

**Table S6.11.** Normal modes of vibration for the $CH_3F\cdots CH_3F$ complex calculated at MP2/aug-cc-pVDZ. Frequency in $cm^{-1}$ and IR intensity in km/mol.

| **Antiparallel** | | **Linear** | | **Skewed-linear** | |
|---|---|---|---|---|---|
| **frequency** | **IR intensity** | **frequency** | **IR intensity** | **frequency** | **IR intensity** |
| 16.2 | 11.5 | 10.2 | 5.6 | 6.8 | 2.9 |
| 49.4 | 0.0 | 15.2 | 5.3 | 8.0 | 3.0 |
| 60.9 | 3.2 | 18.4 | 0.0 | 20.0 | 3.0 |
| 62.5 | 0.0 | 62.0 | 7.5 | 65.3 | 7.8 |
| 105.1 | 0.0 | 62.4 | 7.3 | 67.5 | 6.7 |
| 111.9 | 29.5 | 72.3 | 0.2 | 74.1 | 1.5 |
| 1012.2 | 0.0 | 1023.3 | 254.1 | 1023.1 | 244.9 |
| 1023.3 | 199.3 | 1030.4 | 3.4 | 1030.6 | 11.4 |
| 1186.2 | 3.1 | 1183.8 | 2.0 | 1183.3 | 2.1 |
| 1186.4 | 0.0 | 1184.1 | 1.9 | 1184.5 | 2.6 |
| 1194.2 | 0.8 | 1185.1 | 1.1 | 1184.9 | 0.3 |
| 1195.5 | 0.0 | 1185.3 | 1.0 | 1185.5 | 0.7 |
| 1469.7 | 0.0 | 1465.2 | 0.0 | 1464.7 | 0.1 |
| 1473.4 | 1.5 | 1469.7 | 2.7 | 1470.1 | 2.5 |
| 1487.9 | 5.4 | 1488.4 | 7.4 | 1488.2 | 6.6 |
| 1492.0 | 0.0 | 1488.5 | 7.7 | 1488.4 | 5.9 |
| 1494.9 | 0.0 | 1489.6 | 1.0 | 1489.5 | 2.6 |
| 1497.8 | 6.4 | 1489.7 | 0.9 | 1489.9 | 1.9 |
| 3093.5 | 69.7 | 3093.6 | 44.4 | 3093.4 | 42.6 |
| 3094.7 | 0.0 | 3099.4 | 24.2 | 3099.7 | 25.8 |
| 3205.1 | 0.0 | 3208.8 | 19.3 | 3208.3 | 19.5 |
| 3205.7 | 45.0 | 3208.8 | 19.1 | 3208.6 | 19.0 |
| 3220.8 | 0.0 | 3216.2 | 22.6 | 3215.6 | 23.4 |
| 3221.2 | 10.4 | 3216.5 | 22.1 | 3217.7 | 21.4 |

# CHAPTER 7

# Conclusions, summary and outlook

CHAPTER 7

# CONCLUSIONS, SUMMARY AND OUTLOOK

The structure of a molecule furnishes information about its properties and functions. This Thesis reports the structures of non-covalently bound complexes to understand the nature of inter/intra molecular interactions. The structures are investigated using rotational spectroscopy and the results are complemented by computational studies. A home-built Balle-Flygare type pulsed nozzle Fourier transform microwave spectrometer is used to record the rotational spectra. Bader's Atoms in Molecules (AIM) theory is used to understand the nature of the interactions present in the complex. The complexes studied in this Thesis focus on hydrogen bonded and tetrel bonded interactions. Below we summarize the results of this Thesis focussing first on H-bonded complexes followed by the tetrel bonded complexes.

The rotational spectrum of the hydrogen bonded propargyl alcohol···water complex was studied in *Chapter 3*. This complex provided an opportunity to study the nature of hydrogen bonds and how they influence the structure of the complex when multiple donor/acceptor sites are available for hydrogen bonding. The hydroxyl group can act as either a donor or an acceptor of the H-bond. When a complex is formed between alcohols and water it is of interest to note the donor/acceptor roles played by each monomer unit. The rotational spectrum of the global minimum structure, G-PW-1a was observed. This structure is bound by a strong O-H···O hydrogen bond and a secondary interaction involving an O-H···π bond. The hydroxyl group of the propargyl alcohol donates an O-H···O H-bond to water, while the water donates an O-H···π H-bond to the acetylenic π-bond of the propargyl alcohol, forming a closed H-bonded network. This study also explores the donor/acceptor capabilities of other small alcohols in a complex with water. A general trend is observed, where electron donating

groups on the alcohol make the alcohol an H-bond acceptor in a complex with water, whereas electron withdrawing groups make the alcohol an H-bond donor in a complex with water.

Hydrogen bonds involving the fluorine atom were explored in *Chapter 6*. The rotational spectrum of the hydrogen bonded methyl fluoride···water complex was studied. We find a structure where the $CH_3F$ is bound to $H_2O$ by a bent O-H···F hydrogen bond. The Atoms in Molecules (AIM) analysis reveals that a weak C-H···O hydrogen bond is also present in this structure. In this chapter, we also studied the structures of the methyl fluoride dimer. The AIM analysis finds that the antiparallel structure for the dimer is bound by two symmetrical C-H···F hydrogen bonds. This structure has a zero net dipole moment and hence, we cannot observe a rotational spectrum corresponding to this structure.

*Chapter 5* explores the structure of the $CH_5^+$ protonated methane. The structure of $CH_5^+$ has been debated for years and we intended to approach the structural analysis from the perspective of intermolecular interactions. The $H_3O^+$ and $NH_4^+$ ions are formed by the protonation of $H_2O$ and $NH_3$, respectively. Precursor hydrogen bonded complexes such as $H_2O$···HX and $NH_3$···HX are responsible for the protonation. Global minimum structures for the $CH_4$···HX complexes are the ones where HX donates the H-bond to the C center. One can then expect $CH_5^+$ to form a trigonal bipyramidal structure. However, the prevailing consensus based on experimental and theoretical studies was that it was a loosely bound complex of $CH_3^+$ and $H_2$. This suggests that the $CH_5^+$ can also be thought of as a tetrel bonded complex of $CH_3^+$ with $H_2$ where the σ-electrons of $H_2$ donate electron density to the C center. Surprisingly, the AIM analysis for $CH_5^+$ showed that it is pentacoordinated having five C-H bonds, three shorter and two longer, with no interaction between the H atoms of the two long C-H bonds. The AIM analysis finds that the structures of the congeners $SiH_5^+$ and $GeH_5^+$ are however tetrel bonded complexes, where the tetrel atom accepts electron density from the $H_2$ moiety. This work also led to the classification of the 3c-2e bonds based on their connectivity patterns into six different types, V, Y, T, Δ, L, and I (linear).

A large number of computational studies are available that aim to provide understanding about the tetrel bond. In comparison, experimental data involving these interactions are few. We investigated the rotational spectra of the methyl fluoride···water complex (*Chapter 6*) with the intention of observing a carbon/tetrel

bonded structure. However, as of now only the hydrogen bonded structure could be observed. These searches for the rotational spectra, however led to the observation of other complexes of methyl fluoride which were bound by a tetrel bond. The spectra obtained for the $CH_3F\cdots Ar$ complex indicate the presence of the T-shaped structure. However, the tetrel bonded structure has nearly equal binding energy and the large number of unassigned lines could belong to the tetrel bonded structure. The Ar atom is similar to the $Cl^-$ anion and this tetrel bonded structure bears resemblance to the pre-transition state structures for an $S_N2$ reaction. As mentioned earlier, we cannot observe the rotational spectra for the antiparallel structure of the $(CH_3F)_2$ dimer but lines corresponding to this dimer were observed which indicate the presence of either the linear or skewed-linear structures. These two structures are formed when the electron rich fluorine atom of $CH_3F$ donates electron density to the σ-hole over the methyl face of the other $CH_3F$, forming an $F\text{-}C\cdots F$ tetrel bond.

The rotational spectra of the acetonitrile···carbon dioxide complex have been investigated in *Chapter 4*. Calculations show that all the three carbon atoms present in the system are capable of being involved in tetrel bonding interactions. The observed rotational spectra have been assigned to the two lowest energy structures, the π-stacked and the T-shaped structures. The π-stacked structure is bound by an interaction involving the oxygen end of $CO_2$ and the cyano C atom of $CH_3CN$, as well as a $C\text{-}H\cdots O$ hydrogen bond. The nitrogen end of $CH_3CN$ donates electron density to the central C atom of $CO_2$ forming a $N\cdots C$ tetrel bonded interaction. The other two structures calculated are the linear and L-shaped structures where the oxygen end of $CO_2$ donates electron density to the σ-hole over the methyl face of $CH_3CN$ forming an $O\cdots C$ tetrel bond.

The rotational spectra not only provide information about the geometry but also about the intramolecular motions of the molecule under study. The internal motions couple with the overall rotation of the molecules and cause the rotational transitions to split. This gives a picture of the dynamic structure of the molecule. The nuclear quadrupole coupling also provides interesting structural information, such as the bending of the molecule with respect to its molecular axis. Most of the complexes studied in this thesis show the effects of some internal motion. The rotational spectra have been analyzed for these effects and possible feasible motions realized.

The rotational lines of the propargyl alcohol (PA)···water complex are split. The *a*- and *b*-type transitions are split in to two and the *c*-type lines are split into four. These splitting of the lines indicate the presence of some internal motions. The doubling of the lines for the PA···$H_2O$ complex can be attributed to the rotation of the water moiety about its $C_2$ axis. The *c*-type lines are further split in to two because of the wagging motion of the unbound OH of $H_2O$ in the complex changes the *c*-dipole moment. These internal motions provide insight into the dynamic structure of the PA···$H_2O$ hydrogen bonded complex.

A similar doubling of the lines is observed for the hydrogen bonded $CH_3F$···$H_2O$ complex. There are two possible internal motions present in this complex which could lead to the doubling of the lines. One is the rotation of the water moiety about its $C_2$ axis and the other is the internal rotation of the methyl group about its $C_3$ axis. A detailed analysis of the isotopologue spectra would help to find the exact cause of the observed doubling of the lines. A single deuterium substitution of the $H_2O$ unit would break the symmetry of $H_2O$ leading to the observation of only one set of lines, if the splitting in the parent isotopologue were due to the internal motion of water.

The T-shaped structure of the acetonitrile···carbon dioxide complex is bound by a tetrel bond, where the nitrogen end of $CH_3CN$ interacts with the central C atom of $CO_2$. We find that in the rotational spectrum for this structure the K=1 lines are missing. This is expected for indistinguishable spin-less oxygen nuclei having $C_{2v}$ symmetry. The $C_{2v}$ symmetry of the N-$CO_2$ motif for the complex is maintained because the $CH_3$ group is a free rotor. The nuclear quadrupole coupling constant for this complex provides a measure of the bending of $CH_3CN$ about the molecular axis.

Structural analysis of weakly bound complexes provides pertinent results about the nature of the non-covalent interactions that bind them. The structures of the molecular systems in this Thesis were investigated with the purpose of understanding two important non-covalent interactions, the hydrogen bond and the tetrel bond. The study of the hydrogen bonded PA···$H_2O$ complex provided accurate structural information and confirmed that the water unit acts as an O-H···O H-bond acceptor and an O-H···π H-bond donor. Though the structure of the $CH_5^+$ molecule is yet to be experimentally assigned, the AIM analysis along with other evidences scrutinized in *Chapter 5* offer the conclusion that $CH_5^+$ cannot be considered as a complex between $CH_3^+$ and $H_2$. The congeners, $SiH_5^+$ and $GeH_5^+$ however, have different structures and are clearly a

complex of $TH_3^+$ and $H_2$. This study led to the classification of 3c-2e bonds based on the connectivity of the three nuclei which take part in the 3c-2e bond. As mentioned earlier, we intended to study the rotational spectra of carbon/tetrel bonded structures due to the dearth of experimental data available for tetrel bonded structures. We studied the acetonitrile···carbon dioxide complex and could observe the T-shaped and π-stacked structures. Both these structures are bound by tetrel bonds that involve a π-hole on the carbon center.

Rotational spectroscopy provides accurate structural information about the molecules. However, the time taken to collect the spectra is enormous using a cavity based spectrometer and this time can be significantly reduced using a chirped pulse spectrometer. The cavity spectrometer on the other hand has a higher resolution and sensitivity. The high resolution of the spectrometer helps to assign the hyperfine splitting due to the nuclear quadrupole coupling of nitrogen. In *Chapter 3*, we were able to differentiate between the two lowest energy structures of propargyl alcohol···water complex, G-PW-1a and G-PW-1b, these two structures differ only in the position of the non-bonded hydrogen atom of water. This proves the superiority of rotational spectroscopy over techniques such as the matrix isolation infrared spectroscopy which was unable to differentiate between these two structures. Rotational spectroscopy is limited by the type of molecules that can be investigated. The molecules must be brought into gas phase and must possess a permanent electric dipole moment. In *Chapter 6* it is noted that the rotational spectrum of the antiparallel structure of the $(CH_3F)_2$ dimer will not be observable because of the lack of a permanent electric dipole moment.

Though obtaining geometrical parameters are a crucial part of structural analysis, understanding the network of bonds of that make up the molecular structure are important too. Bader's Atoms in Molecules analysis explores the electron density topology to understand the connectivity of the nuclei that form the molecular structure. As is seen in *Chapter 5* the difference between the structures of $CH_5^+$ and $SiH_5^+$/$GeH_5^+$ were clearly illustrated based on the electron density topology. Moreover, the value of $\rho$ and $\nabla^2\rho$ at the bond critical point identifying a non-covalent interaction provides understanding about the nature of these bonds.

Most experimental studies reported on carbon bonded structures involve sp or $sp^2$ hybridized carbon centers. This means that the electron rich moiety interacts with the π-hole on the carbon center. We have observed two such structures in *Chapter 4* of this Thesis, the π-stacked and T-shaped structures of the $CH_3CN\cdots CO_2$ complex. These interactions are similar to n-$\pi^*$ interactions reported in literature involving the carbonyl group and electron donor moieties. One can then include these n-$\pi^*$ interactions under tetrel bonding interactions. Most non-covalent interactions are defined in terms of the σ-hole interaction. There are numerous reports on π-hole in intermolecular bonds as well. However, the carbon bonded interaction experimentally observed till date mostly involves interactions with the π-hole. Recently, a σ-hole over the carbon center in 3,3-dimethyl-tetracyanocyclopropane was found to form a tetrel bond with THF[1]. This Thesis provides a glimpse of observing a tetrel bond involving a σ-hole in the $CH_3F$ dimer. Studying the rotational spectra of the linear or skewed-linear structure of the $CH_3F\cdots CH_3F$ dimer, $O{=}C{=}O\cdots CH_3CN$, and $H_2O\cdots CH_3F$ complexes could provide experimental evidence of a carbon bond involving a σ-hole.

**References**

(1) L. Heywood, V.; J. Alford, T. P.; J. Roeleveld, J.; Deprez, S. J. L.; Verhoofstad, A.; Vlugt, J. I. van der; R. Domingos, S.; Schnell, M.; P. Davis, A.; J. Mooibroek, T. Observations of Tetrel Bonding between sp3 -Carbon and THF. *Chem. Sci.* **2020**, *11* (20), 5289–5293.

**Complete Citation for *Gaussian 09***

Frisch, M. J.; Trucks, G. W.; Schlegel, H. B.; Scuseria, G. E.; Robb, M. A.; Cheeseman, J. R.; Scalmani, G.; Barone, V.; Mennucci, B.; Petersson, G. A.; Nakatsuji, H.; Caricato, M.; Li, X.; Hratchian, H. P.; Izmaylov, A. F.; Bloino, J.; Zheng, G.; Sonnenberg, J. L.; Hada, M.; Ehara, M.; Toyota, K.; Fukuda, R.; Hasegawa, J.; Ishida, M.; Nakajima, T.; Honda, Y.; Kitao, O.; Nakai, H.; Vreven, T.; Montgomery, Jr., J. A.; Peralta, J. E.; Ogliaro, F.; Bearpark, M.; Heyd, J. J.; Brothers, E.; Kudin, K. N.; Staroverov, V. N.; Kobayashi, R.; Normand, J.; Raghavachari, K.; Rendell, A.; Burant, J. C.; Iyengar, S. S.; Tomasi, J.; Cossi, M.; Rega, N.; Millam, J. M.; Klene, M.; Knox, J. E.; Cross, J. B.; Bakken, V.; Adamo, C.; Jaramillo, J.; Gomperts, R.; Stratmann, R. E.; Yazyev, O.; Austin, A. J.; Cammi, R.; Pomelli, C.; Ochterski, J. W.; Martin, R. L.; Morokuma, K.; Zakrzewski, V. G.; Voth, G. A.; Salvador, P.; Dannenberg, J. J.; Dapprich, S.; Daniels, A. D.; Farkas, Ö.; Foresman, J. B.; Ortiz, J. V.; Cioslowski, J.; Fox, D. J. *Gaussian 09,* Revision D. 01, Gaussian, Inc., Wallingford, CT, **2009**

# LIST OF PUBLICATIONS

1. Molecular Beam and Spectroscopic Techniques: Towards Fundamental Understanding of Intermolecular Interactions/Bonds, S. P. Gnanasekar and E. Arunan in *Intermolecular Interactions in Crystals: Fundamentals of Crystal Engineering*, Novoa, J. (Ed.), **2017**, Royal Society of Chemistry

2. Inter/intramolecular Bonds in $TH_5^+$ (T=C/Si/Ge): $H_2$ as Tetrel Bond Acceptor and the Uniqueness of Carbon Bonds, S. P. Gnanasekar and E. Arunan, *J. Phys. Chem. A*, **2019**, *123,* 1168-1178. (This work appeared on the cover page of the journal)

3. Reply to Comments on 'Inter/intramolecular Bonds in $TH_5^+$ (T=C/Si/Ge): $H_2$ as Tetrel Bond Acceptor and the Uniqueness of Carbon Bonds', S. P. Gnanasekar and E. Arunan, *J. Phys. Chem. A*, **2019**, *123, 42,* 9244-9245.

4. A Detailed Classification of three-centre-two-electron Bonds, S. P. Gnanasekar and E. Arunan, *Aust. J. Chem.,* **2020**, *73,* 767-774.

5. Rotational Spectroscopic Studies on the Propargyl Alcohol-Water Complex, S. P. Gnanasekar and E. Arunan (*manuscript under preparation*).

6. Rotational Spectroscopic Studies on the $CH_3CN$-$CO_2$ Complex, S. P. Gnanasekar and E. Arunan (*manuscript under preparation).*

7. Rotational Spectroscopic Studies on Weakly Bound $CH_3F$ Complexes, S. P. Gnanasekar, M. Goubet, R. Georges, and E. Arunan (*manuscript under preparation*).